Millisecond phenomena in X-ray binaries

Wijnands, R.A.D.

Publication date
1999

Document Version
Final published version

Millisecond phenomena in X-ray binaries

Milliseconde verschijnselen in
röntgendubbelsterren
(met een samenvatting in het Nederlands)

Academisch Proefschrift

ter verkrijging van de graad van doctor aan de Universiteit van Amsterdam, op gezag van de Rector Magnificus prof. dr. J.J.M. Franse, ten overstaan van een door het college voor promoties ingestelde commissie in het openbaar te verdedigen in de Aula der Universiteit op dinsdag 16 februari 1999 te 13.00 uur

door

Rudi Adam Dirk Wijnands

geboren te Noordwijk

promotiecommissie:

promotor:	prof. dr. M. van der Klis
overige leden:	prof. dr. J. van Paradijs
	prof. dr. E.P.J. van der Heuvel
	prof. dr. F. Verbunt
	prof. dr. A. Lagendijk
	dr. H. Bloemen
	dr. J. Heise

Sterrenkundig Instituut 'Anton Pannekoek'
Faculteit der Wiskunde, Informatica, Natuur- en Sterrenkunde
Universiteit van Amsterdam

ISBN 90-5776-020-7

Cover illustration: 'Lighthouse and Stormy Sea' (ref. 1316) by Steve Bloom. More images can be found at http://www.stevebloom.com.

Contents

Chapter 1

Introduction

1.1 A brief introduction to X-ray binaries

In X-ray binary systems a neutron star or a black hole is accreting matter from a nearby companion star, either by Roche-lobe overflow or by wind accretion. Due to conservation of angular momentum the accreted matter does not directly fall onto the compact object, but forms an accretion disk around the compact object (see Fig. 1.1). In this accretion disk, angular momentum is transported outwards as the matter spirals in. A large amount of gravitational energy (up to $\sim 10^{38}$ erg s^{-1}) is released when the matter approaches the compact object, heating the inner accretion disk to very high temperatures ($\sim 10^7$ K) and causing it to emit X-rays. The X-ray binaries can be divided into high-mass X-ray binaries (HMXBs) and low-mass X-ray binaries (LMXBs) after the mass of the companion star. In HMXBs the mass of the companion star usually exceeds ten solar masses; in LMXBs the mass is below one solar mass. Systems which contain a donor star with a mass between one and ten solar masses are rare, due to the low efficiency of wind accretion and the instability of the mass transfer through Roche-lobe overflow when the donor is more massive than the mass receiving star. In this thesis, I concentrate on the LMXB systems, in which the mass transfer is dominated by Roche-lobe overflow.

1.2 Why study X-ray binaries?

1.2.1 Basic physics

X-ray binaries contain either a neutron star or a black hole. By studying the accretion processes onto these objects we might obtain information about them, and thereby about fundamental questions such as the equation of state (EOS) of ultra-dense matter and gravitation theory. The interactions of elementary particles in ultra-dense matter, which determine the EOS, are not well understood.

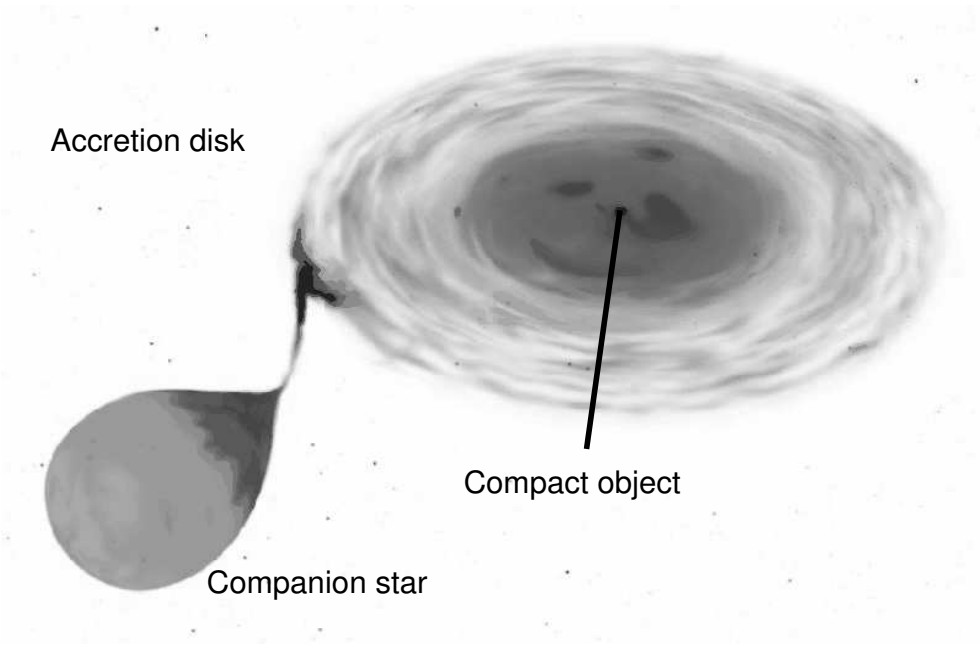

Figure 1.1: An artist's impression of an X-ray binary (credit: NASA/STScI).

Measuring the physical characteristics of neutron stars in X-ray binaries, such as their masses and radii, can constrain the EOS and thus help us understand these interactions. By studying the accretion process in X-ray binaries it may also be possible to examine general-relativistic effects in the strong-field regime. The inner accretion disk is located in a region where such effects are important.

When studying the complex phenomenology of X-ray binaries, the determination of the exact nature of the compact object (neutron star of black hole) in the system is a primary aim. From the X-ray variability the nature of the compact object can be uniquely determined to be a neutron star when phenomena are observed which require a solid surface or a (non-aligned) magnetic field. Typical neutron star phenomena are type I X-ray bursts, which are thought to be thermonuclear flashes on the neutron star surface, and pulsations, which are thought to be due to hot spots (one or multiple) on the neutron star surface spinning around with the star's spin. These phenomena can be used to obtain physical properties of the neutron star, such as its spin rate and its magnetic field strength. However, they have not yet led to reliable estimates of the masses or radii of neutron stars, which are needed in order to constrain the EOS.

Observable black hole phenomena as specific as X-ray bursts or pulsations are not (yet) known. When no bursts or pulsations are observed it is difficult to determine the nature of the compact object using the rapid X-ray variability. Observations have shown that the timing properties up to frequencies of $\sim$100 Hz are very similar between both types of system (see, e.g., Chapter 13), which can

(partly) be understood from the fact that neutron stars are only about three times as large as the Schwarzschild radius of a black hole with a similar mass. To first order one could therefore expect that the accretion flows onto these two types of compact object are very similar, including almost identical characteristic time scales. Only in the innermost part of the disk, closest to the compact object (a few gravitational radii from the center) one would expect that the flow is affected, at least to some level, in different ways in the two types of system, due to the differences in the fundamental physical properties of the compact objects (mass, radius, magnetic moment, spin rate, presence or absence of a solid surface). Therefore, some difference could be present in the rapid X-ray variability of these systems if it originates close to the compact object. The fact that the timing phenomena up to about 100 Hz are very similar in the neutron star and the black hole systems indicates that this part of the rapid X-ray variability originates in the inner disk outside a possible magnetosphere (see also Chapter 13).

1.2.2 Evolutionary history of X-ray binaries and millisecond radio pulsars

The X-ray binaries are also studied because of their role in the evolution of binary stars in general and millisecond radio pulsars in particular. For the general evolutionary history of X-ray binaries I refer to the review by Verbunt & van den Heuvel (1995) and references therein. Here I discuss the link between the X-ray binaries (in particular the LMXBs) and the millisecond radio pulsars.

Ordinary radio pulsars (Hewish et al. 1968) are neutron stars which are formed in supernova explosions of massive stars that take place when these stars reach the end of their lives. When they are born at least some of these neutron stars are rapidly spinning, rotating as fast as 100 times a second (see, e.g., Marshall et al. 1998, for the discovery of a 16 ms single neutron star associated with a $\sim$5000 yr old supernova remnant) and have a high magnetic field strength (10^{12-13} Gauss). The combination of rapid spin and a strong magnetic field produces beamed radio emission at the magnetic poles (see, e.g., Srinivasan 1997 for a more detailed description of pulsar mechanisms) spinning around with the neutron star spin, which shows up on Earth as radio pulses. The pulsar loses energy and slows down within typically 10 million years to a spin rate of one rotation every several seconds. When the pulsar slows down even further the pulsar mechanism is not efficient enough anymore to produce radio emission and the pulsar dies.

In the frame of this model the discoveries (e.g., Backer et al. 1982) of old ($\gg$ 100 million years), low magnetic field (10^{8-9} Gauss), millisecond ($<$ 10 ms) radio pulsars came as a surprise. The fact that these millisecond radio pulsars were often found in binary systems helped to create the following, widely accepted scenario to explain them (see the review by Bhattacharya and van den

Heuvel 1991 and references therein): a millisecond radio pulsar starts off as an ordinary radio pulsar, with the only difference that the pulsar has a low-mass companion star. After the pulsar dies the system continues to evolve on the nuclear time scale of the companion star ($\gg$ 100 million years). Due to the evolution of the companion star or the binary orbital evolution, at a certain moment the companion star fills its Roche lobe. When this happens matter is transferred from the companion star to the old neutron star and the system becomes visible as a LMXB. The accreting matter slightly spins up the neutron star. When the accretion finally stops the matter will have spun up the neutron star to rotation rates of several 100 to perhaps more than 1000 times a second. The accreted matter will possibly also reduce the magnetic field strength of the neutron star, however, the process for this is as yet unknown (see, e.g., Bhattacharya and van den Heuvel 1991). This rapidly rotating, weakly magnetized neutron star will again show up as a radio pulsar, but now as an old millisecond radio pulsar in a binary system. A possible explanation for the single millisecond radio pulsars might be that in very close binaries the intense emission of the pulsars slowly vaporized their companion stars.

The HMXB systems containing a neutron star are most likely not the progenitors of the millisecond radio pulsars. The expected time scales of the evolution of the high-mass companion stars are $< 10^7$ years and the duration of mass transfer in these system would be much less than this. Even at the Eddington mass accretion rate it would take approximately 10^7 years to spin up a neutron star to millisecond rates, i.e., much longer than the mass transfer phase. Therefore, during the X-ray binary phase most likely only in the LMXBs the neutron star can be spun up to such high spin rates. However, in some HMXBs a common envelope phase can occur, in which the neutron star moves through the envelope of its companion star. The very complex physical processes in the common envelope phase require 3-D hydrodynamical calculation and are not sufficiently well understood to determine the precise outcome of the common envelope phase. In some scenarios a millisecond radio pulsar could be formed. For more detailed discussion of this issue and the relation between X-ray binaries and millisecond radio pulsars in general see Bhattacharya and van den Heuvel (1991).

The above described model can explain many characteristics of the millisecond X-ray pulsars, however, problems do exist. For example, the birth rate of the millisecond radio pulsars exceeds that of the LMXBs by a factor of several (see Bhattacharya 1995 for a discussion and references). However, the main observational problem from the point of view of X-ray binaries was, that using data of the LMXBs obtained with the *EXOSAT* and *Ginga* (§ 2.2) satellites did not reveal the predicted coherent millisecond X-ray pulsations in the persistent emission, seriously challenging the model. From the observations of type I X-ray bursts from LMXBs, which only occur when no magnetic field is present or when the magnetic field is weak enough not to affect the burst mechanism (Joss &

Li 1980; Lewin, van Paradijs, & Taam 1993, 1995; Bildsten 1995), the study of their aperiodic timing (§ 1.3.1), and X-ray spectral modeling (Psaltis, Lamb, & Miller 1995) evidence was collected that indeed these systems contain weakly magnetized neutron stars, and that at some level the coherent millisecond X-ray pulsations are expected to be present. A possible explanation for the lack of these pulsations could be the presence of a scattering halo around the neutron star, significantly reducing the amplitude of the coherent oscillations (e.g., Lamb et al. 1985; Brainerd & Lamb 1987). It was only with the *RXTE* satellite (§ 2.3) that this situation changed (see Chapter 11).

1.3 Observing LMXBs in the pre-*RXTE* area

LMXBs have been studied by many X-ray instruments flown in the past. These systems are obvious targets to observe because of their high fluxes and therefore high signal-to-noise ratios. The first known LMXB, Sco X-1, was discovered in 1962 (Giacconi et al. 1962). Early X-ray instruments also discovered the first X-ray pulsars (*Uhuru*; Giacconi et al. 1971) and X-ray bursters (*ANS*, *Vela 5*, *SAS-3*; Grindlay et al. 1976; Belian, Conner, & Evans 1976; Lewin et al. 1976). The study of sustained aperiodic X-ray variability in LMXBs really took off with the *EXOSAT* (1983–86) and the *Ginga* (1987–91; see § 2.2) X-ray satellites. Their relatively large collecting area, long observations of the brightest sources, and their capability to follow up on the discovery of X-ray transients provided a wealth of new information on rapid X-ray variability in LMXBs. The discovery of quasi-periodic oscillations (§ 1.3.1) and the classification of the brightest neutron star LMXBs in Z and atoll sources (§ 1.3.2) considerably improved our knowledge of these objects. With the launch of the *Rossi X-ray Timing Explorer* (see § 2.3) the study of the rapid X-ray variability of LMXBs finally, after more then 30 years, matured.

1.3.1 Discovery of quasi-periodic oscillations

The search for the predicted coherent millisecond X-ray pulsations in the persistent emission of LMXBs (§ 1.2.2) led to the discovery of quasi-periodic oscillations (QPOs) in several of them (see below). In this thesis, the term QPO is used to describe peaks in the power spectrum whose relative width, defined as the ratio between its full width at half maximum and its centroid frequency, does not exceed 0.5. Broader components are usually called 'noise'. However, this criterium is not very strict and sometimes also broad peaked noise components are called QPO. Below, I only discuss the QPOs in the LMXB systems.

The properties of the QPOs (e.g., their frequency and their relation with count rate) discovered in one of the brightest LMXBs (GX 5−1; van der Klis et al. 1985a; Fig. 1.2 *left*) led to the magnetospheric beat-frequency model (Alpar

& Shaham 1985; Lamb et al. 1985) in which inhomogeneities ("clumps") in the inner accretion disk interact with the magnetosphere of the neutron star. These clumps enter the magnetosphere more easily at certain points, for example, near the magnetic poles. Because the magnetosphere is spinning around with the neutron star spin frequency ν_s, the clumps, which revolve around the neutron star with the Keplerian frequency ν_K of the orbit they are in, periodically pass by these points with the beat frequency $\nu_b = \nu_K - \nu_s$. The accretion of a clump on the neutron star is modulated at ν_b and contributes a wave train to the X-ray intensity. The beat frequency is the frequency of the QPO. This model allowed estimations of the magnetic field strength and the spin rate of the neutron star, which were consistent with theoretical expectations (§ 1.2.2).

After this initial discovery of the QPOs in GX 5–1 similar QPOs between 15 and 60 Hz were found in several other systems. However, QPOs with different characteristics were also discovered (Fig. 1.2 *right*; see van der Klis 1995 for details and references). The main differences were their lower frequencies (5–7 Hz) and their different behavior with changing count rate. These QPOs were sometimes seen simultaneously with the other type of QPO. Models of these 5–7 Hz QPO include optical depth oscillations of the radial inflow which are supposed to occur at near Eddington mass accretion rates (Fortner, Lamb, & Miller 1989) and acoustic waves in the accretion disk (Alpar et al. 1992). QPOs were also discovered in BHCs (see van der Klis 1995 for references) but due to scarcity of data containing these QPOs they were not studied in as great a detail as the QPOs in the neutron star systems.

1.3.2 Z and atoll source classification

The introduction of X-ray color-color diagrams (CDs; Hasinger 1988; Hasinger & van der Klis 1989; Hasinger et al. 1989; Schulz et al. 1989) was extremely useful for the study of the correlations between the changes in X-ray spectrum and X-ray timing behavior. Using data obtained with the *EXOSAT* satellite Hasinger & van der Klis (1989) classified the brightest LMXBs into the so-called Z sources and the atoll sources on the basis of this correlated behavior. The Z sources trace out a Z shape like track in the CD (see Fig. 1.3) with the branches called, from top to bottom, the horizontal branch (HB), the normal branch (NB), and the flaring branch (FB). The power spectra of the Z sources show (Fig. 1.3) on the HB, strong band-limited noise (called low frequency noise or LFN) which cuts off below several Hertz, simultaneous with QPOs between 15 and 60 Hz, which are called horizontal branch QPOs or HBOs. On the NB these QPOs can still be seen, often simultaneous with other QPOs between 5 and 7 Hz, which are called normal branch QPOs or NBOs. The NBOs smoothly merge with the 7–20 Hz QPOs seen on the FB, the flaring branch QPOs or FBOs. On all branches also two other noise components are found, one at very low frequencies (the very low frequency noise or VLFN), following a power law, and one at frequencies above

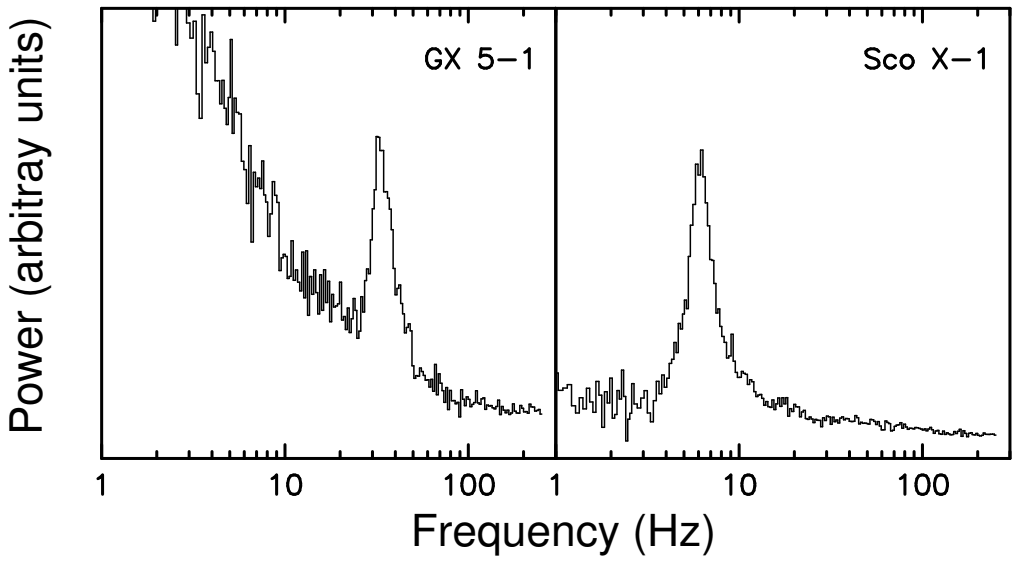

Figure 1.2: The QPOs discovered in the bright LMXBs GX 5–1 (*left*) and Sco X-1 (*right*) using *EXOSAT* data (after van der Klis 1989).

10 Hz (the high frequency noise or HFN), which cuts of between 50 and 100 Hz. Motion of the source along the Z track is thought (e.g., Hasinger & van der Klis 1989) to be due to variations in the mass accretion rate, which is lowest on the HB, increasing on the NB onto the FB, where it reaches the Eddington mass accretion rate.

The atoll sources trace out a curved branch in the CD (see Fig. 1.3), which can be divided in two parts: the island and the banana branch. When the source is in the island motion in the CD is not very fast and can take several weeks. The power spectrum (Fig. 1.3) is dominated by very strong (sometimes more than 20% rms amplitude) band-limited noise, superimposed on which broad bumps or wiggles are sporadically present. These are sometimes called QPOs, although they usually do not fulfill the criterium to be called QPOs (§ 1.3.1). The band-limited noise is also called HFN but it is at much lower frequencies then the HFN observed in the Z sources and most likely they are not related. On the banana branch the source moves much faster through the CD (on time scales of hours to days) and in the power spectrum only a weak (several percent rms amplitude) power law noise component at low frequencies is observed (the VLFN), with sometimes another weak (again several percent rms) noise component at higher frequencies (the HFN) which cuts off around 10 Hz. Some atoll sources have never been observed in the island state, while others have never been observed in the banana state. For atoll sources the mass accretion rate is thought (e.g., Hasinger & van der Klis 1989) to increase when they move from the island onto the banana branch.

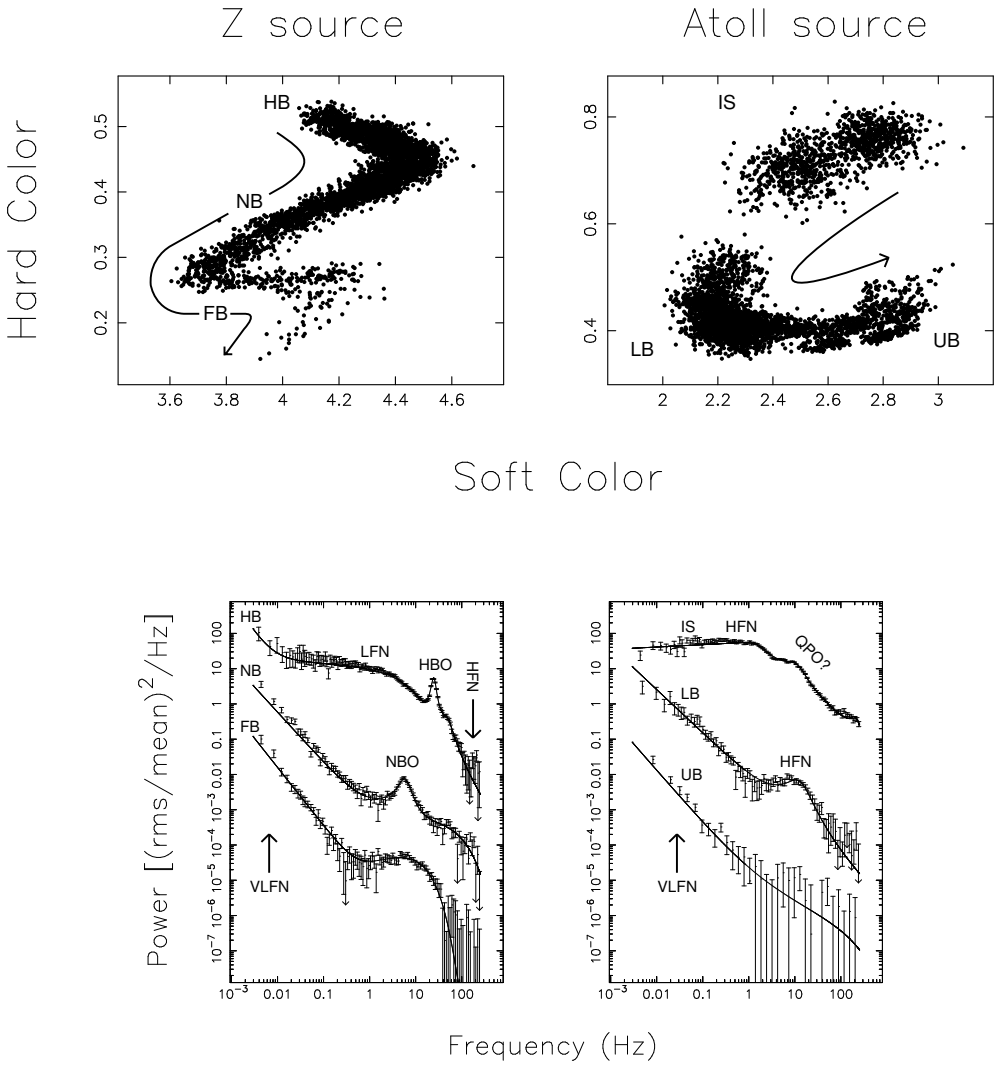

Figure 1.3: X-ray color-color diagrams (*top*) and power spectra (*bottom*) obtained with the *RXTE* satellite typical of Z sources (*left*) and atoll sources (*right*). The direction of $\dot{M}$ is inferred to increase as indicated by the arrows in the color-color diagrams. The soft color is the 3.5–6.4/2.0–3.5 keV count rate ratio and the hard color the 9.7–16.0/6.4–9.7 keV count rate ratio. The power spectra of the HB and the IS are shifted upwards by a factor of 10^4; the power spectra of the NB and the LB by a factor of 10^2.

1.3.3 The *Rossi X-ray Timing Explorer*: its promises

It was expected that with the launch of the *Rossi X-ray Timing Explorer* (*RXTE*) satellite a new window on LMXBs would be opened. Its large collecting area, high telemetry rate, and high throughput would hopefully make it possible to detect periodic and aperiodic kilohertz timing phenomena. Kilohertz aperiodic phenomena are expected because on these time scales a number of processes are likely to take place. For example, circular orbital motion of the inner disk at the general relativistic marginally stable orbit, if the compact object is small enough to allow it, takes place with a period of about 0.6 ms. Various oscillations of the inner disks and the neutron stars are expected to take place on similar time scales. A very important periodic timing phenomenon which it was hoped would be discovered with *RXTE* was the first accretion-driven millisecond X-ray pulsar, which would confirm the evolutionary link between the LMXBs and the millisecond radio pulsars (§ 1.2.2).

Soon after the launch of *RXTE* at the end of December 1995 it fulfilled the aperiodic expectations by discovering nearly coherent oscillations between 330 and 581 Hz during type I X-ray bursts in several atoll sources and QPOs between 200 and 1200 Hz in the persistent emission of many neutron star LMXBs (see van der Klis 1998 for a review). These phenomena promise to allow detailed studies of the inner accretion disk and to finally derive fundamental parameters of the neutron star, such as radii and masses, constraining the equation of state of ultra-dense matter. Very recently, two and a half years after *RXTE*'s launch, at last the first accretion-powered millisecond X-ray pulsar was discovered (Chapter 11). This newly discovered source type promises to make possible unique investigations of the accretion flow near a neutron star, as it will be possible for the first time to measure accretion torques for very small magnetospheric radii, a previously unexplored regime.

1.3.4 Outline

In this thesis, I discuss the rapid periodic and aperiodic X-ray variability in several LMXBs. Most of the data that I have analyzed (see § 2.4 for the analysis methods used) were obtained with the proportional counter array onboard *RXTE* (§ 2.3). However, data obtained with the large area counter onboard the Japanese *Ginga* satellite (§ 2.2) were also used. These data are only used in Chapter 3. There, I discuss a study in which I combined all available data obtained with *Ginga* of the Z source Cyg X-2, and report on the changes in the rapid X-ray timing variability below 100 Hz at different stages of the long-term period of Cyg X-2 (see Wijnands, Kuulkers, & Smale 1996a, not included in this thesis). Although *RXTE* is the best instrument yet for the study of power spectral components below 100 Hz (see, e.g., Chapter 4), most of the major discoveries so far made with *RXTE* data, and reported in this thesis, are the aperiodic (Chapter 5–10)

and periodic (Chapter 11) timing phenomena in LMXBs at frequencies >100 Hz. However, recently also the lower frequency timing phenomena have been receiving more attention (Ford & van der Klis 1998; Psaltis, Belloni, & van der Klis 1999b; Chapters 12 and 13), fueled by a possible interpretation of QPOs with frequency below 100 Hz in terms of Lense-Thirring precession (Stella & Vietri 1998).

Chapter 2

The study of low-mass X-ray binaries

2.1 Introduction

The atmosphere of the Earth prevents us from observing celestial X-rays from the ground. In order to study those X-rays, balloons, rockets or satellites have to be used carrying the X-ray instruments above (most of) the atmosphere. The discovery in 1962 (Giacconi et al. 1962) of the first extra-terrestrial X-ray source besides the sun, Sco X-1 (which turned out to be a LMXB), led to the birth of X-ray astronomy. After this discovery many other celestial X-ray sources were detected using a variety of different X-ray instruments. In this chapter, I discuss the *Ginga* (§ 2.2) and *RXTE* (§ 2.3) satellites and the main X-ray instruments onboard them. I also describe the methods I used to analyze the data obtained with these instruments (§ 2.4).

2.2 The *Ginga* satellite

The Japanese *Astro-C* satellite (Fig. 2.1) was launched from the Kagoshima Space Center on February 5th 1987, after which it was renamed *Ginga*, which means Galaxy. The satellite was put into an orbit at an altitude between 670 km and 510 km, with an inclination of 31°, and an orbital period of ∼96 minutes. It reentered the atmosphere on November 1st 1991. *Ginga* carried three scientific instruments; the large area counter (LAC; § 2.2.1), the all-sky monitor (ASM), and the gamma-ray burst detector (GBD). The ASM consisted of two identical proportional counters, which were sensitive to photons with an energy between 1 and 20 keV. The aim of the ASM was to create an all-sky survey every 1–2 days to look for transient events (which could then be followed up with the LAC) and to collect a long-term record for the brightest X-ray sources. The purpose of the GBD was to detect γ-ray bursts with high energy and time resolution in the energy range 1–400 keV. For a more detailed discussion of the ASM and the GBD I refer to Tsunemi et al. (1989) and Murakami et al. (1989), respectively.

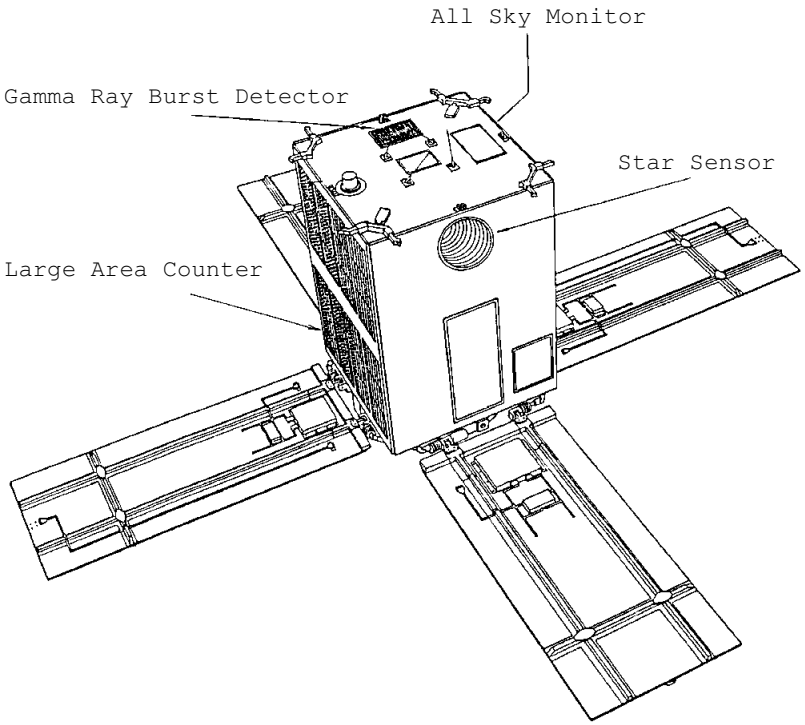

Figure 2.1: The *Ginga* X-ray satellite (after Turner et al. 1989)

2.2.1 The large area counter

The LAC (Turner et al. 1989; Hayashida et al. 1989) was the main scientific instrument onboard *Ginga*. It consisted of eight identical proportional counters with a total effective area of $\sim$4000 cm^2. The instrument was sensitive in the energy range $\sim$1–60 keV, with a best energy resolution of 18% at 6 keV, and had a total field of view of $\sim 1^\circ \times 2^\circ$ FWHM. The data stream obtained with the LAC was interrupted by passages of the satellite through the South Atlantic Anomaly (SAA) and by Earth occultations of the X-ray sources. During SAA passages the instrument was turned off for safety reasons.

With the LAC the X-ray sources could be observed using several different observation modes: the MPC1, MPC2, MPC3, and PC modes. With the MPC1 or MPC2 modes data were obtained in 48 photon energy channels and with a time resolution that could be set between 62.5 ms and 16 s. When the MPC3 mode was used the obtained data had only 12 energy channels but a best time resolution of 7.8 ms. In the PC mode only four overlapping channels were used, and the time resolution was 1 or 2 ms. Although high time resolution modes were available, they were only used sporadically. Only when the satellite was

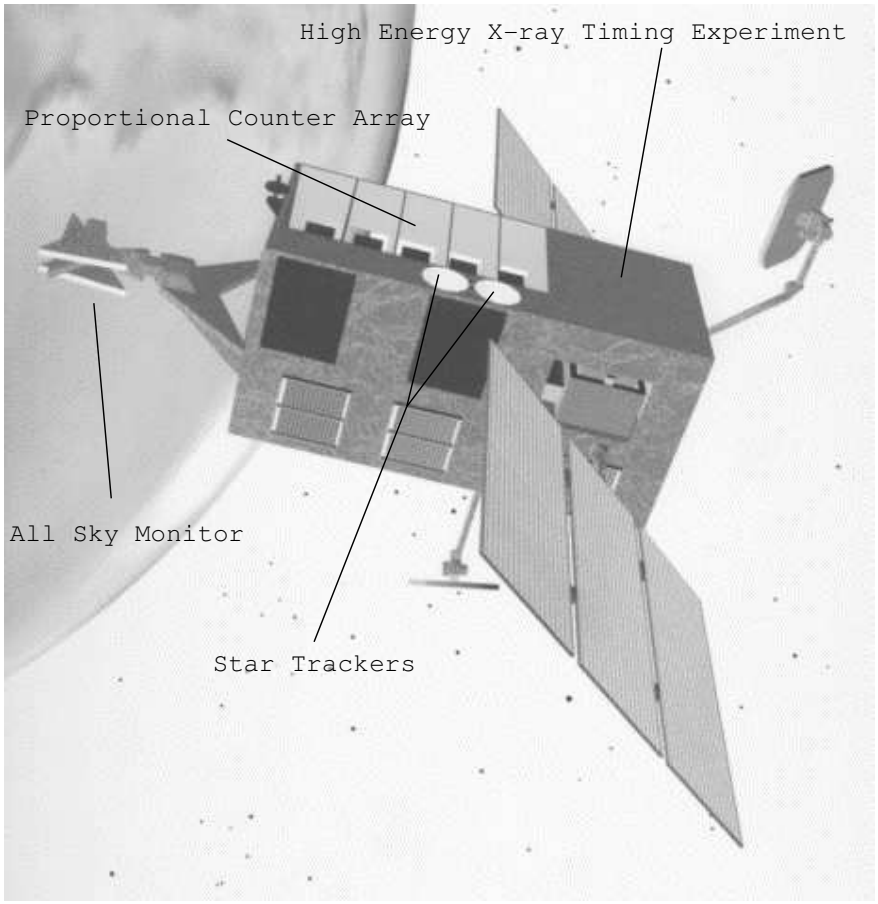

Figure 2.2: The *Rossi X-ray Timing Explorer* satellite (after the cover of *RXTE* Team's 1992 brochure '*XTE – Taking the Pulse of the Universe*')

above Japan in direct contact with the ground station these modes were used. The onboard recorder had insufficient capacity to record the high timing data when direct contact was impossible and, therefore, usually modes with lower time resolution were used.

2.3 The *Rossi X-ray Timing Explorer*

On December 30th 1995, the *X-ray Timing Explorer* (Fig. 2.2) was launched on a Delta II rocket, which put the satellite into a circular orbit at an altitude of 580 km, with an inclination of 22°, and an orbital period of ∼96 minutes. After its successful launch *XTE* was renamed into the *Bruno B. Rossi X-ray Timing Explorer* (or *RXTE*) to honor professor Bruno B. Rossi (1905–1993; Fig. 2.3) for his work as a pioneer in both X-ray astronomy and space plasma physics. The current estimate is that *RXTE* will be operational at least until 2001, and

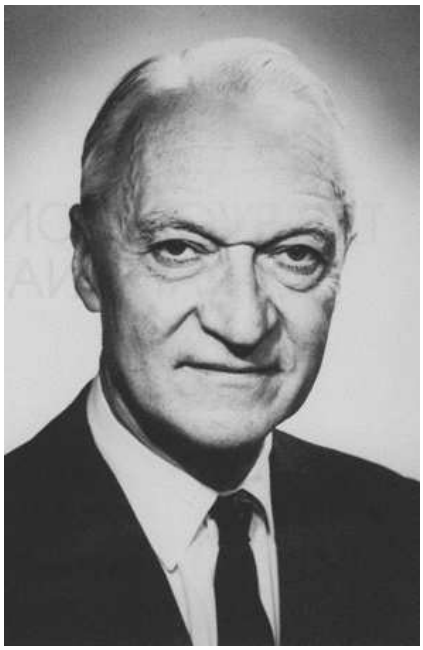

Figure 2.3: Professor Bruno B. Rossi (photograph from the Massachusetts Institute of Technology Museum)

perhaps much longer. *RXTE* carries three instruments; the proportional counter array (PCA; § 2.3.1), the high-energy X-ray timing experiment (HEXTE), and the all-sky monitor (ASM). The data on the X-ray photons detected by HEXTE are processed onboard by HEXTE's own data system before they are sent to Earth; the data from the PCA and the ASM are first processed by an onboard computer called the experiment data system (EDS; Morgan 1994), consisting of eight event analyzers (EAs) of which four are dedicated to the PCA and two to the ASM.

HEXTE consists of two clusters each containing four detectors. Each cluster can rock several degrees (1.5° or 3.0°) away from the source, in order to provide background measurements. HEXTE is sensitive in the energy range 15–250 keV and has a best time resolution of 8 μs. Each cluster has a collecting area of 800 cm^2 and a field of view of 1° FWHM. More information about HEXTE can be obtained from Gruber et al. (1996) and Rothschild et al. (1998).

The ASM (Levine et al. 1996) consists of three wide-angle proportional counters with a total collecting area of 90 cm^2. The ASM is sensitive in the photon energy range 1.3–12.1 keV. The three detectors scan about 80% of the sky every 90 minutes, producing long term X-ray light curves of the ∼100 brightest known X-ray sources (Fig. 2.4). The ASM is also extremely useful to detect within a day source state transitions or outbursts of known and previously unknown X-tray transients (Fig. 2.5), which can then be followed up with pointed PCA/HEXTE observations. The intensities and other basic results obtained with the ASM are immediately made available to the scientific community via internet at: *http://heasarc.gsfc.nasa.gov/docs/xte/asm_products.html*.

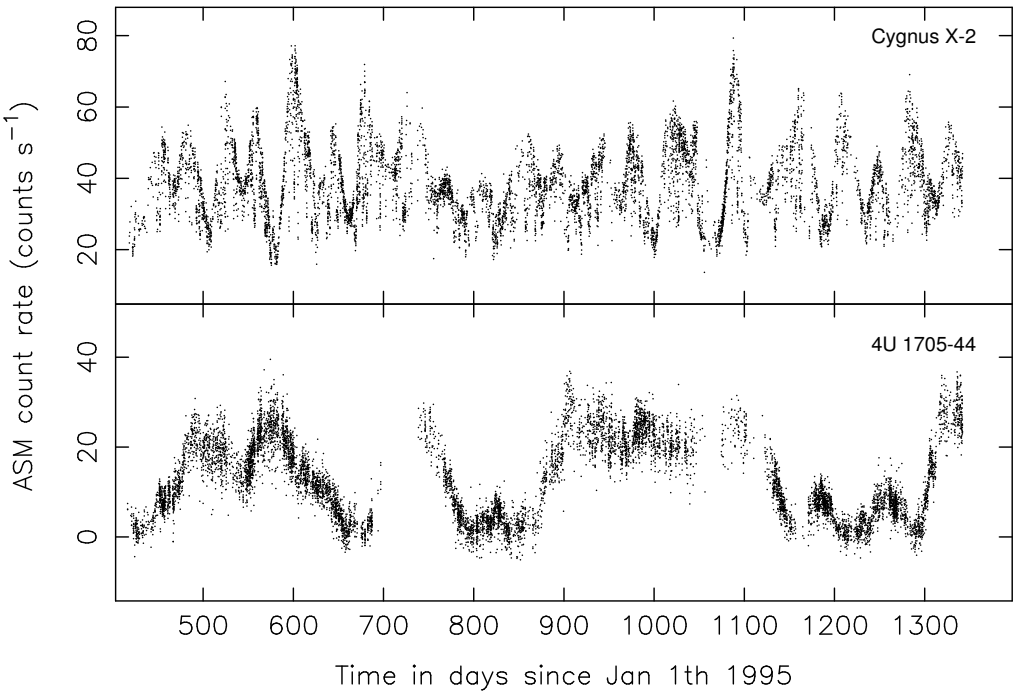

Figure 2.4: The long term *RXTE*/ASM light curves of the Z source Cygnus X-2 (*top*) and the atoll source 4U 1705–44 (*bottom*)

2.3.1 The proportional counter array

The PCA (Zhang et al. 1993) consists of five large proportional counter units (PCUs), with a collimator restricted field of view of 1° FWHM, which is sufficiently small to exclude source confusion in almost all fields (source confusion is still a serious problem in the Galactic center area). The PCUs have a total net area of ∼6500 cm^2 and are effective over the range 2–60 keV with 18% energy resolution at 6 keV and 256 photon energy channels. So far, the gains of the PCUs have been reduced (on March 21 and April 15, 1996) by a total of 30% of their nominal values, changing the effective area below ∼3 keV (a decrease with a factor 2 to 3) and the channel to energy conversion, which should be taken into account in spectral analysis (§ 2.4.1). The data obtained by the PCA are also interrupted by SAA passages of *RXTE* and Earth occultation of the sources. Like the LAC onboard *Ginga* (§ 2.2.1), the PCA is turned off during SAA passages for safety reasons.

In the beginning of March 1996, PCU 3 and 4 experienced serious problems which made it necessary to turn off these detectors temporarily. Although a detailed understanding of the problems has not (yet) been obtained, the *RXTE* team believes that it is beneficial for the detectors to be periodically switched

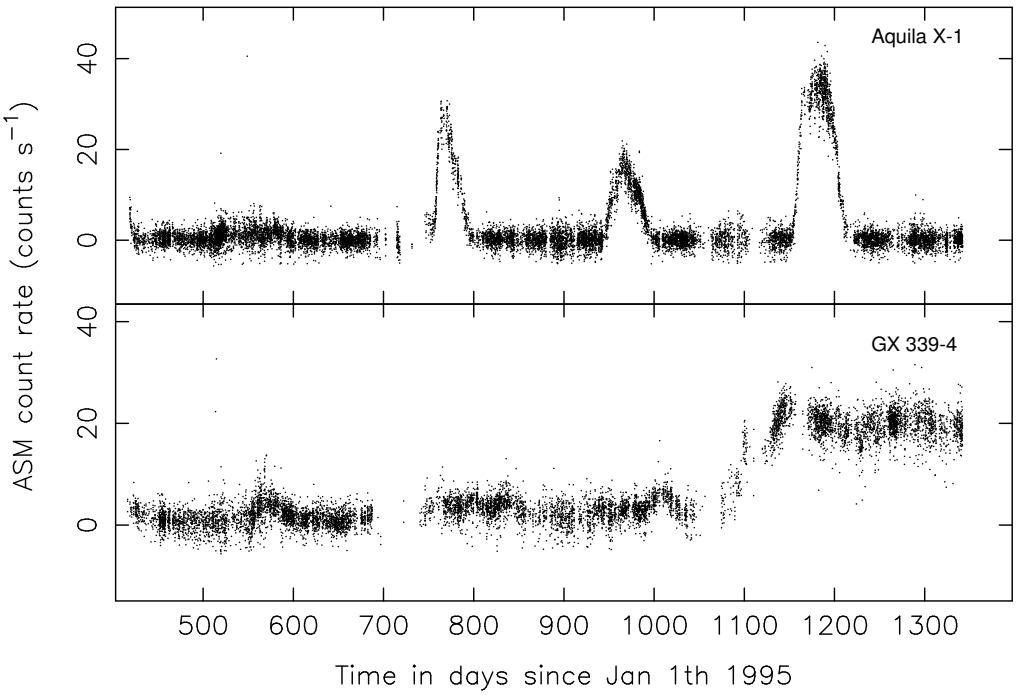

Figure 2.5: The long term *RXTE*/ASM light curves of the neutron star X-ray transient Aquila X-1 (*top*) showing multiple outbursts, and the black hole candidate GX 339–4 (*bottom*) showing a clear state transition near day 1100

off. In practice, these two detectors are switched off during observations of targets which do not require the largest possible area, for example during many monitoring observations. However, also during observations for which the largest collecting area is desired one or both of these two detectors can automatically switch off for safety reasons. So far, the other three detectors do not have these problems. The strategy is to conserve PCU 3 and 4 in order to be able to have all five detectors working when they are really needed. An obvious drawback of observing with two detectors off is the loss of photons and therefore a significant decrease in sensitivity. Another drawback is that the X-ray spectral analysis (§ 2.4.1) becomes more complicated. Due to differences in the energy response matrix of each detector the data of all detectors combined have a different total response matrix than when only three or four detectors are combined. This difference in energy response has to be taken into account during spectral analysis.

2.3.1.1 The standard EDS modes

Two of the six EA's reserved for the PCA are used to collect data in two standard PCA modes with timing and spectral resolutions that will remain unchanged

throughout the mission to provide uniform mission data sets. The two modes are a time series mode (time resolution of 0.125 s in one energy channel; Standard 1 mode) and a spectral mode (time resolution of 16 s in 129 channels; Standard 2 mode). If necessary, though, these modes can be reprogrammed during the life time of *RXTE*.

2.3.1.2 The non-standard EDS modes

The four remaining EA's can be used for other PCA modes with different spectral and timing resolutions. The data in each mode are temporarily stored in a memory buffer before it is read out (which occurs typically every 1 to 16 seconds). The modes can be divided according to the way they record the events. The 'binned' modes record how many events (photons) were detected in a certain selectable time bin. The 'single bit' modes reduce the data to a string of zeroes (representing evenly spaced time bin boundaries) and ones (representing the occurence of an event). However, the science operations facility of *RXTE* will convert these data to a binned mode format before delivery to the observers. In the 'event' and 'goodXenon' modes each event is recorded with its own time marker. When the source is brighter than anticipated, in the binned modes overflows (or rollovers) occur because more events per bin are detected than can be recorded, with the effect that the counting restarts at zero. The other modes can not overflow, however, when the brightness of the source exceeds a certain threshold no more photons can be recorded until the buffer is read out again. This will cause data gaps in the data evenly spaced with the read out time.

Which modes are used best to observe a particular source depends thus on the brightness of the source but also on the scientific goals. In principle the best modes are the goodXenon modes. These modes have the maximal energy resolution of 256 channels and the best time resolution of 1 μs. However, these modes can only be used for relatively weak sources, and will be unable to record all events for the brighter sources. Also, telemetry limits can become a serious consideration. For sources with count rates in excess of 1200 counts s^{-1} in the total PCA energy range modes have to be used with less spectral and time resolution.

The second best modes are the event modes. Already with slightly less spectral and time resolution (e.g., 64 photon energy channels and 122 μs time resolution) the modes can usually record all events. Telemetry limitations then become the dominant factor in determining which modes to choose. Event modes should be used unless the brightness of the source causes the telemetry limitations to be exceeded. In such a circumstance modes have to be used with less spectral or time resolution. If high spectral resolution is desired and sub-millisecond time resolution is not (e.g., to study the spectral behavior of timing phenomena slower than 10 ms) a binned mode, which combines high spectral resolution with modest time resolution, is the most logical choice. If, however, high time resolution is needed to study sub-millisecond timing phenomena, spectral information has

to be sacrificed. Usually single bit modes are used, which have only one energy channel but high time resolution. A total of four of these modes can be used simultaneously (one in each EA) to get some spectral information over the total energy band. If the brightness of the source allows it, a combination of several single bit modes and one event mode can be used to get more spectral resolution at, usually, the highest photon energies. Combination of single bit and/or event modes with a binned mode are also possible in order to obtain more spectral information for the timing phenomena slower than several milliseconds.

The last type of modes often used in observations of LMXBs are the burst trigger and catcher modes. A burst trigger mode continuously monitors the count rate level of the source. When this level exceeds a certain, specifiable threshold the burst catcher mode is activated, which has high spectral or high timing resolution (depending on the scientific aims). The burst catcher modes record the data either in the same way as the binned modes or as the event modes. The event burst catcher modes are only active for a few seconds and are especially useful for catching very bright, but short events. The binned burst catcher modes are particularly useful to observe longer X-ray bursts such as type I X-ray bursts. These modes will record data from several seconds before the trigger until the count rate has dropped below the threshold level. If the count rate stays above this level longer than in a typical X-ray burst it can saturate the telemetry. The combination of a burst trigger and catcher mode is very useful to capture sudden bursts in count rate, which could not be recorded (due to overflows or limitation on the storage capacity) in the modes which continuously record data.

2.3.2 Proprietary and public *RXTE* data

The data obtained with the PCA (and also the HEXTE data) can be either proprietary or public. Proprietary data are data obtained as part of a *RXTE* observing proposal. The principle investigator (PI) on such a proposal can, if desired, create and download the data quickly after the observations are performed from *http://xtesof.nascom.nasa.gov/FITSrequest.html*. The data will be encrypted and only the PI has the password needed to decrypt the data. This fast way of obtaining the data is possible until about 5 days after the observations have been performed. After this time interval the data can not be created anymore and the PI has to wait until the data tape is received in order to be able to analyze the data. One year after the data tape has been sent to the PI the proprietary data will be made public through the *RXTE* public data archive (*http://heasarc.gsfc.nasa.gov/docs/xte/xte_public.html*) or through W^3 Browse (*http://heasarc.gsfc.nasa.gov/W3Browse/*).

The data of some observations are immediately made public to the scientific community at *http://heasarc.gsfc.nasa.gov/docs/xte/SOF/toonews.html*. This occurs for example when observations of a certain source were performed (e.g., this source went in outburst or changed state), and the data obtained were not re-

quested in any active proposals. Also the data of observations performed on alternate targets when the primary targets were unobservable (e.g., they are unexpectedly too dim to be detectable by *RXTE*) are immediately made public.

The data which are available within several days after the observations have been performed (both the proprietary and the public data) are so-called 'real-time data'. This means that the data have not yet undergone final processing to produce the so-called 'production data'. In both data sets the science data are provided, however, in the real-time data the source position and the position of the satellite are not provided, making it for example impossible to correct the arrival times of the photons to the Solar System barycenter, which is needed in certain timing studies (e.g., of pulsars). The production data contain all the necessary information.

2.4 Analysis methods

The analysis of data obtained with X-ray observatories can be divided in the X-ray spectral analysis (§ 2.4.1) and the X-ray timing analysis (§ 2.4.2). However, it has turned out to be extremely fruitful to analyze both the spectrum and the timing behavior simultaneously and correlate the results (§ 2.4.3).

2.4.1 X-ray spectral analysis

In principle, the best way to study the X-ray spectrum of X-ray binaries and in particular LMXBs would be by fitting at any time the obtained X-ray spectrum with the correct physical model, and interpret the changes in the spectrum as physical changes in the system. Despite intensive efforts such a model does not yet exist, and usually the X-ray spectra are fitted with a combination of several physically motivated simple mathematical functions. However, the X-ray spectra can usually be fitted equally well using different parameter sets with the same functions, or by several totally different combination of functions (see, e.g., Christian & Swank 1997). Due to the uncertainties in the physical models and in the response matrices of the X-ray detectors, subtle changes of the X-ray spectrum are very difficult to study and interpret by only fitting the X-ray spectrum, even though they are detected at high statistical confidence. Therefore, to analyze subtle changes in the X-ray spectrum X-ray color-color diagrams (CDs) and hardness-intensity diagrams (HIDs) are usually used.

2.4.1.1 Color-color and hardness-intensity diagrams

To create a CD, the X-ray spectrum is divided into three or four broad (several keV) energy bands. The count rate ratios of those bands provide two colors; a soft color and a hard color. The soft color is the ratio of the count rates in the

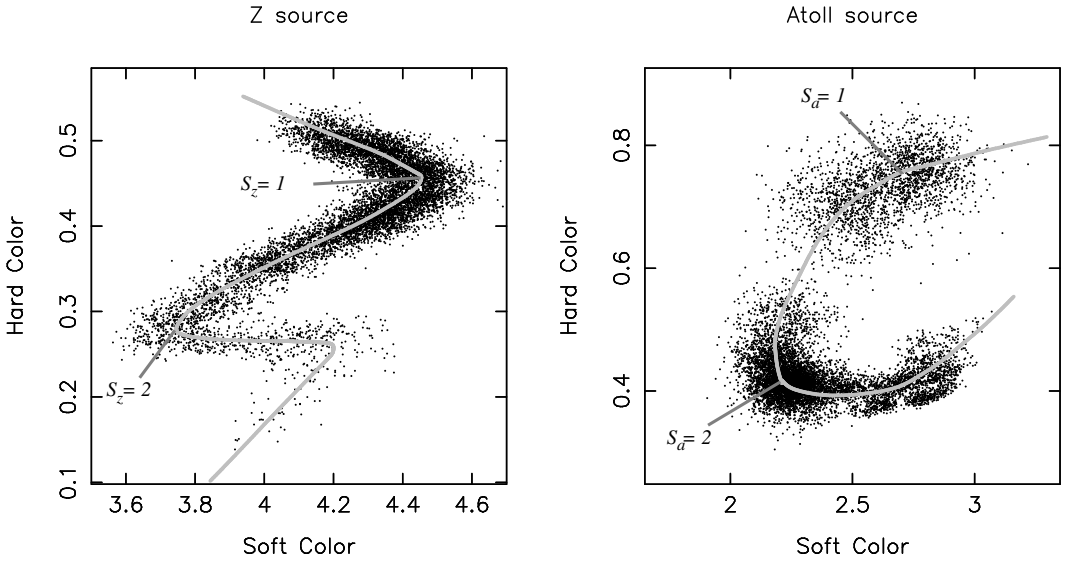

Figure 2.6: Color-color diagram of the Z source GX 340+0 (*left*; Jonker et al. 1998) with the S_z parameterization, and of the atoll source 4U 1608–52 (*right*; Méndez et al. 1999) with the S_a parameterization

two lowest energy bands and the hard color the ratio of the count rates in the two highest energy bands. In both cases, the count rate in the higher energy band of the two is in the enumerator of the ratio: the colors are 'hardness ratios'. A CD is formed by plotting the hard color versus the soft color. In the HID one of the colors (usually the soft color) is replaced by the total count rate, which is called the X-ray intensity, in a certain energy range (usually the total energy range of the three or four bands used to calculate the colors). These diagrams are very sensitive to subtle changes in the X-ray spectrum. However, it is not possible to make a direct comparison of the diagrams obtained with different instruments, or of the diagrams made with the same instrument but before and after changes in the instrumental response have occurred. Due to the different energy responses and channel to energy conversions it is impossible to directly compare diagrams made with data obtained before and after the changes.

The count rates which are used to calculate the colors are corrected for the background. This is especially important for dim sources for which the background (typically 120–150 counts s^{-1} in the total energy range of the PCA) is a significant fraction of the source count rate. The count rates can also be corrected for the dead-time of the instrument, however, in the colors the effect of the dead-time is canceled and usually the data are not dead time corrected. For most sources the dead-time correction on the count rate is smaller than 5%.

Usually with *RXTE*, the CDs and HIDs are made using the Standard 2 data (§ 2.3.1.1). The PCA consists of 5 PCUs, but for safety reasons PCUs 3 and 4

are sometimes switched off (§ 2.3.1). Due to the difference in energy response of the detectors, the CDs and HIDs created with data obtained when all five detectors were on can not directly be compared with diagrams created with the data for which only 3 or 4 detectors were on. In order to know during the whole observation what the position of the source in the diagrams was, only the data obtained with the three detectors which are always on are used. This makes it possible to have intercomparable diagrams covering entire observations.

Using the Standard 2 data to create CDs and HIDs will result in diagrams with a best time resolution of 16 s. Diagrams with better time resolution can be obtained by using the data obtained with the other EDS modes. The advantage of using other modes is that changes in the colors on time scales faster than 16 s can be followed, for example during X-ray bursts or dips. The main disadvantages are the fact that the statistical quality of the colors decreases, the choice of energy bands that can be used is sometimes less free compared to the Standard 2 data, and the boundaries of the energy channels can have been chosen differently between different observations of the same source or between observations of different sources, making comparison of the diagrams more complicated.

2.4.1.2 Measuring the position in the diagrams

In the CDs and HIDs, different types of sources trace out different tracks (i.e., the Z sources trace out a Z-like track and the atoll sources form tracks resembling atolls; see § 1.3.2). The sources do not jump between different branches, but smoothly move along the tracks. It is thought (e.g., Hasinger & van der Klis 1989) that changes in the mass accretion rate onto the compact object are an important cause for the sources to move in the diagrams (although this is not the only reason as shown in Chapter 3).

For the analysis and interpretation of the X-ray timing behavior of the atoll and Z sources it can be very useful to quantify exactly where in the diagrams the source is at a certain time. For Z sources, Hasinger et al. (1990) introduced the concept of rank number along the Z track in the CD as a one-dimensional parameter for the position of the source on the Z track. The motion of the source in the CD is primarily caused by changes in the mass accretion rate, and, therefore, this one-dimensional parameter is directly related to the mass accretion rate. The concept was further refined by Hertz et al. (1992) and Dieters & van der Klis (1999) (see also Chapter 3).

The basic idea is to transform the two color coordinates into one curve length parameter along a spline which has been drawn through the track as defined by the data points (Fig. 2.6 *left*). Two reference points are chosen on this spline; the horizontal/normal branch (§ 1.3.2) vertex (given the value 1) and the normal/flaring branch vertex (given the value 2). The length of the normal branch is thus set to one and all curve lengths along the Z are normalized to this length. In this way, the two colors are transformed into the coordinate S_z, the distance

along the Z track and the coordinate D_z, the distance perpendicular to the Z track. The parameter D_z is only used sporadically. In this S_z parameterization of the data, S_z is then directly related to the mass accretion rate and can be used to describe where on the Z track the source was at any given time.

The S_z parameterization can be performed on the count rate ratios themselves, or on their logarithmic values. In the latter case, the S_z parameterization does not depend on the actual values of these ratios, but only on their relative changes, making it easier to not only to use the S_z parameterization for the CD, but for the HID as well. The advantage of sometimes using the S_z parameterization for the HID instead of for the CD is that in the HID more often a clear Z track is formed, especially at the vertices, were confusion can occur about which branch certain data points belong to. However, this should be used with caution because the exact place of the vertices (which is judged by the analyzing scientist) can occur at different colors in the CD than in the HID, giving different results when plotting source parameters, such as the QPO frequencies, versus S_z.

The S_z parameterization was developed for measuring the position of the Z sources in the CDs and HIDs, but it can also be used for the atoll sources (Fig. 2.6 *right*; see also Méndez et al. 1999). For atoll sources this method is called the S_a parameterization. However, for atoll sources it is not unambiguous how to normalize curve length (i.e., at which point in the diagrams $S_a = 1$ and $S_a = 2$). In order for S_a to be positively correlated to the mass accretion rate (similar to S_z), S_a should increase from the island state to the banana branch.

2.4.2 X-ray timing analysis

To analyze the X-ray timing behavior of the source it is possible to examine the time series directly; however, usually the data are transformed from the time domain to the frequency domain. This is done when the main interest lies in the averaged properties of the timing phenomena (such as random processes in which the details are of minor interest), when the counting noise dominates the variations in the time series, or when the variations in the time series are complex and it is difficult to disentangle the different processes in the time domain. For evenly spaced data usually the fast Fourier transform (FFT) technique is used; however, sometimes different approaches are used, such as the wavelet transform (e.g., Daubechies 1988). For unevenly spaced data, methods such as Lomb-Scargle periodograms (Lomb 1976; Scargle 1982; suited for analysis of both periodic and aperiodic timing phenomena) or phase dispersion minimization (e.g., Stellingwerf 1978; only to study periodic timing behavior) are used. The LAC (§ 2.2.1) and the PCA (§ 2.3.1) usually produce data in bins which are evenly spaced. The all sky monitors, however, usually produce data which are unevenly spaced.

Fourier analysis provides estimates of the amplitude and the phase of fluctuations as a function of frequency. The basic technique is to divide the data into equal-length segments and calculate FFTs of these segments. Power spectra

are then obtained by taking the square of the absolute value of the FFTs, thus discarding all phase information. Usually several to many power spectra are averaged in order to suppress the noise and thus to increase sensitivity. The various features detected in the average power spectrum are then interpreted in terms of the presence of aperiodic and periodic variability in the X-ray intensity. When calculating FFTs, one should use data segments which are sufficiently short to allow the detection of changes in the X-ray variability as the source changes state, and sufficiently long to measure low-frequency variability components. Time lags (or phase lags) of the periodic and aperiodic variability components in the time series can be studied by multiplying the FFT in one channel with the complex conjugate of the FFT in an other channel. This technique is not used in this thesis and I shall not discuss it further. For a more detailed account about this and about using Fourier analysis for timing studies in X-ray binaries in general I refer to van der Klis (1989).

2.4.3 Correlated spectral and timing analysis

A successful approach in the study of LMXBs is to correlate the spectral changes and the changes in the rapid X-ray variability. From first principles it is obvious that some correlation should exist. Both are produced in the inner part of the accretion disk and changes in the mass accretion rate dominate both the spectral changes and the changes in the variability (see also Hasinger & van der Klis 1989). To correlate the spectral changes with the changes in rapid variability one usually selects different regions in the CD or HID either by directly using the X-ray colors or by using the S_z or S_a parameterization (§ 2.4.1.2), and calculates FFTs using the data contained in those regions. This method will give the rapid X-ray variability properties of the source at different positions in the CDs and HIDs, and thus at different mass accretion rates. This method also allows to average more power spectra obtained from data with approximately the same mass accretion rate taken at different epochs in a straightforward manner, which increases the sensitivity to weak aperiodic or periodic phenomena.

Chapter 3

Ginga observations of Cygnus X-2

R. A. D. Wijnands, M. van der Klis, E. Kuulkers, K. Asai, & G. Hasinger
Astronomy & Astrophysics **323**, 399–414 (1997)

Abstract

We have analyzed all available data on the low-mass X-ray binary Cygnus X-2 obtained with the *Ginga* satellite. A detailed analysis of the spectral and fast timing behavior of these 4 years of data provides new insights in the behavior of this Z source. We confirm the previously observed recurrent patterns of behavior in the X-ray color-color and hardness-intensity diagrams consisting of shifts and shape changes in the Z track. However, we find a continuous range of patterns rather than a discrete set. The source behavior in the diagrams is correlated with overall intensity, which varied by a factor of 1.34 in the *Ginga* data. We find that when the overall intensity increases, the mean velocity and acceleration of the motion along the normal branch of the Z track increase, as well as the width of the normal branch in the hardness-intensity diagram. Contrary to previous results we find that, during different observations, when the source is at the same position in the normal branch of the Z track the rapid X-ray variability differs significantly. During the Kuulkers et al. (1996) "medium" level, a normal branch quasi-periodic oscillation is detected, which is not seen during the "high" overall intensity level. Also, during the high overall intensity level episodes the very-low frequency noise on the lower normal branch is very strong and steep, whereas during the medium overall intensity level episodes this noise component at the same position in the Z track is weak and less steep. The explanation of the different overall intensity levels with a precessing accretion disk is difficult to reconcile with our data. Furthermore, we found that the frequency of the horizontal branch quasi-periodic oscillation decreases when Cygnus X-2 enters the upper normal branch, giving a model dependent upper limit on the magnetic

field strength at the magnetic equator of $\sim 8.5 \times 10^9$ G. We also report five bursts, with durations between two and eight seconds, whose occurrence seems to be uncorrelated with location in the Z track, overall intensity level or orbital phase. The burst properties indicate that they are not regular type I bursts.

3.1 Introduction

Cygnus X-2 (discovered by Bowyer et al. 1965) is a very well studied bright low-mass X-ray binary (LMXB). Hasinger & van der Klis (1989) classified the brightest LMXBs into two sub-classes, i.e., the "Z" sources and the "atoll" sources, on the basis of their correlated X-ray spectral and fast timing behavior. Cygnus X-2 was classified as a Z source. In the X-ray color-color diagram (CD) Z sources trace out a Z shaped track and move smoothly, without jumps, through the branches. In all the six known Z sources, except GX 349+2, three branches have been identified, the horizontal branch (HB), the normal branch (NB) and the flaring branch (FB). The transition between the HB and the NB is called the hard vertex, and between the NB and the FB the soft vertex. The variation of one single parameter, i.e., the mass transfer rate to the compact object ($\dot{M}$), is thought to produce the tracks (e.g., Hasinger & van der Klis 1989; Lamb 1991).

Recent studies of *EXOSAT* data of the Z sources (see Kuulkers et al. 1994a, 1996, 1997; Kuulkers & van der Klis 1996) indicate that the Z sources can be divided into two groups, the Cyg-like sources (Cyg X-2, GX 5-1, and GX 340+0) and the Sco-like sources (Sco X-1, GX 349+2, and GX 17+2). The Cyg-like sources show motion of the Z pattern in the color-color diagram and the hardness-intensity diagram (HID), their HBs are horizontal, and when the sources are on their short FBs the X-ray intensity generally decreases. The Sco-like sources, instead, do not display significant motion of their Z pattern in the CD, their HBs are almost vertical, and the X-ray intensity increases when they move onto their extended FBs. It was proposed (see Kuulkers & van der Klis 1995b, and references therein) that the Sco-like sources are viewed face-on (low orbital inclination) and the Cyg-like sources more edge-on (higher orbital inclination), and that the motion of the Cyg-like sources could be caused by accreting material, such as a precessing accretion disk getting into the line of sight.

Theoretical studies (Psaltis, Lamb, & Miller 1995) indicate that a difference of magnetic field strength can explain some of the differences between the Cyg- and the Sco-like sources. In their model, the Cyg-like sources have a somewhat higher magnetic field strength ($B \sim 5 \times 10^9$ Gauss) than the Sco-like sources ($B \sim 10^9$ Gauss). Their so-called unified model can explain the Z tracks in the CDs and HIDs and the difference in the Z shapes between the Cyg-like and Sco-like sources. However, no explanation is given for the fact that the Cyg-like sources display motion of the tracks, whereas the Sco-like sources do not.

Cygnus X-2 shows the most pronounced motion of the Z pattern in the CD

Table 3.1: Log of the observations

Nr	start (UT)	end (UT)	total time (h)	mode	binary phase[a]
1	1987-06-07 15:29	1987-06-10 21:43	6.74	MPC1, MPC3, PC	0.70-0.03
2	1988-06-10 05:33	1988-06-14 04:05	28.80	MPC2, MPC3, PC	0.14-0.54
3	1988-10-06 00:50	1988-10-07 23:40	18.24	MPC1, MPC2, MPC3, PC	0.12-0.30
4	1989-10-22 01:41	1989-10-24 01:06	8.07	MPC1, PC	0.81-0.01
5	1990-11-30 16:13	1990-12-02 13:31	2.32	MPC1, MPC3	0.91-0.11
6	1991-05-15 01:16	1991-05-16 10:00	7.83	MPC1, MPC3	0.71-0.85
7	1991-06-09 18:26	1991-06-11 06:41	11.32	MPC1, MPC2, MPC3	0.33-0.48

[a] orbital phase using the ephemeris given by Crampton & Cowley (1980), see Kuulkers et al. (1996) note 4.

and the HID of all Z sources. One of the first observations of Z pattern motion in the HID was found by Vrtilek et al. (1986) using Einstein MPC data. They observed a factor of two increase in intensity between different epochs but also an increase of the intensity on time scales less than a day. At that time the Z track behavior of Cygnus X-2 was not yet known, so they interpreted the variations as due to orbital effects. Nowadays we know that most of the intensity variations of Cygnus X-2 are due to the non-periodic motion of the source through the Z track, and most likely associated with changes in $\dot{M}$. However, not all intensity variations that were found by Vrtilek et al. (1986) can be explained in this manner. In their Figure 2, three branches are present which now can probably be identified as NBs. These branches are shifted with respect to each other, making this in retrospect the first indication that Cygnus X-2 displays motion of the Z-track in the HID.

Clear evidence for Z track motion in the CD and the HIDs was found when different *EXOSAT* observations of Cygnus X-2 were compared with each other (Hasinger et al. 1985b; Hasinger 1987, 1988). Hasinger (1987) discussed six *EXOSAT* observations of Cygnus X-2. He found that the Z tracks of different observations were displaced in the HIDs with respect to each other. Hasinger et al. (1985b) and Hasinger (1988) reported a state of Cygnus X-2 with very low count rates. The count rates, especially in the high energy bands, flared and the spectrum was hard. In the CD, this observation looked like a large FB, and it is displaced to harder colors with respect to other Cygnus X-2 *EXOSAT* observations (see also Kuulkers et al. 1996).

Vrtilek et al. (1988) investigated the long-term temporal variability of Cygnus X-2 using six different instruments on three satellites (*OSO 8*, *HEAO 1*, and *Einstein*). Three count rate states between 2 and 10 keV were found. During the lowest state the spectrum was harder than during the other two states.

The motion of the Z trough the CD and HID was again reported in early *Ginga* observations of Cygnus X-2 reported by Hasinger et al. (1990). They found that the Z track in the HID during the October 1988 observation was shifted to higher intensities (by a factor two) with respect to the July 1988 observation. In the

CD the Z track of the October 1988 observation was shifted downward parallel to the NB with respect to the July 1988 observation. The shape of the Z track in both the CD and the HID was different between these two observations. During the July 1988 observation the Z track performed a loop in the HID at the NB-FB transition, such that along the FB the source first rose in intensity and later decreased. During the October 1988 observation no such loop was found. Instead, along the FB the source immediately started to decrease in intensity. In the CD of the July 1988 observations the HB is diagonal and the FB is large. In the October 1988 CD the HB is horizontal and the FB is very small.

Kuulkers et al. (1996) reanalyzed all *EXOSAT* observations of Cygnus X-2. They also reported motion of the Z pattern and different shapes of the Z track. They compared their results with all previous reports on Cygnus X-2, and described the phenomenology in terms of three different intensity levels (possibly part of a continuous sequence). In the rare low level Cygnus X-2 displays a hard spectrum at the lowest intensities. These episodes seemed to occur at binary phases 0.8-0.2 (with phase 0.0 defined as the X-ray source superior conjunction), however not in each orbital cycle. Vrtilek et al. (1988) and Kuulkers et al. (1996) discussed various possible explanations, e.g., that at these times the secondary hides its heated face and/or part of our view of the inner disk region, so that most of the observed radiation then comes from a scattering hot corona surrounding the inner accretion disk, or that a tilted disk or a hot spot at the outer disk hide much of the inner disk region from our view. The other two intensity levels were called the medium and the high level. A periodicity in the occurrence of these intensity levels could not be found. The shape of the Z track in the HIDs was dependent on these intensity levels. As the source moves onto the FB during high level episodes, the intensity immediately starts to decrease and the FB in the HID is almost horizontal. They called this a 'color-independent' dip. When the source moves up the FB during medium level episodes the intensity first increases and then decreases. The FB in the HID is also pointed upwards and therefore referred to as a 'color-dependent' dip. No Z track was observed during the low level.

The fast timing behavior of Z sources is closely related to the position of the sources in the CD and HID (Hasinger & van der Klis 1989). On all branches a very-low frequency noise (VLFN) and a high frequency noise (HFN) component in the power spectra can be identified. On the horizontal and normal branches also low frequency noise (LFN) can be identified which decreases in amplitude from the HB to the upper normal branch and disappears on the lower normal branch. Quasi-periodic oscillations (QPOs) are found on the horizontal branch (called HBOs) with a frequency from $\sim$12 Hz at the left end of the HB up to $\sim$55 Hz near the hard vertex, and then remains constant up to halfway the normal branch. However, a decrease of the frequency of what is probably the HBO down the NB in GX 17+2 was found (Chapter 4). On the NB QPOs (NBOs) are observed with a frequency between 5–7 Hz. Sometimes the HBO is seen simultaneously with

the NBO, indicating different mechanisms are responsible for these QPOs. On the flaring branch sometimes a QPO (FBO) is seen with a frequency near 7 Hz at the beginning of the FB, but rapidly increasing in frequency up to ∼20 Hz further up the FB. The 7–20 Hz flaring branch QPO has not been found on Cygnus X-2. However, Kuulkers & van der Klis (1995a) detected a QPO on the FB of Cygnus X-2 with a frequency of 26 Hz. This QPO was found in an intensity dip on the FB and is believed to be a different phenomenon from the 7–20 Hz FBO.

Two Z sources are known to show bursts. GX 17+2 (Tawara et al. 1984; Kahn & Grindlay 1984; Sztajno et al. 1986; Kuulkers et al. 1994b, 1997) shows bona fide type I burst (thermonuclear flashes on the neutron star surface, Hoffman et al. 1978). In Cygnus X-2 burst-like events have been reported (Kahn & Grindlay 1984; Kuulkers, van der Klis, van Paradijs 1995). Kuulkers et al. (1995) detected 9 burst-like events in the archival *EXOSAT* data of Cygnus X-2. These burst-like events had a short duration (t_{burst}∼3 s), did not show evidence for cooling, and did not occur in specific regions of the Z track. To date it is unclear whether these burst-like events are genuine type I bursts.

In this chapter, I present an uniform analysis of all available data obtained by the Large Area Counter (LAC) instrument on board the *Ginga* satellite.

3.2 Observations and analysis

3.2.1 The satellite and the observations

Cygnus X-2 was observed with the *Ginga* satellite (Makino and the *ASTRO-C* team 1987) during 7 observations. For a log of the observations we refer to Table 3.1. Due to Earth occultations and the high background in the South Atlantic Anomaly (SAA) the observations were broken up into many pieces with a length of several tens of minutes.

The LAC instrument (Turner et al. 1989) on board *Ginga* was used in several different observation modes: the MPC1, MPC2, MPC3, and the PC modes. In the MPC1 and the MPC2 (hereafter MPC1/2) modes, the source was observed in 48 photon energy channels and the time resolution ranged from 62.5 ms to 16 s. In the MPC3 mode, the source was observed in 12 channels with a best high time resolution of 7.8 ms. In the PC mode, only four overlapping channels were used and the time resolution was 1 or 2 ms. By manipulating the coarse gain (CG) amplifier, which had two levels, the energy range could be set to either 0.5–37 keV (low CG level) or to 0.3–18.7 keV (high CG level). By changing the high voltage (HV) levels the energy range could be extended to even higher energies (e.g., up to 60 keV). Due to these different CG amplifier settings, HV level settings and lower discriminator settings (see Turner et al. 1989) different sets of energy channels were used at different times.

Table 3.2: The energy bands used to create color-color and hardness-intensity diagrams. We used the following definitions of the colors: Soft Color = ^{10}log(Band 2/Band 1), Hard Color = ^{10}log(Band 3/Band 2). The intensity is the count rate in the energy range given in column 6

Observation period	Mode	Band 1 (keV)	Band 2 (keV)	Band 3 (keV)	Energy range used for the total intensity (keV)
1987 and 1988	MPC1/2 and MPC3	2.3–4.7	4.7–7.0	7.0–18.6	2.3–18.6
1991	MPC1/2	2.3–4.7	4.7–7.0	7.0–18.6	2.3–18.6
1991	MPC3	2.4–4.7	4.7–7.1	7.1–18.8	2.4–18.8
1989 and 1990	MPC1/2	2.9–4.8	4.8–6.7	6.7–19.0	2.9–19.0
1989 and 1990[a]	MPC1/2 and MPC3	1.2–3.8	3.8–7.6	7.6–19.0	1.2–19.0
1987	PC	0.6–2.9	2.9–9.1	7.9–12.3	0.6–9.1 + 0.8–12.3
1988	PC	0.8–2.9	2.9–9.1	7.9–12.3	0.8–9.1 + 0.8–12.3
1989	PC	1.2–5.7	1.2–15.7	5.7–17.9	1.2–17.9 + 1.2–15.7

[a] These bands were used in order to determine in which part of the Z Cyg X-2 was during the 1990 MPC3 observation (see § 3.3.2.2).

Generally the satellite attitude control system kept the viewing direction within 30 arcmin from the position of Cygnus X-2, which corresponds to a collimator transmission of $\gtrsim$ 70%. The systematic error in the observed count rates due to uncertainties in the collimator transmission is of the order of a few percent (Hertz et al. 1992). Due to, e.g., a long period without attitude control measurements the offset angle sometimes increased causing the collimator transmission to decrease to about 40%. The LAC collimator shows energy-dependent transmission effects due to reflection of soft X-rays (below ∼6 keV) from the collimator walls at large offset angles (Turner et al. 1989). This low energy reflection was not taken into account when the intensities were corrected for collimator transmission (§ 3.2.2), which gives rise to an overestimation of the count rates for the lowest energy channels. When we encountered data with a collimator transmission below ∼60% we used Figures 13 and 14 of Turner et al. (1989) in order to correct the count rates below 6 keV. Usually this means that the count rates were corrected for an overestimation of 3%–4%. Sometimes the offset angle was even higher and the collimator transmission came below ∼20%. At such high offset angle the collimator response is independent of incident photon energy (Turner et al. 1989). However, at these times the fractional uncertainty in the collimator transmission, and thus in the corrected count rates, due to aspect jitter is $\gtrsim$15% (Hertz et al. 1992). For this reason, we did not use any data with a collimator transmission $\lesssim$ 40% in our analysis.

3.2.2 Color-color and hardness-intensity diagram analysis

For our studies of the CDs and the HIDs we used data rebinned to a time resolution of 4 seconds, which were background subtracted and corrected for dead-time and aspect using the ISAS analysis system. The PC binned data were not corrected for background because no good background determinations are available for them. The 16 s resolution MPC1 data of the November 1990 and June 1991 observations had multiple register overflows and were left outside our analysis. The 4 s resolution MPC1 data of the June 1987, the October 1989, the May/June 1991 observations, and the 2 s resolution MPC2 data of the June/October 1988 and the June 1991 observations had single overflows and the true count rates could be recovered.

In order to make CDs and HIDs, we calculated the soft color, the hard color, and the total intensity. The definitions of those quantities and the energy bands used in order to calculated them, are given in Table 3.2. Instead of the colors and intensities, usually used in the literature, we used the logarithmic value of those quantities. Any process which influences the intensity in the specified energy bands by multiplication, i.e., the instrumental response, produces only a shift in the CD and the HIDs. Using logarithmic values of the colors and the intensity therefore makes it easier to compare data of the same source obtained by different instruments, by simply shifting the diagrams. Also, the S_z parameterization (§ 3.2.3) in this way does not depend on the actual values of the quantities or the count rates, but only on their changes. It can now be used not only for the CD but for the HIDs as well.

Usually, the total intensity was taken as the sum of the count rates in the same energy bands as were used to calculate the colors. However, for the PC data of the 1987 and the 1988 observations, the total intensity was defined as the count rate in all four energy channels. For the 1989 PC data, the count rates in the three lowest energy channels were summed, as the fourth channel only contained background photons. The lowest energy boundary of the 1987 PC data differs slightly from the lowest boundary in the 1988 PC data (Table 3.2). The effect on the Z in the CD and HID is negligible and therefore we discuss the 1987 and 1988 PC data together. The 1989 PC data is discussed separately because of the different energy boundaries (see below).

In order to compare the MPC1/2 data with the MPC3 data we rebinned the MPC1/2 data to 12 channels using the same energy boundaries as the MPC3 data. Although in the 1991 observations the MPC3 data had slightly different energy boundaries compared to the MPC1/2 data (Table 3.2), the difference was small and had no significant effect on the place of the Z in the CD and HID.

Due to the HV and CG levels of 1989 and 1990 observations (energy range 1–60 keV), the energy boundaries of their spectral channels differ from those of the other five observations. Due to the broad energy channels, the energy

boundaries of these observations could not be successfully interpolated to the boundaries of the others. Therefore, we discuss the 1989 and 1990 observations separately from the other observations. In order to get an approximately uniform analysis we took for the MPC1 mode data colors which resembles the colors used in the other observations.

3.2.3 S_z parameterization

Hasinger et al. (1990) introduced the concept of rank number of the Z track in the CD. This concept was refined by Hertz et al. (1992) and by Dieters & van der Klis (1999). Here, we use the method described by Dieters & van der Klis (1999) for the measurement of the position along the Z, with the difference that we perform all operations on the logarithmic colors and intensity values (see § 3.2.2). We therefore transform the two logarithmic color coordinates (hard color and soft color) into the coordinates S_z (the distance along the Z track) and D_z (the distance perpendicular to the Z track). We also calculated the velocity (V_z) and the acceleration (A_z) along the Z track, as defined as

$$V_z(i) = [S_z(i+1) - S_z(i-1)]/[T(i+1) - T(i-1)], \tag{3.1}$$

where $S_z(i)$ is the position in the Z track on time $T(i)$, and

$$A_z(i) = [V_z(i+1) - V_z(i-1)]/[T(i+1) - T(i-1)], \tag{3.2}$$

respectively (see also Dieters & van der Klis 1999). The length of the NB is scaled to 1 and positions on the HB and FB are normalized to the length of the NB. The hard vertex corresponds to $S_z = 1$, and the soft vertex to $S_z = 2$. We applied the S_z parameterization also on the Z tracks in the HID. We obtained a different set of S_z and D_z values which we call S_z^{hid} and D_z^{hid}.

The distribution of D_z or D_z^{hid} is a measure for the thickness of the branches in the CD or HID, respectively. To quantify the thickness of the branches we calculated the sample standard deviation of the D_z and D_z^{hid} distributions using the method described in the Appendix. As a measure of the overall velocity and acceleration in the CD the standard deviations of the V_z and A_z distribution were used, again using the method outlined in the Appendix.

3.2.4 Power-spectral analysis

For the power-spectral analysis we used the MPC3 and PC data. We made FFTs of 128 s data segments which resulted in a frequency range of 0.0078–64 Hz (MPC3 7.8 ms resolution data) or 0.0078–256 Hz (PC 1.95 ms resolution data) in the power spectra. We calculated the FFTs for the energy interval 1.2–18.6 keV (June 1987, June/October 1988, and May/June 1991 MPC3 observations) or 1.2–19.0 keV (November 1990 MPC3 observation). For the PC mode we used

the sum of the energy intervals 0.8–12.3 keV and 0.6–9.1 keV (June 1987), or 0.8–12.3 keV and 0.8–9.1 keV (June and October 1988), or 1.2–17.9 keV and 1.2–15.7 keV (October 1989).

The average level of the photon counting noise, modified by dead-time processes (the Poisson level), was estimated and subtracted using a counter dead-time of 206 μs (MPC3 data) and 16.5 μs (PC data) (see Mitsuda & Dotani 1989). In the resulting power spectra several components can be identified:

- very low frequency noise (VLFN), which we fitted with $A_{\rm V}\nu^{-\alpha_{\rm V}}$, where ν is the frequency, $\alpha_{\rm V}$ is the power-law index, and $A_{\rm V}$ the normalization constant.

- low frequency noise (LFN) and a high frequency noise (HFN), are fitted with $A_{\rm L,H}\nu^{-\alpha_{\rm L,H}}e^{-\nu/\nu_{\rm L,H}}$, where $\alpha_{\rm L,H}$ is the power-law index, $\nu_{\rm L,H}$ the cut-off frequency, and $A_{\rm L,H}$ the normalization constant, for the LFN (L) and HFN (H), respectively.

- HBO, its harmonic, NBO, and FBO, are fitted with Lorentzians:

  $A_{\rm Q}\frac{1}{(\nu-\nu_{\rm C})^2+(\Delta\nu/2)^2}$, where $\nu_{\rm C}$ the centroid frequency, $\Delta\nu$ the full width at half maximum (FWHM) of the QPO, and $A_{\rm Q}$ the normalization constant.

The fractional rms amplitudes of the various noise components were determined by integrating their contribution over the following frequency ranges; VLFN: 0.001–1 Hz, LFN: 0.01–100 Hz, HFN: 0.01–100 Hz. We note that variations in the collimator transmission could influences the VLFN (see, e.g., the *EXOSAT* data of GX 17+2; Kuulkers et al. 1997). The errors in the parameter values were calculated using an error scan through χ^2 space using $\Delta\chi^2 = 1$. Due to the poor statistics it was not always possible to fit a HFN component. When HFN was fitted we used $\alpha_{\rm H} = 0$ because in Z sources this index was found to be consistent with zero (Hasinger & van der Klis 1989; Dieters & van der Klis 1999). The best way to examine the correlations between the timing behavior and the position on the Z track is to select a small part of the Z track, using the $S_{\rm z}$ parameterization and determine what the corresponding timing properties are for that segment. However, our data did not allow this procedure as we did not have enough data at high time resolution for this procedure to give sufficient statistics. Therefore, we first selected parts of the data that covered a relatively small $S_{\rm z}$ range and afterwards determined an average $S_{\rm z}$ value and range for each data set.

3.3 Results: the spectral variations

The CDs and HIDs for all observations are presented in Figures 3.1–3.6. Each point represents a time interval of 120 seconds of which >50% contained data.

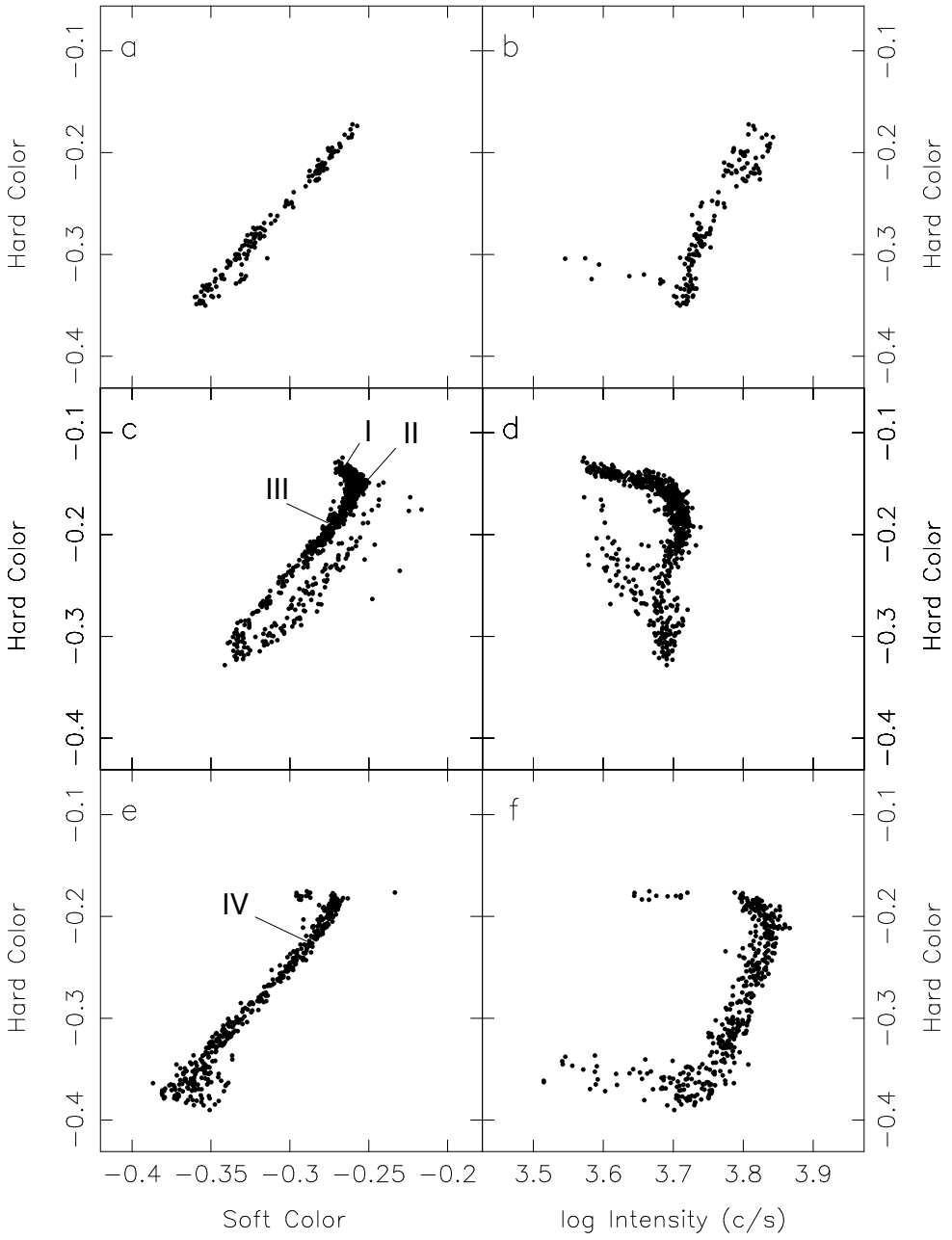

Figure 3.1: *The June 1987, June 1988, and October 1988 observations.* MPC modes: *a*, *c*, and *e* are the color-color diagrams and *b*, *d*, and *f* are the hardness-intensity diagrams for the June 1987, June 1988, and October 1988 observation, respectively. For the definitions of the colors and the intensity see text and Table 2. The positions of the I, the II, and the III (*c*) indicate the position in the Z track were the three June 1988 burst occurred. The position of the IV (*e*) indicates were in the Z the October 1988 burst occurred

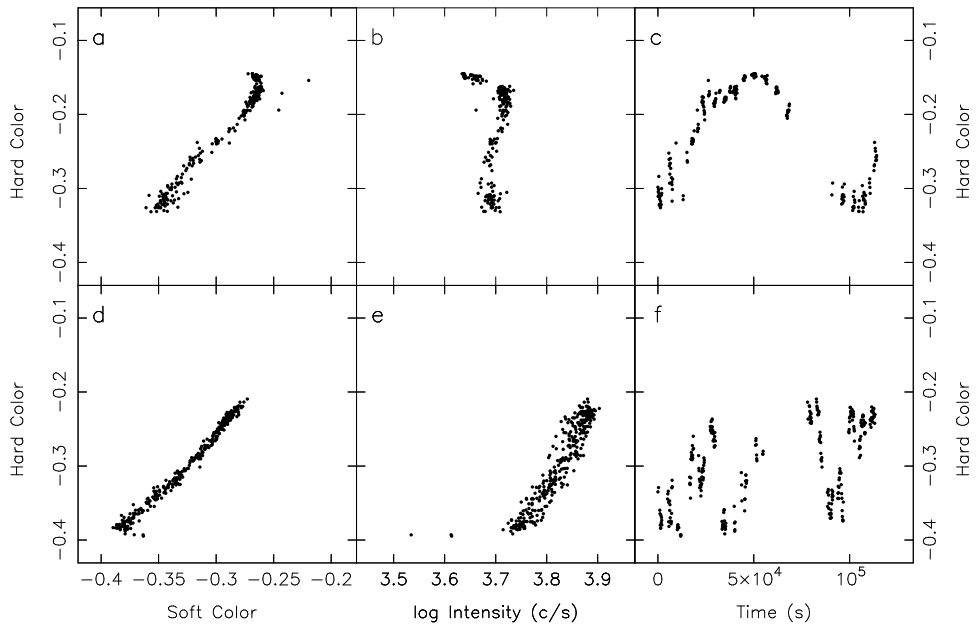

Figure 3.2: *The May 1991 and June 1991 observations.* MPC modes: *a* and *d* are the color-color diagrams, *b* and *e* are the hardness-intensity diagrams, and *c* and *f* are the hard color curves for the May and June observations, respectively

3.3.1 The 1987, 1988, and 1991 observations

3.3.1.1 June 1987

In both the CD and HID of the MPC-data (Figs. 3.1*a* and *b*) a NB can be seen. No HB is present. The FB is only just seen in the CD, but it is clearly visible in the HID. The count rate decreases as soon as the source enters this FB. In the HID, the upper NB is approximately twice as broad as the middle and lower NB. This broadening of the upper NB is not seen in the CD. The PC data (Figs. 3.5*a* and *b*) only show a NB. The June 1987 data were previously discussed by Mitsuda & Dotani (1989), however, they used 16-second data points. Due to the scatter induced by Poisson statistics they could not detect the broadening of the upper NB in the HID.

3.3.1.2 June 1988

This observation was already discussed by Hasinger et al. (1990). Parts of the data (from 1988 June 12 02:16 to 1988 June 13 08:49 UT and from 1988 June 14 01:29 to 03:59 UT) were obtained when the offset angle was about 1°, giving a collimator transmission of 40%–60%. We corrected these data for the overestimation of the count rates in the low photon energy bands (§ 3.2.1). In the CDs of the MPC and PC data (Figs. 3.1*c* and 3.5*c*, respectively) clearly a HB, a

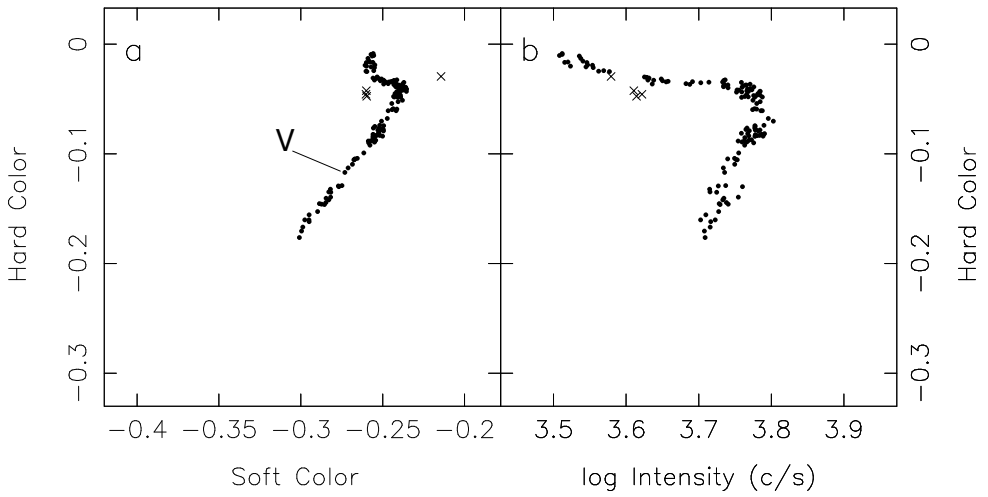

Figure 3.3: *The October 1989 and November 1990 observations.* MPC1 modes: *a* is the color-color diagram and *b* is the hardness-intensity diagram. The dots (•) are the October 1989 data, the crosses (x) are the November 1990 data. The position of the V indicates where in the Z the October 1989 burst occurred

NB and an extended FB are visible. The horizontal branch is not horizontal but diagonal. The HIDs of the MPC and PC data (Figs. 3.1*d* and 3.5*d*, respectively) also show all three branches. When the source moves into the FB, the count rate first slightly increases and then decreases.

3.3.1.3 October 1988

The CD and HID of the MPC data (Figs. 3.1*e* and *f*) were reported before by Hasinger et al. (1990). In the CD and HID all three branches are visible. The HB is really horizontal and when the source enters the FB the count rate decreases immediately. In the CD and HID of the PC data (Figs. 3.5*e* and *f*, not previously reported), three separate areas of points are visible. Comparing these figures with the MPC data of this observation, the upper and the middle area (indicated by HV and SV, respectively) are probably near the hard and soft vertices, respectively. This is confirmed by the fast timing analysis (see § 3.4). The status of the third, lowest area (indicated by E) is unclear. The fast timing properties (see § 3.4 and Table 3.4) suggest that Cygnus X-2 was near the soft vertex, either on the NB, or on the FB.

3.3.1.4 May 1991

Part of the data of this observation (from 1991 May 15 01:16 to 04:53 UT) was obtained when the offset angle was large and the collimator transmission low

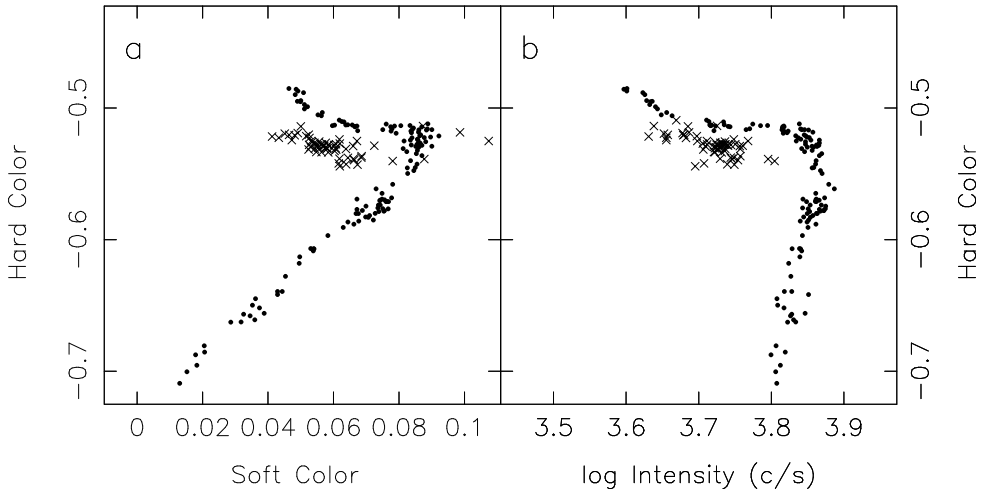

Figure 3.4: *The October 1989 and November 1990 observation.* MPC1 and MPC3 modes: *a* is the color-color diagram and *b* is the hardness-intensity diagram. The dots (•) are the October 1989 data, the crosses (x) are the November 1990 data. The definitions of colors differ from the ones used in Figure 3.3, see text and Table 3.2

(40%–60%). We attempted a correction to the low photon energy channels for the count rate overestimation (§ 3.2.1). During the time of low transmission, Cygnus X-2 seemed to be on the NB, as judged from the CD, but in the HID the same data points were displaced from the NB. Correcting the count rates for the low-energy flux overestimation was not enough to place the points exactly on the NB in the HID. In order to show more clearly the soft vertex and the beginning of the FB (see below), we did not include these points in the HID, and did not use them in our further analysis. In the CD (Fig. 3.2*a*), the HB is short and diagonal. No clear FB can bee seen, but a full NB can. In the HID (Fig. 3.2*b*) the beginning of a FB can be seen, which is not made up of the points with the low collimator transmission. The count rate increases when the source enters the FB.

3.3.1.5 June 1991

During part of this observation (from 1991 June 10 10:06 to 16:02 UT) Cygnus X-2 was observed with a very large offset angle and a collimator transmission of 10%–20%. We did not include these data in our analysis because of the large uncertainties in the count rates (§ 3.2.1). The remaining data (Figs. 3.2*d* and *e*) show a clear NB, and a hint for a FB, which is most clearly seen in the HID. When examining the data at higher time resolution we see a more developed FB. No HB is observed. When the source moves onto the FB the count rate decreases immediately. The FB is approximately horizontal. Notice that the very broad NB in the HID corresponds to a narrow NB in the CD.

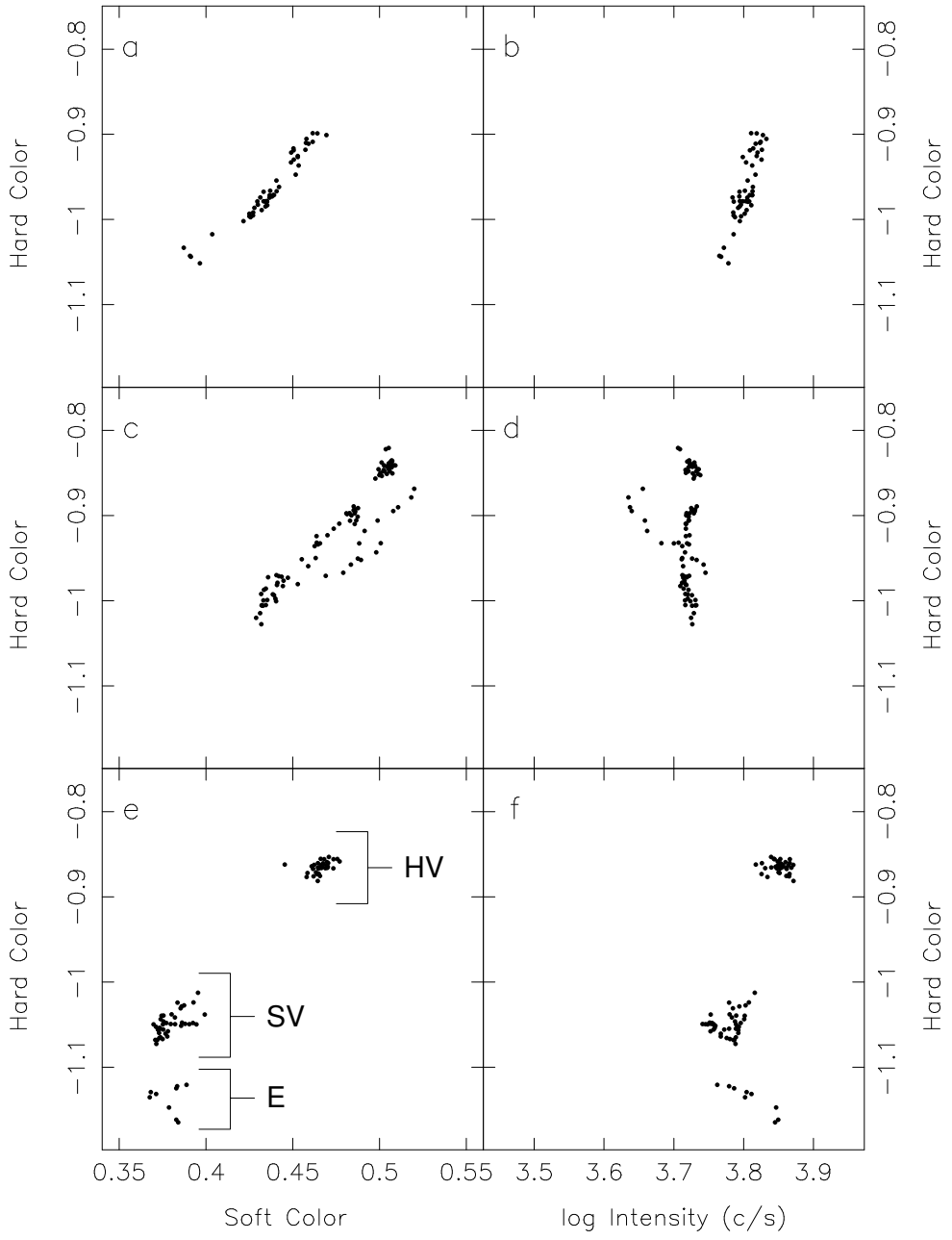

Figure 3.5: *The June 1987, June 1988, and October 1988 observations.* PC mode: *a*, *c*, and *e* are the color-color diagrams and *b*, *d*, and *f* are the hardness-intensity diagrams for the June 1987, June 1988, and October 1988 observation, respectively. Most likely the parts of the Z in the CD of the October 1988 observation (*e*) indicated by HV and SV belong to the hard vertex and soft vertex, respectively. The state of the area indicated by E is unclear. See further text

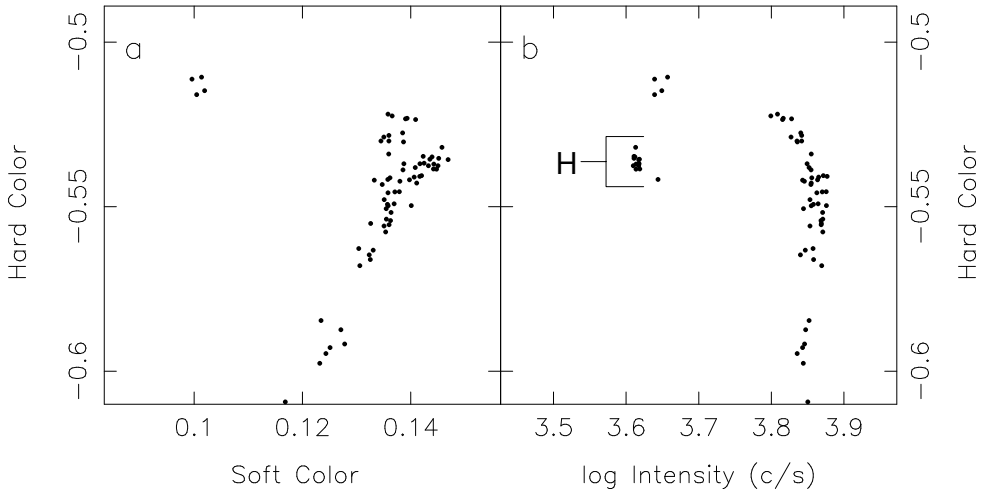

Figure 3.6: *October 1989 observation.* PC mode: *a* is the color-color diagram and *b* is the hardness-intensity diagram. An harmonic of the HBO was seen in the part of the Z in the HID (*b*) which is indicated by the H. See also text

3.3.1.6 Comparison of the 1987, 1988, and 1991 observations

Comparing the five observations we find the following. The overall intensity level, defined as the mean count rate on the NB, changed by a factor of 1.34 between the observations. The lowest intensities were observed in June 1988 and May 1991, the highest intensities in October 1988 and June 1991. Intermediate intensities were observed in June 1987. Following the classification of Kuulkers et al. (1996) our lowest overall intensities correspond to their "medium level" and our highest overall intensities to their "high level". We shall adopt this terminology in what follows. As we also observe a level intermediate between these two, it is obvious from our data that the medium and high levels are probably part of a continuous range instead of a discrete set. We did not observe Cygnus X-2 when it was in the so-called "low level" (Kuulkers et al. 1996). We confirm the previously reported (Hasinger et al. 1990; Kuulkers et al. 1996 and references therein) correlation between the shape of the Z in the CDs and HIDs and the overall intensity level.

In the *medium level*, the HB is not horizontal but oriented under an $\sim$45°angle in the CD. It is less steep in the HID. In the CD, the HB is quite short compared to the NB. In the HID, the HB and NB are of the same length. The NB is nearly exactly vertical in the HID, with almost no changes in intensity. The FB is very well developed in the CD, with large color changes. In the HID, when the source enters the FB the count rate first increases, then, further up the FB, decreases. In the *high level*, the HBs in both CD and HID are nearly horizontal. In the CD, the HB is again short compared to the NB, while in the HID it is approximately the same length as the NB. The NB in the HID shows a positive correlation

between hard color and intensity. The FB in the CD is hardly visible, with hardly any color changes. In the HID, the FB is well developed and horizontal (little color changes), and when the source moves onto the FB the count rate immediately decreases. The *"intermediate" level* shows characteristics of both the medium and the high level. Due to lack of data nothing can be said about the orientation of the HB during the intermediate level. The hard color of the NB in the HID shows a positive correlation with intensity, similar to the high level, although not as clear. The FB in the CD is hardly visible, with small color changes, also similar to the high level. When the source moves on the FB in the HID, which is not horizontal, this is similar to the medium level, the count rate immediately decreases (like in the high level). In the CD and HIDs, the Z-track shifts downward (to softer colors), parallel to the NB in the CD, when the overall intensity level increases. In the medium level, it is at its highest position (hard color), in the intermediate level it is lower, and in the high level it is lowest.

When we compare the NBs in the HIDs we see that the branch width changes with overall intensity. In the high level, the NB is broader than in the medium level. The NB in the intermediate level is only broad in its upper part. Comparing the hard color curves (Figs. 3.2*c* and *f*), we see that the character of the motion through the NB depends on intensity level. In the medium level, the colors change slower than in the high level. These new results are discussed in the next section.

3.3.1.7 The motion through the Z using S_z

The S_z parameterization makes it possible to investigate the kinematics of the motion along the Z track in more detail (see Dieters & van der Klis 1999). When examining S_z as a function of time, it is evident that the source does not jump through the branches, but moves smoothly along the Z track. In the high level, Cygnus X-2 seems to move faster up and down the normal branch than when the overall intensities are lower (compare Figs. 3.2*c* and *f*). In order to investigate this, we calculated the velocity (V_z) and acceleration (A_z) distributions (§ 3.2.3; Dieters & van der Klis 1999). We find that the distributions are symmetric about zero: there is no difference in the motion up and down the Z track. The scatter of V_z and A_z increases from the HB, through the NB, to the FB indicating that the source moves through the Z most slowly on the HB, faster on the NB and fastest on the FB. On the NB the scatter of V_z and A_z increases when the overall intensity increases. In order to quantify this, we determined the standard deviations of V_z (σ_{V_z}) and A_z (σ_{A_z}). On the NB, σ_{V_z} and σ_{A_z} show a strong correlation with overall intensity (see Figs. 3.7*a* and *b*). They increase by a factor $\sim$1.4 and $\sim$1.5, respectively, when the overall intensity increases by a factor of 1.34. No correlations between σ_{V_z} and σ_{A_z} on the FB and the overall intensity were found. For the HB the data do not allow a conclusion on this point.

In order to examine the width of the NB in the HID, we applied the S_z parameterization on the Z track in the HID (§ 3.2.3). The D_z^{hid} time series are

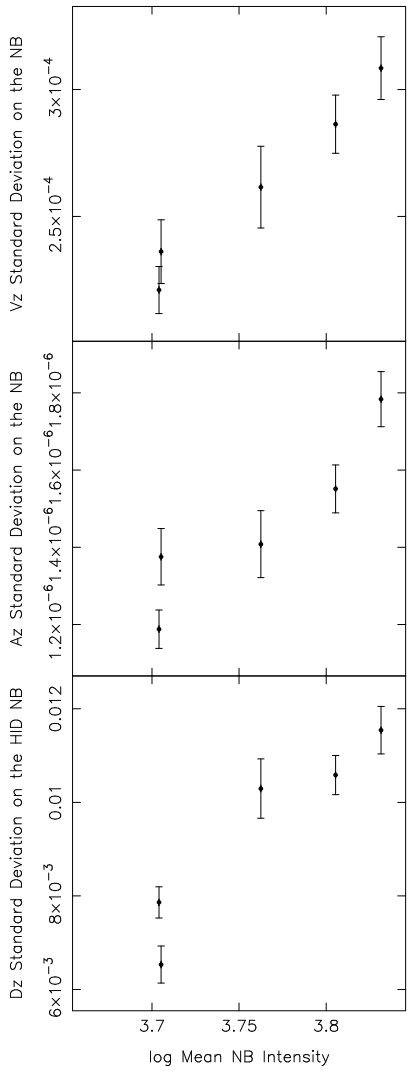

Figure 3.7: Standard deviation of V_z (a), A_z (b) and D_z^{hid} (c) on the NB against the log mean intensity (counts s^{-1}) on the NB during the different observations

symmetric around zero. The lack of points on the HBs and FBs makes a definitive conclusion about the evolution of the width of the Z from the HB, via the NB to the FB, impossible. However, when two or more branches are present the Z width seems to increase from the HB to the NB, and further on the FB. As mentioned earlier (§ 3.3.1.6) we find that the NB width in the HID increases when the overall intensity increases. This effect is visible as a strong increase in the standard deviation of D_z^{hid} on the NB with overall intensity (Fig. 3.7c). When the overall intensity increases by a factor $\sim$1.34, the standard deviation of D_z^{hid} on the NB increases by a factor $\sim$1.75. On the other branches the standard deviation of D_z^{hid} stays approximately the same at all overall intensities. When we examine the NB width in the CDs, we do not find any increase in the standard deviation of D_z with overall intensity: the NB has approximately the same width at all intensity levels in the CDs.

3.3.2 The 1989 and the 1990 observations

3.3.2.1 The MPC1 mode data

In order to be able to compare these observations roughly with the other observations, and because of the very broad photon energy channels of the MPC3 mode (see § 3.2.2), we made CDs and HIDs of the MPC 1 data only. Because during the November 1990 observation the MPC1 mode was used only very briefly, we combined the October 1989 (dots) and November 1990 (crosses) data in Figure 3.3. In both the CD and the HID the HB and the NB are clearly visible. No FB is present. An upward curve can be seen at the beginning of the HB during the October 1989 observation. Such an upward curve of the HB was previously reported by Kuulkers et al. (1996) in the 1985 *EXOSAT* observation on day 301/302. The color points of the November 1990 observation are displaced with respect to the October 1989 data.

3.3.2.2 The MPC3 mode data

In order to include the MPC3 data and to find out on which part of the Z track the source was in during the November 1990 observation, we had to use different colors, with broader energy bands. For comparison, we did the same for the October 1989 data. The energy bands used are given in Table 3.2. Figure 3.4 shows a clear HB and NB for the October 1989 data (dots), as before, and the curve upwards of the HB, although less pronounced. The November 1990 data (crosses) show only a HB which is shifted in color with respect to the October 1989 data. No upward curve is visible in the November 1990 data.

3.3.2.3 The PC mode data

The October 1989 PC data CD and the HID (Fig. 3.6) show a NB, the hard vertex, and parts of the HB. In the HID, the points (indicated by the H) on the HB with the lowest intensity and low hard color are not on the HB in the CD. They are placed on the hard vertex in the CD. The fast timing behavior would suggest that those points are at the left end of the HB (see § 3.4.4)

3.3.2.4 Comparison of the 1989 and 1990 observations to the other observations

The 1989 and 1990 observations were performed using different energy bands as compared to the other observations. Therefore, we cannot directly compare their overall intensity levels. However, if we assume that the difference in the total count rate between 2.3–18.6 keV and 2.9–19.0 keV is minor we see that the overall intensity of the October 1989 observation is about the same as for the June 1987 observations. There is no NB available for the November 1990

observation so no direct comparison with the other observations of the mean NB intensity can be made. However, the shift of the HB during this observation with respect to the October 1989 HB indicates that the overall intensity of the November 1990 observation was higher than the overall intensity of the October 1989 observation. Therefore, we conclude that the October 1989 observation was taken at an overall intensity level in between the medium and high level, and the November 1990 observation during a high level episode.

3.4 Results: the fast timing behavior

The results of the power spectra analysis are shown in Tables 3.3 and 3.4.

3.4.1 Very-low frequency noise

Since in the HB the VLFN is low (e.g., Hasinger & van der Klis 1989), we were in some cases unable to measure the VLFN, at the left end of the HB. In the June 1987 and June 1988 observations, we fixed the power law index of the VLFN when Cygnus X-2 is on the HB.

We have high time resolution data of the same part of the Z track (especially near the soft vertex) but during different overall intensity levels. The comparison of these data reveals a very significant difference of the VLFN properties between the medium and high overall intensity levels in the lower part of the NB. During the medium overall intensity observations (June 1988 and May 1991) we detect a weak (0.5%–1% rms amplitude) and flat (power law index of $\sim$1) VLFN on the lower NB and near the soft vertex. The rms amplitude and power law index increase to $\sim$5.3% and $\sim$1.4, respectively, on the upper FB in the June 1988 observation. However, during the high overall intensity observations (October 1988 and June 1991) we detect a very strong (8.5% and 4.5% rms, respectively) and steep (index of 1.4–1.7) VLFN on the lower NB and near the soft vertex. The VLFN decreases in strength to about 6.7% rms amplitude on the FB in the October 1988 observation. We note that this strong VLFN near the soft vertex cannot be caused by changing collimator response. During the intermediate overall intensity observation (June 1987) we see VLFN with a strength of $\sim$1.5% rms and power law index of $\sim$1.1 near the soft vertex, which increases to $\sim$4.2% and $\sim$1.4, respectively, on the FB. This gradual change in the strength and steepness of the VLFN as a function of overall intensity level is clearly visible in Figures 3.8*a*–*i*. These figures show the power spectra in the medium level, the intermediate level, and the high level at approximately the same S_z values.

It is remarkable that when Cygnus X-2 is in the high level, the VLFN near the soft vertex is strong and steep and that when the source is in the medium level the VLFN at the same S_z values is much weaker and less steep. During intermediate levels, the VLFN is weak and flat on the NB but strong and steep

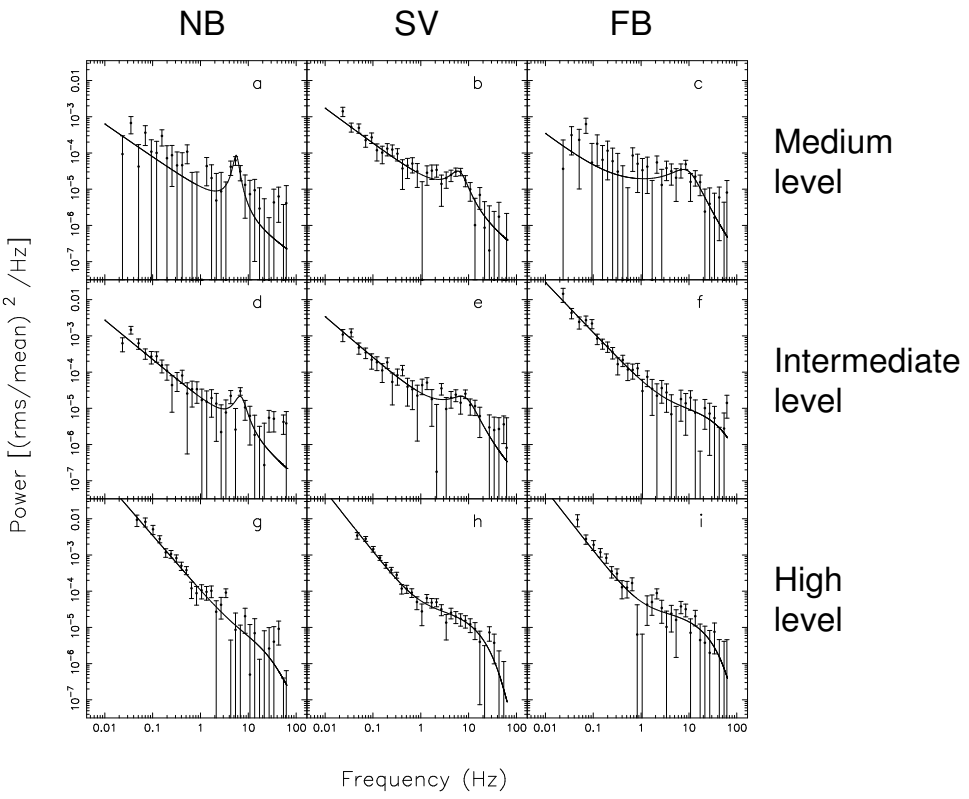

Figure 3.8: Power spectra of different observations at about the same S_z, the power spectra in the column indicated with NB, SV, and FB, are taken on the lower normal branch, the soft vertex, and the flaring branch, respectively: *a*, *b*, and *c* are the May 1991 power spectra at S_z=1.79±0.07, 1.97±0.10, and 2.05±0.06, respectively, *d*, *e*, and *f* are the June 1987 power spectra at S_z=1.83±0.02, 1.97±0.07, and 2.10±0.03, respectively, and *g*, *h*, and *i* are the October 1988 power spectra at S_z=1.856±0.008, 2.00±0.02, and 2.10±0.01, respectively

on the FB. The correlation of the amplitude and steepness of the VLFN near the soft vertex with mean overall intensity level is not strict. At the highest overall intensities (1991 June) the amplitude is about the half of the one at the second highest overall intensity (1988 October), and the spectrum is less steep.

3.4.2 Low-frequency noise and high-frequency noise

Due to the scarcity of high time resolution data when Cygnus X-2 was on the HB or near the hard vertex and the difficulty in determining S_z, comparisons of the LFN between the observations are difficult. The June 1987 and 1988 observations show a LFN with an rms of ∼4.7% on the HB which decreases to ∼3.0% on the hard vertex and upper NB. The November 1990 observation shows that the rms

of the LFN increases from the beginning of the HB to the hard vertex (from ∼5.8% to ∼6.5% rms). The same is seen in the October 1989 observation (LFN rms from 4.5% to 5.5%), but in this observation the rms decreases to 3.8% when the source moves into the upper NB. No clear correlation between the power law index (0.0–0.3) or the cut-off frequency (4.0–13 Hz) with S_z is seen.

When LFN or NBO were fitted, it was difficult to fit the HFN simultaneously, possibly due to interference between them (see also Kuulkers et al. 1994a). When it was necessary to fit a HFN component it had an rms between 1%–2% and cut-off frequencies between 10 and 20 Hz. The October 1989 PC data show a strong HFN (∼6% rms) with a high cut-off frequency between 30 and 50 Hz.

3.4.3 Normal branch QPO

Normal branch QPOs (NBOs) were detected in the medium and intermediate level observations. To our surprise, none were detected in the high level observations (see Fig. 3.8), although we had high timing data in the lower NB for them. The rms 2σ upper limits ($< 0.9\%$) are significantly lower than the rms (1%–2.5%) of the NBOs in the medium and intermediate levels. This also shows that during different overall intensity levels the rapid X-ray variability at the same position on the Z track differs significantly from each other.

When NBOs are seen, no clear relation is detected between the amplitude of the NBO and S_z. However, the FWHM and the centroid frequency seems to increase from the middle of the NB to the FB. The FWHM increases from ∼2.4 Hz to ∼13 Hz and the centroid frequency from ∼5 Hz to ∼8 Hz. In the June 1987, the June 1988, and May 1991 observations it was impossible to make a distinction between a broad NBO or a HFN on the lower FB, although a NBO provided a better fit (e.g., for the June 1987 observation $\chi^2/\mathrm{dof} = 27.5/29$ for the NBO versus 31.0/30 for the HFN).

3.4.4 Horizontal branch QPO

Horizontal branch QPOs are seen during all overall intensity levels, on the HB as well as in the upper NB. Taking all data into account, we find that the frequency of the HBO increases from ∼31 Hz at the left end of the HB to ∼55 Hz at the hard vertex. The PC data of the June 1987 and October 1989 observations indicate that when the source moves down the NB the HBO frequency decreases again to ∼47 Hz. The rms amplitude decreases from the HB to the upper NB, from ∼4% to ∼1%.

As already mentioned in § 3.3.2.3, the PC data of October 1989 show several points at low intensities and high soft color. Those points are placed in the CD near the hard vertex but in the HID near the left end of the HB. The power spectrum corresponding to these points is shown in Figure 3.9. A HBO at 25 Hz is clearly visible (3.8% rms amplitude) and indicates that Cygnus X-2 was indeed at

Table 3.3: Results of power spectral fits of the MPC3 data[a]

Observation	S_z[c]	VLFN		LFN			NBO			HBO			HFN		χ^2	DOF
		rms (%)	α	rms (%)	α	ν (Hz)	rms (%)	$\Delta\nu$ (Hz)	ν (Hz)	rms (%)	$\Delta\nu$ (Hz)	ν (Hz)	rms (%)	ν (Hz)		
87 June	1.19±0.01	2.59±0.16	1.50[b]	3.04±0.08	0.30±0.06	$11.0^{+1.9}_{-1.5}$				1.74±0.10	12.7[b]	49.1±1.0			116.0	83
	1.60±0.01	1.77±0.10	1.02±0.05				1.56±0.12	2.38±0.46	5.36±0.17	$1.02^{+0.24}_{-0.16}$	$4.8^{+4.9}_{-15.1}$	$52.4^{+2.7}_{-0.9}$			83.5	82
	1.83±0.02	1.31±0.13	1.09±0.12				1.09±0.29	$4.0^{+3.5}_{-2.8}$	$6.74^{+0.88}_{-0.68}$						53.5	44
	1.97±0.07	1.45±0.19	1.13±0.15				$1.81^{+0.47}_{-0.32}$	$10.7^{+6.4}_{-4.1}$	$7.1^{+1.5}_{-2.6}$						27.5	29
	2.10±0.03	$4.19^{+0.83}_{-0.57}$	1.39±0.12										$1.76^{+0.68}_{-0.40}$	$32.1^{+\infty}_{-22.3}$	21.1	30
88 June	0.95±0.01	1.06±0.24	1.00[b]	4.73±0.12	0.21±0.06	$13.1^{+1.9}_{-1.6}$				1.24±0.32	$7.7^{+6.2}_{-3.6}$	54.0±2.3			57.6	70
	1.16±0.03	1.11±0.23	1.00[b]	3.02±0.15	0.12±0.13	$5.4^{+1.4}_{-1.1}$				1.87±0.30	$12.7^{+7.3}_{-5.3}$	54.5±2.0			70.2	70
	1.38±0.03	1.69±0.10	0.79±0.07				$1.65^{+0.56}_{-0.34}$	$3.1^{+2.7}_{-1.5}$	$4.79^{+0.51}_{-0.87}$						23.6	44
	2.37±0.02	$2.17^{+1.40}_{-0.43}$	1.50±0.35										2.20±0.33	$14.0^{+9.1}_{-6.0}$	48.8	45
	2.72±0.03	2.38±0.24	1.05±0.13										$1.58^{+0.48}_{-0.64}$	15.00[b]	44.0	31
88 October	1.856±0.008	$8.5^{+1.8}_{-1.3}$	1.53±0.10				<0.87	3.00[b]	5.5[b]				0.87±0.77	15.00[b]	52.2	54
	2.00±0.02	$6.35^{+1.10}_{-0.78}$	1.67±0.09				<0.76	6.00[b]	6.0[b]				1.78±0.14	$10.3^{+3.0}_{-2.3}$	62.7	77
	2.10±0.01	$6.7^{+1.6}_{-1.1}$	1.69±0.13				<1.60	12.00[b]	7.0[b]				2.00±0.30	$14.9^{+8.3}_{-4.8}$	52.2	53
91 May	1.79±0.07	0.70±0.15	$0.91^{+0.44}_{-0.26}$				1.45±0.23	$1.57^{+0.81}_{-0.52}$	5.57±0.22						47.0	58
	1.97±0.10	1.11±0.07	0.98±0.10				1.56±0.25	$5.5^{+2.4}_{-1.7}$	$5.98^{+0.58}_{-0.68}$						63.2	85
	2.05±0.06	0.48±0.21	1.00[b]				$2.60^{+0.52}_{-0.35}$	$12.5^{+7.7}_{-4.4}$	$7.7^{+1.5}_{-2.0}$						41.8	59
91 June	1.74±0.03	$3.95^{+0.46}_{-0.37}$	1.39±0.08				<0.84	3.00[b]	5.5[b]				1.22±0.38	$14.9^{+37.3}_{-8.8}$	49.0	59
	1.95±0.01	4.46±0.35	1.57±0.05				<0.84	6.00[b]	6.0[b]				1.75±0.20	$26.6^{+15.3}_{-7.8}$	67.7	59
90 November	3.624 < Int < 3.670			5.79±0.17	0.01±0.06	$6.69^{+1.02}_{-0.84}$				3.84±0.35	$10.5^{+2.8}_{-2.0}$	31.01±0.83			63.3	57
	3.675 < Int < 3.701			5.76±0.23	0.08±0.07	$8.0^{+1.7}_{-1.3}$				$4.05^{+0.71}_{-0.50}$	$13.5^{+8.4}_{-4.5}$	$33.7^{+1.5}_{-1.0}$			58.7	57
	3.702 < Int < 3.717			6.26±0.18	0.26±0.05	$10.2^{+1.7}_{-1.4}$				3.72±0.50	$20.6^{+7.7}_{-5.3}$	41.3±2.2			50.4	57
	3.717 < Int < 3.738			6.49±0.08	0.31±0.02	11.23±0.79				2.52±0.24	$11.4^{+3.3}_{-2.5}$	41.03±0.85			66.3	81

[a] All errors are determined from an error scan through the χ^2 space using $\Delta\chi^2 = 1$. Whenever no value of a component is given, this component was not significantly detected in the average power spectrum.
[b] Parameter fixed.
[c] The error is defined as the standard deviation in the mean of the S_z points in the chosen segment. If no S_z value could be determined, the chosen intensity (Int) range is indicated.

Table 3.4: Results of power spectral fits of the PC data[a]

Observation	S_z[c]	VLFN		LFN			NBO			HBO			HFN		χ^2	DOF
		rms (%)	α	rms (%)	α	ν (Hz)	rms (%)	$\Delta\nu$ (Hz)	ν (Hz)	rms (%)	$\Delta\nu$ (Hz)	ν (Hz)	rms (%)	ν (Hz)		
87 June	0.457 <SC< 0.467	2.32±0.13	0.84±0.05				2.34±0.22	$2.89^{+0.75}_{-0.58}$	5.00±0.19	$1.58^{+0.33}_{-021}$	$5.6^{+5.1}_{-4.6}$	$52.2^{+0.8}_{-1.3}$			97.0	100
	−0.918 <HC< −0.893															
	0.446 <SC< 0.455	2.17±0.15	0.90±0.07				2.21±0.28	$3.4^{+1.1}_{-0.9}$	5.02±0.25	1.66±0.35	10.3±6.8	$54.8^{+2.0}_{-2.4}$			93.5	100
	−0.947 <HC< −0.923															
	0.435 <SC< 0.444	1.96±0.15	0.84±0.07				1.95±0.15	1.83±0.34	5.30±0.13	$1.50^{+0.44}_{-0.30}$	$9.5^{+9.2}_{-3.8}$	54.3±2.0			129.0	100
	−0.974 <HC< −0.951															
	0.421 <SC< 0.434	2.42±0.17	1.12±0.07				2.06±0.16	$3.60^{+0.71}_{-0.60}$	5.61±0.22	1.88±0.27	$18.8^{+8.5}_{-6.3}$	$51.0^{+2.6}_{-3.0}$			60.8	84
	−1.003 <HC< −0.975															
	0.387 <SC< 0.415	0.89±0.16	0.60±0.14				<1.18	3.50[b]	5.50[b]						36.3	38
	−1.051 <HC< −1.015															
88 June	0.97± 0.02	1.25±0.26	1.50[b]	4.07±0.09	0.34±0.04	$11.4^{+1.7}_{-1.5}$				2.66±0.22	$20.3^{+6.0}_{-4.2}$	$54.5^{+1.2}_{-1.4}$			116	101
	1.31±0.04	1.61±0.06	0.78±0.03				2.46±0.12	2.46±0.32	5.53±0.09	1.45±0.22	7.6±3.1	54.1±1.4			99.5	100
	1.54±0.05	0.95±0.10	0.75±0.10				2.76±0.13	1.64±0.24	5.78±0.07						76.9	70
	1.940±0.004	1.25±0.10	1.01±0.12				2.30±0.28	$10.2^{+3.3}_{-2.5}$	8.20±0.92						78.6	70
	2.16±0.24	$2.03^{+1.45}_{-0.44}$	1.38±0.39										2.58±0.48	$19.3^{+23.4}_{-10.2}$	8.24	13
	2.72±0.08	$5.31^{+0.95}_{-0.68}$	1.44±0.10										2.09±0.40	$23.0^{+\infty}_{-10.8}$	14.3	21
88 October	HV[d]	$3.19^{+1.10}_{-0.54}$	1.82±0.25	4.36±0.14	0.28±0.05	9.1±1.2				2.41±0.18	$11.4^{+1.8}_{-1.7}$	51.70±0.42	2.61±0.34	50.00[b]	84.0	99
	SV	2.64±0.17	1.35±0.06				<0.90	6.00[b]	6.00[b]				2.24±0.09	$13.4^{+1.8}_{-1.5}$	102.0	88
	E	$2.79^{+1.05}_{-0.53}$	1.43±0.24										1.53±0.55	15.00[b]	17.7	18
89 October	3.595 <Int< 3.670			$4.50^{+0.41}_{-0.30}$	0.20[b]	$6.14^{+1.12}_{-0.82}$	$2.48^{+0.82}_{-0.36}$	$8.9^{+7.3}_{-2.8}$	$49.19^{+0.81}_{-1.09}$	3.83±0.21	4.12±0.57	25.05±0.18	$5.78^{+0.42}_{-0.66}$	33.6±5.1	161.0	114
	−0.550 <HC< −0.525															
	3.61 <Int< 3.68			$4.70^{+0.75}_{-0.61}$	0.20[b]	$8.2^{+2.6}_{-2.0}$				$3.24^{+0.47}_{-0.34}$	$3.4^{+3.7}_{-2.7}$	$32.98^{+0.35}_{-0.56}$	$6.39^{+0.65}_{-0.80}$	$46.7^{+15.0}_{-9.6}$	50.3	68
	−0.520 <HC< −0.503															
	3.785 <Int< 3.850			5.98±0.13	0.35±0.03	$13.6^{+2.0}_{-1.7}$				$3.53^{+0.41}_{-0.33}$	$19.3^{+7.6}_{-4.9}$	53.3±1.2			103.0	86
	−0.534 <HC< −0.520															
	3.828 <Int< 3.897	2.22±0.16	1.00[b]	3.90±0.13	0.14±0.08	$10.4^{+1.6}_{-1.3}$				2.79±0.12	$11.2^{+1.5}_{-1.4}$	52.13±0.43			122.0	101
	−0.547 <HC< −0.529															
	3.800 <Int< 3.880	$2.30^{+1.07}_{-0.10}$	0.88±0.05				$2.03^{+0.33}_{-0.24}$	$4.7^{+1.6}_{-1.2}$	5.10±0.39	1.91±0.30	$16.4^{+6.7}_{-6.1}$	46.8±2.4			42.3	50
	−0.570 <HC< −0.580															

[a] All errors are determined from an error scan through the χ^2 space using $\Delta\chi^2 = 1$. Whenever no value of a component is given, this component was not significantly detected in the average power spectrum.
[b] Parameter fixed.
[c] The error is defined as the standard deviation in the mean of the S_z points in the chosen segment. If no S_z value could, be determined the chosen intensity (Int), soft color (SC), or hard color (HC) range is indicated.
[d] The power spectra of the October 1988 observation indicated with HV, SV, and E were calculated for the area given by HV, SV, and E, respectively, in Figure 3.5e.

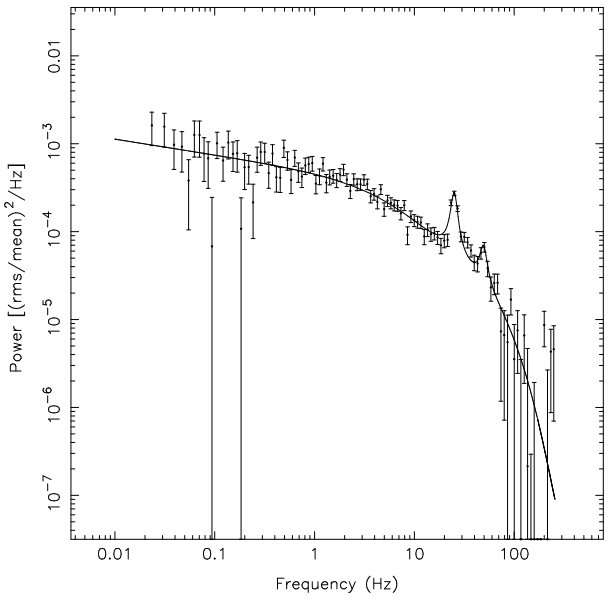

Figure 3.9: The power spectrum of the beginning of the horizontal branch taken in the October 1989 observation. A harmonic of the HBO is visible at about 50 Hz

the left end of the HB (see Fig. 3.6, the points marked H). A second QPO is visible at ∼49 Hz with a rms amplitude of 2.5%. Hasinger et al. (1985) and Hasinger (1987) found already evidence for the harmonic of the HBO in the *EXOSAT* data of Cygnus X-2. However, the frequency ratio was smaller (1.85±0.03) than expected for a second harmonic. Our frequency ratio (1.96±0.05) indicates that this feature is indeed the second harmonic of the HBO.

3.5 Results: the bursts

We found five 2–8 s bursts similar to the burst-like events reported by Kuulkers et al. (1995). The times and the properties are given in Table 3.5. In Figures 3.1*c* and *e*, and Figure 3.3*a* it is indicated where in the Z track the bursts occurred. The occurrence of the burst seems to be uncorrelated with the overall intensity level, the orbital phase, or the location in the Z track (although no burst were detected on the FB).

For the ratio, α, of the average persistent flux to the time-averaged flux emitted in the bursts (which reflects the ratio between the gravitational and nuclear burning energy per gram of accreted matter for thermonuclear bursts), we could only obtain lower limits (Table 3.5), since there are many interruptions by SAA and/or Earth occultations. They were calculated using the average count rate from the start of the last data gap to just before the burst. The other typical burst parameters γ, the ratio of the mean persistent pre-burst flux and net peak burst flux, and τ, the ratio of the total integrated net burst flux and the net burst peak flux (a representation of the burst duration) were also calculated (see Table 3.5). The count rates used in order to calculate the burst parameters were

Table 3.5: Bursts

No.	Date	Start (UT)	t_{burst} (s)	Mode	Time res. (s)	S_z	Orbital phase[a]	α	γ	τ (s)
I	1988-06-12	03:56:34	∼8	MPC2	2	1.000	0.33	>105	1.92	3.66
II	1988-06-12	10:25:52	∼4	MPC2	2	0.931	0.36	>94	3.52	2.00
III	1988-06-13	10:47:27	∼8	MPC2	0.0625	1.229	0.47	>4.1	0.63	1.51
IV	1988-10-06	02:32:25	∼2	MPC2	0.0625	1.222	0.11	>13.3	1.74	1.09
V	1989-10-22	08:04:47	∼4	MPC1	4	1.4–1.5[b]	0.84	> 105	2.67	4.00

[a] X-ray phase using the ephemeris given by Crampton & Cowley (1980), see Kuulkers et al. (1996) note 4.
[b] Only an estimate of S_z, due to the lack of a soft vertex.

corrected for dead-time, background, and aspect. Burst IV was observed during time when the satellite was slewing to the source. Therefore, during that time the collimator transmission was low ($\lesssim$50%) and the uncertainty on the count rate large. The count rate for burst IV was not corrected for the overestimation of the count rates in the low photon energy bands, due to the reflection of low energy photons (below 6 keV) against the collimator walls (see § 3.2.1).

Due to the low time resolution of the data obtained during the occurrence of bursts I, II, and V, we did not examine the burst profiles and spectral properties of these events. The burst profiles, for different energy bands, of bursts III and IV are shown in Figures 3.10 and 3.11. These bursts do not show evidence for spectral cooling as would expected for bona fide type I bursts. Instead, it is clearly visible that burst III shows evidence for spectral hardening: the higher the energies, the broader the event. Also, the post-burst count rate is higher than the pre-burst count rate. This effect is most prominent at the higher energies. Although these phenomena are not seen during event IV, no evidence for spectral cooling is seen either. In the nine bursts in the *EXOSAT* data of Cygnus X-2, hints for spectral hardening were already found (Kuulkers et al. 1995), although the poor statistics made a definite conclusion impossible. Taking all bursts into account, we conclude that these events are probably not bona fide type I. We searched for QPOs and periodic oscillations during burst III and IV and found none. Statistics were insufficient to set meaningful upper limits.

3.6 Discussion

We have found several characteristics in the behavior of Cygnus X-2 which seem to depend on overall intensity level. In the following, we discuss some of those characteristics in more detail and suggest possible explanations for the different overall intensity levels and associated phenomena.

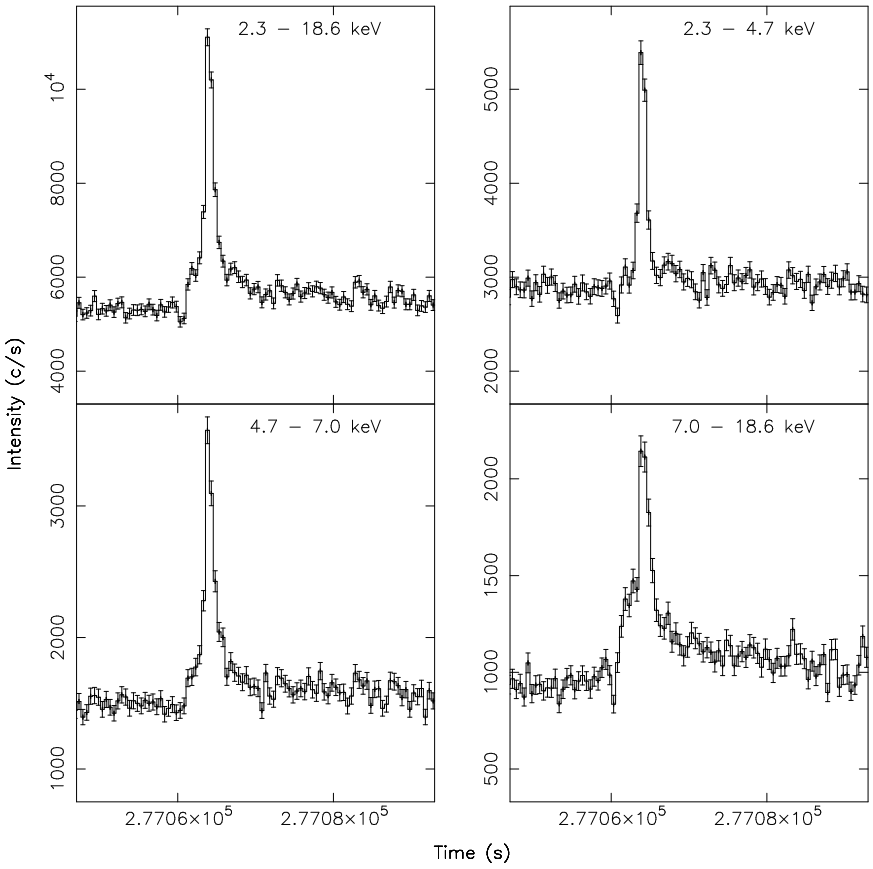

Figure 3.10: The June 1988 burst (III) in the MPC2 high bitrate mode, time resolution is 0.5 seconds. Time is given from the beginning of the observation

3.6.1 The rapid X-ray variability during different overall intensity levels

We find conclusive evidence that the rapid X-ray variability at the same point on the NB differs between different observations. We find a different kind of high timing behavior near the soft vertex when Cygnus X-2 is in the medium level and the high level (see Fig. 3.8). In the medium level weak, flat VLFN is detected and a pronounced NBO occurs. In the high level the VLFN is stronger and steeper, and the NBO is not detectable. In the intermediate intensity level, the VLFN is strong and steep in the FB, but weak and flat in the NB, and the NBO is about the same strength as during the medium level. Our results are the first unambiguous detection of differences in the rapid X-ray variability at a specific position in the Z track (near the soft vertex) between different observations (see Dieters & van der Klis 1999 for a study of Sco X-1 with respect to this issue).

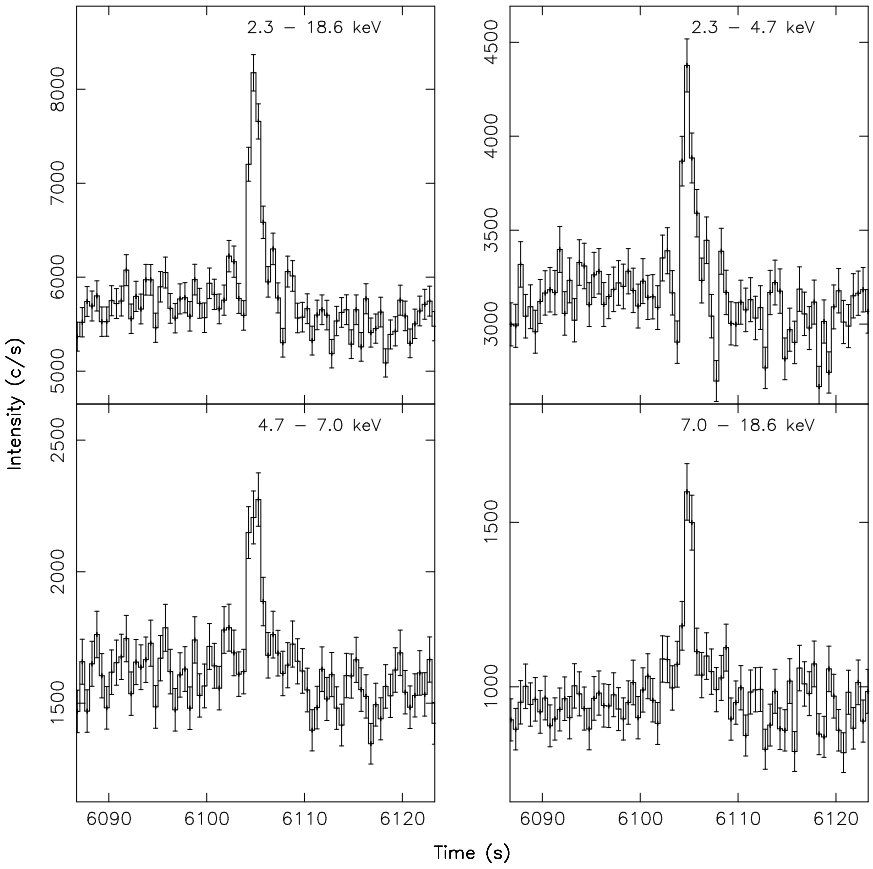

Figure 3.11: The October 1988 burst (IV) in the MPC2 high bitrate mode, time resolution is 0.5 seconds. Time is given from the beginning of the observation

So far, we find no evidence for any difference between the properties of the X-ray variability during different intensity levels on other parts of the Z track (such as the HB). However, our data do not allow a very detailed comparison of the timing behavior on those parts of the Z track.

It is thought (van der Klis et al. 1985a, 1987a; Hasinger & van der Klis 1989; Lamb 1991) that variations in $\dot{M}$ are responsible for the changes in the rapid X-ray variability along the Z and the formation of the Z track, and that for this reason the rapid X-ray variability is closely related to the position of the source on the Z track. However, the shifting and shape changing of the Z track in Cygnus X-2 and other Z sources suggest that variations in $\dot{M}$ cannot explain all aspects of the formation of the Z track. We, therefore, suggest that both the shape of the Z track and the rapid X-ray variability are not totally determined by the mass accretion rate onto the compact object, but also partly by a so far unknown process, which may also cause the long-term intensity variations (see § 3.6.4).

Two other Z sources, GX 5-1 and GX 340+0, display motion of their Z track in the CD (Kuulkers et al. 1994a; Kuulkers & van der Klis 1996), although not as pronounced as Cygnus X-2. Kuulkers et al. (1994a) and Kuulkers & van der Klis (1996) did not find any significant changes in the rapid X-ray variability in GX 5-1 and GX 340+0, respectively, when the Z track moved through the CD and HID. If the motion of the Z track in the CD and HID in Cygnus X-2, GX 5-1, and GX 340+0 are caused by the same phenomenon, we then predict that the rapid X-ray variability in GX 5-1 and GX 340+0 changes when the Z tracks of those sources move through the diagram. The reason why so far no changes have been found is most likely due to the much lower amplitude of the motion of the Z through the CD and HID of GX 5-1 and GX 340+0, as compared to Cygnus X-2, which suggest that the amplitude of the difference of the rapid X-ray variability would also be much smaller. Moreover, in Cygnus X-2 so far only differences in the rapid X-ray variability were found near the soft vertex and not on, e.g., the HB, while GX 5-1 and GX 340+0 were mainly observed in the HB and upper NB, and hardly near the soft vertex. Kuulkers et al. (1994a) and Kuulkers & van der Klis (1996) could not make a good comparison of the rapid X-ray variability near the soft vertex when the Z track of GX 5-1 and GX 340+0, respectively, moved in the CD and HID.

3.6.2 Velocity of motion along the Z track

Van der Klis (1991) suggested that the VLFN could be (partly) due to motion of the source along the Z track. In our analysis, we found that both the VLFN fractional amplitude and the velocity of motion along the Z track increase when the overall intensity level increases. However, the strongest VLFN was not observed during the most extreme high level, but during the less extreme, slightly lower one, whereas the highest velocity was indeed observed during the most extreme high level. Therefore, we conclude that the motion along the Z track is at most only partly responsible for the VLFN. As differences in NB slope in the HID cannot explain this, part of the intensity variations causing the VLFN must take place perpendicular to the NB.

The increase in velocity along the Z track when the overall intensity increases indicates that the spectrum changes more rapidly during high level episodes than during medium level episodes. If the Z track is traced out by changes in the mass accretion rate onto the neutron star, then an increase in the velocity of motion along the Z track indicates that $\dot{M}$ changes more rapidly when the overall intensity level increases. However, it then seems unlikely that variations in $\dot{M}$ can explain the shifts and changes in shape of the Z track between intensity levels (see also § 3.6.1). It is possible that the increase in velocity of motion along the Z track is due to the same phenomenon causing the Z tracks to shift and the shapes to change.

3.6.3 The width of the NB in the HID

The width of the NB in the HID increases when the overall intensity increases, while the width of the NB in the CD remained approximately constant. This indicates that the difference in the width of the NB in the HID is due to intensity variations and not due to spectral variations. However, at the same time the velocity of motion along the Z track increases, which indicates an increase in spectral variations. So, in the HID, when the source moves perpendicular to the Z track (change in intensity), it also moves along the Z track (change in spectrum). Perhaps colors are well correlated with $\dot{M}$, but the intensity varies also due to another (unspecified) process that is more prominent in the high overall intensity level.

3.6.4 The overall intensity variations

Several models have been proposed (Priedhorsky & Holt 1987, and references therein) in order to explain long-term intensity variations in X-ray binaries, e.g., long-term variations in $\dot{M}$ and precessing accretion disks. Precessing neutron stars have also been proposed to explain the variations (see Priedhorsky & Holt 1987; Schwarzenberg-Czerny 1992, and references therein).

3.6.4.1 Variations in the mass accretion rate

Long-term changes in the mass accretion rate have been proposed (see Priedhorsky & Holt 1987) to explain the long-term intensity variations in low-mass X-ray binaries other than Cygnus X-2 (e.g., 4U 1820-30, the Rapid Burster, Aql X-1, excluding Her X-1). However, Kuulkers et al. (1996) and Wijnands et al. (1996a) argued that the long-term intensity variations in Cygnus X-2 cannot be due to variations in the mass accretion rate. The main argument is that variations in the mass accretion rate are thought to produce motion of the source along the Z track (see, e.g., Hasinger & van der Klis 1989), while the Z track is observed during several different intensity levels.

3.6.4.2 A precessing accretion disk

In order to explain long term intensity variations, not related to orbital variations, in high-mass X-ray binaries and Her X-1, precessing accretion disks have been proposed (see Priedhorsky & Holt 1987 and references therein). The recent detection (Smale, Kuulkers, & Wijnands 1996a; Wijnands et al. 1996a) of a 78 day period in the *RXTE*, *Vela 5B* (see also Smale & Lochner 1992), and *Ariel V* all sky monitor data of Cygnus X-2 favors a precessing accretion disk in Cygnus X-2.

However, explaining the long-term X-ray variations of Cygnus X-2 with a precessing accretion disk is not without serious contradictions. If we assume that,

during the medium overall intensity level, the emission region is blocked by (part of) the accretion disk and much radiation is absorbed, scattered, and/or reflected, the power spectrum should be blurred and quasi-periodic oscillations (both the NBO and the HBO) should be harder to detect than when the emission region is not blocked by the accretion disk (the high level). However, we see exactly the opposite: no NBO is detected during high overall intensity levels. The upper limits are significantly lower than the actually detected values during the medium levels. If we assume that not during the medium level but during the high level the emission region is blocked by the accretion disk, then the difference between the power spectra are not totally unexpected. However, it is difficult to explain the increase of the count rate when the accretion disk is blocking our view of the emission region.

Another possibility is that the accretion disk blocks, during the medium overall intensity levels, a localized emission area (e.g., the neutron star surface), which is not blocked during the high levels. In this region, no NBO occurs and therefore the fractional amplitude of the NBO during the high level is diluted by the additional flux. However, not only the strength of the NBO should be affected, but also the strength of the HBO, except when the HBO would originate from this localized area, in which case we would expect an inverse effect. This, however, is unlikely, because during all intensity levels HBOs are observed at approximately the same fractional amplitude.

Therefore, it is unlikely that the increase in count rates from the medium to the high level is caused by an localized emission region, which is sometimes hidden from our view by a precessing accretion disk, or by a precessing accretion disk, which sometimes blocks part of the total X-ray radiation.

Kuulkers et al. (1996) proposed that the difference in overall count rates in the Cyg-like sources is caused by anisotropic emission, the radiation being scattered preferentially into the equatorial plane by a puffed-up inner disk structure. In this model, with increased scattering in the high level, the decrease in NBO amplitude follows naturally due to light travel time effects in the scattering process. Our observations therefore support their model.

3.6.4.3 A precessing neutron star

Another option is that the differences between the levels are due to changes in the properties of the emission region. A precessing neutron star could produce changes in the inner disk region. Due to the precession of the neutron star the orientation of the magnetic field with respect to the accretion disk changes. According to numerical calculations (Psaltis et al. 1995) the strength of the magnetic field is enough for the field to have a profound effect on the spectrum of the source and possibly also on the count rate. A change in the effective magnetic field, caused by a different orientation of the field, could maybe explain the different Z tracks during the different levels. Also, the rapid X-ray variability would

be affected, although it is not clear if this could explain the differences that we found. The behavior of the HBO should differ between the different intensity levels due to the different effective magnetic field, but no difference is found. It is also not clear why the NBO should differ between intensity levels.

3.6.5 The decrease of the HBO frequency down the NB

The decrease of the HBO frequency from the hard vertex down the NB in the June 1987 and October 1989 PC data allows us to apply the method described in Chapter 4, in order to derive an upper limit for the equatorial magnetic field strength. Assuming that the radius of the neutron star is $\sim 10^6$ cm we derive an upper limit of $\sim 8.5 \times 10^9$ G on the star's magnetic field at the magnetic equator. This value is similar to the value found for GX 17+2 (Chapter 4). This upper limit is consistent with numerical computations on the X-ray spectrum of Cygnus X-2 (Psaltis et al. 1995). As noted in Chapter 4, a further decrease of the frequency down the NB will reduce this upper limit. The fact that we see the HBO frequency decrease on the NB in Cygnus X-2 supports the interpretation that the QPO on the NB in GX 17+2, which also decreases in frequency (Chapter 4), is the HBO.

3.7 Conclusion

We observed Cygnus X-2 over a broad range of intensities. The source alternated between the known medium and high overall intensity levels and also sometimes in a state in between these two levels, both in intensity and other source characteristics. We found new correlations between several characteristics of the source and the overall intensity level:

- The velocity and acceleration along the normal branch increase when the overall intensity increases. During the high intensity level Cygnus X-2 moves faster and more irregularly up and down the normal branch than during lower levels.

- The width of the normal branch in the hardness-intensity diagram increases when the overall intensity increases.

- The very-low frequency noise near the soft vertex increases in amplitude and in steepness when the overall intensity increases.

- The normal branch quasi-periodic oscillation is not detectable ($\lesssim$0.9% rms) near the soft vertex when Cygnus X-2 is in the high level. During the other levels a NBO can be easily detected at a level of 1%–2.5% (rms).

The following correlations were already known and are confirmed by our analysis:

- The overall intensity changes with a factor of $\sim$1.34 between the medium and the high overall intensity level.
- The shape of the Z-track in the color-color diagram and hardness-intensity diagram changes when the overall intensity changes. In the color-color diagram the horizontal and the flaring branch become more horizontal when the overall intensity increases. When the source enters the flaring branch during the medium overall intensity level the intensity first increases and later decreases. When the source enters the flaring branch during the high overall intensity level the intensity immediately starts to decrease.
- The whole Z-track shifts to softer colors when the overall intensity increases.

We also found several other previously unreported phenomena:

- Clear detection of overall intensity level episodes in-between the medium and the high overall intensity level, indicating that the different overall intensity levels are part of a continuous range instead of a discrete set.
- The frequency of the horizontal branch quasi-periodic oscillation decreases down the NB, giving a model dependent upper limit on the magnetic field strength at the magnetic equator of $\sim 8.5 \times 10^9$ G.
- Detection of five bursts in the *Ginga* data, which do not show the characteristics of bona fide type I bursts.

Acknowledgments. This work was supported in part by the Netherlands Organization for Scientific Research (NWO) under grant PGS 78-277 and by the Netherlands Foundation for Research in Astronomy (ASTRON) under grant PGS 781-76-017. E. K. acknowledge receipts of an ESA fellowship.

Appendix A: calculating the standard deviation of sample standard deviations

For the sample x_1, x_2, ..., x_n let

$$\overline{x} = \text{mean} = \sum_{i=1}^{n} x_i/n \tag{A1}$$

The sample standard deviation (s) is defined by

$$s = (\sum_{i=1}^{n} \frac{(x_i - \overline{x})^2}{n})^{\frac{1}{2}} \tag{A2}$$

The standard deviation of sample standard deviations is defined by (Burington & May 1970)

$$\sigma_s = [\frac{n-1}{n} - [b(n)]^2]^{\frac{1}{2}}\sigma_x \tag{A3}$$

with σ_x^2 the variance of the population given by the unbiased estimate $s^2 n/(n-1)$, $b(n) = (\frac{2}{n})^{\frac{1}{2}}\Gamma(\frac{n}{2})/\Gamma(\frac{n-1}{2})$, and n the total number of points.

Chapter 4

Discovery of a variable–frequency, 50–60 Hz quasi-periodic oscillation on the normal branch of GX 17+2

R. A. D. Wijnands, M. van der Klis, D. Psaltis, F. K. Lamb, E. Kuulkers,
S. Dieters, J. van Paradijs, & W. H. G. Lewin
Astrophysical Journal **469**, L5–L8 (1996)

Abstract

We report the discovery, with the *Rossi X-ray Timing Explorer*, of a 50–60 Hz quasi-periodic oscillation (QPO) in GX 17+2. The QPO is seen when GX 17+2 is on the normal branch in the X-ray color-color diagram. Its frequency initially increases from 59 to 62 Hz as the source moves down the normal branch, but below the middle of the normal branch it decreases to ∼50 Hz. Together with this frequency decrease the QPO peak becomes much broader, from ∼4 Hz in the upper part of the normal branch to ∼15 Hz in the lower normal branch. The rms amplitude remains approximately constant between 1% and 2% along the entire normal branch. From a comparison of the properties of this QPO with those of QPOs previously observed along the normal branch in other Z sources, we conclude that it is most likely the horizontal branch QPO (HBO). However, this QPO displays a number of unusual characteristics. The decrease in the QPO frequency along the lower normal branch is not in agreement with the predictions of the beat frequency model for the HBO unless the mass flux through the inner disk decreases as the source moves down the lower normal branch. We tentatively suggest that the required decrease in the mass flux through the inner disk is caused by an unusually rapid increase in the mass flux in the radial inflow as GX 17+2 moves down the normal branch. Assuming that this explanation is correct, we can derive an upper bound on the dipole component of the star's magnetic field at the magnetic equator of 5×10^9 G for a 1.4 $M_\odot$ neutron star with a radius of 10^6 cm.

4.1 Introduction

GX 17+2 is a bright low-mass X-ray binary. Hasinger & van der Klis (1989) classified it as a Z source using its correlated spectral and fast timing behavior. Z sources trace out a Z shape in the color-color diagram. The three limbs of the Z are called the horizontal branch (HB), the normal branch (NB), and the flaring branch (FB). Variations in the total mass accretion rate are thought to produce the Z track. The properties of the rapid X-ray variability in Z sources are closely related to the position of the sources on their Z track (van der Klis 1995 for a review). On the horizontal branch a quasi-periodic oscillation (QPO) can be seen, which varies in frequency from as low as 12 Hz at the left end of the HB to as high as 55 Hz near the HB-NB junction. The frequency of this HB QPO (or HBO) at the junction depends on the source (Cygnus X-2: $\sim$55 Hz, Chapter 3; GX 5$-$1 and GX 340+0: $\sim$50 Hz, Lewin et al. 1992; Penninx et al. 1991; Kuulkers et al. 1994a; Kuulkers & van der Klis 1996; and probably $\sim$45 Hz for Sco X-1, van der Klis et al. 1996e). The HBO is sometimes still detectable in the upper part of the NB. In all observations of Z sources up to now, on the NB the frequency of the HBO remained approximately constant at the value it had at the junction. The HBO frequency is thought to be the beat frequency between the Keplerian frequency at the inner edge of the accretion disk and the spin frequency of the neutron star (Alpar & Shaham 1985; Lamb et al. 1985). When the mass accretion rate increases, the disk penetrates deeper into the magnetic field of the neutron star, and the Keplerian frequency of the inner edge of the disk, and hence the frequency of the HBO, increases. Near the middle of the NB, the HBO is sometimes seen together with another QPO with a frequency of 5–7 Hz. This is the normal branch QPO (NBO). The frequency of the NBO stays approximately the same when the source is on the NB. When the source enters the FB, it sometimes remains present, evolving to a higher frequency; this is the so-called flaring branch QPO (FBO).

GX 17+2 displayed all three branches when it was observed with *EXOSAT* (Hasinger & van der Klis 1989; Langmeier, Hasinger, & Trümper 1990; Kuulkers et al. 1997) and *Ginga* (Penninx et al. 1990). An HBO with an amplitude of 1%–2% (rms) was observed on the HB with frequencies between 18 and 30 Hz. No HBO was seen on the NB. NBO and FBO were also seen in the appropriate branches. In this chapter, I describe a new QPO phenomenon on the NB that differs in several important respects from the standard picture just sketched.

4.2 Observations

GX 17+2 was observed with the proportional counter array (PCA) onboard the *Rossi X-ray Timing Explorer* (*RXTE*; Bradt, Rothschild, & Swank 1993) from 1996 February 7 13:20 UT until February 8 05:29 UT and from 1996 February

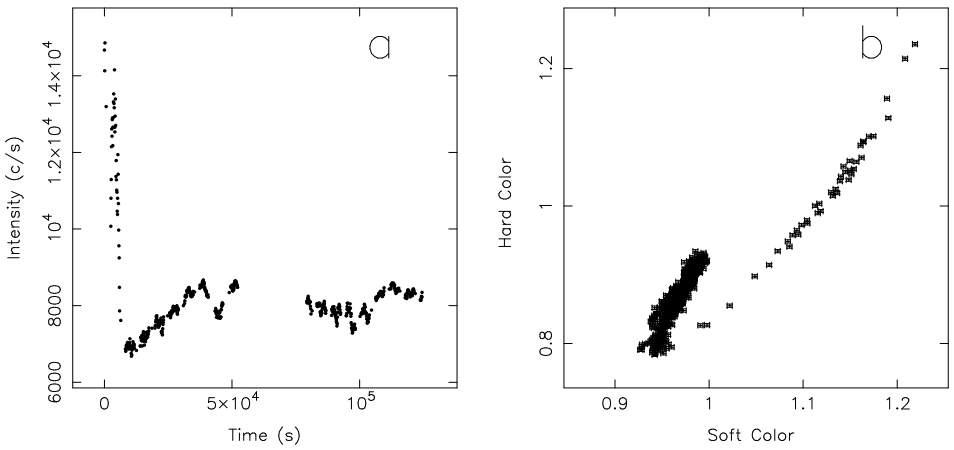

Figure 4.1: X-ray light curve (*a*) and the X-ray color-color diagram (*b*). The count rate in the light curve is taken in the 2.3–19.2 keV energy range. The soft color is the (4.6–7.0)/(2.3–4.6) keV, the hard color is the (7.0–19.2)/(4.6–7.0) keV count-rate ratio. Each data point corresponds to 96 s of data. The error bars are plotted in the figures. Note that in the light curve the error bars are smaller than the points.

8 11:13 UT until February 9 00:04 UT. The data were broken up in segments of ∼40 minutes due to Earth occultations, passage through the South Atlantic Anomaly, or both. Throughout the entire observation, data were collected in the 2–11.7 keV energy range in 16 energy bands with a time resolution of 2 ms. Data were also recorded simultaneously with 16 s resolution in 129 energy bands covering the 2–60 keV energy range.

4.3 Analysis and results

The 16 s data were used to produce a light curve and an X-ray color-color diagram (Fig. 4.1). At the beginning of the observation, GX 17+2 was on the flaring branch and count rates ranged up to 15,000 counts s^{-1}. It then made a transition to the normal branch, where it remained for the rest of the observation time. In order to correlate the properties of the rapid X-ray variability with changes in the X-ray spectrum, we used the S_z (distance along the Z track) parameterization (see Hertz et al. 1992; Dieters & van der Klis 1999). The length of the NB was set to 1.0, with the highest point of the NB in our data assigned the value $S_z = 1$ and the NB-FB junction $S_z = 2$. We divided the NB into 10 equal S_z segments, and calculated an average power spectrum of the 2–11.7 keV high time resolution data corresponding to each segment. The lowest frequency in the power spectrum

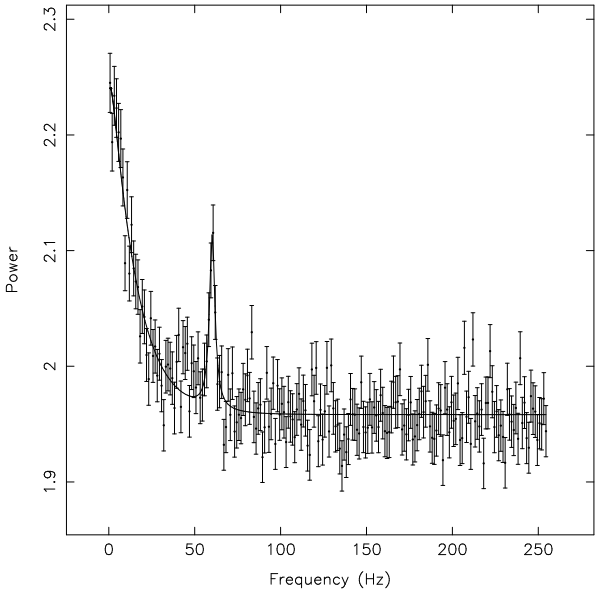

Figure 4.2: Power spectrum in the upper normal branch, between $S_z = 1.1$ and 1.2, showing the LFN and the narrow 60 Hz QPO peak. The spectrum is Leahy-normalized. The fit is also plotted.

was 1/16 Hz; the highest frequency was 256 Hz. We used a function composed of a constant (the Poisson level) plus a power law (the low-frequency noise) plus Lorentzian peaks (the HBO and NBO) to fit the power spectra. The fit results (Table 4.1) were corrected for background and differential dead-time (van der Klis 1989).

On the upper normal branch, $S_z < 1.4$, we see a narrow QPO peak near 60 Hz (Fig. 4.2), with a FWHM of only ∼4.0 Hz and a rms amplitude of 1%–2%. Its frequency increased slightly, from 59 to 62 Hz, when GX 17+2 moved down the NB from $S_z = 1$ to $S_z = 1.4$. Between $S_z = 1.4$ and $S_z = 1.5$, the frequency decreased to ∼55 Hz, and, moving down to $S_z = 1.6$, it dropped further to ∼50 Hz. At the point ($S_z = 1.4$) at which the frequency reached its maximum, the QPO peak broadened to a FWHM of 10–15 Hz. The amplitude stayed approximately the same along the entire NB, between 1% and 2% (rms). The frequency, FWHM, and rms amplitude of the QPO are plotted versus S_z in Figure 4.3. At around $S_z = 1.8$ the 50–60 Hz QPO disappears. At that point, another QPO has already appeared around 7 Hz, obviously the well-known NBO. Both QPO peaks are simultaneously visible in the power spectrum for S_z between 1.6 and 1.8. The analysis of the 7 Hz QPO and the noise components will be discussed by Homan et al. 1999b.

4.4 Discussion

We have found a QPO around 60 Hz in the X-ray flux of GX 17+2 when this source was on the normal branch. As the source moved from the upper part of the NB downward, the QPO frequency first increased from 59 Hz to 62 Hz and

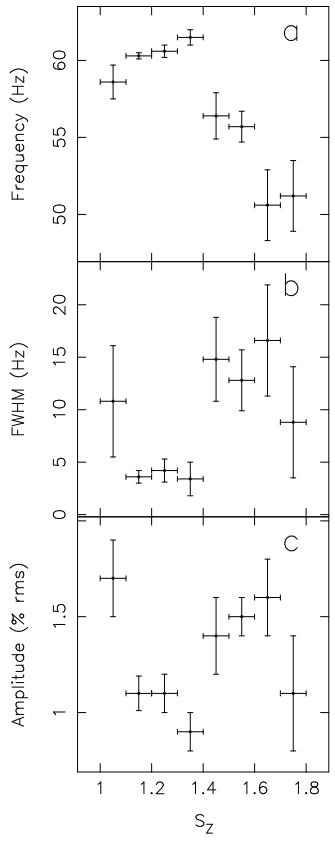

Figure 4.3: The QPO properties as function of the S_z value. Figs. *a*, *b* and *c* show the frequency, the FWHM and the rms amplitude, respectively, of the QPO. Error bars correspond to $\Delta\chi^2 = 1$.

then decreased to ∼50 Hz. In the upper part of the NB, the QPO peak was very narrow, ∼4 Hz. In the following we argue that this QPO is most likely the horizontal branch QPO.

In the other Z sources in which an HBO is observed on the NB, GX 5−1 (Lewin et al. 1992; Kuulkers et al. 1994a), Cygnus X-2 (Chapter 3), and GX 340+0 (Kuulkers & van der Klis 1996), we see that the HBO frequency increases when the source moves along the HB to the HB-NB junction, but remains constant at a frequency consistent with that at the junction when the source moves down the NB. In GX 17+2, the HBO had previously only been observed on the HB. With *EXOSAT* the entire Z was observed (Hasinger & van der Klis 1989; Langmeier et al. 1990; Kuulkers et al. 1997). The HBO was detected on the HB with a frequency that increased from ∼24 Hz at the left end of the HB to ∼28 Hz halfway across the HB, at which point the HBO disappeared into the noise (Kuulkers et al. 1997). No HBO was found on the NB. However, *EXOSAT* was not sensitive enough to detect in GX 17+2 a QPO as weak as we detected using *RXTE*. *Ginga* was sensitive enough to detect such a weak QPO, but much of the NB, particularly the upper part and the HB-NB junction, was not seen when GX 17+2 was observed at high time resolution (Penninx et al. 1990). The HBO was detected on the HB and was found to increase in frequency from ∼18 Hz at the left of the

Table 4.1: QPO parameters

S_z	Rms Amplitude (%)	FWHM (Hz)	Frequency (Hz)
1.05±0.05	1.7±0.2	10.8±5.3	58.6±1.1
1.15±0.05	1.1±0.1	3.6±0.6	60.3±0.2
1.25±0.05	1.1±0.1	4.2±1.1	60.6±0.4
1.35±0.05	0.9±0.1	3.4±1.6	61.5±0.5
1.45±0.05	1.4±0.2	14.8±4.0	56.4±1.5
1.55±0.05	1.5±0.1	12.8±2.9	55.7±1.0
1.65±0.05	1.6±0.2	16.6±5.3	50.6±2.3
1.75±0.05	1.1±0.3	8.8±5.3	51.2±2.3

[a] All errors correspond to $\Delta\chi^2 = 1$.
[b] For all fits, χ^2/d.o.f. ∼1.0.

HB to ∼30 Hz at the rightmost part of the HB seen in these observations. It is possible that the right end of the HB and HB-NB junction were not observed, so that the HBO frequency at the HB-NB junction is higher than ∼30 Hz. Thus HBOs on the NB with frequencies near 60 Hz have been found in other Z sources, and previous satellites were either insufficiently sensitive or did not observe at the right moment in the right mode to detect the weak 50–60 Hz QPO we found in the NB. In addition, the frequency of the HBO of GX 17+2 at the HB-NB junction has never been measured.

For these reasons, we think that the 50–60 Hz QPO we found in the NB of GX 17+2 is most likely the HBO. If true, then this HBO has a number of new characteristics. On the upper part of the NB, the HBO has a higher frequency and is much more coherent than seen previously. Whereas, for other Z sources the HBO frequency on the NB is consistent with being constant, for GX 17+2 it can be shown for the first time that the frequency of the HBO varies by ∼10 Hz. We note that our interpretation can be tested by performing an observation of GX 17+2 moving through the HB-NB junction and observing the frequency variations of the HBO. The HBO frequency should increase along the HB up to ∼60 Hz at the HB-NB junction.

A decrease in HBO frequency along the NB, such as we observe between $S_z = 1.4$ and 1.6, is not in accordance with the predictions of the beat frequency model if all the mass flux is through the inner disk, since, under the usual interpretation of the Z track, motion down the NB is thought to be caused by an increase of mass flux onto the neutron star and should therefore produce an

increase of the HBO frequency. In the following, we discuss one possible solution to resolve this discrepancy between our interpretation of the data and the beat-frequency model. This solution makes use of a previous proposal (Fortner, Lamb, & Miller 1989) that not all of the mass flux towards the neutron star is by way of a thin disk but part of it accretes instead by way of an approximately radial inflow. In this picture, one is naturally led to find the explanation for the unexpected behavior of the HBO frequency as a function of mass accretion rate in a change in mass flux ratio between disk and radial flow as the source moves down the NB. We note, that although the behavior of the HBO frequency on the NB that we discovered had not been predicted, neither is the introduction of a radial flow in addition to a thin disk entirely ad hoc. The presence of a radial flow was proposed earlier, based on the properties of the NBO, which strongly suggest the presence of Comptonizing medium of variable optical depth (Fortner et al. 1989). The specific behavior of the mass flux as the source moves down the NB that we assume below, however, is suggested only by our specific data and needs additional tests. We shall mention examples of such tests later on.

In the models of Alpar & Shaham (1985) and Lamb et al. (1985), the frequency of the HBO is not determined by the total mass accretion rate $\dot{M}_{NS}$ onto the neutron star (which in the unified model of Z and atoll sources [see Lamb 1989] increases monotonically as a source moves down the NB) but by the accretion rate $\dot{M}_i$ trough the inner part of the Keplerian disk to the stellar surface. $\dot{M}_{NS}$ is the sum of $\dot{M}_i$ and the mass flux $\dot{M}_r$ through an approximately radial flow from the inner disk onto the neutron star.

To keep this model consistent with the behavior of the 50–60 Hz QPO found in the present study, we assume that $\dot{M}_{NS}$ onto the neutron star increases down the NB but that, from $S_z = 1.4$ onwards $\dot{M}_i$ decreases. $\dot{M}_i$ can decrease only if $\dot{M}_r$ increases faster than $\dot{M}_{NS}$ as GX 17+2 moves down the NB. It is uncertain what determines the exact value of $\dot{M}_i/\dot{M}_r$. A significant increase in $\dot{M}_r$ between $S_z = 1.4$ and $S_z = 1.6$, when the N/FBO appears, is qualitatively consistent with the unified model (Fortner et al. 1989).

Assuming that the magnetic field of the neutron star at the inner edge of the Keplerian flow is approximately dipolar, we can derive an upper bound on the dipole magnetic moment μ of the neutron star. The inner part of the accretion disk around the neutron star is expected to be radiation pressure-dominated. For such a disk, the beat frequency ν_B is

$$\nu_B = 1.71 \left(\frac{\dot{M}_i}{\dot{M}_E}\right)^{0.225} \left(\frac{M_{NS}}{M_\odot}\right)^{0.695} \left(\frac{\mu}{10^{30}\ \mathrm{G\ cm^3}}\right)^{-0.765} - \nu_s \quad \mathrm{H}z \tag{4.1}$$

(see Ghosh & Lamb 1992), where ν_s is the spin frequency of the neutron star, $\dot{M}_E$ is the mass flux that would produce the Eddington critical luminosity for accreting matter of cosmic composition, and M_{NS} is the mass of the neutron

star. Assuming that the $\dot{M}_{NS}$ at $S_z = 1.8$ is greater than at $S_z = 1.4$ and that $\dot{M}_r$ is less than 30% of $\dot{M}_{NS}$ (as expected in the unified model; see Fortner et al. 1989), we obtain from equation (4.1) the inequality

$$\mu < 5 \times 10^{27} \left(\frac{\nu_{1.4} - \nu_{1.8}}{10 \text{ Hz}} \right)^{-1.3} \left(\frac{M_{NS}}{1.4\ M_\odot} \right)^{0.91} \left(\frac{\dot{M}_{1.4}}{\dot{M}_E} \right)^{0.29} \text{ G cm}^3 , \qquad (4.2)$$

where $\nu_{1.4}$ and $\nu_{1.8}$ are the observed values of the QPO frequency at $S_z = 1.4$ and $S_z = 1.8$ and $\dot{M}_{1.4}$ is the total mass flux $\dot{M}_{NS}$ at $S_z = 1.4$. $\dot{M}_{1.4}/\dot{M}_E$ is expected to be $\sim$0.8 (Psaltis, Lamb, & Miller 1995), so the last factor on the right is close to unity. Using the observed values of $\nu_{1.4}$ and $\nu_{1.8}$ and the relation $B_s^{\rm eq} = \mu/R^3$ between the dipole component of the star's magnetic field at the magnetic equator and the dipole magnetic moment μ and radius R of the star, inequality (4.2) gives an upper bound $\sim 5 \times 10^9$ G on $B_s^{\rm eq}$ for $R = 10^6$ cm. This upper bound is consistent with numerical computations of the X-ray spectrum of GX 17+2 (Psaltis et al. 1995). If in subsequent observations the HBO is detected further down the NB and its frequency is found to become even smaller than 51 Hz, the upper bound on the dipole magnetic field of the neutron star can be reduced.

As mentioned earlier, the idea that $\dot{M}_i$ decreases and that $\dot{M}_r$ strongly increases as the source moves down the NB, needs observational verification. There are various observable affects of the radial flow on the X-ray spectrum, as well as on the energy dependence of the rapid time variability. In particular, the flow affects the average X-ray spectrum by Comptonization (Psaltis et al. 1995) and produces time lags in the HBO due to propagation-time differences. We are currently performing extensive numerical simulations, based on our derived change of $\dot{M}_r$, to predict the X-ray spectral and time-lag behavior of GX 17+2 on the NB. These will be reported in a later paper.

Acknowledgments. This work was supported in part by the Netherlands Organization for Scientific Research (NWO) under grant PGS 78-277 and by the Netherlands Foundation for Research in Astronomy (ASTRON) under grant 781-76-017. W. H. G. L., J. v. P., F. K. L., and D. P. acknowledge support from the National Aeronautics and Space Administration. F. K. L. and D. P. also received support from the National Science Foundation.

Chapter 5

Discovery of kilohertz quasi-periodic oscillations in GX 17+2

R. Wijnands, J. Homan, M. van der Klis, M. Méndez, E. Kuulkers,
J. van Paradijs, W. H. G. Lewin, F. K. Lamb, D. Psaltis, & B. Vaughan
Astrophysical Journal **490**, L157–L160 (1997)

Abstract

We observed the low-mass X-ray binary and Z source GX 17+2 with the *Rossi X-ray Timing Explorer* during 1997 February 6–8, April 1–4, and July 26–27. The X-ray color-color diagram shows a clear Z track. Two simultaneous kHz quasi-periodic oscillations (QPOs) are present in each observation, whose frequencies are well correlated with the position of the source on the Z-track. At the left end of the horizontal branch (HB) only the higher frequency peak is observed, at 645±9 Hz, with an rms amplitude of 5.7%±0.5%, and a FWHM of 183±35 Hz. When the source moves down the Z track to the upper normal branch the frequency of the kHz QPO increases to 1087±12 Hz, and the rms amplitude and FWHM decrease by a factor 2. Farther down the Z, the QPO becomes undetectable, with rms upper limits of typically 2.0%. Halfway down the HB, a second QPO appears in the power spectra with a frequency of 480±23 Hz. The frequency of this QPO also increases when the source moves along the Z track, up to 781±11 Hz halfway down the normal branch, while the rms amplitude and FWHM stay approximately constant at 2.5% and 70 Hz. The QPO frequency difference is constant at 293.5±7.5 Hz. Simultaneously with the kHz QPOs we detect HB QPOs (HBOs). The simultaneous presence of HBOs and kHz QPOs excludes the magnetospheric beat-frequency model as the explanation for at least one of these two phenomena.

5.1 Introduction

GX 17+2 is a bright low-mass X-ray binary and Z source (Hasinger & van der Klis 1989). Along the Z track traced out in the X-ray color-color diagram (CD), the mass accretion rate ($\dot{M}$) is thought to increase from the horizontal branch (HB) via the normal branch (NB) to the flaring branch (FB). On the HB and upper NB, 18–60 Hz quasi-periodic oscillations (QPOs) are present (called HBOs), and on the lower NB and FB, 5–20 Hz QPOs (N/FBOs) are present. Atoll sources have no Z track in the CD (Hasinger & van der Klis 1989) and do not exhibit HBO or N/FBO[1]. However, many show kHz QPOs between 300 and 1200 Hz (see van der Klis 1998 for a recent review). Usually, two simultaneous kHz QPOs (hereafter "twin peaks") are seen, whose frequencies increase with $\dot{M}$ while their difference (the twin peak separation) remains constant. In X-ray bursts oscillations are seen with a frequency once or twice the twin peak separation. This strongly suggest a model in which the burst oscillation frequency is the spin frequency (or twice that), the higher kHz QPO frequency some inner disk frequency, and the lower kHz QPO frequency is their beat.

So far, two Z sources have shown kHz QPOs: Sco X-1, with frequencies in the range 550–1100 Hz (van der Klis et al. 1996e, 1997b), and GX 5−1 (325–896 Hz; van der Klis et al. 1996d). Both sources showed twin peaks. In GX 5−1 the QPO frequencies increased from the left end of the HB to the upper NB (van der Klis et al. 1996d), and they increased in Sco X-1 from the upper NB to the FB (van der Klis et al. 1996e, 1997b). In view of the similarities between the kHz QPOs in Z and atoll sources, both are most likely caused by the same mechanism. The only difference so far is that in atoll sources the peak separation is constant, whereas in Sco X-1 it decreases when the QPO frequencies increase. In this chapter, I report the discovery of twin kHz QPOs in the Z source GX 17+2 (see also van der Klis et al. 1997a).

5.2 Observations and analysis

We observed GX 17+2 with the PCA onboard the *Rossi X-ray Timing Explorer* on 1997 February 6–8, April 1–4, and July 26–27. A total of 120.5 ks of good data were obtained. During February 8 (1.1 ks) and a small part of February 7 (7.8 ks) and July 27 (4.8 ks), only four of the five detectors were on. The source then covered parts of the Z track also well covered with five detectors. As adding the four-detector data did not improve the results significantly, we only used the five-detector data to have the most accurate CD possible. Data were collected with 16 s time resolution in 129 photon energy bands (energy range, 2–60 keV)

[1] Although in several of them, broad QPO-like peaks are found with frequency around 20 Hz (e.g., Hasinger & van der Klis 1989; Chapter 8)

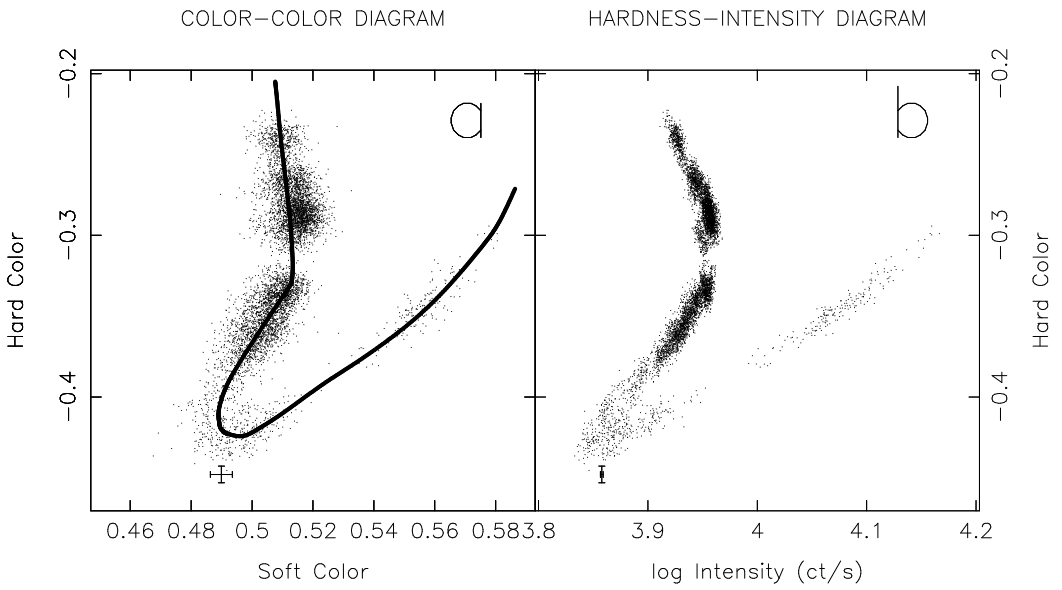

Figure 5.1: Color-color diagram (*a*) and hardness-intensity diagram (*b*) of GX 17+2. The soft color is the logarithm of the ratio of the count rates between 3.5–6.4 and 2.0–3.5 keV; the hard color is the logarithm of the ratio of the count rates between 9.7–16.0 and 6.4–9.7 keV; and the intensity is the logarithm of the count rate in the photon energy range 2.0–16.0 keV. The background, which is almost negligible (50 counts s^{-1} in the energy range 2.0–16.0 keV), was subtracted, but the intensity was not dead-time corrected. All points are 16 s averages. The heavy line in the CD is the spline which was used to determine S_z. Typical error bars are shown at one of the points.

and simultaneously with 122 μs time resolution in four bands: 2–5, 5–6.4, 6.4–8.6, and 8.6–60 keV.

We made power density spectra from the 122 μs data, using 16 s data segments. To measure the kHz QPOs we fitted the 96–4096 Hz power spectra with a function described by a constant, one or two Lorentzian peaks, and a broad sinusoid to represent the dead-time modified Poisson noise (Zhang et al. 1995; Zhang 1995). The Very Large Event window (van der Klis et al. 1997b) was set to 55 μs, so that its effect on the Poisson noise was small enough that it could be absorbed by the broad sinusoid. To measure the HBOs we fitted the 8–256 Hz power spectra with a constant, one or two Lorentzian peaks, and a power law representing the continuum. Differential dead-time (van der Klis 1989) was negligible. We determined errors using $\Delta\chi^2 = 1.0$ and upper limits using $\Delta\chi^2 = 2.71$, corresponding to a 95% confidence level. Upper limits on the kHz QPOs were determined using a fixed FWHM (100 Hz). In the presence of one kHz peak, the upper limit on the other was determined by fixing its frequency at the fre-

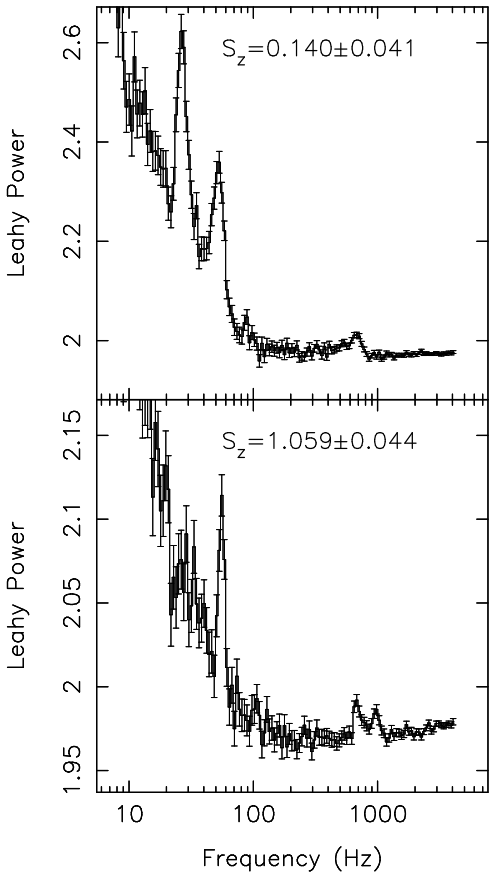

Figure 5.2: Typical Leahy normalized power spectra in the energy range 6.4–60 keV. In the top panel, for $S_z = 0.140 \pm 0.041$, clearly the HBO, its second harmonic, and the higher frequency QPO at 675 Hz are visible. In the bottom panel, for $S_z = 1.059 \pm 0.044$, the HBO fundamental, the lower frequency QPO (680 Hz), and the higher frequency QPO (986 Hz) are visible. The upward trend of the power at kHz frequencies, best seen in the bottom panel, is a result of instrumental deadtime.

quency of the detected QPO plus or minus the mean peak separation (depending on whether the lower or higher frequency QPO was detected, respectively). Upper limits on the HBO second harmonic were determined using a fixed FWHM (10 Hz) and a frequency twice that of the first harmonic.

In the CD and the hardness-intensity diagram (HID) we used for the soft color the log of the 3.5–6.4/2.0–3.5 keV count rate ratio, for the hard color the log of the 9.7–16.0/6.4–9.7 keV ratio, and as intensity the log of the count rates in the 2.0–16.0 keV band. We used the S_z parameterization (Chapter 3 and references therein) for measuring the position along the Z track. The HB/NB vertex is at $S_z = 1.0$, the NB/FB vertex at $S_z = 2.0$. By using logarithmic values for the colors, S_z does not depend on the values of the colors but only on their variations (Chapter 3). We selected the power spectra according to S_z and determined the average S_z value for each average power spectrum. The S_z error bars represent the standard deviation of the S_z distributions.

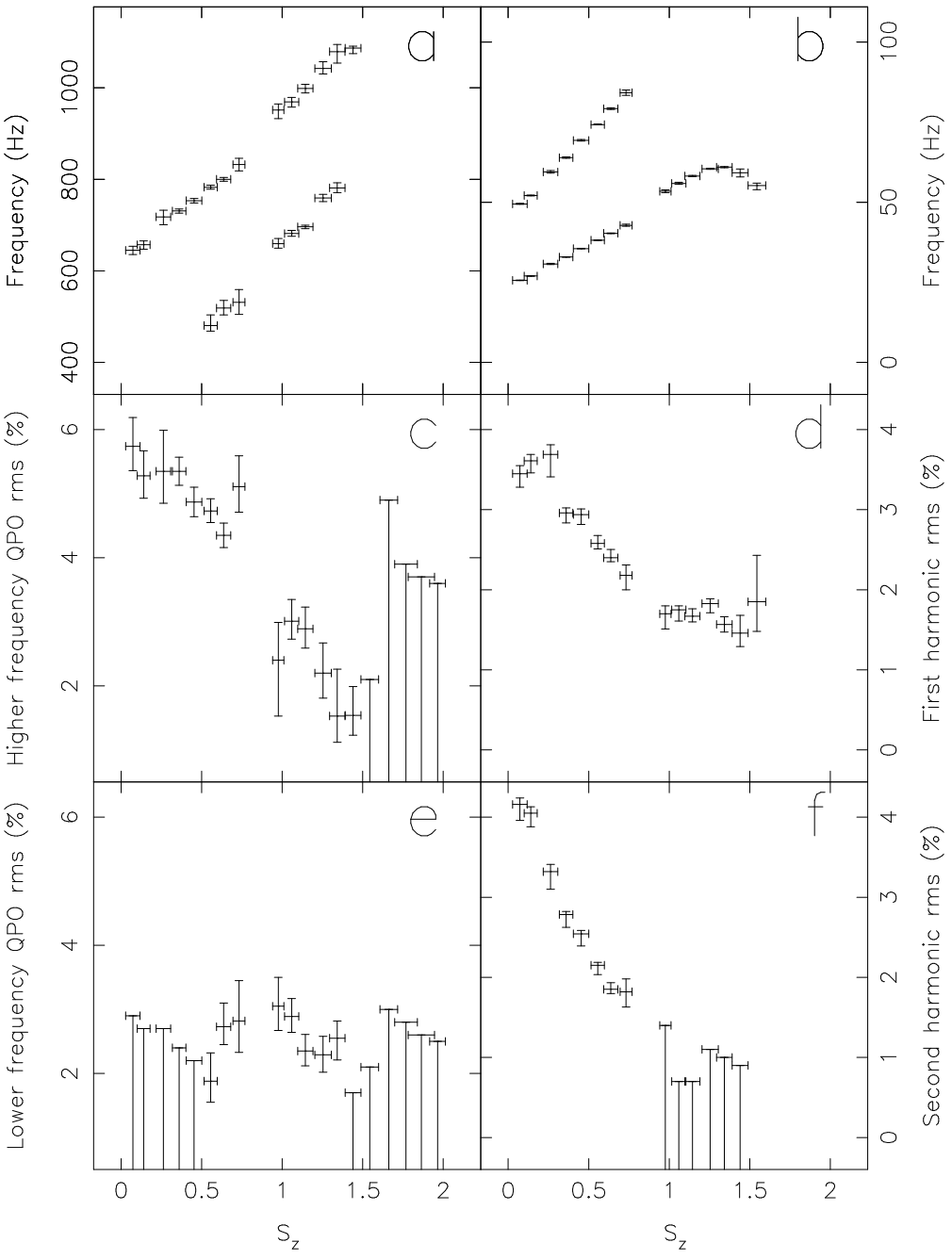

Figure 5.3: (*a*) Frequency of the kHz QPOs; (*b*) frequency of the first and second harmonic of the HBO; (*c*) the rms amplitude of the higher frequency kHz QPO; (*d*) the rms amplitude of the first harmonic of the HBO; (*e*) the rms amplitude of the lower frequency kHz QPO; and (*f*) the rms amplitude of the second harmonic of the HBO as a function of S_z.

5.3 Results

In April the source traced out a full Z track in the CD and HID (Fig. 5.1). In February the HB/NB vertex and the upper NB were covered, and in July the HB was covered. The February data fall right on top of the April data, indicating that the Z track did not move appreciably between February and April. The July data have higher count rate and higher soft color. Such shifts have been observed before in GX 17+2 (Kuulkers et al. 1997), and in other Z sources (Cyg X-2: Hasinger et al. 1990; GX 5−1: Kuulkers et al. 1994a). In all observations we detected kHz QPOs in the 8.6–60 keV band. In the 6.4–8.6 keV band the QPOs were not, or were marginally, detected. Combining both bands, the significance of the QPOs increased, although the rms amplitude decreased a little. Therefore, we used the 6.4–60 keV range for the analysis of the QPOs.

We detected the kHz QPO only for $S_z < 1.5$ (Table 5.1). Typical power spectra are shown in Figure 5.2. Note the simultaneous presence of the HBO and its harmonic (*upper frame*), and the kHz QPOs. The properties of the QPOs as a function of S_z are shown in Figure 5.3. The higher frequency QPOs increase in frequency from 645±9 Hz at $S_z = 0.07\pm0.05$ to 1087±12 Hz at $S_z = 1.44\pm0.05$ (Fig. 5.3*a*), while their rms amplitude and FWHM decrease from 5.7%±0.5% to 1.5%±0.4% (Fig. 5.3*c*), and from 183±35 Hz to 21±20 Hz. Above $S_z = 1.5$, the higher frequency QPO is undetectable (upper limits typically of 2.5% rms). For $S_z < 0.5$ the lower frequency QPO is not detected, with upper limits near 2.5% rms. From $S_z = 0.56\pm0.04$ to $S_z = 1.34\pm0.05$, the lower frequency QPO is detected at a frequency increasing from 480±23 Hz to 781±11 Hz (Fig. 5.3*a*). The rms amplitude (Fig. 5.3*e*) and FWHM of the lower frequency QPO are about constant between 2%–3% and 50–150 Hz. When both QPOs are detected the frequency difference is consistent with being constant at 293.5±7.5 Hz.

The QPOs were strongest at high energy. We combined all data with $S_z < 0.5$ ($S_z = 0.23\pm0.14$) and with S_z between 1.0 and 1.3 ($S_z = 1.15\pm0.10$) to detect the QPOs at lower energy. When $S_z > 1.0$, both QPOs are seen. Both get stronger with energy, and both have about the same amplitude in each band (see Table 5.2). When $S_z < 0.5$, only the higher frequency QPO is seen. Apart from an overall increase in amplitude, its energy dependence is approximately the same as for $S_z > 1.0$ (see Table 5.2).

The kHz QPOs and HBO and its second harmonic occur simultaneously (see Fig. 5.2). The HBO frequency increases from the left end of the HB onto the upper NB (Fig. 5.3*b*; Table 5.3). At $S_z = 1.34\pm0.05$, it reaches a maximum of 61±0.2 Hz, and farther down the NB it decreases again. On the HB the rms amplitude of the fundamental decreases with S_z; on the NB it is about constant at 1.5%–2% (Fig. 5.3*d*). Above $S_z = 1.6$ it is not detected with upper limits of 2.0% rms. The rms amplitude of the second harmonic decreases on the HB with S_z (Fig. 5.3*f*). A detailed analysis of the HBO and N/FBO will be reported by Homan et al. (1999b).

Table 5.1: The kHz QPO properties vs. S_z[a]

S_z[b]	Lower frequency kHz QPO			Higher frequency kHz QPO		
	rms[c] (%)	FWHM (Hz)	Frequency (Hz)	rms[c] (%)	FWHM (Hz)	Frequency (Hz)
0.07±0.05	<2.9			5.7±0.5	183^{+35}_{-29}	$645.0^{+8.6}_{-9.4}$
0.14±0.04	<2.7			5.3±0.4	166^{+32}_{-27}	$657.0^{+8.4}_{-9.7}$
0.26±0.05	<2.7			5.4±0.6	201^{+58}_{-44}	718±17
0.36±0.04	<2.4			5.4±0.2	142±15	730.8±4.6
0.45±0.05	<2.2			4.9±0.2	147±18	753.4±5.0
0.56±0.04	1.9±0.4	88^{+61}_{-42}	480^{+23}_{-12}	4.7±0.2	150±14	782.7±4.5
0.64±0.04	2.7±0.4	150^{+50}_{-34}	519±17	4.4±0.2	125±13	800.0±4.3
0.73±0.04	2.8±0.6	134^{+70}_{-47}	531±28	5.1±0.5	203^{+41}_{-32}	832±14
0.98±0.04	3.1±0.5	82^{+34}_{-25}	659±11	$2.4^{+0.6}_{-0.9}$	77^{+60}_{-42}	952^{+13}_{-19}
1.06±0.04	2.9±0.3	77^{+22}_{-17}	682±7	3.0±0.3	115^{+37}_{-25}	969±11
1.14±0.05	2.4±0.3	46^{+15}_{-12}	696±4	2.9±0.3	103^{+35}_{-27}	$998.7^{+9.0}_{-9.8}$
1.25±0.05	2.3±0.3	59^{+20}_{-16}	759±8	2.2±0.5	83^{+55}_{-38}	1042^{+15}_{-12}
1.34±0.05	2.6±0.3	86^{+38}_{-28}	781±11	$1.5^{+0.7}_{-0.4}$	54^{+114}_{-36}	1079^{+16}_{-25}
1.44±0.05	<1.7			$1.5^{+0.5}_{-0.3}$	21^{+28}_{-17}	$1086.6^{+4.4}_{-11.7}$
1.54±0.06	<2.1			<2.1		
1.66±0.06	<3.0			<4.9		
1.77±0.07	<2.8			<3.9		
1.86±0.08	<2.6			<3.7		
1.97±0.05	<2.5			<3.6		

[a] The errors on the fit parameters are determined using $\Delta\chi^2 = 1$. Upper limits are determined using $\Delta\chi^2 = 2.71$ and a FWHM of 100 Hz

[b] The error on each S_z value is the standard deviation of each selection

[c] The energy range is 6.4–60 keV

5.4 Discussion

We detected two simultaneous kHz QPOs in GX 17+2. After Sco X-1 (van der Klis et al 1996e, 1997b) and GX 5−1 (van der Klis et al. 1996d), this is the third Z source displaying kHz QPOs[2]. The QPO frequency increases down the HB and onto the NB. For atoll sources an increase in frequency is thought to be due to an increase in $\dot{M}$. Because of the very similar properties of the kHz QPOs in atoll sources and in GX 17+2, our observations confirm that $\dot{M}$ indeed increases when the source moves down the Z track, even when (on the NB) the count rate decreases, as previously concluded by Hasinger & van der Klis (1989).

Although the behavior of the X-ray spectra changes significantly at $S_z = 1$

[2]Recently, we also found kHz QPOs in Cygnus X-2 (Chapter 6).

Table 5.2: kHz QPO rms amplitude versus photon energy[a]

	$S_z = 0.5 \pm 0.14$	$S_z = 1.15 \pm 0.10$	
Energy (keV)	Upper peak rms (%)	Upper peak rms (%)	Lower peak rms (%)
2–5.0	< 1.9	< 1.1	< 1.2
5.0–6.4	3.4 ± 0.5	2.0 ± 0.5	< 1.9
6.4–8.6	3.9 ± 0.5	2.2 ± 0.4	1.7 ± 0.5
8.6–60	7.4 ± 0.2	3.6 ± 0.3	4.1 ± 0.2
5.0–60[b]	5.2 ± 0.2	2.1 ± 0.2	2.3 ± 0.2

[a] All errors correspond to $\Delta\chi^2 = 1$. The upper limits correspond to the 95% confidence level.

[b] Added for comparison with Cygnus X-2 (Chapter 6).

when the source enters the NB, and the X-ray flux begins to decrease with S_z there, the frequencies of all QPOs continue to increase with S_z in the same manner as on the HB. The only evidence that the rapid variability is affected as the source enters the NB is by the HBO rms amplitude. Decreasing with S_z on the HB, the amplitude is about constant on the NB.

Between $S_z = 1.4$ and 1.5, the HBO frequency decreases. A similar decrease in HBO frequency on the NB for GX 17+2 was seen in the "variable-frequency" QPO on the NB reported in Chapter 4. Although supporting evidence for a decreasing HBO frequency on the NB was found in *Ginga* data on Cygnus X-2 (Chapter 3), it was unclear if the "variable-frequency" QPO in GX 17+2 was indeed the HBO (see Kuulkers et al. 1997). From Figure 5.3*b* it is now evident that indeed it was and that it was the fundamental and not, as proposed by Kuulkers et al. (1997), the second harmonic. The data reported here and in Chapter 4 show that the behavior of the HBO did not change significantly over 1 yr. In the data presented here, the HBO does not decrease to the same frequency as in 1996; this is due to a lack of data on the NB.

Beat-frequency models (BFMs) are the best models so far to explain the kHz QPOs in atoll sources. In GX 17+2 kHz QPOs and HBOs are observed simultaneously, so if the magnetospheric BFM explains the HBO (Alpar & Shaham 1985; Lamb et al. 1985), it can not explain the kHz QPOs (the same is true for Sco X-1; van der Klis et al. 1997b). The sonic-point BFM for the kHz QPOs in atoll sources (Miller, Lamb, & Psaltis 1998) assumes that the highest frequency is due to orbital motion around the neutron star at the sonic radius and the lower frequency to its beat with the neutron star spin frequency. This model predicts a constant twin peak separation, as observed for atoll sources. According to this model, the spin period of the neutron star in GX 17+2 would be 3.41 ± 0.03 ms.

Table 5.3: The HBO properties versus S_z[a]

	HBO fundamental			HBO second harmonic		
S_z[b]	rms[c] (%)	FWHM (Hz)	Frequency (Hz)	rms[c] (%)	FWHM (Hz)	Frequency (Hz)
0.07±0.05	3.5±0.2	5.0±0.5	25.59±0.08	$4.16^{+0.08}_{-0.20}$	$10.1^{+0.4}_{-0.9}$	49.4±0.2
0.14±0.04	$3.61^{+0.08}_{-0.15}$	$6.8^{+0.3}_{-0.5}$	26.97±0.09	$4.05^{+0.08}_{-0.17}$	$12.1^{+0.5}_{-0.8}$	52.1±0.2
0.26±0.05	$3.7^{+0.1}_{-0.3}$	$8.3^{+0.6}_{-1.2}$	30.7±0.2	$3.32^{+0.09}_{-0.22}$	$10.8^{+0.8}_{-1.3}$	59.4±0.4
0.36±0.04	$2.96^{+0.06}_{-0.13}$	5.9±0.4	32.89±0.09	$2.79^{+0.04}_{-0.16}$	$9.6^{+0.3}_{-1.0}$	63.9±0.2
0.45±0.05	$2.94^{+0.07}_{-0.12}$	7.4±0.5	$35.50^{+0.12}_{-0.08}$	$2.54^{+0.04}_{-0.15}$	$11.1^{+0.4}_{-1.3}$	69.3±0.3
0.56±0.04	$2.58^{+0.10}_{-0.07}$	$6.7^{+0.7}_{-0.2}$	38.13±0.06	$2.15^{+0.04}_{-0.12}$	$10.7^{+0.3}_{-1.2}$	74.2±0.2
0.64±0.04	$2.40^{+0.10}_{-0.05}$	$7.0^{+0.6}_{-0.3}$	40.3±0.1	$1.85^{+0.08}_{-0.05}$	$9.4^{+1.0}_{-0.7}$	79.2±0.3
0.73±0.04	2.2±0.2	$7.0^{+1.0}_{-1.3}$	42.8±0.3	1.8±0.2	10.0±2.3	84.2±0.8
0.98±0.04	1.7±0.2	$4.5^{+0.8}_{-1.0}$	53.4±0.4	<1.4		
1.06±0.04	$1.75^{+0.05}_{-0.14}$	$5.5^{+0.5}_{-0.9}$	$55.9^{+0.5}_{-0.3}$	<0.7		
1.14±0.05	$1.67^{+0.09}_{-0.07}$	3.6±0.5	58.2±0.2	<0.7		
1.25±0.05	$1.83^{+0.06}_{-0.11}$	$3.6^{+0.4}_{-0.6}$	60.4±0.2	<1.1		
1.34±0.05	1.6±0.1	3.2±0.6	61.0±0.2	<1.0		
1.44±0.05	1.5±0.2	$6.7^{+2.5}_{-1.8}$	59.2±1.3	<0.9		
1.54±0.06	$1.9^{+0.6}_{-0.4}$	$7.2^{+7.4}_{-3.7}$	$55.2^{+0.7}_{-1.3}$	<1.3		

[a] The errors on the fit parameters are determined using $\Delta\chi^2 = 1$. Upper limits on the second harmonic are determined using $\Delta\chi^2 = 2.71$, a FWHM of 10 Hz, and a frequency of twice the fundamental frequency

[b] The error on each S_z value is the standard deviation of each selection

[c] The energy range is 6.4–60 keV

In Sco X-1 the twin peak separation decreases when the frequencies of the kHz QPOs increase (van der Klis et al. 1997b). Although the peak separation in GX 17+2 is consistent with being constant, its error bars are larger than in Sco X-1, and a decrease similar to that in Sco X-1 can not be excluded (see Fig. 5.4). Note that the decrease of the peak separation in Sco X-1 was observed when this source was moving down the NB onto the beginning of the FB. We could not observe the kHz QPOs this far down the Z in GX 17+2.

Another explanation that has been proposed for kHz QPOs is the photon bubble oscillation (PBO) model of Klein et al. (1996). These oscillations have been modeled to occur below 0.4 $L_{\rm Edd}$ and only weakly (or not at all) above 1.1 $L_{\rm Edd}$ (Klein et al. 1996; R. Klein 1997, private communication). The amplitudes of the PBOs decrease and their frequencies increase with $\dot{M}$, just as we

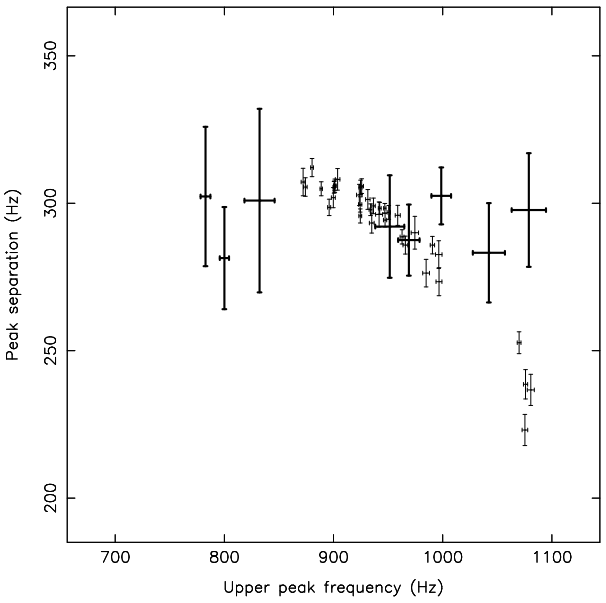

Figure 5.4: The kHz peak separation vs. the frequency of the higher frequency QPO. The heavy points with the large error bars are for GX 17+2, the light points with the small error bars are for Sco X-1 (taken from van der Klis et al. 1997b, their Fig. 3*a*).

observe. However, in calculations so far, PBOs near 1200 Hz occur at 0.4 $L_{\rm Edd}$, a factor 2 lower than the inferred luminosity when we observed 1200 Hz QPOs. Calculations for luminosities between 0.4 and 1.1 $L_{\rm Edd}$ covering a wider range of parameters are needed to compare the properties of the PBOs more accurately with the observed properties of the kHz QPOs in Z sources.

GX 17+2 and Sco X-1 have similar timing properties. The highest observed frequency of the kHz QPOs in both sources is approximately 1100 Hz, and the peak separations are more or less equal (see Fig. 5.4). However, several aspects of the timing behavior differ significantly between the two sources. In Sco X-1 the highest frequency for the kHz QPOs is observed at the beginning of the FB (van der Klis et al. 1996e), but in GX 17+2 this frequency is already reached on the upper NB. This difference is remarkable, because both sources are thought to reach $L_{\rm Edd}$ near the NB/FB vertex (i.e., $S_{\rm z} = 2$). So the same frequency is reached in GX 17+2 further from the Eddington critical value than in Sco X-1.

Also, in Sco X-1 the frequency of the HBO does not decrease as $\dot{M}$ increases (van der Klis et al. 1997b). In Chapter 4, it was suggested that an increase in the mass flux through the radial inflow as GX 17+2 moves down the NB could produce the decrease of mass flux through the inner disk needed in the magnetospheric BFM to explain the observed decrease of the HBO frequency with increasing $\dot{M}$. It remains to be seen if indications can be found for a different radial inflow behavior between the two sources, as would be required to explain the difference in the HBO frequency changes with $\dot{M}$ within this framework.

Acknowledgments. This work was supported in part by ASTRON, NSF, and NASA. M. M. is a fellow of the Consejo Nacional de Investigaciones Científicas y Técnicas de la República Argentina.

Chapter 6

Discovery of kilohertz quasi-periodic oscillations in the Z source Cygnus X-2

R. Wijnands, J. Homan, M. van der Klis, E. Kuulkers, J. van Paradijs,
W. H. G. Lewin, F. K. Lamb, D. Psaltis, & B. Vaughan
Astrophysical Journal **493**, L87–L90 (1998)

Abstract

During observations with the *Rossi X-ray Timing Explorer* from 1997 June 31 to July 3 we discovered two simultaneous kHz QPOs near 500 and 860 Hz in the low-mass X-ray binary and Z source Cygnus X-2. In the X-ray color-color diagram and hardness-intensity diagram (HID), a clear Z track was traced out, which shifted in the HID within 1 day to higher count rates at the end of the observation. Z track shifts are well known to occur in Cygnus X-2; our observation for the first time catches the source in the act. A single kHz QPO peak was detected at the left end of the horizontal branch (HB) of the Z track, with a frequency of 731±20 Hz and an amplitude of $4.7^{+0.8}_{-0.6}$% rms in the energy band 5.0–60 keV. Further to the right on the HB, at somewhat higher count rates, an additional peak at 532±43 Hz was detected with an rms amplitude of $3.0^{+1.0}_{-0.7}$%. When the source moved down the HB, thus when the inferred mass accretion rate increased, the frequency of the higher frequency QPO increased to 839±13 Hz, and its amplitude decreased to $3.5^{+0.4}_{-0.3}$% rms. The higher frequency QPO was also detected on the upper normal branch (NB) with an rms amplitude of $1.8^{+0.6}_{-0.4}$% and a frequency of 1007±15 Hz; its peak width did not show a clear correlation with inferred mass accretion rate. The lower frequency QPO was most of the time undetectable, with typical upper limits of 2% rms; no conclusion on how this QPO behaved with mass accretion rate can be drawn. If the peak separation between the QPOs is the neutron star spin frequency (as required in some beat-frequency models), then the neutron

star spin period is 2.9±0.2 ms (346±29 Hz). This discovery makes Cygnus X-2 the fourth Z source which displays kHz QPOs. The properties of the kHz QPOs in Cygnus X-2 are similar to those of other Z sources. Simultaneous with the kHz QPOs, the well known horizontal branch QPOs (HBOs) were visible in the power spectra. At the left end of the HB, the second harmonic of the HBO was also detected. We also detected six small X-ray bursts. No periodic oscillations or QPOs were detected in any of them, with typical upper limits of 6%–8% rms.

6.1 Introduction

The low-mass X-ray binary (LMXB) and Z source (Hasinger & van der Klis 1989) Cygnus X-2 is one of the best studied LMXBs. In the X-ray color-color diagram (CD) a Z-shaped track is traced out. Its branches are called horizontal branch (HB), normal branch (NB), and flaring branch (FB). The rapid X-ray variability in Z sources is closely related to the position of the sources on the Z. Quasi-periodic oscillations (QPOs) are present on the HB and the upper NB with a frequency between 18 and 60 Hz (called HBO). QPOs with a frequency between 5 and 20 Hz are present on the lower part of the NB and on the beginning of the FB (called N/FBOs). Both the X-ray spectral changes and the rapid X-ray variability are thought to be due to changes in the mass accretion rate ($\dot{M}$) (e.g., Hasinger & van der Klis 1989; Lamb 1991), which is inferred to be lowest on the HB, increasing along the Z and reaching the Eddington mass accretion rate at the NB/FB vertex.

Recent studies of Cyg X-2 (*EXOSAT*: Kuulkers, van der Klis, & Vaughan 1996; *Ginga*: Chapter 3) show that Cyg X-2 displays motion of the Z track in the hardness-intensity diagram (HID). Following Kuulkers et al. (1996), we call the different positions of the Z track in the HID different "overall intensity levels". When the overall intensity level changes, the morphology of the Z changes, and the whole Z moves in the CD as well as in the HID. In Chapter 3, it was found that the X-ray timing behavior on the lower part of the NB differs significantly for different overall intensity levels. The fact that the X-ray spectral and X-ray timing behavior change with changing overall intensity level suggests that something else in addition to $\dot{M}$ determines the Z track and the timing properties of Cyg X-2. A precessing accretion disk, strongly suggested by the 78 day period found in Cyg X-2 using the ASM/*RXTE* long-term X-ray light curve (Wijnands, Kuulkers, & Smale 1996a), is a possible explanation of the long-term changes.

In numerous LMXBs, mostly atoll sources (Hasinger & van der Klis 1989), kHz QPOs have been observed (see van der Klis 1998 for a recent review on kHz QPO properties). So far, kHz QPOs have been found in three Z sources (Sco X-1: van der Klis et al. 1996e, 1997b; GX 5−1: van der Klis et al. 1996d; GX 17+2: Chapter 5). In this chapter, I report the discovery of two simultaneous kHz QPOs in the Z source Cygnus X-2.

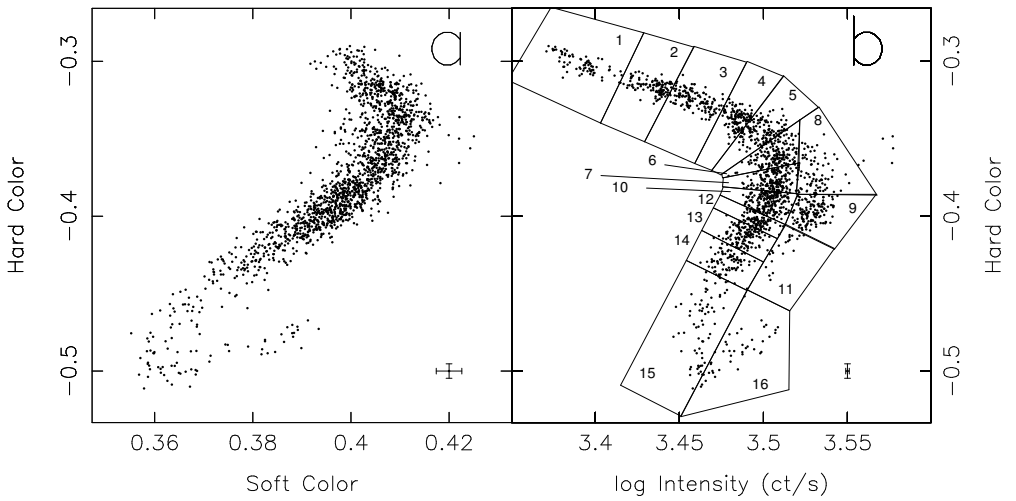

Figure 6.1: Color-color diagram (*a*) and hardness-intensity diagram (*b*) of Cygnus X-2. The soft color is the logarithm of the count rate ratio between 3.5–6.4 keV and 2.0–3.5 keV; the hard color is the logarithm of the count rate ratio between 9.7–16.0 keV and 6.4–9.7 keV; the intensity is the logarithm of the 3-detector count rate in the photon energy range 2.0–16.0 keV. Both diagrams are corrected for background ($\sim$50 counts s^{-1} in the energy range 2.0–16.0 keV); the count rate is not dead-time corrected (4%–6% correction). All points are 64 s averages. Typical error bars are shown at the bottom right corners of the diagrams. The boxes in the HID are the regions which were selected to study the timing behavior.

6.2 Observations and analysis

We observed Cygnus X-2 with the *Rossi X-ray Timing Explorer* (*RXTE*) from 1997 June 30 until July 3. A total of 108 ks of data was obtained. Data were collected simultaneously with 16 s time resolution in 129 photon energy channels (effective energy range 2–60 keV), and with 122 μs time resolution in two channels (2–5.0 keV, 5.0–60 keV). A CD and HID were made using the 16 s data, and power density spectra were calculated from the 122 μs data using 16 s data segments.

For measuring the kHz QPO properties we fitted the 128–4096 Hz power spectra with a constant plus a broad sinusoid representing the dead-time modified Poisson level (Zhang 1995; Zhang et al. 1995), and one or two Lorentzian peaks representing the kHz QPOs. For measuring the HBO we fitted the 8–256 Hz power spectra with a constant plus a power law representing the continuum, and one or two Lorentzian peaks representing the HBO and its second harmonic. Differential dead-time effects (van der Klis 1989) were negligible due to the relatively low count rates. The errors on the fit parameters were determined using $\Delta\chi^2 = 1.0$; upper limits were determined using $\Delta\chi^2 = 2.71$, corresponding to 95% confidence levels. The kHz QPOs were only detected in the 5.0–60 keV band.

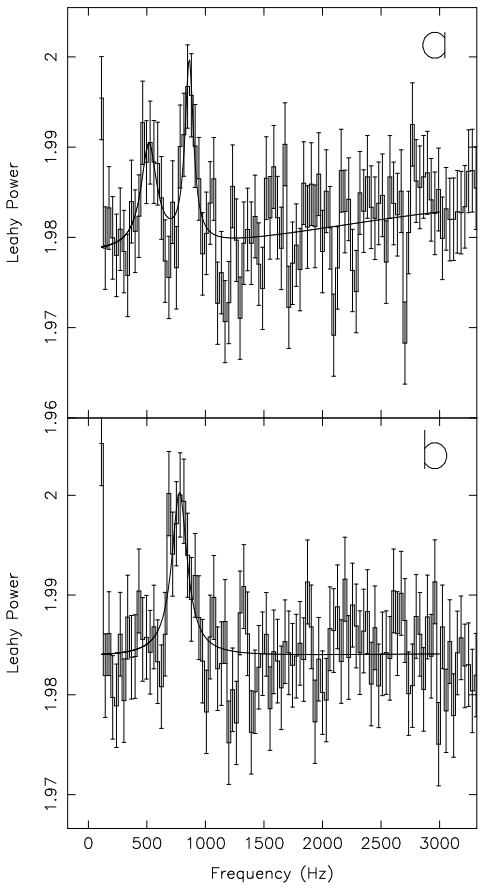

Figure 6.2: Typical Leahy normalized power spectra in the energy range 5.0–60 keV showing the kHz QPOs. The upwards slope at kHz frequencies is due to instrumental dead-time. (*a*) is the power spectrum for the interval 1997 July 2 UT 03:36–08:19; (*b*) the power spectrum for the interval 1997 July 2 UT 09:37–12:57.

In the 2–5.0 keV and the combined 2–60 keV energy bands, the kHz QPOs were undetectable. Therefore, we used the 5.0–60 keV band throughout our analysis.

For the CD we used for the soft color the logarithm of the count rate ratio between 3.5–6.4 keV and 2.0–3.5 keV, and for the hard color the logarithm of the ratio between 9.7–16.0 keV and 6.4–9.7 keV. For the HID we used as intensity the logarithm of the count rates in the energy band 2.0–16.0 keV, and for the hardness we used the hard color from the CD. For ∼12% of the time, detector 4 or 5 was off. For the CD and HID we only used the data of the three detectors which were always on in order to get the position of Cygnus X-2 on the Z during the whole observation. For the power density spectra, we used all available data.

We used the S_z parameterization (see Chapter 3 and references therein) for measuring the position along the Z (HB/NB vertex at $S_z = 1$, NB/FB vertex at $S_z = 2$). Owing to the fact that the position on the Z could be much better determined in the HID than in in the CD, we used the S_z parameterization for the Z track in the HID. Thus, the S_z-values quoted in this chapter represent the position of the source on the Z track in the HID. By using logarithmic values for the colors and the intensity, S_z does not depend on the values of those quantities but only on their variations (Chapter 3).

Table 6.1: The kHz QPO properties vs. S_z[a]

Section	S_z[b]	Lower frequency kHz QPO			Higher frequency kHz QPO		
		rms[c] (%)	FWHM (Hz)	Frequency (Hz)	rms[c] (%)	FWHM (Hz)	Frequency (Hz)
1	−0.09±0.10	<1.9			$4.7^{+0.8}_{-0.6}$	145^{+59}_{-44}	731±20
2	0.26±0.06	<3.1			3.5±0.5	122^{+47}_{-34}	821±17
3	0.46±0.07	$3.0^{+1.0}_{-0.7}$	203^{+166}_{-93}	532^{+37}_{-43}	3.3±0.5	139^{+48}_{-36}	857±21
4	0.67±0.04	<2.6			<2.5		
5	0.78±0.04	$2.5^{+0.7}_{-0.5}$	157^{+99}_{-68}	659^{+38}_{-43}	<2.1		
6+7+8	0.97±0.07	<1.9			$1.8^{+0.6}_{-0.4}$	82^{+84}_{-40}	1007±15
9	1.21±0.04	<2.5			<1.9		
10	1.13±0.04	<1.3			1.6±0.4	34^{+32}_{-17}	993^{+11}_{-7}
12	1.23±0.02	<2.2			<3.7		
13	1.32±0.04	<2.8			<2.8		
14	1.46±0.05	<3.6			<3.6		
15	1.76±0.14	<2.3			<3.2		
16	2.13±0.13	<3.6			<3.6		

[a] The errors on the fit parameters are determined using $\Delta\chi^2 = 1$. Upper limits are determined using $\Delta\chi^2 = 2.71$ and a FWHM of 150 Hz

[b] The error on each S_z-value is the standard deviation of each selection

[c] The energy range is 5.0–60 keV

6.3 Results

In Figure 6.1, the CD and the HID are shown. Cygnus X-2 traced out an almost complete Z track. The HID (Fig. 6.1*b*) clearly shows that part of the data near the HB/NB vertex (regions 8, 9, and 11 in Fig. 6.1*b*) was shifted to higher count rate with respect to the rest. No sudden jump in count rate is visible in the X-ray light curve so Cygnus X-2 moved smoothly to higher count rates. At the end of the observation, the source moved in 0.7 days from the HB/NB vertex to the left of the HB and back to the vertex again, which by then had shifted to higher count rates. This is the first time we catch the source in the act. Previously, shifted Z's were only detected on time scales of weeks to months (between observations), not during one observation. In the CD (Fig. 6.1*a*) the shift is not visible due to the fact that this shift takes place parallel to the NB (see also Chapter 3), and therefore all data overlap. Also, the error bars in the CD are large, giving larger uncertainties than in the HID. Some of the timing properties have previously been observed to change when the Z track shifts in the CD and HID (Chapter 3). For the small shift in the Z track in our observation these changes were undetectable for the QPOs discussed in this chapter.

Between 1997 July 2 UT 03:36 and 08:19 (5.8 ks exposure time) we detected two simultaneous kHz QPOs (Fig. 6.2*a*) with frequencies of 516±27 Hz and 862±11 Hz (peak separation of 346±29 Hz), at 3.4σ and 4.4σ significance, respectively. The FWHM and rms amplitude were 170^{+66}_{-51} Hz and $3.6^{+0.6}_{-0.5}$% for the lower frequency QPO, and 94^{+31}_{-25} Hz and 3.5%±0.4% for the higher frequency QPO. Upper limits to the rms amplitude of the QPOs for the same time interval in the energy range 2–5.0 keV were 2.4% and 1.1% rms, respectively. Simultaneously with these kHz QPO we detected the HBO. Between 1997 July 2 UT 09:37 and 12:57 (7 ks exposure time) we detected a single kHz QPO (Fig. 6.2*b*) with a frequency of 779±16 Hz at 4.9σ significance, with a FWHM of 177^{+52}_{-40} Hz, and an amplitude of $4.7^{+0.6}_{-0.5}$% rms. The upper limit on the amplitude of the QPO in the 2–5.0 keV band was 2.7% rms; kHz QPOs were detected at several other times, although usually below a 3σ significance level.

The Z track in the HID was not homogeneously covered. In order to get at all positions on the Z track enough statistics to detect the kHz QPOs or determine useful upper limits, we selected power spectra in the regions of the HID indicated in Figure 6.1*b*. Afterwards, we determined the average S_z-value of the power spectra selected. The frequency and the rms amplitudes of the kHz QPOs versus S_z are shown in Figure 6.3 (see also Table 6.1). At the left most end of the HB (lowest count rates) only the higher frequency QPO could be detected. When the source moved to somewhat higher count rates, a second, lower frequency kHz QPO became detectable. Further to the right on the HB the lower frequency kHz QPO was undetectable again with upper limits of 2%–3%. Near the HB/NB vertex the higher frequency QPO was detected, but further down the NB the higher frequency peak became undetectable, with upper limits of 2%–4% rms. With increasing $\dot{M}$, the frequencies of the higher frequency kHz QPOs increased and its amplitude decreased (Fig. 6.3*a* and *c*). The FWHM of the peak did not show a clear correlation with $\dot{M}$. Owing to the small number of detections of the lower frequency QPO, no conclusions can be drawn about the behavior of this QPO with $\dot{M}$, although there are indications that its frequency also increases with $\dot{M}$ (see Fig. 6.3*a*). It was not possible to determine if the kHz QPO properties changed significantly as the Z track moved in the HID (regions 6, 7, and 12 vs. 8 and 9 in Fig. 6.1*b*). This was also true for the properties of the HBO.

Simultaneously with the kHz QPOs, we detected the HBO. Its properties (in the 5.0–60 keV band) versus S_z are also shown in Figure 6.3 (see also Table 6.2). The HBO second harmonic was only detectable in region 1 ($S_z = -0.09\pm0.1$) of Figure 6.1*b* with a frequency of 73.6±0.8 Hz, an rms amplitude of $3.1^{+0.2}_{-0.4}$%, and a FWHM of 13^{+2}_{-3} Hz. The HBO fundamental in this region had a frequency of 36.2±0.2 Hz, an rms amplitude of $4.5^{+0.1}_{-0.3}$%, and a FWHM of $6.8^{+0.4}_{-0.7}$ Hz. When the source moved further to the right on the HB, the second harmonic became undetectable with typical upper limits on the amplitude of 1%–2% rms. The HBO fundamental was detected down to about halfway the NB (region 14; $S_z = 1.46\pm0.05$). Its frequency increases from 36.2±0.2 Hz at the left end of the

Table 6.2: The HBO properties vs. S_z[a]

Section	S_z[b]	HBO fundamental			HBO second harmonic		
		rms[c] (%)	FWHM (Hz)	Frequency (Hz)	rms[c] (%)	FWHM (Hz)	Frequency (Hz)
1	–0.09±0.10	$4.5^{+0.1}_{-0.3}$	$6.8^{+0.4}_{-0.7}$	36.2±0.2	$3.1^{+0.2}_{-0.4}$	$12.6^{+1.8}_{-3.2}$	73.6±0.8
2	0.26±0.06	2.5±0.2	$5.5^{+0.6}_{-0.8}$	43.7±0.3	<1.7		
3	0.46±0.07	1.9±0.2	$4.0^{+0.6}_{-1.2}$	46.1±0.3	<1.7		
4	0.67±0.04	1.1±0.2	2.4±1.0	53.8±0.4	<0.6		
5	0.78±0.04	$1.7^{+0.3}_{-0.1}$	$4.1^{+1.8}_{-0.7}$	55.7±0.4	<0.7		
6+7+8	0.97±0.07	$2.47^{+0.05}_{-0.08}$	6.0±0.5	56.4±0.1	<0.9		
9	1.21±0.04	2.7±0.2	$13.3^{+1.9}_{-2.4}$	55.7±0.6	<0.8		
10	1.13±0.04	2.8±0.1	12.5±1.5	56.4±0.5	<0.6		
12	1.23±0.02	2.7±0.4	$21.5^{+8.3}_{-5.0}$	$55.8^{+1.1}_{-1.7}$	<1.3		
13	1.32±0.04	$1.9^{+0.5}_{-0.1}$	$16.1^{+10.9}_{-3.2}$	$54.7^{+1.3}_{-2.3}$	<1.2		
14	1.46±0.05	1.9±0.5	23^{+16}_{-11}	$54.2^{+4.5}_{-3.9}$	<1.4		
15	1.76±0.14	<2.0			<1.9		
16	2.13±0.13	<1.3			<1.4		

[a] The errors on the fit parameters are determined using $\Delta\chi^2 = 1$. Upper limits are determined using $\Delta\chi^2 = 2.71$, a FWHM of 15 Hz, and the frequency of the second harmonic was fixed to twice the frequency of the fundamental.
[b] The error on each S_z-values is the standard deviation of each selection
[c] The energy range is 5.0–60 keV

HB to 56.4±0.1 Hz at the HB/NB vertex (Fig. 6.3*b*). After that its frequency remained approximately constant. The rms amplitude of the HBO first decreased on the HB with increasing $\dot{M}$, but around $S_z = 0.6$ it started to increase again (Fig. 6.3*d*). At around $S_z = 1.1$ it decreased again with increasing $\dot{M}$ until it became undetectable further down the NB. Its FWHM also first decreased on the HB with increasing $\dot{M}$ (Fig. 6.3*f*), and at the same position on the Z where the amplitude of the HBO started to increase again with increasing $\dot{M}$, the FWHM also started to increase again.

We detected six bursts in the X-ray light curve (typical durations of 4–6 s), which are very similar to those found in *EXOSAT* (Kuulkers, van der Klis, & van Paradijs 1995) and *Ginga* (Chapter 3) data. We searched for periodic oscillations and QPOs during the bursts, but none were detected (typical upper limits of 6%–8% rms). A more detailed study of the X-ray bursts will be reported elsewhere.

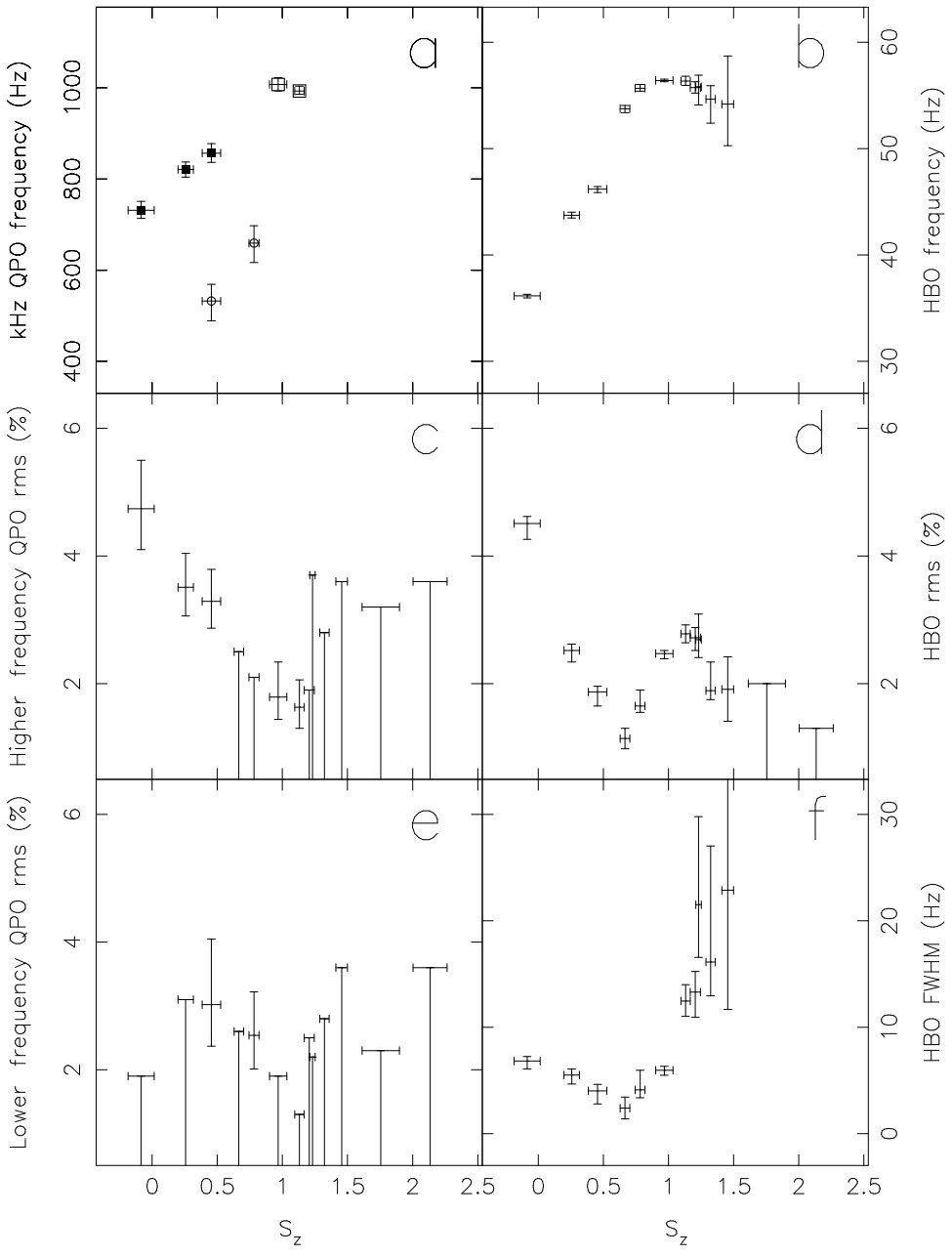

Figure 6.3: (*a*) Frequency of the kHz QPOs; (*b*) frequency of the HBO fundamental; (*c*) the rms amplitude of the higher frequency kHz QPO; (*d*) the rms amplitude of the HBO fundamental; (*e*) the rms amplitude of the lower frequency kHz QPO; and (*f*) the FWHM of the HBO fundamental as a function of S_z. In (*a*) the squares represent the higher frequency QPO and the circles the lower frequency QPOs. Open symbols represent detections of the kHz QPOs with significance between a 2 and 3σ; the filled points represent detections with $>3\sigma$ significance.

6.4 Discussion

We have discovered two simultaneous kHz QPOs near 500 and 860 Hz in the Z source Cygnus X-2. The frequency of the higher frequency QPO increased when the source moved from the left end of the HB to the upper NB, and there are indications that the same is true for the frequency of the lower frequency QPO. Cygnus X-2 is the fourth Z source which displays kHz QPOs. Most likely the remaining two Z sources (GX 340+0 and GX 349+2) will also display kHz QPOs when they are observed on the (left end of the) HB (note that GX 349+2 has never been observed in the HB).

The properties of the kHz QPOs in Z sources are very similar to each other. In each source the kHz QPOs increase in frequency and the higher frequency QPO decreases in amplitude when the sources move down the Z, thus when $\dot{M}$ increases. The amplitude of the lower frequency QPO and the FWHM of the peaks do not have a clear correlation with $\dot{M}$. The kHz QPOs in Z sources are also very similar to what is observed (e.g., Strohmayer et al. 1996d; Zhang et al. 1996; Berger et al. 1996; Smale et al. 1997) in other, less luminous LMXBs (the atoll sources; Hasinger & van der Klis 1989). In both types of sources, the frequency of the kHz QPOs increases with inferred $\dot{M}$, the kHz QPOs are strongest in the highest photon energy band, the maximum frequencies so far detected are between 1000 and 1200 Hz, and the separation between the kHz QPOs lies between 250 and 370 Hz (see van der Klis 1998 for a recent review on kHz QPO properties). Therefore, it seems likely that kHz QPOs in atoll sources and in Z sources are produced by the same mechanism.

In Sco X-1 (van der Klis et al. 1996e, 1997b) the peak separation between the two kHz QPOs decreases with increasing $\dot{M}$[1]. In GX 17+2 a similar decrease in peak separation could not be excluded (Chapter 5), and owing to the sparsity of detections with two simultaneous kHz QPO in the present data, nothing can be said for Cygnus X-2. If the peak separation was a measure for the neutron spin frequency, then the spin frequency in Cygnus X-2 is 346±29 Hz (spin period of 2.9±0.2 ms). In the four Z sources for which kHz QPOs have been discovered, the kHz QPOs were detected simultaneously with the HBO, ruling out the possibility that both the HBOs and the kHz QPOs are magnetospheric beat frequencies (van der Klis et al. 1997b).

At the left end of the HB, the amplitude, in the energy range 5–60 keV, of the higher frequency QPO in Cyg X-2 is $4.7^{+0.8}_{-0.6}$% rms. This amplitude is smaller than the typical amplitudes of the kHz QPOs in the atoll sources, which are thought to have significantly weaker magnetic fields, as predicted by the sonic-point model (Miller, Lamb, & Psaltis 1998). The QPOs in Cyg X-2 are similar in strength to those in GX 17+2 (2%–5% rms in 5–60 keV), even though GX 17+2 may have

[1]Recently, Méndez et al. (1998a) found that also in the atoll source 4U 1608−52 the peak separation may not be constant.

a weaker magnetic field, as suggested by its weaker HBO and by X-ray spectral modeling (Psaltis, Lamb, & Miller 1995). This indicates that if the strength of the stellar magnetic field affects the amplitudes of the kHz QPOs, it is not the only variable that does so, and that other variables, such as the multipolar structure and orientation of the magnetic field, and the spin rate of the star, also play a role. If the orientation of the magnetic field with respect to the plane of the disk plays a role, its effect should be visible in the amplitude of the kHz QPOs in Cygnus X-2 when these QPOs are detected during different overall intensity levels, thus at different phases of the 78 day long-term X-ray cycle.

Note added in manuscript After submission of this chapter to the *Astrophysical Journal Letters* we discovered also two simultaneous kHz QPOs in the Z source GX 340+0 at 348^{+20}_{-16} Hz and 722±13 Hz (peak separation of 374±24 Hz, when the source was on the horizontal branch (Jonker et al. 1998). The FWHM and rms amplitude (in the energy range 5.0–60 keV) were 114^{+64}_{-39} Hz and $2.5^{+0.5}_{-0.4}$% for the lower frequency QPO, and 177^{+58}_{-45} Hz and $3.8^{+0.5}_{-0.4}$% for the higher frequency QPO.

Acknowledgments. This work was supported in part by the Netherlands Foundation for Research in Astronomy (ASTRON) grant 781-76-017 and by NSF grant AST 96-18524. B. V. (NAG 5-3340), F. K. L. (NAG 5-2925), J. v. P. (NAG 5-3269, NAG 5-3271) and W. H. G. L. acknowledge support from the United States National Aeronautics and Space Administration. We thank the *RXTE* Science Operations Facility, and especially John Cannizzo, for rapidly providing the real-time data used in this analysis.

Chapter 7

Discovery of kilohertz quasi-periodic oscillations in the Z source GX 5−1

R. Wijnands, M. Méndez, M. van der Klis, D. Psaltis, E. Kuulkers, & F. K. Lamb
Astrophysical Journal **504**, L35–L38 (1998)

Abstract

We discovered two simultaneous kHz quasi-periodic oscillations (QPOs) in the bright low-mass X-ray binary and Z source GX 5−1 with the *Rossi X-ray Timing Explorer*. In the X-ray color-color and hardness-intensity diagram a clear Z track is traced out, which shifted between observations. The frequencies of the two kHz QPOs increased from ∼215 and ∼500 Hz on the left part of the horizontal branch to ∼700 and ∼890 Hz, respectively, on the upper part of the normal branch. With increasing frequency the FWHM and rms amplitude (8.6–60 keV) of the higher frequency kHz QPO decreased from 300 to 30 Hz, and from 6.6% to 2.4%, respectively. The FWHM and amplitude of the lower-frequency kHz QPO (50–100 Hz and 3%–4% rms) did not correlate with the position of the source on the Z track. The kHz QPO separation was consistent with being constant at 298±11 Hz. Simultaneously with the kHz QPOs horizontal branch oscillations (HBOs) were detected with frequencies between 18 and 56 Hz.

7.1 Introduction

The bright low-mass X-ray binary (LMXB) and Z source (Hasinger & van der Klis 1989) GX 5−1 traces out a clear Z track in the X-ray color-color diagram (CD). The limbs of this track are called the horizontal branch (HB), normal branch (NB), and flaring branch (FB). It is thought (see, e.g., Hasinger & van

der Klis 1989) that the mass accretion rate ($\dot{M}$) increases when the source moves from the left end to the right end of the HB, down the NB, and onto the FB. Two types of quasi-periodic oscillations (QPOs) were so far detected in GX 5−1: on the HB, oscillations called HBOs were detected with a frequency between 13 and 50 Hz (van der Klis et al. 1985a), and on the NB, oscillations called NBOs with a frequency of ∼6 Hz (see, e.g., Lewin et al. 1992). No QPOs were detected on the FB of GX 5−1.

Recent, two simultaneously kHz QPOs were discovered in the Z sources Sco X-1 (van der Klis 1996e, 1997b), GX 17+2 (Chapter 5), Cyg X-2 (Chapter 6), GX 340+0 (Jonker et al. 1998), and GX 349+2 (Zhang, Strohmayer, & Swank 1998b). The properties of these QPOs are remarkably similar to each other. They are best detected on the HB and the upper part of the NB. So far, Sco X-1 is the only Z sources in which kHz QPOs have been detected on the lower part of the NB and the FB. The frequencies of the kHz QPOs increase from the left end of the HB to the upper part of the NB. In Sco X-1, their frequencies continue to increase as the source moves down the NB and onto the lower part of the FB. Similar kHz QPOs have been detected (see, e.g., Strohmayer et al. 1996d; Berger et al. 1996; Zhang et al. 1996) in the less luminous LMXBs, called the atoll sources (Hasinger & van der Klis 1989). The many similarities (e.g., the frequencies and the dependence of the kHz QPO parameters on inferred $\dot{M}$) between the kHz QPOs detected in the Z and atoll sources suggest that these QPOs are produced by the same physical mechanism in both types of LMXBs (see van der Klis 1998 for a review of kHz QPOs).

In this chapter, I report the discovery of two simultaneous kHz QPOs in the Z source GX 5−1. A preliminary announcement of the discovery of the kHz QPO was already made by van der Klis et al. (1996d).

7.2 Observations and analysis

We observed GX 5−1 on 1996 November 2, 6, and 16 (the AO1 data), and on 1997 May 30, June 5, and July 25 (the AO2 data) using the proportional counter array onboard the *Rossi X-ray Timing Explorer* (*RXTE*). We obtained a total of 102 ks of good data. During 17% of the observing time only three or four out of the five detectors were active. In constructing the CD and the hardness-intensity diagrams (HIDs) we used only the data of the three detectors that were always on. For the power spectral analysis we used all available data. Data were obtained in 129 photon energy channels (2–60 keV) with a time resolution of 16 s. Simultaneous data were collected in two photon energy bands (2–8.6 and 8.6–60 keV; the AO1 data) or four (2–5.0, 5.0–6.4, 6.4–8.6, and 8.6–60 keV; the AO2 data) with a time resolution of 122 μs. The CD and HIDs were constructed using the 16 s data; power density spectra were calculated using the 122 μs data.

To determine the properties of the kHz QPOs, we fitted the 64–4096 Hz power

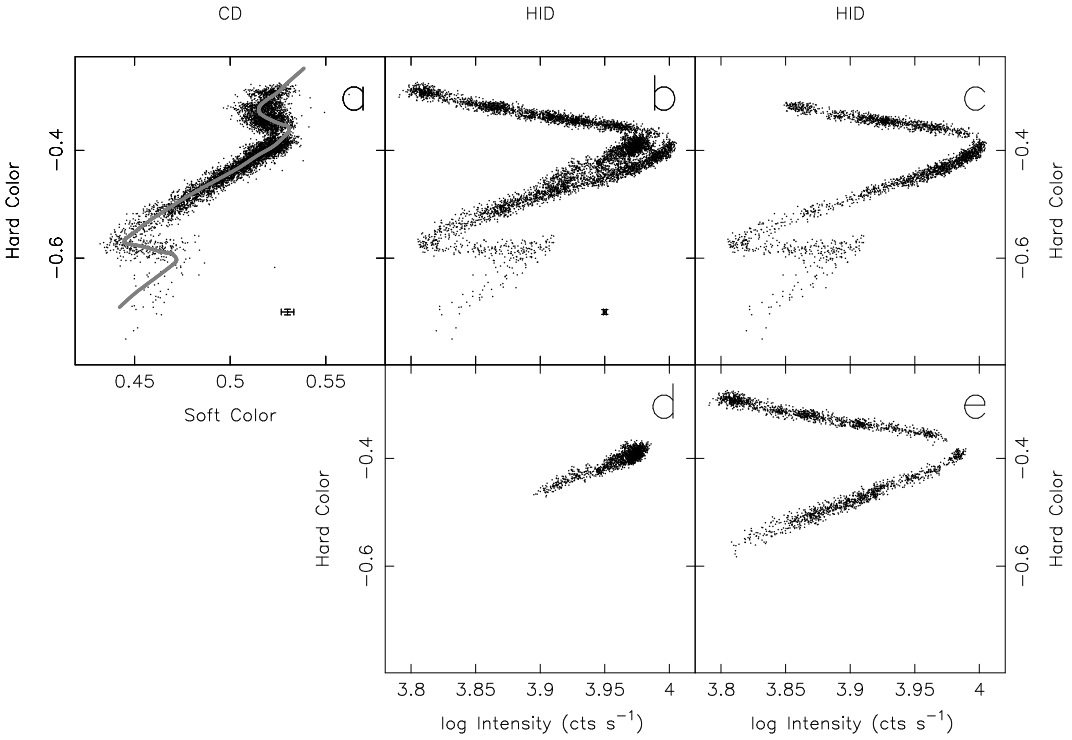

Figure 7.1: Color-color and hardness-intensity diagrams of GX 5−1: (*a*) the CD of all data, (*b*) the HID of all data, (*c*) the HID of the AO1 data, (*d*) the HID of the AO2 1997 May 30 and June 5 data, and (*e*) the HID of the AO2 1997 July 25 data. In all diagrams the soft color is the logarithm of the 3.5–6.4 keV/2.0–3.5 keV count rate ratio, the hard color the logarithm of the 9.7–16.0 keV/6.4–9.7 keV count rate ratio, and the horizontal axis the logarithm of the 2.0–16.0 keV count rate. Background was subtracted but no dead-time correction (3%–5%) has been applied. All points are 16 s averages. Typical error bars are plotted in the bottom right corner of (*a*) and (*b*). The gray solid line in (*a*) is the track used to calculated the S_z-values (see § 7.3).

density spectra with a function containing one or two Lorentzians (to represent the kHz QPOs), a constant plus a broad sinusoid (the dead-time modified Poisson level; Zhang et al. 1995), and sometimes an extra Lorentzian with a centroid frequency below 50 Hz to represent the power spectral continuum below 200 Hz. The Very Large Event (van der Klis et al. 1997b) window was set to 55 μs. Its effect on the Poisson noise was small and could be incorporated in the broad sinusoid. The properties of the HBOs and the NBOs were determined by fitting the 0.125–192 Hz power density spectra with one or two Lorentzians (the HBO and its second harmonic; the NBO), and an extra Lorentzian (with a centroid frequency $\sim$0 Hz) to represent the underlying continuum.

The uncertainties in the fit parameters were determined using $\Delta\chi^2 = 1$ and upper limits using $\Delta\chi^2 = 2.71$, corresponding to 95% confidence levels. Upper

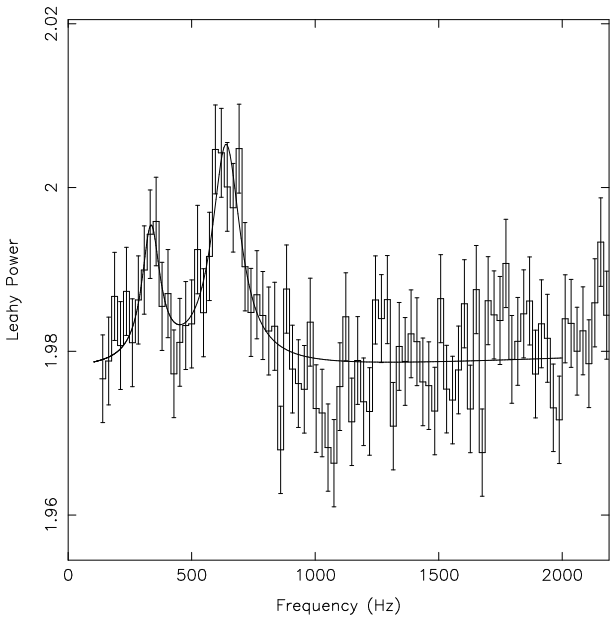

Figure 7.2: Typical Leahy normalized power density spectrum in the energy range 8.6–60 keV showing the two simultaneous kHz QPOs.

limits on the kHz QPOs amplitude were determined using a FWHM of 150 Hz. When only one of the kHz QPOs was detected, the upper limit on the other kHz QPO was determined by fixing its frequency to the frequency of the detected kHz QPO plus or minus (depending on which kHz QPO was detected) the mean peak separation. Upper limits on the amplitude of the HBO and its second harmonic were determined using a FWHM of 10 Hz or 20 Hz, respectively, and the frequency of the second harmonic was fixed at twice the frequency of the HBO.

Table 7.1: Amplitude of the kHz QPOs[a]

Energy (keV)	Lower frequency peak[b] (rms)	Higher frequency peak[c] (rms)
2–5.0	$< 1.3\%$	$< 2.0\%$
5.0–6.4	$< 2.2\%$	$< 2.6\%$
6.4–8.6	$< 2.3\%$	$2.6\pm0.5\%$
8.6–60	$3.1^{+0.6}_{-0.4}\%$	$4.7\pm0.4\%$

[a] The values were calculated at $S_z = 0.86\pm0.05$
[b] FWHM $= 98^{+53}_{-34}$ Hz, frequency $= 340^{+11}_{-13}$ Hz
[c] FWHM $= 150^{+28}_{-24}$ Hz, frequency $= 647\pm10$ Hz

Figure 7.3: The properties of the kHz QPOs versus position on the Z track, S_z (see § 7.3): (*a*) frequency of the kHz QPOs, (*b*) frequency of the HBO fundamental and 2nd harmonic, (*c*) the rms amplitude of the higher frequency kHz QPO, (*d*) rms amplitude of the HBO fundamental, (*e*) rms amplitude of the lower frequency kHz QPO, and (*f*) rms amplitude of the HBO 2nd harmonic. The black points are the AO1 data, and the red points the AO2 July 25 data.

Table 7.2: The kHz QPO properties vs. S_z during AO1[a]

	Lower frequency kHz QPO			Higher frequency kHz QPO		
S_z[b]	rms[c] (%)	FWHM (Hz)	Frequency (Hz)	rms[c] (%)	FWHM (Hz)	Frequency (Hz)
0.80±0.02	2.5±0.7	49^{+37}_{-26}	225±15	7.6±0.8	288^{+64}_{-52}	560±19
0.87±0.02	$3.1^{+1.6}_{-0.8}$	100^{+151}_{-66}	326^{+45}_{-17}	6.3±0.8	238^{+69}_{-56}	650±20
0.92±0.02	$2.7^{+0.8}_{-0.6}$	100^{+92}_{-47}	341±21	4.3±0.5	122^{+36}_{-29}	682±11
0.98±0.04	$4.3^{+1.0}_{-0.7}$	201^{+125}_{-70}	419^{+28}_{-22}	3.7±0.5	90^{+33}_{-23}	740±9
1.14±0.04	$4.0^{+1.1}_{-0.8}$	192^{+113}_{-79}	622^{+42}_{-49}	$3.2^{+1.4}_{-0.7}$	119^{+145}_{-98}	876^{+26}_{-34}
1.26±0.04	1.6±0.5	41^{+43}_{-32}	660^{+12}_{-22}	2.4±0.6	87^{+46}_{-54}	888±23
1.38±0.05	$1.6^{+0.7}_{-0.4}$	19^{+40}_{-8}	699^{+8}_{-5}	<3.4		
1.50±0.04	<4.0			<4.0		
1.63±0.04	<5.0			<5.0		
1.75±0.04	<6.0			<5.8		
1.89±0.05	<5.7			<7.1		

[a] The errors on the fit parameters are determined using $\Delta\chi^2 = 1$. Upper limits are determined using $\Delta\chi^2 = 2.71$ and a FWHM of 150 Hz

[b] The error on each S_z-value is the standard deviation of each selection.

[c] The energy range is 8.6–60 keV

In the CD and the HIDs, the soft color is defined as the logarithm of the 3.5–6.4 keV/2.0–3.5 keV count rate ratio, the hard color as the logarithm of the 9.7–16.0 keV/6.4–9.7 keV count rate ratio, and the intensity is the logarithm of the 2.0–16.0 keV count rate. By using logarithmic values for the colors and the intensity, the S_z parameterization (see § 7.3) does not depend on the values of those quantities but only on their variations (Chapter 3). The count rates used in the diagrams are background subtracted but not dead-time corrected. The dead-time correction is 3%–5%.

7.3 Results

The CD and HID of all data combined is shown in Figures 7.1*a* and *b*, respectively. Clearly, in the HID (Fig. 7.1*b*) the Z track is multiple. The reason for this is that it shifted slightly between observations. The AO1 data form one Z track with an extra branch trailing off the FB (Fig. 7.1*c*). The AO2 data are located at three different places in the HID. The 1997 July 25 data (Fig. 7.1*e*) show a HB and NB

Table 7.3: The kHz QPO properties vs. S_z during AO2[a]

S_z[b]	Lower frequency kHz QPO			Higher frequency kHz QPO		
	rms[c] (%)	FWHM (Hz)	Frequency (Hz)	rms[c] (%)	FWHM (Hz)	Frequency (Hz)
0.68±0.03	3.7±0.7	99^{+57}_{-38}	214^{+11}_{-8}	6.6±0.5	216^{+39}_{-31}	505±13
0.77±0.03	<3.4			5.1±0.6	181^{+51}_{-42}	600±16
0.82±0.04	$2.2^{+1.2}_{-0.6}$	50^{+110}_{-33}	370^{+11}_{-43}	4.7±0.5	123^{+32}_{-27}	619±11
0.89±0.02	2.6±0.4	39^{+16}_{-11}	342±0.5	5.0±0.5	176^{+44}_{-38}	688±13
0.96±0.02	$3.3^{+1.1}_{-0.8}$	131^{+125}_{-73}	467±29	$3.3^{+0.9}_{-0.7}$	89^{+69}_{-48}	776^{+21}_{-13}
1.08±0.05	<4.7			<3.7		
1.17±0.04	<3.9			<3.9		
1.33±0.04	<3.2			<2.8		
1.46±0.04	<3.0			<3.1		
1.57±0.04	<3.4			<4.4		
1.70±0.06	<4.7			<4.6		
1.88±0.05	<5.1			<6.0		

[a] The errors on the fit parameters are determined using $\Delta\chi^2 = 1$. Upper limits are determined using $\Delta\chi^2 = 2.71$ and a FWHM of 150 Hz

[b] The error on each S_z-value is the standard deviation of each selection.

[c] The energy range is 8.6–60 keV

which are displaced from the AO1 track to lower count rates. The upper NBs of the AO1 and AO2 data do not fall on top of each other, but the lower NBs *do* (Fig. 7.1*b*), indicating that the NB/FB vertex moved around less than the HB/NB vertex. The 1997 May 30 and June 5 data cover a segment of the NB (Fig. 7.1*d*) located slightly to the right of the 1997 July 25 NB. The rapid X-ray variability (see below) confirms that GX 5−1 was on the upper part of the NB during the 1997 May 30 and June 5 observations. In the CD (Fig. 7.1*a*) the Z track is clearly visible with the extra branch trailing the FB and a slight upturn of the HB, which is only marginally visible in the HIDs (Fig. 7.1*b*). The motion of the Z track is in the CD obscured by the errors in the X-ray colors.

Because of the motion of the Z track in the HID, we decided to analyze the power spectra of the AO1, the May/June AO2, and the July AO2 data (hereafter referred to as the AO2 data, unless otherwise mentioned) separately. We selected the power density spectra according to the position of GX 5−1 on the Z track in the HIDs of the AO1 (Fig. 7.1*c*) and AO2 (Fig. 7.1*e*) data, and measured for each selection the average position of GX 5–1 along the Z track using the

Table 7.4: The HBO properties vs. S_z during AO1[a]

	HBO fundamental			HBO second harmonic		
S_z[b]	rms[c] (%)	FWHM (Hz)	Frequency (Hz)	rms[c] (%)	FWHM (Hz)	Frequency (Hz)
0.80±0.02	11.4±0.1	4.5±0.1	22.36±0.04	5.5±0.4	$21.5^{+3.5}_{-2.9}$	44.5±0.9
0.87±0.02	9.51±0.09	6.6±0.2	29.44±0.06	4.9±0.3	21.3±3.1	58.7±0.8
0.92±0.02	7.80±0.08	6.6±0.2	34.13±0.06	4.3±0.3	20.2±2.9	67.2±0.8
0.98±0.04	6.6±0.2	10.4±0.6	38.64±0.15	$4.1^{+0.6}_{-0.4}$	$32.8^{+10.9}_{-6.8}$	$74.0^{+1.9}_{-2.6}$
1.14±0.04	5.0±0.3	14.6±1.8	48.97±0.47	<1.1		
1.26±0.04	4.0±0.2	16.4±1.8	50.43±0.45	<1.1		
1.38±0.05	<3.2			<1.2		
1.50±0.04	<3.1			<1.8		
1.63±0.04	<3.6			<3.0		
1.75±0.04	<3.9			<2.7		
1.89±0.05	<3.9			<1.6		

[a] The errors on the fit parameters are determined using $\Delta\chi^2 = 1$. Upper limits are determined using $\Delta\chi^2 = 2.71$, a FWHM of 10 (the fundamental) or 20 Hz (the second harmonic), and the frequency of the second harmonic was fixed to twice that of the fundamental

[b] The error on each S_z-value is the standard deviation of each selection.

[c] The energy range is 8.6–60 keV

S_z parameterization (see, e.g., Chapter 3) applied to the combined CD (Fig. 7.1*a*). The errors on the S_z-values are the standard deviation of each selection.

Two simultaneous kHz QPOs were detected in the AO1 and AO2 HB and upper NB data (Fig. 7.2). These kHz QPOs were most significant in the highest photon energy band (8.6–60 keV). As adding the lower energy data did not improve the significance, we used the 8.6–60 keV energy band throughout our analysis. The rms amplitude upper limits and the detected values of the kHz QPOs at different photon energies are displayed in Table 7.1. Note, that not all kHz QPO detections were highly significant. For example, the three detections of the kHz QPOs in the AO1 data with the highest S_z-value (see Fig. 7.3*a*) are only significant at the 1.7–2.3 σ level.

The properties of the kHz QPOs versus S_z are shown in Figure 7.3 (see also Tables 7.2 and 7.3). The two simultaneous kHz QPO peaks increased in frequency (Fig. 7.3*a*) from the left end of the HB (∼500 and ∼215 Hz, respectively) to the HB/NB vertex and the upper part of the NB (∼890 and ∼700 Hz). Over this interval the rms amplitude (Fig. 7.3*c*) and the FWHM of the higher frequency

Table 7.5: The HBO properties vs. S_z during AO2[a]

	HBO fundamental			HBO second harmonic		
S_z[b]	rms[c] (%)	FWHM (Hz)	Frequency (Hz)	rms[c] (%)	FWHM (Hz)	Frequency (Hz)
0.68±0.03	13.07±0.09	4.71±0.08	17.56±0.02	7.8±0.3	27.8±2.1	32.6±0.8
0.77±0.03	11.58±0.08	6.1±0.1	24.37±0.04	6.4±0.3	24.1±2.4	47.7±0.6
0.82±0.04	10.1±0.1	6.4±0.2	27.71±0.05	7.9±0.6	$43.0^{+5.7}_{-5.3}$	50.3±2.2
0.89±0.02	8.2±0.1	6.9±0.2	33.55±0.06	5.7±0.3	$28.0^{+3.7}_{-3.0}$	64.8±0.9
0.96±0.02	6.0±0.2	9.0±0.7	40.1±0.2	3.4±0.5	$21.9^{+7.0}_{-6.0}$	80.8±2.0
1.08±0.05	5.0±0.5	10.0±2.2	46.5±0.7	<3.1		
1.17±0.04	5.1±0.2	$20.2^{+3.0}_{-2.4}$	50.8±0.7	<1.5		
1.33±0.04	$3.4^{+0.7}_{-0.5}$	$24.2^{+12.3}_{-8.1}$	56.0±2.8	<2.4		
1.46±0.04	<3.5			<3.5		
1.57±0.04	<3.6			<3.6		
1.70±0.06	<2.1			<2.1		
1.88±0.05	<3.7			<3.7		

[a] The errors on the fit parameters are determined using $\Delta\chi^2 = 1$. Upper limits are determined using $\Delta\chi^2 = 2.71$, a FWHM of 10 (the fundamental) or 20 Hz (the second harmonic), and the frequency of the second harmonic was fixed to twice that of the fundamental

[b] The error on each S_z-value is the standard deviation of each selection.

[c] The energy range is 8.6–60 keV

peak decreased from 6.6% to 2.4%, and from 300 Hz to 30 Hz, respectively. The rms amplitude (3%–4%; Fig. 7.3*e*) and FWHM (50–100 Hz) of the lower frequency kHz QPO show no clear relation with S_z. In the combined AO2 1997 May 30 and June 5 data kHz QPOs were detected only on the upper part of the NB, with an rms amplitude, FWHM, and frequency of 2.0%±0.4%, 93^{+47}_{-39}Hz, and 557^{+21}_{24}Hz for the lower frequency kHz QPO, and $2.4^{+0.5}_{-0.4}$%, 122^{+71}_{-43}Hz, and 856^{+19}_{-17}Hz for the higher frequency kHz QPO, respectively. Lower down the NB, the upper limits on the kHz QPOs were 2.2% rms and 3.4% rms for the lower and higher frequency kHz QPOs, respectively. During the AO1, the AO2 May/June, and the AO2 July data the peak separation was consistent with being constant at 297±17 Hz, 298±11 Hz, and 299±15 Hz, respectively. The average peak separation for all observations combined was 298±11 Hz.

Simultaneously with the kHz QPOs, the HBO and its second harmonic were detected. The frequency of the HBO increased from 18 to 56 Hz as the source moved from the left end of the HB to the HB/NB vertex and onto the upper part of the NB (Fig. 7.3*b*; Tables 7.4 and 7.5). Over this interval the rms amplitude

Table 7.6: The NBO properties vs. S_z during AO1[a]

S_z[b]	NBO		
	rms[c] (%)	FWHM (Hz)	Frequency (Hz)
1.26±0.04	5.76±0.08	8.4±0.3	5.82±0.10
1.38±0.05	6.80±0.06	4.6±0.1	5.63±0.04
b1.50±0.04	7.40±0.09	3.5±0.1	5.63±0.04
1.63±0.04	6.22±0.19	3.8±0.4	5.73±0.12
1.75±0.04	5.23±0.39	6.3±1.5	5.69±0.35
1.89±0.05	<4.6		

[a] The errors on the fit parameters are determined using $\Delta\chi^2 = 1$; upper limits using $\Delta\chi^2 = 2.71$ and a FWHM of 10 Hz.

[b] The error on each S_z-value is the standard deviation of each selection.

[c] The energy range is 8.6–60 keV

of the HBO fundamental decreased from 11% to 3% (8.6–60 keV; Fig. 7.3*d*). The rms amplitude of the second harmonic (detected only below $S_z = 1$) decreased from 8% to 3% (Fig. 7.3*f*). The FWHM of the fundamental increased from 5 to 24 Hz, and the FWHM of the second harmonic remained approximately constant at ∼25 Hz. In the AO2 May/June data the HBO was also detected simultaneously with the kHz QPOs, with an amplitude, FWHM, and frequency of 4.70%±0.9% rms, 16.0±0.8 Hz, and 50.9±0.2 Hz, respectively. NBOs with frequencies of ∼5.7 Hz were detected between $S_z \sim 1.1$ and $S_z \sim 1.8$ (Tables 7.6 and 7.7). The NBOs were detected simultaneously with the HBO fundamental on the upper NB, but never simultaneously with the HBO second harmonic. No QPOs were detected further down the NB, on the FB, and on the extra branch.

7.4 Discussion

We have discovered two simultaneous kHz QPOs on the HB of the Z source GX 5−1. Kilohertz QPOs have now been discovered in all six of the known Z sources. The frequencies of both peaks increased with inferred $\dot{M}$. The rms amplitude and the FWHM of the higher frequency kHz QPO decreased as its frequency increased; the rms and the FWHM of the lower frequency kHz QPO remained roughly constant. In Sco X-1 the peak separation decreased when

Table 7.7: The NBO properties vs. S_z during AO2[a]

S_z[b]	NBO		
	rms[c] (%)	FWHM (Hz)	Frequency (Hz)
1.17±0.04	5.1±0.3	12.1±1.6	5.8±0.4
1.33±0.04	6.4±0.1	4.9±0.3	5.67±0.09
1.46±0.04	6.9±0.1	3.7±0.2	5.61±0.06
1.57±0.04	6.6±0.1	3.7±0.2	5.68±0.06
1.70±0.06	4.5±0.2	4.6±0.6	5.8±0.2
1.88±0.05	<3.0		

[a] The errors on the fit parameters are determined using $\Delta\chi^2 = 1$; upper limits using $\Delta\chi^2 = 2.71$ and a FWHM of 10 Hz.

[b] The error on each S_z-value is the standard deviation of each selection.

[c] The energy range is 8.6–60 keV

the source moved from the upper NB to the lower NB onto the FB. The peak separation for GX 5−1 is consistent with being constant, but also with being similar to Sco X-1. This is true for the other Z sources as well, so that in the simplest description *all* peak separations vary, providing a challenge for beat frequency models where the peak separation is identified with the neutron star spin rate (see Psaltis et al. 1998 for a critical discussion of the peak separations).

In the leftmost part of the HB, i.e., at the lowest inferred $\dot{M}$, during the AO2 observation we detected the lower frequency kHz QPO at a frequency of $213.6^{+11.1}_{-7.5}$ Hz. The corresponding higher frequency kHz QPO has also a rather low frequency ($504.5^{+10.4}_{-12.6}$ Hz), but not unusually low (e.g., Strohmayer et al. 1996d; Ford et al. 1997a; Jonker et al. 1998). The lower frequency kHz QPO covers a total range in frequency of a factor 3.5. This QPO has the lowest frequency and the largest dynamic range for a kHz QPO so far detected in any LMXB. The frequency range falls in the 200–1000 Hz frequency range expected if the lower frequency kHz QPO is identified with the beat of the Keplerian frequency at the sonic-point with the neutron star spin frequency (Miller, Lamb, & Psaltis 1998). The corresponding range for the sonic-point radius would be 17–26 km, assuming a neutron star mass of 1.4 $M_\odot$ and that the peak separation is the spin frequency.

Recently, Stella & Vietri (1998) proposed that the low frequency QPOs observed in atoll sources are due to a precession of the innermost disk region, dom-

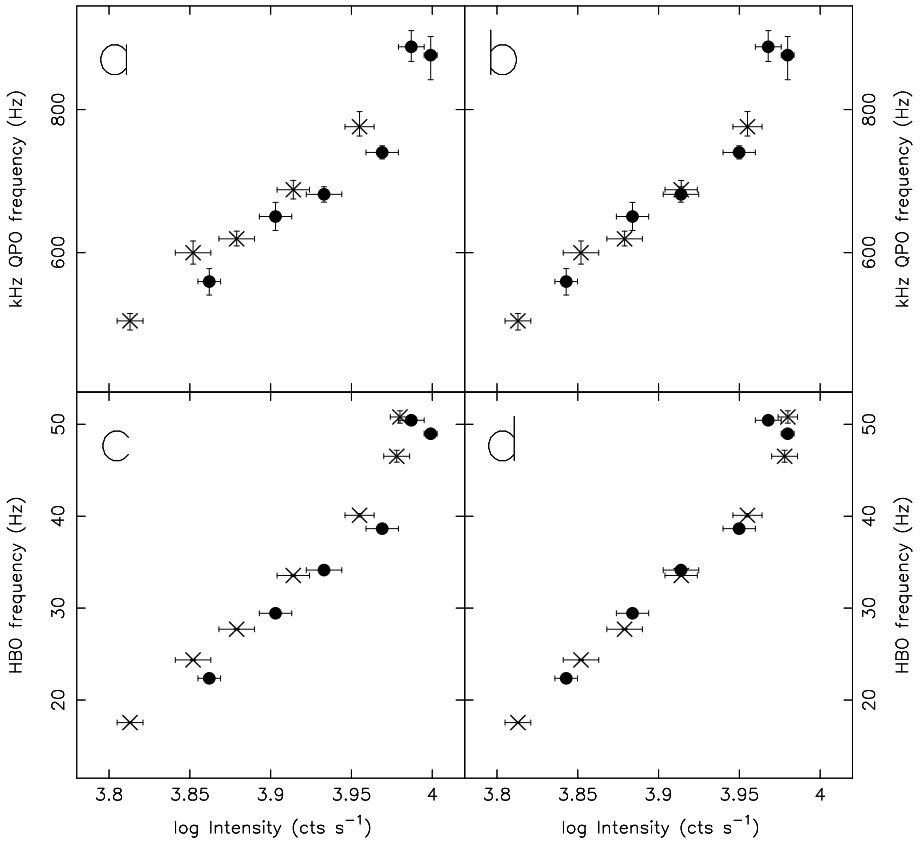

Figure 7.4: The higher frequency kHz QPO frequencies (*a* and *b*) and the HBO frequencies (*c* and *d*) versus the intensity. The definition of the intensity is the same as in Fig. 7.1. The bullets are the AO1 data and the crosses the AO2 July 25 data. In *b* and *d* the count rates of the AO1 data were corrected for the shift of the Z track (see Fig. 7.1; § 7.4).

inated by the Lense-Thirring effect. They also suggested that the HBO in Z sources could arise from the same mechanism. However, the precession frequencies predicted for GX 5−1 are about a factor 2.5 smaller than that of the HBO frequencies (see also Stella & Vietri 1998), unless I/M (with I the moment of inertia of the neutron star and M its mass) is a factor of 2.5 higher than predicted by neutron star models with realistic equations of state, the kHz QPO peak difference is half the neutron star spin frequency, or the HBOs are not the fundamental frequencies but the second harmonics. For a detailed discussion about the Lense-Thirring interpretation of the HBO in Z sources we refer to Psaltis et al. (1999a).

The Z track of GX 5−1 shifts between observations. The Z track of the AO1 data is at ∼4.5% higher count rates and ∼2% softer hard colors than the Z track of the AO2 data. Similar shift were already reported by Kuulkers et al. (1994a) using EXOSAT data, although in their observations the variations in

count rate and colors were slightly larger (∼8% and ∼6%, respectively). When plotting the frequency of the higher frequency kHz QPO and the HBO versus count rate (Fig. 7.4*a* and *c*) the AO1 data are slightly displaced to higher count rates compared to the AO2 data. If we correct the count rates of the AO1 data for the shifts in count rate derived above the kHz QPOs and HBO frequencies as a function of count rate are consistent with being the same during both epochs (Fig. 7.4*b* and *d*). The same is also true for the frequency of the lower frequency kHz QPO (not shown here) and the rms and the FWHM of all the QPOs. The only difference could be the rms amplitude of the higher frequency kHz QPOs at the lowest inferred mass accretion rate, however, the difference is marginal. This demonstrates that not the X-ray count rate determines the properties of the QPOs (both the kHz QPOs *and* the HBO), but the position of GX 5−1 on the Z track does. Kuulkers et al. (1994a) also reported that the HBO properties were consistent with being the same when the Z track of GX 5−1 was displaced in the HID. In their observations the tracks were displaced more than our tracks indicating that even for larger shifts the HBO properties do not change. Jonker et al. (1998) found the same for the HBO (the statistics did not allow to conclude anything for the kHz QPOs) in GX 340+0. For Cygnus X-2 (Chapter 3) it was shown that the NBO properties changed significantly when the Z track of this source moved around in the HID. However, due to limited available data nothing could be concluded for the HBO properties in Cygnus X-2.

Acknowledgments. This work was supported in part by the Netherlands Foundation for Research in Astronomy (ASTRON) grant 781-76-017 and by NSF grant AST 96-18524. F. K. L. acknowledges support from the United States National Aeronautics and Space Administration (NAG 5-2925). M. M. is a fellow of the Consejo Nacional de Investigaciones Científicas y Técnicas de la República Argentina. M. K. gratefully acknowledges the Visiting Miller Professor Program of the Miller Institute for Basic Research in Science (UCB).

Chapter 8

Discovery of two simultaneous kilohertz quasi-periodic oscillations in KS 1731−260

Rudy A. D. Wijnands & Michiel van der Klis
Astrophysical Journal **482**, L65–L68 (1997)

Abstract

We have discovered two simultaneous quasi-periodic oscillations at 898.3±3.3 Hz and 1158.6±9.0 Hz (kHz QPOs) in the 1996 August 1 observation of the low-mass X-ray binary KS 1731−260 with the *Rossi X-ray Timing Explorer*. The rms amplitude and FWHM of the lower frequency QPO were 5.3%±0.7% and 22±8 Hz, whereas those of the higher frequency QPO were 5.2%±1.0% and 37±21 Hz. At low inferred mass accretion rate ($\dot{M}$) both QPOs are visible, at slightly higher $\dot{M}$ the lower frequency QPO disappears and the frequency of the higher frequency QPO increases to ∼1178 Hz. At the highest inferred $\dot{M}$ this QPO is only marginally detectable (2.1σ) near 1207 Hz, which is the highest frequency so far observed in an X-ray binary. The frequency difference (260.3±9.6 Hz) between the QPOs is equal to half the frequency of the oscillations observed in a type I burst in this source (at 523.92±0.05 Hz; Smith, Morgan, & Bradt 1997a). This suggests that the neutron star spin frequency is 261.96 Hz (3.8 ms), and that the lower frequency QPO is the beat between the higher frequency QPO, which could be a preferred orbital frequency around the neutron star, and the neutron star spin. During the 1996 August 31 observation we detected an additional QPO at 26.9±2.3 Hz, with a FWHM and rms amplitude of 11±5 Hz and 3.4%±0.6%.

8.1 Introduction

Kilohertz quasi-periodic oscillations (QPOs) have been found so far in the persistent emission of nine low-mass X-ray binaries (LMXBs), three Z sources (Sco X-1: van der Klis et al. 1996e, 1997b; GX 5−1: Chapter 7; GX 17+2: Chapter 5), and six atoll sources (4U 1636−53: Zhang et al. 1996; Chapter 9; 4U 1728−34: Strohmayer et al. 1996d; 4U 1608−52: Berger et al. 1996; 4U 0614+09: Ford et al. 1997a; 4U 1735−44: Chapter 10; 4U 1820−30: Smale, Zhang & White 1997). In the sources 4U 1636−53, 4U 1728−34, 4U 0614+09, 4U 1820−30, Sco X-1, GX 5−1, and GX 17+2 two kilohertz QPOs are seen simultaneously, with a frequency separation between 250 and 360 Hz; in 4U 1608−52 and 4U 1735−44 so far only one QPO has been observed. In the sources 4U 1636−53 and 4U 1728−34 (Zhang et al. 1997; Strohmayer et al. 1996d) oscillations were observed during type I bursts whose frequency (or half of it) was consistent with being equal to the frequency separation between the two kilohertz QPOs, which in some beat-frequency models is interpreted as being the neutron star spin frequency. Smith, Morgan, & Bradt (1997a) discovered coherent 523.92±0.05 Hz oscillations, which they interpreted as the neutron star spin frequency, during a type I X-ray burst in the low-mass X-ray binary KS 1731−260, and found no QPOs near 1 kilohertz, with upper limits on the amplitude of 1% rms. We reanalyzed part of the public archive data of KS 1731−260, also used by Smith et al. (1997a), and report the discovery of two simultaneous QPOs in the persistent emission near 898 Hz and 1159 Hz, with a frequency separation consistent with being equal to half the frequency of the oscillations in the burst.

8.2 Observations and analysis

We analyzed the public archive data of KS 1731−260 obtained by the *Rossi X-ray Timing Explorer* (*RXTE*; Bradt, Rothschild, & Swank 1993) on 1996 August 1 1646–2044 UT and on 1996 August 31 1738 – 1941 UT. Due to Earth occultations and South Atlantic Anomaly passages the data were split up in three segments during the August 1 observation, and two segments during the August 31 observation each with a duration of 2000–3000 s. The (2.1–18.9 keV) source count rate varied between 1620 and 1990 counts s^{-1} on August 1 and between 1970 and 2360 counts s^{-1} on August 31. The background was typically 50 counts s^{-1}. Fitting the spectra with a thermal bremsstrahlung model (Sunyaev 1989; Smith et al. 1997a), we derive the following 2–10 keV fluxes: 3.2×10^{-9} and 3.8×10^{-9} ergs cm^{-2} s^{-1}.

During both observations data were collected with a time resolution of 16 s (129 photon energy channels), and a time resolution of 62 μs (32 channels). Both modes covered the entire 2-60 keV range over which *RXTE*'s proportional counter array is sensitive. X-ray color-color diagrams (CDs) were constructed from the

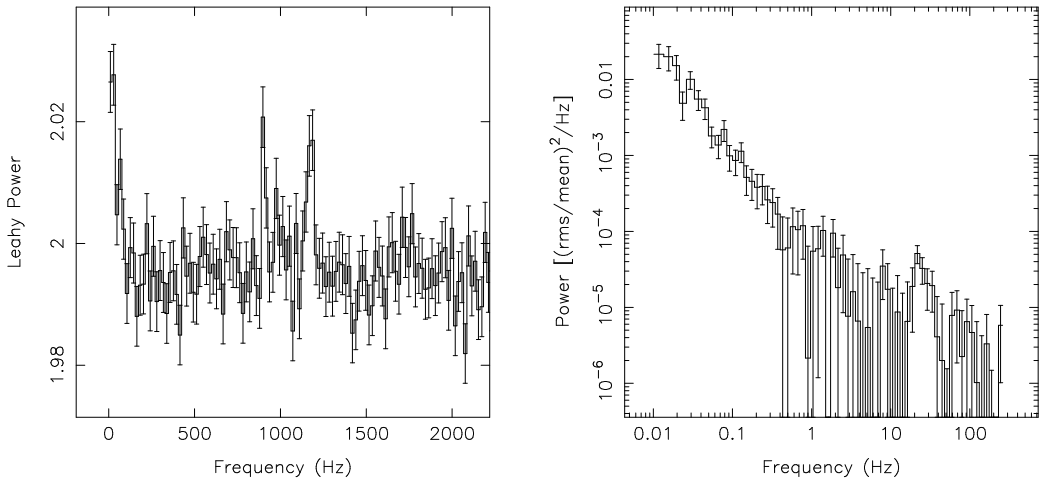

Figure 8.1: Leahy-normalized power spectra (5.7–24.1 keV) of KS 1731−260 during the 1996 August 1 observation (*left*), and the rms normalized power spectra (2.8–24.1 keV) during the 1996 August 31 observation (*right*). The left-hand figure is not corrected for counting statistics or dead-time.

16 s data, and power spectra were calculated from the 62 μs data using 16 s and 256 s data intervals. The power spectra were fitted using a power law (the very low frequency noise [VLFN], measured between 0.01–1 Hz), Lorentzians (the QPOs, if present), a broken power law (the high frequency noise [HFN], measure between 1–100 Hz), and a constant level (the Poisson noise). We found the QPOs to be strongest at high energy (this is in accordance with all previous results on kHz QPOs), and for that reason the 5.7–24.1 keV band provides the most significant detection. We have used this band throughout our analysis. The results of the fits were corrected for background and differential dead-time (see van der Klis 1989). The errors were determined using $\Delta\chi^2 = 1.0$ and the upper limits using $\Delta\chi^2 = 2.71$, which corresponds to the 95% confidence level. The reduced χ^2 values of the fits were all $\sim$1.

8.3 Results

Combining all data of the August 1 observation, two simultaneous QPOs are detected at frequencies of 900.1±2.4 Hz and 1176.2±2.9 Hz (Fig. 8.1, *left*). The rms amplitude (5.7–24.1 keV, see § 8.2) and FWHM were 3.4%±0.5% and 15±6 Hz, and 4.5%±0.5% and 27±10 Hz, respectively. During the first data segment of this observation we detect only the higher frequency QPO at 1176.2±2.2 Hz, with a FWHM of 16±8 Hz and an amplitude of 4.5%±0.6% rms. The 95% confidence upper limit on the amplitude of a QPO near 900 Hz with a FWHM of

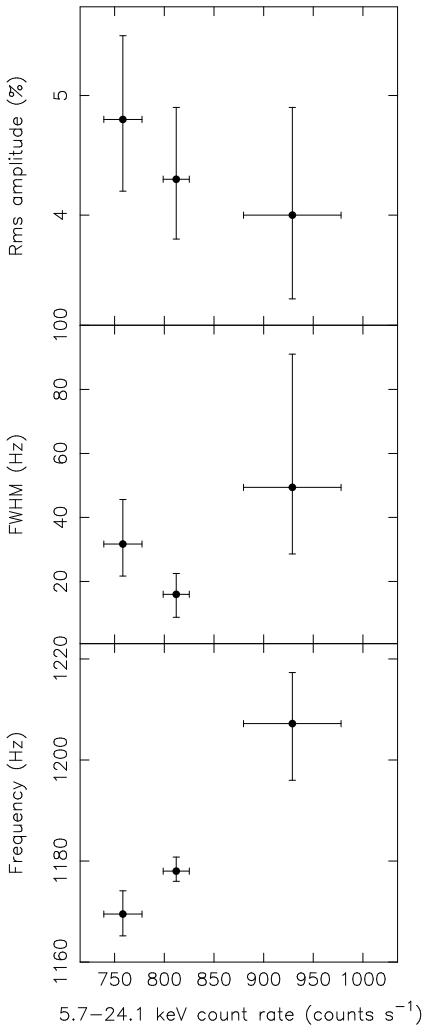

Figure 8.2: Rms amplitude (*top*), the full width at half maximum (*middle*), and the frequency (*bottom*) of the higher frequency kilohertz QPO vs. the 5.7–24.1 keV count rate. The error bars of the count rate represent the standard deviation of the count rate distribution in the count rate interval, which was selected to calculate the properties of the QPO.

15 Hz is 3.1% rms. During the second segment we find two QPOs at frequencies of 898.3±3.3 Hz and 1158.6±9.0 Hz, and a FWHM and rms amplitude of 22±8 Hz and 5.3%±0.7%, and 37±21 Hz and 5.2%±1.0%, respectively. During the third and last segment we could only marginally detect the QPOs at 899.8±4.3 Hz (1.7σ) and 1182.9±13.0 Hz (2.6σ). The FWHM and rms amplitude were 13±8 Hz and 3.8%±1.0% for the lower frequency QPO, and 10±9 Hz and 3.7%±0.7% for the higher frequency QPO.

Combining all the data of the August 31 observation only the higher frequency QPO was detected, although marginally (2.1σ), at 1197±10 Hz, with a FWHM of 38±32 Hz and a rms amplitude of 3.8%±0.9%. The lower frequency QPO had an amplitude upper limit of 2.4% rms (FWHM of 25 Hz).

We combined the power spectra of the August 1 and August 31 observations to study the dependence of the kilohertz QPO properties on 5.7–24.1 keV count rate. We selected the power spectra corresponding to count rates below

790 counts s^{-1} (288 spectra), between 790 and 840 counts s^{-1} (208 spectra), and above 840 counts s^{-1} (250 spectra). The selected power spectra, which were mixed in time (in the highest count rate selection power spectra from both observations were combined), were averaged and fitted to determine the kilohertz QPO properties (Table 8.1, Fig. 8.2). There is a clear correlation between kilohertz QPO frequency and count rate, similar to what was observed in other burst sources.

We made a single combined X-ray color-color diagram (CD) for both observations (Fig. 8.3) to study the dependence of the the kilohertz QPO properties on position of the source in the CD. From Fig. 8.3 it is clear that the kilohertz QPO properties are correlated with the position of the source in the color-color diagram. When the source is at the upper left part in the CD (low soft colors, high hard colors) two kilohertz QPOs are visible in the power spectrum. When the soft color increases and the hard color decreases both QPOs decrease in amplitude (the lower frequency QPO becomes undetectable) and the frequency of the higher frequency QPO increases. The overall count rate of the source also increases in this sense (from upper left to lower right in the CD).

Due to the low signal-to-noise ratio in the individual energy channels the dependence of the rms amplitude of the kilohertz QPOs on photon energy could not be determined in detail. In the energy range 2.8–4.6 keV both QPOs were not detectable, with rms amplitude upper limits of 3.4%. In the energy range 4.6–8.2 keV the rms amplitude of the lower and higher frequency QPO were 4.0%±0.7% and 3.9%±0.6%, respectively. In the energy range 8.2–24.1 keV the lower frequency QPO was not detectable (amplitude upper limit of 10% rms); the rms amplitude of the higher frequency QPO was 5.1%±1.1%.

The VLFN during the August 1 observation had a rms amplitude of 5.9±0.6% and a power law index of 1.61±0.07. The peaked HFN had a amplitude of 4.6±0.4% rms, a power law index of 0.8±0.6, and a cut-off frequency of 22±13 Hz. The VLFN during the August 31 observation had an rms amplitude of 7.1±0.6%, and a power law index of 1.51±0.06. Although no HFN could be detected in that observation, a QPO at the frequency 26.9±2.3 Hz is seen in the power spectrum (Fig. 8.1, *right*). The FWHM and amplitude of this QPO is 11.1±5.2 Hz and 3.4±0.6% (5.7–24.1 keV).

8.4 Discussion

We detected for the first time two simultaneous kilohertz QPOs in KS 1731−260, at frequencies near 898 Hz and 1159 Hz. The amplitudes of these QPOs increase with increasing photon energy. Both QPOs are visible at the lowest count rates. At higher count rates the lower frequency QPO disappears, the amplitude of the higher frequency QPO decreases, and its frequency increases. At the highest count rates the higher frequency QPO is only marginally detected at 1207±11 Hz. If that QPO is real then its frequency is the highest so far observed in an X-ray

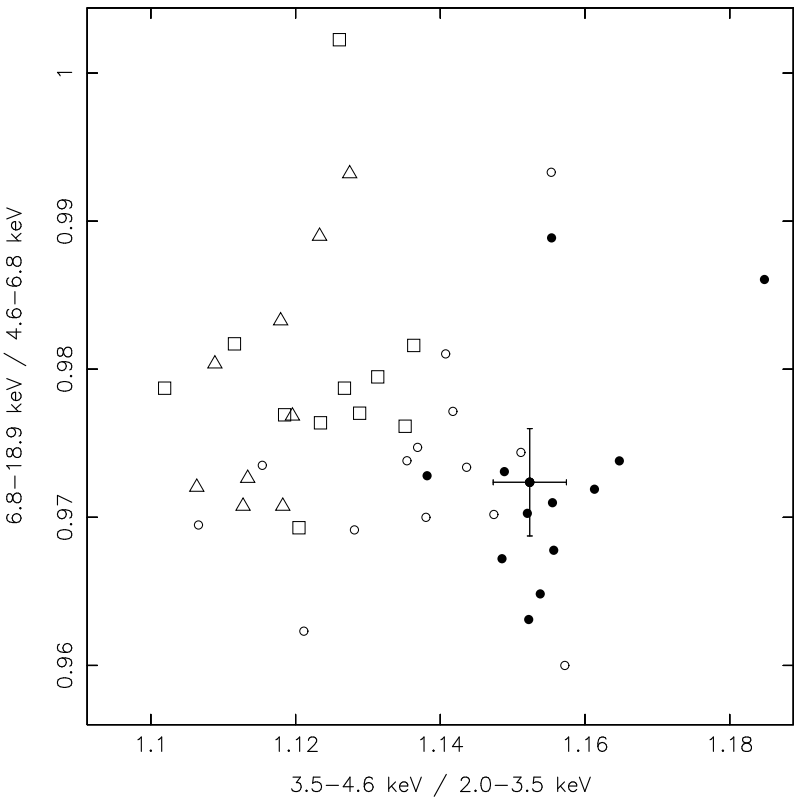

Figure 8.3: X-ray color-color diagram of the 1996 August 1 and August 31 observations. The open circles, the open triangles, and the open squares are data segments one, two, and three, respectively, of the August 1 observation. The filled circles are all data of the August 31 observation. Typical statistical error bars for the colors are shown. All points are 256 s averages. The background was not subtracted; part of the variations in the colors may therefore be due to background fluctuations.

binary. When the lower frequency QPO is detected its frequency is consistent with being constant. The minor differences in its frequency between slightly different data sets are within the statistical errors.

When we combine all power spectra from the August 1 observation, the peak separation of the two QPOs (276.1±3.8 Hz) is not consistent with being equal to half the frequency of the 523.92±0.05 Hz oscillations found by Smith et al. (1997a) in a type I burst. However, this inconsistency is artificial. In order to obtain a better signal-to-noise ratio we summed the power spectra of all three data segments obtained during this observation. During the first segment we see only the higher frequency QPO near 1176 Hz, during the second segment we see both QPOs near 898 and 1159 Hz, and during the third segment only the higher frequency peak can be significantly detected near 1183 Hz. Combination of these three data segments gives rise to an artificial increase of the peak separation, due

Table 8.1: The kilohertz QPOs[a] vs. 5.7–24.1 keV count rate

	Lower frequency QPO			Higher frequency QPO		
Count rate[b] counts s^{-1}	rms Amplitude (%)	FWHM (Hz)	Frequency (Hz)	rms Amplitude (%)	FWHM (Hz)	Frequency (Hz)
758±19	4.3±0.6	20±3	903.3±2.7	4.8±0.7	32±14	1169.5±4.6
812±13	< 4.7[c]			4.3±0.6	16±7	1178.0±2.8
929±49	< 2.9[c]			4.0±0.9[d]	49±42	1207±11

[a] All errors of the QPO properties correspond to $\Delta\chi^2 = 1$. The upper limits correspond to a 95% confidence level.

[b] Errors are the standard deviation of the count rate distribution in the count rate interval which was selected to calculate the properties of the QPO.

[c] The upper limits are for QPOs near 900 Hz, with a FWHM of 50 Hz.

[d] At a 2.1 σ level.

to the different focus in time of the two QPOs. When both kilohertz QPOs are present (segment 2) the peak separation is 260.3±9.6 Hz, which is almost exactly half the oscillation frequency (261.96) during the type I burst. This result strongly supports models in which the neutron spin frequency is 261.96 Hz (3.8 ms), the higher frequency QPO a preferred orbital frequency around the neutron star, and the lower frequency QPO the beat between these two. Such a model, with the preferred orbital radius the magnetospheric radius, was already suggested for the three QPOs found in 4U 1728−34 (Strohmayer et al. 1996d). Miller, Lamb, & Psaltis (1998) proposed a model where the preferred radius is the sonic radius. A problem for these models is the case of Sco X-1, in which the frequency difference is not constant (van der Klis et al. 1997b) as would be expected.

The positive correlation between soft color and X-ray count rate and the negative correlation between hard and soft color (Fig. 8.3), the properties of the VLFN, and the decrease in the HFN strength with count rate taken together indicate that KS 1731−260 probably is an atoll source, which in our observations was in the lower banana branch, with the inferred accretion rate somewhat higher on August 31 than on August 1. The large scatter in the CD may in part be due to background fluctuations. The 27 Hz QPO is not uncommon in atoll sources (Hasinger & van der Klis 1989; Strohmayer et al. 1996d) and seems to be closely related to the HFN ("peaked HFN").

So, the properties of the kilohertz QPOs in KS 1731−260 are consistent with what is known from observations of kilohertz QPOs in other atoll sources. The QPOs decrease in amplitude with mass accretion rate (as inferred from the count rate, the 2-10 keV fluxes, and the position in the CD), and where we can measure it (in the higher frequency QPO) the frequency of the QPO increases with mass accretion rate.

Acknowledgments. This work was supported in part by NWO grant PGS 78-277 and by ASTRON grant 781-76-017. This research has made use of data obtained through the High Energy Astrophysics Science Archive Research Center Online Service, provided by the NASA/Goddard Space Flight Center.

Chapter 9

Discovery in 4U 1636−53 of two simultaneous quasi-periodic oscillations near 900 Hz and 1176 Hz

R. A. D. Wijnands, M. van der Klis, J. van Paradijs, W. H. G. Lewin, F. K. Lamb, B. Vaughan, & E. Kuulkers
Astrophysical Journal **479**, L141–L144 (1997)

Abstract

Using the *Rossi X-ray Timing Explorer*, we observed the low-mass X-ray binary 4U 1636−53 on 1996 February 28, April 23, and May 29. On February 28 two simultaneous quasi-periodic oscillations (QPOs) occur at frequencies between 890 and 920 Hz and between 1150 and 1193 Hz. The rms amplitude and FWHM of the lower frequency QPO were 7.3%±0.4% and 26±4 Hz, whereas those of the higher frequency QPO were 6.1%±0.8% and 64±25 Hz. Averaged over minutes, the FWHM of the lower frequency QPO was sometimes as low as 4 Hz. The rms amplitudes of the QPOs increase with photon energy. The frequency of the lower frequency QPO increases, and its amplitude decreases, with accretion rate as inferred from the position of the source in the X-ray color-color diagram. The frequency difference between the two QPOs is consistent with being constant at 276±10 Hz. The frequency of the higher frequency QPO is the highest frequency so far observed in a low-mass X-ray binary. Assuming that this frequency is the orbital frequency of gas in stable Keplerian orbit around the neutron star, we derive upper limits on the mass and radius of the neutron star of 2.1 $M_\odot$ and 16.5 km. On April 23 we detected no kilohertz QPOs (95% confidence upper limits were typically 3%–5.5% rms in the frequency range 100–2000 Hz). On May 29 we detected a single 853–896 Hz QPO with an amplitude of ∼7% rms that increases with photon energy and decreases with QPO frequency. There was no significant correlation between the frequency of this QPO and the count rate or spectral changes.

9.1 Introduction

Zhang et al. (1996) recently reported the discovery of a single ∼870 Hz quasi-periodic oscillation (QPO) in the low-mass X-ray binary (LMXB) and atoll source (Hasinger & van der Klis 1989; Prins & van der Klis 1997) 4U 1636−53. Kilohertz QPOs have been found so far in the persistent emission of eight LMXBs, two Z sources (Sco X-1: van der Klis et al. 1996e, 1997b; GX 5−1: Chapter 7), and five other atoll sources besides 4U 1636−53 (4U 1728−34: Strohmayer et al. 1996d; 4U 1608−52: Berger et al. 1996; 4U 0614+09 [probably an atoll source]: Ford et al. 1997a; 4U 1735−44: Chapter 10; 4U 1820−30: Smale, Zhang & White 1997). In the sources Sco X-1, GX 5−1, 4U 1728−34, 4U 0614+09, and 4U 1820−30, two kilohertz QPOs are seen simultaneously; in the others only one QPO peak has so far been seen at any one time. In this chapter, I report the first detection in 4U 1636−53 of two simultaneous QPOs, at frequencies between 890 and 920 Hz and between 1150 and 1193 Hz. The latter QPO frequency is the highest found so far in any source. Interpretation of this frequency in terms of Keplerian orbital motion would strongly constrain the mass-radius relation of neutron stars. A preliminary announcement of this discovery has already been made by van der Klis et al. (1996c).

9.2 Observations and analysis

We observed 4U 1636−53 on 1996 February 28 0550–0829 UT, on April 23 0124–0333 UT, and on May 29 0114–0247 UT, using the proportional counter array (PCA) on board the *Rossi X-ray Timing Explorer* (Bradt, Rothschild, & Swank 1993). Earth occultations and South Atlantic Anomaly passages split the data into 2000–3000 s segments. The source count rate varied between 1950 and 2258 counts s^{-1} (2.1–19.1 keV) on February 28, between 2200 and 2400 counts s^{-1} on April 23, and between 1600 and 1850 counts s^{-1} on May 29 (both 2.0–19.0 keV). The background was typically 50 counts s^{-1}. Due to intervening PCA gain changes, the count rates and the colors of the first observation cannot be compared directly with those of the other two. Fitting the spectra with a two-component (black-body plus power-law) model, we derive the following 2–10 keV fluxes: 4.0×10^{-9}, 4.1×10^{-9} and 3.2×10^{-9} ergs cm^{-2} s^{-1}, respectively.

Data were collected on February 28 with time resolutions of 16 s (129 photon energy channels covering the range 1–65 keV), 4 ms (four channels: 1–5.8 keV), and 8 μs (eight channels: 5.8–65.5 keV), and on April 23 and May 29 with time resolutions of 16 s (129 channels: 1–98.9 keV), and 8 μs (eight channels: 8.7–98.9 keV). On May 29 data were also collected with time resolutions of 250 μs (one channel: 1–18.3 keV) and 4 ms (four channels: 1–8.7 keV).

We constructed color-color diagrams (CDs) from all 16 s data. For the Febru-

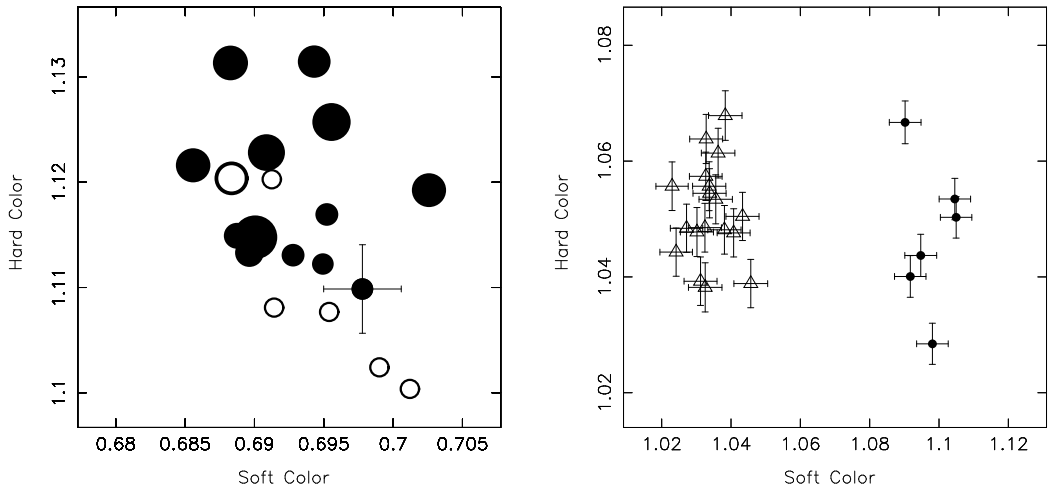

Figure 9.1: Color-color diagrams of the February 28 data (*left*) and of the April 23 and May 29 data (*right*). In the left panel, the area of the filled dots indicates the amplitude of the lower frequency QPO. The area of the open dots indicates 95% confidence upper limits on the QPO amplitude. The symbol areas scale linearly with rms amplitude (from 5% to 12%). Typical error bars for the colors are shown. In the right panel, the April 23 data are represented by dots and the May 29 data by triangles. For the definitions of the colors, see § 9.2. All points are 256 s averages.

ary 28 observation we define the soft and hard colors as the (3.7–4.8 keV)/(2.1–3.7 keV) and the (6.9–19.1 keV)/(4.8–6.9 keV) count rate ratios, respectively, and for the April 23 and May 29 observations as the (3.5–4.6 keV)/(2.0–3.5 keV) and the (6.9–19.0 keV)/(4.6–6.9 keV) ratios. The remaining data were used to calculate power spectra, which were fitted with a power law (the very low frequency noise [VLFN], measured between 0.01–1 Hz), one or two Lorentzians (the QPOs, if present), and a constant level (the Poisson noise). We corrected the results of the fits for background and differential dead-time (see van der Klis 1989). The errors were determined using $\Delta\chi^2 = 1.0$ and the upper limits using $\Delta\chi^2 = 2.71$, which corresponds to the 95% confidence level. The reduced χ^2 values of the fits were all $\sim$1.

9.3 Results

9.3.1 The February 28 observation

From the CD (Fig. 9.1, *left*) it is not obvious whether the source was in the banana state or the island state during this observation. The weak VLFN, which had an rms amplitude ranging from 0.7%±0.2% at 1 keV to 2.3%±0.4% at 19 keV,

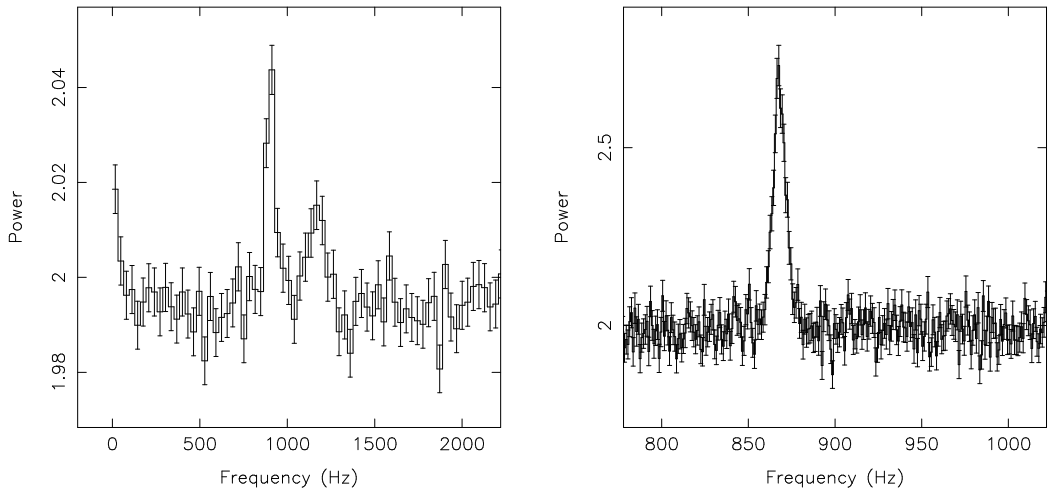

Figure 9.2: Leahy-normalized power spectra of 4U 1636−53. The left panel is for February 28, and shows two kilohertz QPOs. The right panel is from the first 3000 s of the data taken May 29 and shows a single kilohertz QPO. These figures are not corrected for counting statistics or dead-time.

and the absence of a strong high-frequency noise (HFN) component in the power spectrum indicate (see Prins & van der Klis 1997) that 4U 1636−53 was on the lower part of the banana branch.

When all four data segments (∼2000 s each; see § 9.2) are combined, two highly significant QPOs are seen near 900 Hz and 1176 Hz, both with rms amplitudes of 6%–7% (Fig. 9.2, left panel; Table 9.1). No signal was detected at the 276 Hz difference frequency (<2.0% rms) or at the 1453 Hz frequency of the higher frequency QPO plus the difference frequency (<3.0% rms). In the combined data of segments 1 and 2, we detected only the higher frequency QPO; in the data of segment 3, both QPOs; and in all the data of segment 4, only the lower frequency peak (Table 9.1). During a 4 minute part of segment 4, both QPOs were detected (Table 9.1). The lower frequency QPO was much broader during this interval than during segment 3 and the rest of segment 4. When two peaks were present, their frequency difference was consistent with being constant at 276±10 Hz. The amplitudes of both QPOs increase with photon energy in the same way (Table 9.1).

During segments 1 and 2 the QPOs were not strong enough to detect them in smaller intervals of data, but they were during segments 3 and 4. We divided the latter into 256 s intervals, during which only the very narrow (∼5 Hz), lower frequency QPO could be detected. During segment 3, the QPO frequency decreased from 920 to 890 Hz, and during segment 4 from 905 to ∼895 Hz. The amplitude of the lower frequency QPO decreased when its frequency increased

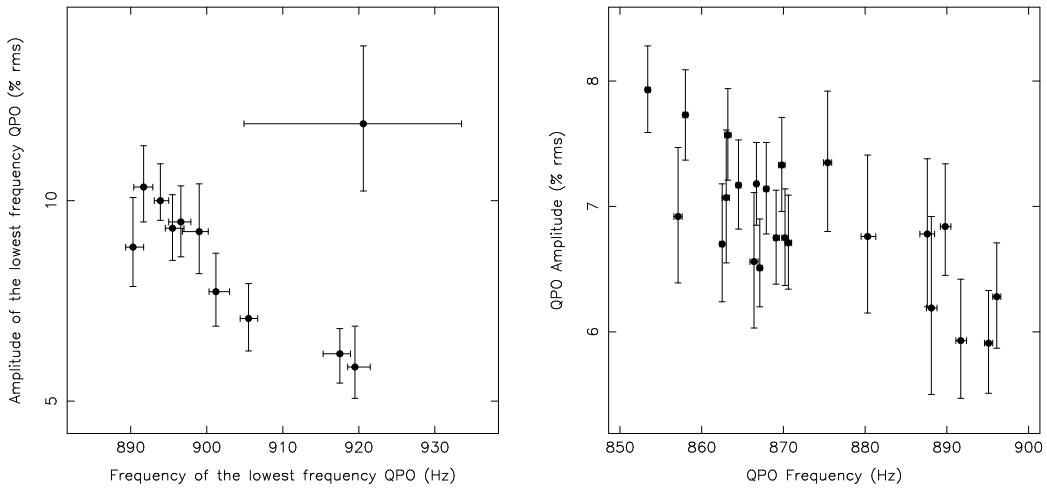

Figure 9.3: The amplitudes of the lower frequency QPO observed on February 28 (*left*) and of the single kilohertz QPO observed on May 29 (*right*) plotted vs. their frequencies. The energy range used was 5.8–65.5 keV on February 28 and 1–18.3 keV on May 29.

(Fig. 9.3, *left*). One point (which corresponds to the 4 minute interval) does not follow this correlation. When the source moved further up the banana branch (from upper left to lower right in Fig. 9.1, *left*), to higher inferred mass accretion rates ($\dot{M}$), the amplitude of the lower frequency QPO decreased and its frequency increased. No correlation was found between the FWHM (typically ∼5 Hz) and the frequency of this QPO, or between its frequency and the count rate.

9.3.2 The April 23 and May 29 observations

No strong HFN is present in the April 23 or May 29 power spectra, indicating that 4U 1636−53 was on the banana branch at both times (see Prins & van der Klis 1997). The CD (Fig. 9.1, *right*) indicates that 4U 1636−53 was further up the banana branch (i.e., the $\dot{M}$ was higher) on April 23 than on May 29. This is confirmed by the fact that, in the energy range 10.6–12.4 keV, the VLFN rms amplitude during the April 23 observation (4.0%±0.4%) was about twice that during the May 29 observation (2.1%±0.4%). The part of the power spectrum below 100 Hz on May 29 is very similar to that on February 28. Both have no strong HFN and similar VLFN. We tentatively suggest that on February 28 and May 29 4U 1636−53 was at about the same point on the banana branch.

On April 23 no QPOs were detected above 100 Hz. The 95% confidence upper limit for QPOs in the range 100-2000 Hz are 3%–5.5% rms (8.7–96.6 keV), depending on FWHM (10–50 Hz). On May 29 we see a very significant QPO at 865 Hz (Fig. 9.2, *right*), with an amplitude of 7.1%±0.3% rms and a typi-

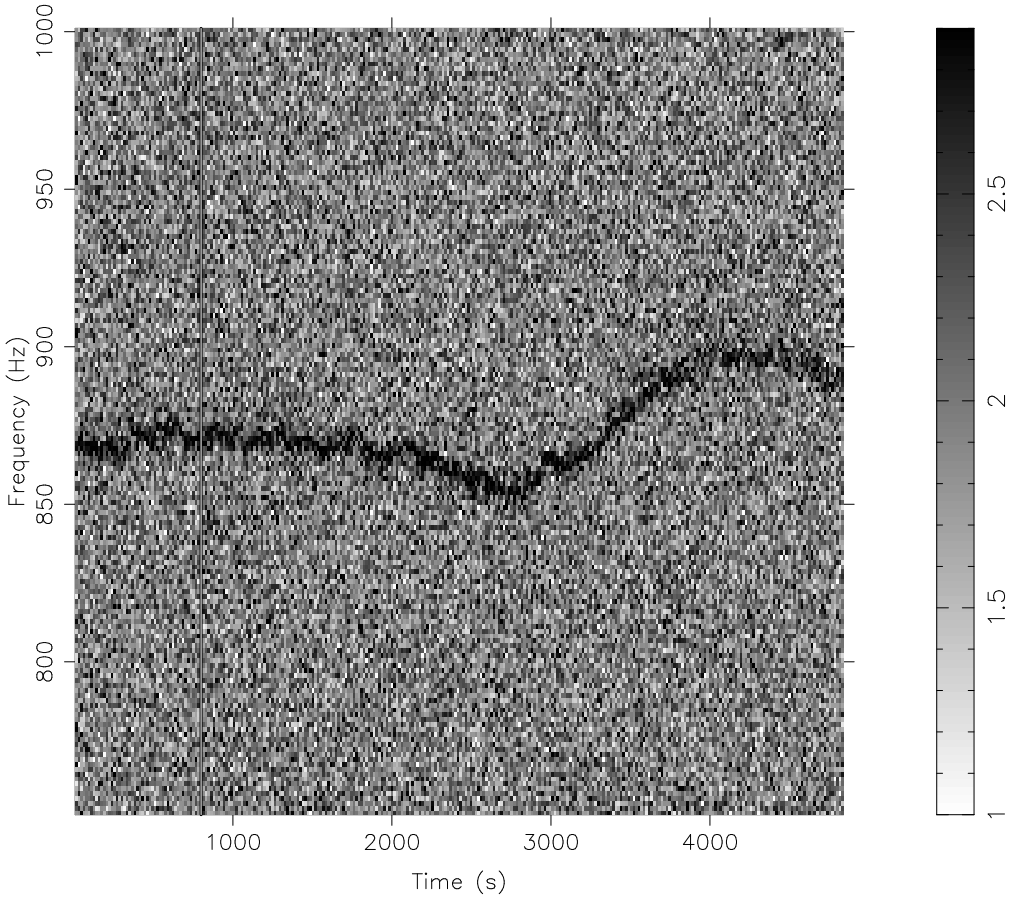

Figure 9.4: Dynamical power density spectrum of the May 29 data. Time is measured from 1996 May 29 0114 UT. A gap near 800 s (*vertical line*) is ignored.

cal FWHM of 4–6 Hz when averaged over minutes. The frequency of this peak wandered between 870 and 900 Hz during the observation (see Fig. 9.4). Dividing the data into 256 s (or 128 s, when rapid changes in frequency occurred) intervals and fitting the power spectra, we find no significant correlation between the frequency and the count rate or position of 4U 1636−53 in the CD. However, no significant motion along the banana branch was detected. The QPO amplitude is anticorrelated with its frequency (Fig. 9.3, *right*). The QPO rms amplitudes as a function of photon energy are 7.1%±0.1%, 14.9%±0.8%, 15.1%±1.3%, 18.3%±1.7%, 17.8%±3.2%, and 16.0%±2.1%, at 1–18.3, 8.7–10.6, 10.6–12.4, 12.4–14.6, 14.6–16.8, and 14.6–22.7 keV, respectively. Assuming that the oscillation at 1–8.7 keV is in phase with the oscillation at 8.7–18.3 keV, the rms amplitude of the former is ∼5%. Thus, the rms amplitude increases from ∼4 keV to ∼11 keV, but above that it stays approximately constant.

Table 9.1: QPO parameters[a] during the February 28 observation

		Lower frequency QPO			Higher frequency QPO		
Segment	Energy (keV)	rms Amplitude (%)	FWHM (Hz)	Frequency (Hz)	rms Amplitude (%)	FWHM (Hz)	Frequency (Hz)
All	5.8–65.6	7.3±0.4	26±4	899.5±1.5	6.1±0.8	64±25	1176±10
1 + 2	5.8–65.6	< 5.9	25[c]	921.9±7.7	5.5±0.9[d]	28±13	1193±5
3	5.8–65.6	8.0±0.5	17±3	897.5±1.0	6.6±1.0[e]	56±36	1147±13
4	5.8–65.6	8.8±0.7	25±6	901.3±1.9	< 7.5	50[c]	1183±15
4[b]	5.8–65.6	11.9±2.0	77±37	920±16	8.8±1.3	23±10	1183±4
All	5.8–8.5	6.0±1.2	50±36	910±12	5.1±1.6	48±43	1194±19
	8.5–11.7	8.2±1.0	19±11	903.9±3.5	6.8±1.1	50[c]	1183±13
	11.7–25.9	11.9±1.9	22±12	900.3±4.6	11.3±1.2	62±45	1174±17

[a] All errors correspond to $\Delta\chi^2 = 1$. The upper limits correspond to the 95% confidence level.
[b] Only a small part of segment 4 : 1996 February 28 07:09:38–07:13:44 UT
[c] Parameter fixed.
[d] At a 3.2 σ level.
[e] At a 2.8 σ level.

9.4 Discussion

We detected for the first time two simultaneous kilohertz QPOs in 4U 1636−53, at frequencies near 900 Hz and 1176 Hz, during our February 28 observation. The source was then probably on the lower banana branch. Both QPOs disappeared when the source moved further up the banana branch and $\dot{M}$ probably increased. On May 29, when the source was also in the lower banana branch, we found a single ∼860 Hz QPO, with properties similar to those found by Zhang et al. (1996)[1]. During their observation, the source was probably also on the banana branch, in view of the lack of a strong HFN component in the power spectrum (see their Fig. 1). Their similarities suggest that the single kilohertz QPO observed by Zhang et al. (1996) and our May 29 single kilohertz QPO are the same phenomenon. Because of the gain changes (see § 9.2) it is not clear whether or not the source was further up the banana branch (at higher $\dot{M}$) on February 28, when two QPO peaks were detected, than on May 29, when only one peak was detected. On April 23 the source was much further up the banana branch, and no QPOs were seen. The amplitude of all the kilohertz QPOs in 4U 1636−53 have about the same dependence on photon energy.

When we compare all atoll sources which show kilohertz QPOs with one another, we see that kilohertz QPOs are observed in both the island state and on the banana branch, but that so far they have displayed different characteristics. In the sources 4U 1728−34 (Strohmayer et al. 1996d), 4U 0614+09 (Ford et

[1] The count rates during the Zhang et al.'s (1996) observation and our May 29 observation were about the same (1800–1900 counts s^{-1}). The count rates reported by Zhang et al. (1996) were too high by a factor ∼2 (W. Zhang 1997, private communication).

al. 1997a), 4U 1735−44 (Chapter 10), and 4U 1820−30 (Smale et al. 1997), kilohertz QPOs have been observed when the sources were in the *island state* (as judged by the low-frequency part of their power spectra or their count rate). In 4U 1728−34, 4U 0614+09, and 4U 1820−30, two peaks are seen and their frequencies are well correlated with count rate. At low count rates only the higher frequency QPO is observed, but it still fits well on the frequency-count rate relation. So far, the only two sources in which kilohertz QPOs have been seen on the *banana branch* are 4U 1636−53 (Zhang et al. 1996; this chapter) and 4U 1608−52 (Berger et al. 1996). The double QPOs observed in 4U 1636−53 on the lower banana branch are probably the same phenomenon as the QPOs seen in the island state of the other atoll sources, due to their same dependence on inferred $\dot{M}$. The single kilohertz QPOs in 4U 1636−53 and 4U 1608−52 resemble each other in many respects. Both sources have shown a very narrow, single 850–900 Hz QPO. This QPO displays drifts in frequency on time scales of half an hour, which look remarkably similar for both sources (cf., e.g., Fig. 9.4 with Fig. 2*a* of Berger et al. 1996). The properties of those QPOs are not significantly correlated with count rate or with spectral changes.

On the basis of the observations of kilohertz QPOs made so far we tentatively conclude that there are differences in the QPO behavior that roughly correlate with source state (i.e., $\dot{M}$). However, we can neither exclude nor confirm the possibility that the double QPOs usually (but not always) seen in the island state and the single QPO seen so far only in the banana state are caused by different mechanisms.

In a small part of the data, the higher frequency peak is at 1193 ± 5 Hz, which is the highest frequency so far observed for a kilohertz QPO. If the lower frequency QPO is the beat between the higher frequency QPO and the neutron star spin frequency, as in the sonic-point (Miller, Lamb, & Psaltis 1998) and magnetospheric (Strohmayer et al. 1996d; Ford et al. 1997a) beat-frequency models, then the spin frequency is 276 ± 10 Hz (3.6 ± 0.1 ms). Assuming that the higher frequency QPO is at the orbital frequency of gas in stable Keplerian orbit around the neutron star, as required by these models, it can be used to place upper limits on the mass and radius of the star (Miller et al. 1998). A higher frequency QPO at 1193 Hz and a spin frequency of 276 Hz imply that the star's mass and radius are less than 2.1 $M_\odot$ and 16.5 km for a wide range of equations of state (C. Miller 1997, private communication). These limits include the effects of frame-dragging.

Note added in manuscript: After we submitted this chapter to the *Astrophysical Journal Letters*, Zhang et al. (1997) reported 581 Hz oscillations in type I bursts in 4U 1636−53, which they interpret as either the fundamental or first overtone of the neutron star spin frequency. They also reported two simultaneous QPOs with similar peak separation to ours, close to half the burst oscillation frequency.

Chapter 10

Discovery of kilohertz quasi-periodic oscillations in 4U 1735−44

R. Wijnands, M. van der Klis, M. Méndez, J. van Paradijs, W. H. G. Lewin, F. K. Lamb, B. Vaughan, & E. Kuulkers
Astrophysical Journal **495**, L39–L42 (1998)

Abstract

We discovered a single kHz quasi-periodic oscillation (QPO) near 1150 Hz in the *Rossi X-ray Timing Explorer* X-ray light curve of the low mass X-ray binary and atoll source 4U 1735−44. The rms amplitude of this peak was 2%–3%, and the FWHM 6–40 Hz. There are indications that the kHz QPO frequency decreased from 1160 Hz to 1145 Hz when the count rate increased, which would be quite different from what is observed in other atoll sources for which kHz QPOs have been discovered. In the X-ray color-color diagram and hardness-intensity diagram, the source traced out the curved branch (the so-called banana branch) which has been found by previous instruments. The kHz QPO was only detected when the source was at the lowest count rates during our observations, i.e., on the lower part of the banana branch. When 4U 1735−44 was at higher count rates, i.e., on the upper part of the banana branch and at higher inferred mass accretion rate with respect to that on the lower part of the banana branch, the QPO was not detected. Besides the kHz QPO, we discovered a low-frequency QPO with a frequency near 67 Hz, together with a complex broad peaked noise component below 30 Hz. This 67 Hz QPO may be related to the magnetospheric beat-frequency QPO, which is observed on the horizontal branch of Z sources. This idea is supported by the (peaked) noise found in both 4U 1735−44 and Z sources at frequencies just below the QPO frequency.

10.1 Introduction

The low-mass X-ray binaries (LMXBs) can be divided into two subclasses, the atoll sources and the Z sources, after the track they trace out in the X-ray color-color diagram (CD) (Hasinger & van der Klis 1989). Atoll sources trace out an atoll-like shape in the CD (see, e.g., Fig. 6.9 of van der Klis 1995), with a curved branch called the banana branch (divided in the upper part and lower part of the banana branch according to the position in the CD), and one or more patches corresponding to the island state, in which the colors do not change much on time scales of a day. The exact morphology of the island state track, if any, is unknown as it apparently takes a long time to trace it out. Atoll sources have lower mass accretion rates ($\dot{M}$) than Z sources (e.g., Hasinger & van der Klis 1989). In atoll sources $\dot{M}$ varies considerably between sources, and even within a single source. It is thought that $\dot{M}$ is lowest when the sources are in the island state, increases on the banana branch, and is highest on the upper part of the banana branch. The properties of the rapid X-ray variations that are observed in these sources are correlated with their position on the atoll. When the sources are in the island state strong band-limited noise is detected (called high frequency noise or HFN, with cutoff frequencies between 10 and 30 Hz). This noise is much weaker when atoll sources are on the lower part of the banana branch, and it is undetectable when they are on the upper part of the banana branch.

Quasi-periodic oscillations (QPOs) at kilohertz (kHz) frequencies have been observed in a large number of LMXBs (see van der Klis 1998 for a recent review). The kHz QPOs in atoll sources are usually found when the sources are in the island state and, rarely, when they are on the lower part of the banana branch. When they are on the upper part of the banana branch, so far no kHz QPOs have been detected, with stringent upper limits (Chapter 9; Smale, Zhang, & White 1997). Usually, two simultaneous kHz QPOs are detected, whose frequencies increase with $\dot{M}$. Sometimes, a single kHz QPO is detected (4U 1636−53: Zhang et al. 1996; Chapter 9; Aql X-1: Zhang et al. 1998a). In this chapter, I report the discovery of a single kHz QPO near 1150 Hz in the atoll source 4U 1735−44. A preliminary announcement of this discovery was made by Wijnands et al. (1996b).

10.2 Observations and analysis

We observed 4U 1735−44 on 1996 August 1, September 1, 4, and 28, and November 29 using the proportional counter array (PCA) onboard the *Rossi X-ray Timing Explorer* (*RXTE*; Bradt, Rothschild, & Swank 1993) and obtained a total of 27 ks of data. During part of the September 28 observation only four of the five PCA detectors were on. During all observations data were collected in 129 photon energy channels (effective energy range 2–60 keV) with a time resolution

of 16 s. Simultaneously, data were collected during the August 1, September 28, and November 29 observations in one broad energy channel (effective range: 2–18.2 keV) with a time resolution of 122 μs. During the September 1 and 4 observations data were collected in three broad energy bands with a time resolution of 122 μs (total effective energy band: 2–17.8 keV).

For the analysis of the X-ray spectral variations we used the 16s data of the four detectors which were always on. In constructing the CD, we used for the soft color the count rate ratio between 3.9–6.0 and 2.0–3.9 keV, and for the hard color the ratio between 8.6–18.9 keV and 6.0–8.6 keV. For the hardness-intensity diagram (HID), we used as intensity the count rates in the energy band 2.0–18.9 keV, and for the hardness, we used the same as that used for the hard color in the CD. For the analysis of the rapid time variability we made power density spectra of all the available 2–18.2 keV and 2–17.8 keV data and combined these. For determining the properties of the kHz QPOs we fitted the 128–2048 Hz power spectra with a function consisting of a constant and one or two Lorentzian peaks. For measuring the high-frequency noise and the low-frequency QPO, we fitted the 0.1–512 Hz power spectra with a constant, an exponentially cutoff power law, and one or two Lorentzian peaks. The errors on the fit parameters were determined using $\Delta\chi^2 = 1.0$; the upper limits were determined using $\Delta\chi^2 = 2.71$, corresponding to a 95% confidence level. Upper limits on the kHz QPOs were determined using a fixed FWHM of 50 Hz.

10.3 Results

10.3.1 Atoll source state

The CD and HID for all data combined are shown in Figure 10.1. The source traced out a clear banana branch in both diagrams. There is more scatter on the upper part of the banana branch in the HID than in the CD, which is due to the fact that during the Sep 1 and 4 observations when the source was on the upper part of the banana branch, the count rate was slightly higher than during the other observations. From the CD and the strength of the HFN (see § 10.3.3) it is clear that 4U 1735−44 was never in the island state during our observations.

10.3.2 Kilohertz QPO

We selected power spectra according to the position of the source on the banana branch in the HID (thus effectively by count rate level in the HID). In the combined data of regions 1, 2, and 3 (see Fig. 10.1*b*), we detected a kHz QPO at 1149±4 Hz at an amplitude that differed from zero by 5.6 times the 1σ uncertainty (Table 10.1), quite significant when taking into account the ∼30 trials implicit in our procedure to search the power spectrum out to 1200 Hz. The

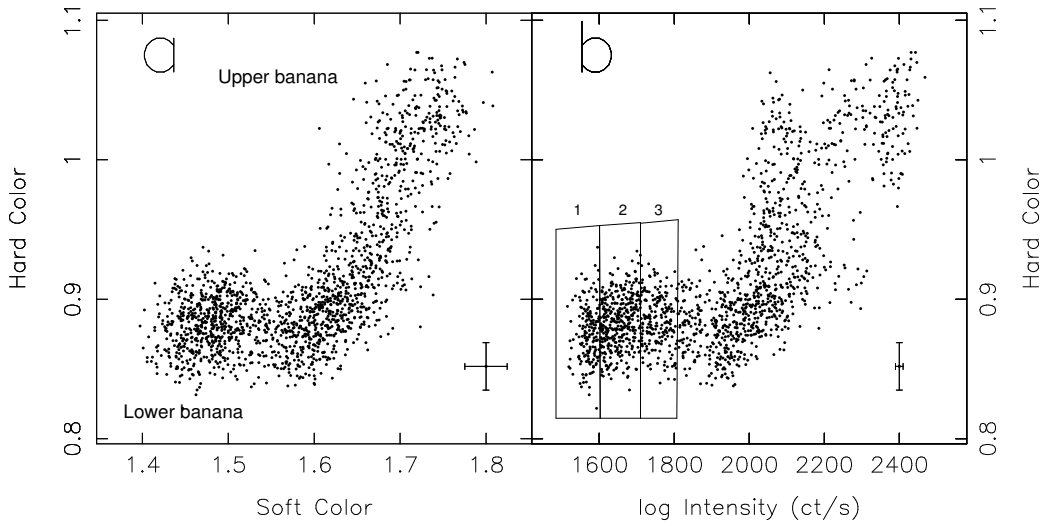

Figure 10.1: (*a*) CD and (*b*) HID of 4U 1735−44. The soft color is the count rate ratio between 3.9–6.0 and 2.0–3.9 keV; the hard color is the count rate ratio between 8.6–18.9 and 6.0–8.6 keV; the intensity is the four-detector count rate in the photon energy range 2.0–18.9 keV. The count rates are background subtracted, but not dead-time corrected (typically 1% correction). All points are 16 s averages. In the HID, the three boxes are shown which were used to select power spectra to study the timing properties. Typical error bars on the colors and intensity are plotted in the lower right-hand corner of the diagrams.

QPO was not detected in the rest of the data. In order to determine the behavior of the kHz QPO with changing position of the source in the HID, we divided the region in which the kHz QPO was found into three parts (see Fig. 10.1*b* and Table 10.1). In the data corresponding to regions 1 and 2, we detected the kHz QPO at 1161±1 Hz (3.3σ) and 1144±4 Hz (4.8σ), respectively. In the data of region 3, the kHz QPO was not detected.

We also made power spectrum selections based on continuous time intervals (mainly different *RXTE* data segments). In the first 8000 s (5040 s of data; 1996 August 1 14:17–16:15 UTC) of the observation on August 1, we detected a kHz QPO at 1149±3 Hz (4.5σ). We divided this data segment in the intervals 0–2000 s (1296 s of data) and 2000–8000 s (3744 s of data) and detected the 1160 Hz QPO in the first interval (4.0σ; 1567±25 count s^{-1} for 2–18.9 keV) and the 1145 Hz QPO in the second interval (4.8σ; 1623±49 count s^{-1} for 2–18.9 keV; see Fig. 10.2*a*). The 1145 Hz QPO was also detected in the time interval 1996 September 28 12:50–13:49 UT (3.8σ; 3520 s of data).

In both cases, the kHz QPO near 1160 Hz was the narrowest and least significant. Applying an F-test to the χ^2 of the fits with and without this QPO, we obtain probabilities of 3.0×10^{-5} and 1.3×10^{-5} for the count rate selection

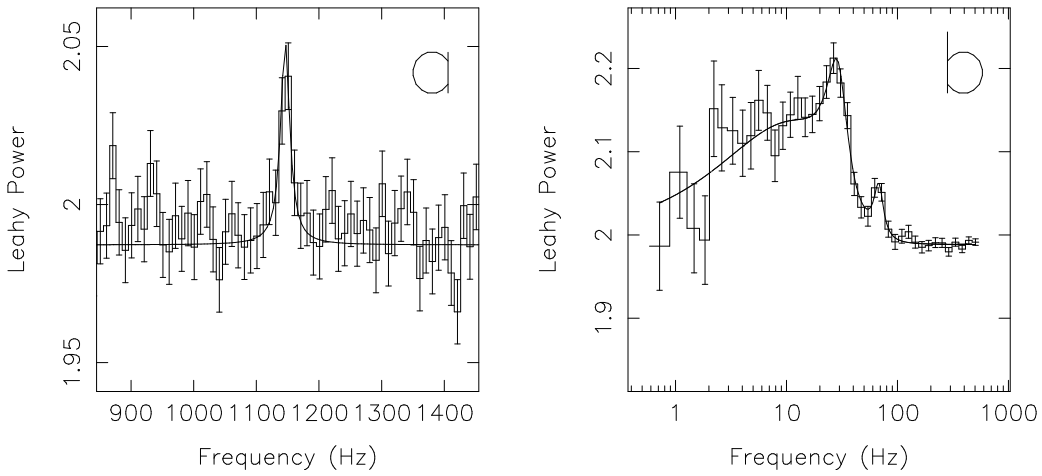

Figure 10.2: Typical Leahy normalized power spectra in the energy range 2–18 keV. (*a*) the kHz QPO; (*b*) the complex high-frequency noise and the 67 Hz QPO. Both power spectra were selected for the time interval 1996 August 1 15:12–16:15 UTC.

data and the time selection data respectively, for the hypothesis that the 1160 Hz QPO was not present in the data. Since the effective number of trials implicit in our search for a peak near 1149 Hz was about 14, the 1160 Hz QPO was detected at high confidence.

We tested the significance of the frequency change between HID regions 1 and 2, and between the 0–2000 s and 2000–8000 s intervals by fitting simultaneously the two power spectra and by either forcing the frequency to be the same in both fits or leaving both frequencies free. Applying an F-test to the χ^2 values of these fits, we obtain probabilities of 2×10^{-2} and 3×10^{-4}, respectively, for the hypothesis that the frequency of the kHz QPOs did not change in the sense reported. The probability differs considerably between the two selection methods. Although there are no trials in this determination, this frequency shift needs further confirmation

It is known from other LMXBs that the kHz QPOs are strongest at the high photon energies. However, due to the lack of energy resolution of the high timing data when the kHz QPO was present, we could not check this for 4U 1735−44.

In the power spectrum of the combined region 1, 2, and 3, we detected simultaneously with the 1149 Hz QPO a second peak at 900±14 Hz (FWHM of 68±29 Hz; amplitude of 2.6%±0.4% rms; 3.4σ). Applying an F-test to the χ^2 of the fit with and without the 900 Hz QPO, we obtain a probability of 2.2×10^{-4} for the hypothesis that the 900 Hz QPO was not present in the data, indicating that the 900 Hz QPO was detected at a 3.8σ level. Taking into account the number of trials ($\sim$8) this QPO is only marginally significant. Shifting the 1160 Hz QPO to

Table 10.1: kHz QPO properties[a]

Selection [b]	Count rate[c] (counts s^{-1})	rms[d] (%)	FWHM (Hz)	Frequency (Hz)
1+2+3	1660±72	3.1±0.3 (5.6 σ)	42±13	1149±4
1	1570±18	2.2±0.3 (3.3 σ)	7±5	1161±1
2	1652±30	3.3±0.4 (4.8 σ)	34±12	1144±4
3	1758±24	<3.1		
Rest	2065±157	<1.7		

[a] All errors correspond to $\Delta\chi^2 = 1$. The upper limits are for 50 Hz FWHM and correspond to the 95 % confidence level ($\Delta\chi^2 = 2.71$).

[b] The sets used are shown in Fig. 10.1*b*.

[c] The errors are the standard deviation of the count rate distribution of the selection used. The energy range is 2–18.9 keV

[d] The energy range is 2–18.2 keV.

1140 Hz and averaging all QPO data together (cf. Méndez et al. 1998a) did not improve the significance of the second QPO. If this second QPO is really present the frequency separation would be ∼250 Hz, not uncommon as a peak difference.

10.3.3 Low-frequency power spectrum

In the power spectrum below 100 Hz for the time interval 1996 August 1 15:12–16:15 UTC, a 67 Hz QPO and peaked noise below 30 Hz were clearly detected (Fig. 10.2*b*). The peaked noise component had a complex form. We fitted this noise component with an exponentially cutoff power law plus a Lorentzian. Including this Lorentzian in the fits considerably improved the quality of the fits and made the properties of the 67 Hz QPOs much easier to determine. The rms amplitude, power law index, and cutoff frequency of the cutoff power law were 3.7%±0.7%, −1.1±0.5, and 8±3 Hz. The rms amplitude, FWHM, and frequencies of the extra Lorentzian and the 67 Hz QPO were, 5.1%±0.7% (3.9 σ) and 3.0%±0.3% (4.9 σ), 17±3 Hz and 17±5 Hz, and 28.7±0.9 Hz and 67±2 Hz, respectively. The 67 Hz QPO and the noise component were best detected when 4U 1735−44 was on the lower part of the banana branch, at count rates below 1800 count s^{-1} (regions 1, 2, and 3 of Fig. 10.1*b*). The behavior of the properties of the 67 Hz QPO with count rate and position of the source on the banana branch could not be accurately determined. However, it was clear that the 67 Hz QPO and the peaked-noise component are weaker at somewhat higher count rates and not detected when the source is on the upper part of the banana branch.

10.4 Discussion

We detected for the first time a kHz QPO in 4U 1735−44. Its frequency was near 1149 Hz. A second kHz QPO might be present at ∼900 Hz, but this needs confirmation. The kHz QPO was only detected when the source was at the lowest count rates during our observations (i.e., on the lower part of the banana branch). There is an indication that the kHz QPO frequency decreased with increasing count rate, which would be quite different from what is observed in other LMXBs showing kHz QPOs. Most kHz QPOs increase in frequency with increasing $\dot{M}$. Perhaps the small frequency decrease indicates that the inner accretion disk reached the innermost stable orbit, during our observations. When the inner disk reaches the innermost stable orbit it is expected (Kaaret, Ford, & Chen 1997; Miller, Lamb, & Psaltis 1998) that the increase in kHz QPO frequency with $\dot{M}$ levels off. The frequency of the kHz QPO could then change erratically (Kaaret et al. 1997), and a small frequency decrease could be observed.

On the basis of its luminosity and its burst properties (e.g., van Paradijs et al. 1979, 1988; Lewin et al. 1980), 4U 1735−44 is believed to have a higher $\dot{M}$ than the lower luminosity atoll sources (e.g., 4U 0614+09, 4U 1728+28), but a lower $\dot{M}$ than the more luminous sources (e.g., GX 9+9, GX 9+1). Thus, 4U 1735−44 is believed to have intermediate $\dot{M}$ for an atoll source. The detection of only a weak kHz QPO, only at low $\dot{M}$, supports this. So far, for the atoll sources with the highest $\dot{M}$ no kHz QPOs have been found, with upper limits of typically 1%–2% (GX 9+9, GX 9+1: Wijnands, van der Klis, & van Paradijs 1998; GX13+1: Homan et al. 1998a; GX3+1: Strohmayer et al. 1998). For the sources with lower $\dot{M}$, kHz QPOs are often detected with rms amplitudes of 6%–11% in the total PCA energy range (see, e.g., Strohmayer et al. 1996d; Zhang et al. 1996; Berger et al. 1996; Méndez et al. 1997). The weak kHz QPO in 4U 1735−44 detected only at the lowest count rates during our observations (i.e., when the source was on the lower part of the banana branch) fits naturally in this scheme. We expect that if $\dot{M}$ for 4U 1735−44 would drop below our lowest level, the kHz QPOs would become stronger and two peaks would be detected simultaneously.

KHz QPOs in atoll sources are usually found when the sources are at low inferred $\dot{M}$, i.e., when they are in the island state (Strohmayer et al. 1996d; Méndez et al. 1997; Yu et al. 1997) and on the lower part part of the banana branch (Chapter 9; Smale et al. 1997). At the lowest inferred $\dot{M}$ in the island state of 4U 0614+09, no kHz QPOs were detected. So far, no kHz QPOs have been detected when the sources are at higher inferred $\dot{M}$, i.e., when they are on the upper part of the banana branch, with stringent upper limits (Chapter 9; Smale et al. 1997). The kHz QPO in 4U 1735−44 is only detected when the source was at the lowest count rates during our observations (on the lower part of the banana branch) and undetectable at higher count rates (further up the banana branch, at higher inferred $\dot{M}$). It seems that the kHz QPOs in atoll sources are present at low $\dot{M}$, but possible not at the lowest $\dot{M}$ (Méndez et al. 1997), and

disappear when $\dot{M}$ increases.

Besides the kHz QPO, we detected a QPO at 67 Hz. Also, peaked noise with a complex form below 30 Hz is detected, obviously the well-known high frequency noise (HFN) in atoll sources (Hasinger & van der Klis 1989). The HFN was not detected when the source was on the upper part of the banana branch (at the highest count rates during our observations), and the 67 Hz QPO already disappeared when the source was in the middle part of the banana branch. Similar low-frequency QPOs were detected in several other atoll sources (e.g., Hasinger & van der Klis 1989; Strohmayer et al. 1996d; Chapter 8; Homan et al. 1998a). It is possible that the 67 Hz QPO detected in 4U 1735−44 is similar to the horizontal branch QPOs (HBOs) in Z sources. This is supported by the facts that the frequency of this QPO is similar to the frequencies of the HBOs in Z sources (although a fundamental frequency as high as 67 Hz has never been observed for a HBO in Z sources), and that it is accompanied by a (peaked) noise component similar to what is found in the Z sources (the so-called low-frequency noise [LFN]). Van der Klis (1994a) already suggested that the HFN in atoll sources is due to the same physical process as the LFN in Z sources.

Recently, Stella & Vietri (1998) proposed that the low frequency QPOs observed in atoll sources are due to a precession of the innermost disk region, dominated by the Lense-Thirring effect. If we assume that the 900 Hz QPO is real, then the frequency difference would be 249 Hz. Following their reasoning and assumptions, and assuming that the neutron star spin frequency is this frequency difference, we derive a maximum precession frequency of ∼28 Hz. The 67 Hz QPO we discovered in 4U 1735−44 can not easily be explained by this model without an I/M (with I is the moment of inertia of the neutron star and M the neutron star mass) which is more than 2 times larger than allowed for any mass and equation of state. However, the complex nature of the HFN, and especially the peak near 29 Hz, could be due to the precession of the inner disk.

Acknowledgments. This work was supported in part by the Netherlands Foundation for Research in Astronomy (ASTRON) grant 781-76-017 and by NSF grant AST 93-15133. B. V. (NAG 5-3340), F. K. L (NAG 5-2925), J. v. P. (NAG 5-3269, NAG 5-3271) and W. H. G. L. acknowledge support from the United States NASA grants. M. M. is a fellow of the Consejo Nacional de Investigaciones Científicas y Técnicas de la República Argentina.

Chapter 11

A millisecond pulsar in an X-ray binary system

Rudy Wijnands & Michiel van der Klis
Nature **394**, 344–346 (1998)

11.1 Introduction

Ordinary radio pulsars (Hewish et al. 1968) are neutron stars with magnetic fields of $\sim 10^{12}$ Gauss and spin periods in the range 0.1 to 3 seconds. In contrast, millisecond radio pulsars (Backer et al. 1982) have much weaker fields ($\sim 10^{9}$ Gauss), and faster, millisecond spin rates. For both types of pulsar, the energy driving the radio pulsations is thought to be derived from the rotation of the neutron star. The star gradually 'spins down' as energy is radiated away. Millisecond radio pulsars are often located in binary systems (Hulse & Taylor 1975). In a widely accepted theoretical model (Radhakrishnan & Srinivasan 1982; Alpar et al. 1982), they started as ordinary pulsars which lost most of their magnetic field and were 'spun up' to millisecond periods by the accretion of matter from a companion star in an X-ray binary system. Evidence for this model has gradually mounted (van der Klis et al. 1985a, 1996e; Strohmayer et al. 1996d; Alpar & Shaham 1985; Lamb et al. 1985; Miller, Lamb, & Psaltis 1998), but direct proof - in the form of the predicted coherent millisecond X-ray pulsations in the persistent flux of an X-ray binary has been lacking, despite many searches (Leahy et al. 1983; Mereghetti & Grindlay 1987; Wood et al. 1991; Vaughan et al. 1994). In this chapter, I report the discovery (Wijnands & van der Klis 1998) of such a pulsar, confirming theoretical expectations. The source will probable become a millisecond radio pulsar when the accretion turns off completely.

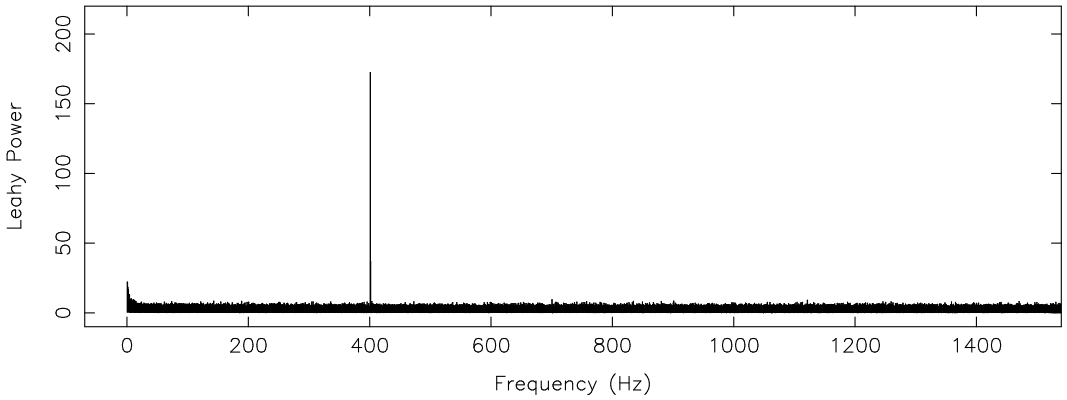

Figure 11.1: Leahy (Leahy et al. 1983) normalized power density spectrum of the 1998 April 11 20:38–21:21 UT persistent emission of XTE J1808–369. The 2–60 keV source count rate varied between 892 and 1007 counts s^{-1}, including a ∼130 counts s^{-1} background. No X-ray bursts were observed. The spectrum shows clear evidence for X-ray pulsations near a frequency of 401.0 Hz, with an amplitude of ∼4.1% (rms) of the source flux in the 2–60 keV range.

11.2 The discovery

The transient X-ray burst source SAX J1808.4–3658 was discovered (in 't Zand et al. 1998) in September 1996 with the Wide Field Cameras on board *BeppoSAX*. Two X-ray burst of type I, generally accepted to be due to a thermonuclear runaway on the surface of a neutron star, were observed, and the source was classified as a low-mass X-ray binary (LMXB), containing a low-magnetic-field neutron star accreting matter from a companion star of less than one solar mass. The probable distance of the source is 4 kpc (in 't Zand et al. 1998). Recently, a transient X-ray source designated XTE J1808–369 was detected (Marshall 1998) with the Proportional Counter Array (PCA) on board the *Rossi X-ray Timing Explorer* (*RXTE*). This source is positionally coincident to within a few arcminutes with SAX J1808.4–3658, and it is likely that both sources are the same object.

XTE J1808–359 was observed by the *RXTE* team at Goddard Space Flight Center with the PCA on 11 April 1998. The data were placed in the online public *RXTE* data archive, allowing rapid analysis of the data by the scientific community. We obtained the data and performed a series of fast Fourier transforms designed to be sensitive to various types of rapid variability, including strictly periodic pulsations (van der Klis 1989). We discovered (Wijnands & van der Klis 1998) clear evidence for X-ray pulsations with a frequency near 401.0 Hz in the resulting power density spectrum (Fig. 11.1). The frequency was stable to within 0.01%, far exceeding the stability of any previously known phenomenon in an accreting low-magnetic-field neutron star, and making it practically certain that we were detecting the neutron star spin rate. Triggered by this discovery,

a series of further observations was performed (Chakrabarty & Morgan 1998b). Here, I report on the initial, 2-h *RXTE* observing span.

During this observation the pulsation frequency drifted slightly due to the Doppler shifts caused by the orbital motion of the satellite around the Earth, and the pulsar around its companion star. Although the satellite ephemeris was not yet available at the time of our analysis and we could not therefore determine the pulsar's orbit, we were able to correct empirically for the frequency drift and to fold the pulsations coherently for several million cycles (Fig. 11.2). This leaves no other interpretation than the presence of a millisecond X-ray pulsar in the system (Wijnands & van der Klis 1998). The fact that this pulsar is detected in the (accretion-driven) outburst of a transient X-ray source shows that during our observations it is powered by accretion from a companion star, and not by its rotation.

In a subsequent analysis Chakrabarty and Morgan (1998a, 1998b) have found the orbital period of this pulsar ($\sim$2 h, close to the satellite orbital period) and measured its orbit. A detailed analysis of the pulsar's orbit is presented in this companion paper so we shall not repeat it here. This work confirms that the pulsar is a member of a low-mass X-ray binary system, and provides important additional information on the stability of the pulsation frequency, which will eventually allow determination of whether the pulsar is still spinning up, or has already reached an equilibrium spin rate.

11.3 The magnetic field strength

We can use the observed spin rate of the millisecond X-ray pulsar to constrain the magnetic field strength B of the neutron star, and thus test the prediction that it should be similar to that of millisecond radio pulsars, as would be required for this system to be the missing link between X-ray binaries and millisecond radio pulsars. For accretion to proceed, the centrifugal force on the accreting matter co-rotating in the magnetosphere must be less than the local gravitational force (Stella, White, & Rosner 1986). Using standard magnetospheric disk accretion theory (Ghosh & Lamb 1979) this leads to an upper limit on B of (2–6)$\times 10^8$ G, far below the $\sim 10^{12}$ G typical of slower accretion-powered pulsars. Centrifugal inhibition of the accretion occurs when the magnetospheric radius $r_M = 18\,\xi \mu_{26}^{4/7} m^{1/7} R_6^{-2/7} L_{37}^{-2/7}$ km is larger than the co-rotation radius $r_{co} = 15\,m^{1/3} P_{\rm 1ms}^{2/3}$ km, where μ_{26} is the magnetic moment in units of 10^{26} G cm^3, L_{37} the bolometric luminosity in units of 10^{37} erg s^{-1}, m the neutron star mass in solar masses, R_6 its radius in units of 10^6 cm, ξ a dimensionless factor that is probably between 0.5 and 1, and $P_{\rm 1ms}$ the spin period in ms. Given the 2.49 ms spin period and a bolometric luminosity of $\sim 6 \times 10^{36}$ erg s^{-1}, estimated from the information available on the X-ray spectrum (in 't Zand 1998; Marshall 1998; Heindl, Marsden, & Blanco 1998), this can be used to set an upper limit of 31

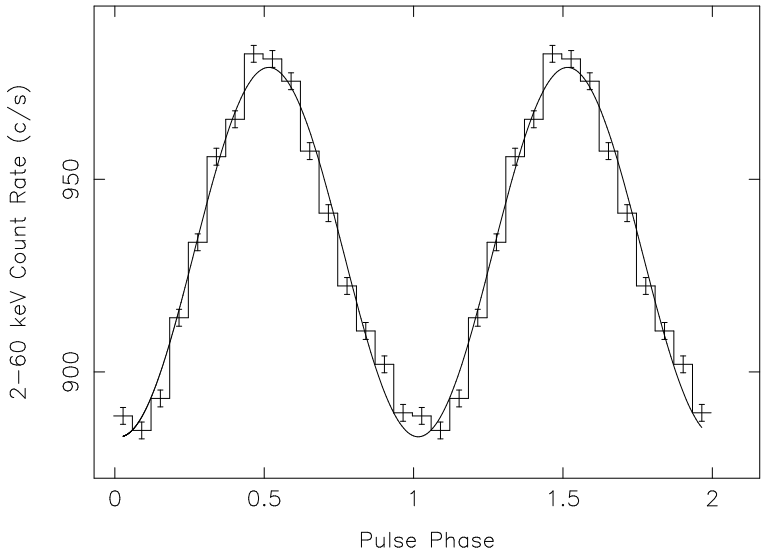

Figure 11.2: The 2–60 keV light curve folded at the 2.49 ms period. Two cycles are plotted for clarity. The solid line is the best-fitted sinusoid. To produce this plot, we divided the data into 128 second segments and determined the phase and the frequency of the pulsations in each segment by an epoch-folding technique. The results were consistent with a smooth, approximately sinusoidal ∼110-min variation of the frequency between 400.986 and 401.022 Hz. After correcting the phases for the effects of this drift, the pulsations could be folded coherently. The resulting grand-average folded pulse profile is near-sinusoidal, with no significant difference between different photon energy bands. Fitting the folded light curve with a harmonic series, we find that the amplitudes of the harmonics at 2 and 3 times the 401.0 Hz frequency are ∼11% and ∼4% of the 401.0 Hz amplitude, respectively. There is no evidence that the true spin frequency is 200.5 Hz: we find no significant difference in shape between the odd and even pulses when folding the data on twice the period and harmonics at 1, 3, and 5 times 200.5 Hz are not detected, with typical upper limits on the amplitude of ∼5% of the 401.0 Hz amplitude.

km on r_M and thus to constrain B. In calculating the upper limit on B given above, we have assumed a 1.4 $M_\odot$ neutron star with a radius of 10 km. As the bolometric luminosity drops, the limit on B comes down further.

Such a low magnetic field strength is indeed in the range of values inferred for millisecond radio pulsars (Bhattacharya & van den Heuvel 1991). The object seems to be located above the radio pulsar "death line" (below which the field is too weak for the radio pulsar mechanism to operate; Bhattacharya & van den Heuvel 1991), so when the accretion phase of the binary finally ends and the source turns off as an accretion-powered X-ray pulsar, it would probably switch on as a rotation-powered radio pulsar. This might even happen *between* X-ray outbursts (Campana et al. 1998), if the density of the accreting matter in the

pulsar environment, at least out to the light cylinder at 120 km, drops sufficiently. So, this LMXB could indeed be one of the progenitors of the millisecond radio pulsars, and it might be an intermittent radio pulsar now.

We do not know the circumstances under which the neutron star was spun up to its present rapid rate. Current data (in 't Zand et al. 1998; Marshall 1998) suggest a typical outburst mass accretion rate of 5×10^{-10} $M_\odot$ yr^{-1} and a duty cycle of $\sim$5% for the transient outbursts. At that rate, the total spin up time would be $\sim 2 \times 10^9$ yr.

11.4 Comparison with other LMXBs

Previous indications for high spin rates and low field strengths of the neutron stars in LMXBs have been numerous, but were all indirect. Evidence for high (several hundred Hz) spin rates came from the detection (van der Klis et al. 1985a, 1996e; Strohmayer et al. 1996d) of frequencies interpreted (Strohmayer et al. 1996d; Alpar & Shaham 1985; Lamb et al. 1985; Miller et al. 1998) as beat-frequencies between the star's spin frequency and the orbital frequency of clumps of matter orbiting the star. Further evidence for this was obtained from drifting frequencies observed (Strohmayer et al. 1996d) during thermonuclear X-ray bursts, which are probably caused by thermonuclear hot spots in the star's surface layers, spinning around at approximately the star's spin rate. Indications for low (10^8 to several 10^9 G) field strengths came from thermonuclear burst theory (Joss & Li 1980; Bildsten 1995; Bildsten & Brown 1997), which says that the occurrence of X-ray bursts requires the field to be weak, and from various other indirect methods (Alpar & Shaham 1985; Lamb et al. 1985; Psaltis, Lamb, & Miller 1995; White & Zhang 1997). The spin and field we deduce for XTE J1808–369 are in accordance with these previous estimates for other LMXBs. If XTE J1808–369 is the same source as SAX J1808.4–3658, then the source is the first pulsar to show both coherent pulsations in its persistent emission and thermonuclear bursts, in agreement with our conclusion that XTE J1808–369 is by far the lowest-field accretion-driven pulsar known.

As both the spin rate and the field strength of XTE J1808–369 resemble those inferred for other, non-pulsing LMXBs, the question arises: why is XTE J1808–369 the only known LMXB with a millisecond X-ray pulsar? The pulsations in XTE J1808–369 are strong enough to ensure that similar-amplitude pulsations would have been noticed in other systems as well. The most straightforward explanation would seem to be that the magnetic field of XTE J1808–369 is considerably stronger than that of other systems of similar (relatively low) X-ray luminosity. The more efficient magnetic channeling of the accreting matter in XTE J1808–369 would then lead to higher pulsation amplitudes, making the pulsar easier to detect. This would mean that the fields of the other low-luminosity LMXBs have been overestimated, which is possible in view of the large uncer-

tainties in those estimates. If this is true, then it remains to be seen whether these other systems can also be millisecond radio pulsar progenitors such as we deduce XTE J1808–369 to be. As XTE J1808–369 is a weak, transient X-ray source, it is possible that it is the first example of a class of millisecond radio pulsar progenitors that has not been noticed until now.

Acknowledgments. We thank L. Bildsten, J. van Paradijs, R. Fender, and R. Ramachandran for comments on versions of this manuscript, the aforementioned, J. Arons and F. Verbunt for discussions, and the *RXTE* team for promptly making the data available online. M. K. was supported by the Visiting Miller Professor Program of the Miller Institute for Basic Research in Science (UCB). This work was supported by the Netherlands Organization for Research in Astronomy ASTRON.

Chapter 12

The broad-band power spectrum of SAX J1808.4–3658

Rudy Wijnands & Michiel van der Klis
Astrophysical Journal **507**, L63–L66 (1998)

Abstract

We analyzed the rapid aperiodic X-ray variability of the recently discovered millisecond X-ray pulsar SAX J1808.4–3658. The power density spectrum is dominated by a strong band-limited noise component, which follows a power law with index 1.0–1.3 at high frequencies with a break that varies between 0.25 and 1.6 Hz, below which the spectrum is relatively flat. Superimposed on this, a broad bump is present with a centroid frequency that varies well correlated with the break frequency between 2.4 and 12.0 Hz. These characteristics are very similar to what is commonly seen in other low-luminosity low-mass X-ray binaries. Between 100 and 400 Hz, a third broad noise component is present similar to that recently reported in the low-luminosity low-mass X-ray binary 4U 1728–34 (Ford & van der Klis 1998). We find a similar high-frequency noise component also in other low-luminosity neutron star systems. We conclude that at any given epoch, the rapid aperiodic X-ray variability of the millisecond X-ray pulsar is indistinguishable from that of other low-luminosity neutron star systems. However, contrary to what has been found in those sources, the break frequency of the band-limited noise does not have a strict correlation with mass accretion rate. With decreasing mass accretion rate, the break frequency first decreased, then increased again. This previously unobserved behavior could be typical for the very low mass accretion rates we observe near the end of the outburst of SAX J1808.4–3658, or it could be related to it being a pulsar.

12.1 Introduction

Recently, using the *Rossi X-ray Timing Explorer* (*RXTE*), the first (and so far only) accretion-powered millisecond X-ray pulsar was discovered (Wijnands & van der Klis 1998; Chapter 11). This source is positionally coincident with the known transient X-ray burster and low-mass X-ray binary (LMXB) SAX J1808.4–3658 (in 't Zand et al. 1998; Marshall 1998), which makes it the first source which exhibits coherent X-ray pulsations and thermonuclear X-ray bursts. The pulsar is in an $\sim$2 hr binary with a companion star of less than 0.1 $M_\odot$ (Chakrabarty & Morgan 1998a, 1998b).

This discovery verified the 20 yr old prediction that the progenitors of the millisecond radio pulsars are LMXBs (see Bhattacharya & van den Heuvel 1991 for a review of millisecond radio pulsars), for which a lot of circumstantial evidence was already present (see Chapter 11 for references). The derived magnetic field of the millisecond X-ray pulsar is in the range of the fields of the millisecond radio pulsars (Chapter 11; Chakrabarty & Morgan 1998b; Gilfanov et al. 1998; Cui et al. 1998b), but it is lower than that estimated for some other LMXBs using indirect methods (see Chapter 11 for references). It is therefore not clear why other LMXBs, particularly those at similarly low accretion rates as SAX J1808.4–3658, are not also millisecond pulsars. Perhaps previous field estimates are wrong and the magnetic fields in the other LMXBs are lower than that in SAX J1808.4–3658, or perhaps in SAX J1808.4–3658 some special geometric condition, such as low inclination or large spin and magnetic axis misalignment, uniquely allows it to pulse.

In this chapter, we study the rapid aperiodic X-ray variability of this millisecond X-ray pulsar and compare it with that of other low-luminosity LMXBs. We conclude that apart from the pulsations the rapid variability of SAX J1808.4–3658 is very similar to that of other low-luminosity neutron star LMXBs; we do, however, identify one possible unusual aspect.

12.2 Observations and analysis

During the decay of its 1998 April outburst, SAX J1808.4–3658 was frequently observed with the *RXTE* proportional counter array (PCA) until May 6 (Fig. 12.3*a*; see also Gilfanov et al. 1998; Heindl & Smith 1998; Cui et al. 1998b). During these observations, data were collected with a time resolution of 122 μs in 64 channels, except on April 13 when a mode with 1 μs in 256 channels was used. We used these data to calculate 512 s fast Fourier transforms. After subtraction of the dead-time modified Poisson level, the resulting 0.004–4096 Hz power density spectra were averaged to form 21 different spectra, one for each observation (although some observations were combined in order to increase sensitivity). Each average spectrum contains between 1 and 23 ks of data. The spectra were fitted with

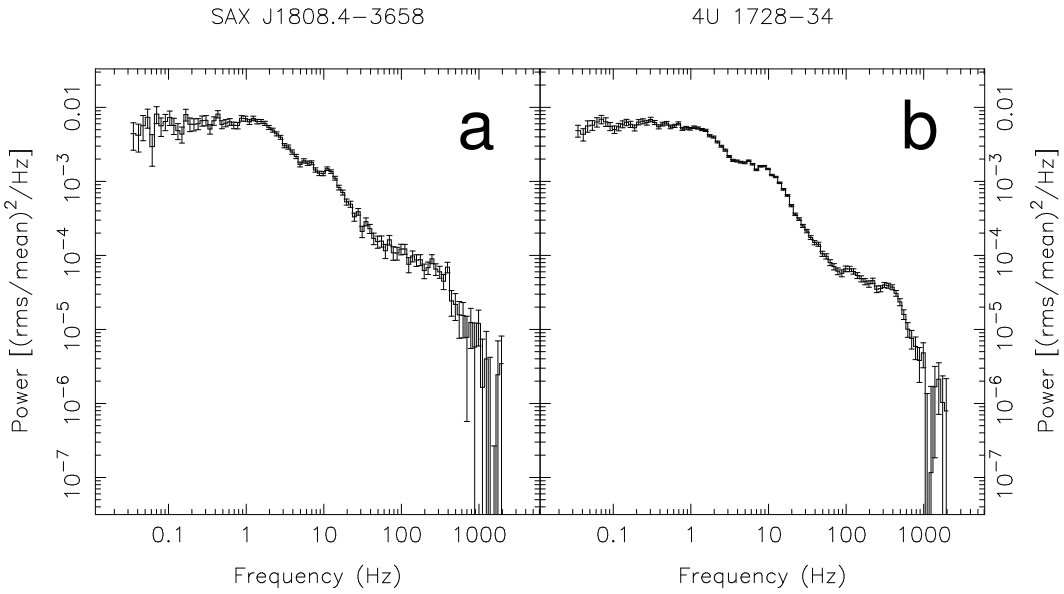

Figure 12.1: Typical power spectra of (*a*) SAX J1808.4–3658 and (*b*) 4U 1728–34. The dead-time modified Poisson level has been subtracted.

a fit function that is described in § 12.3. The errors on the fit parameters were calculated using $\Delta\chi^2 = 1.0$. The upper limits were calculated using $\Delta\chi^2 = 2.71$, corresponding to 95% confidence levels.

12.3 Results

A typical power density spectrum of SAX J1808.4–3658 is shown in Figure 12.1*a*. Besides the very significant periodic signal at 401 Hz (see Fig. 11.1) which is hardly visible in this broad-band representation, several noise components are visible. The overall shape is dominated by a strong broad band-limited noise component, which follows a rough power law at high frequencies with a break near 1 Hz, below which the spectrum is almost flat. On top of this noise component, at frequencies near 10 Hz a bump is present, which may have some substructure. At frequencies above 100 Hz, a third noise component is present which cuts off around 200–300 Hz. This spectral shape is very similar to that seen in other low-luminosity LMXBs; in Figure 12.1*b* we show for comparison a power spectrum of 4U 1728–34. We used archival *RXTE*/PCA data of 1996 March 1 of 4U 1728–34 to calculate this power spectrum (see also Ford & van der Klis 1998).

We fitted the power spectra with a fit function consisting of a broken power law (representing the band limited noise; $P \propto \nu^{-\alpha_{\rm below,above}}$, with $\alpha_{\rm below,above}$ are the power law index below and above the break frequency, respectively), a Lorentzian (representing the ∼10 Hz bump), and an exponentially cutoff power law (repre-

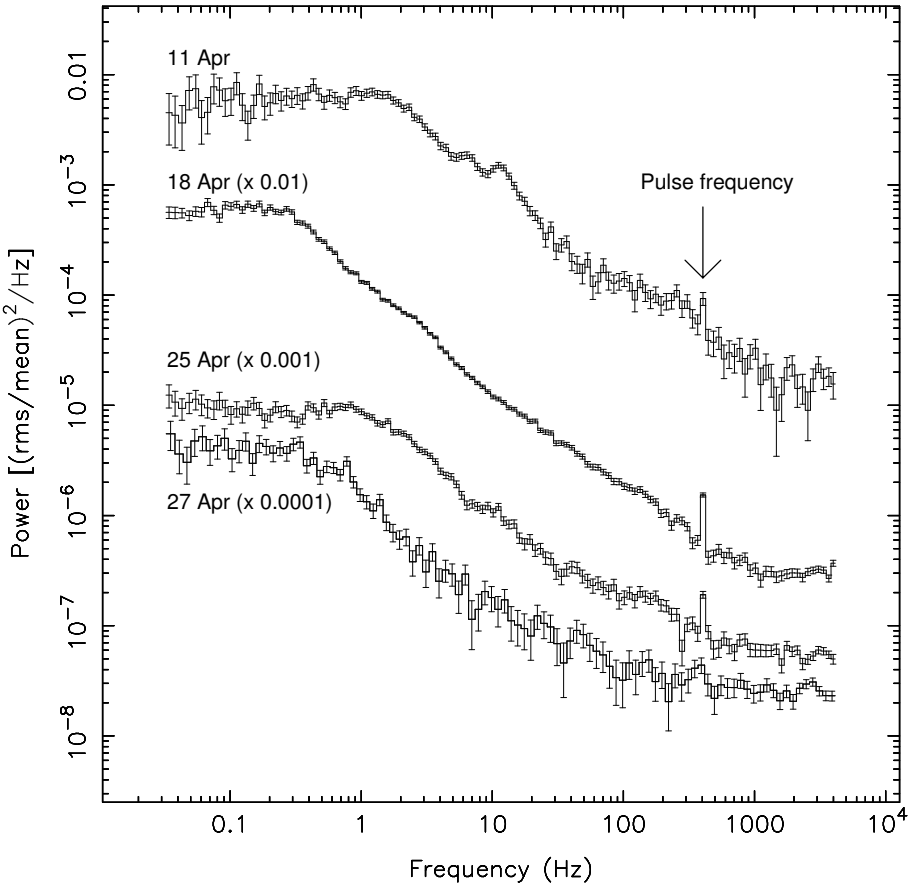

Figure 12.2: Power density spectra of SAX J1808.4–3658 on different dates during the 1998 outburst. The spectra appear flat at high frequencies, as for display purposes only 97.5% of the modified Poisson level was subtracted.

senting the noise component at higher frequency; $P \propto \nu^{-\beta} e^{-\nu/\nu_{\rm cutoff}}$). The higher frequency noise component could also be fitted with a broken power law or a broad Lorentzian; this did not affect its measured rms amplitude. Figure 12.2 illustrates the changes in the power spectrum of SAX J1808.4–3658 during the course of the outburst; changes in the break frequency are clearly seen.

The behavior of the fit parameters during the decay of the outburst are plotted together with the 3–25 keV X-ray flux in Figure 12.3 (see also Table 12.1). Both the break frequency and the frequency of the bump decreased (from 1.60 to 0.25 Hz and from 12 to 2.4 Hz, respectively) while the flux dropped (Fig. 12.3*c* [*squares and triangles*]). After a 5–7 day interval during which these frequencies remained at their minimum values, they increased again (to 1.2 and 5.7 Hz, respectively), while the flux went on decreasing. After April 26 the flux dropped within less than 3 days by a factor of 20 (see also Gilfanov et al. 1998; Heindl & Smith 1998; Cui et al. 1998b); at this time, the break frequency decreased again

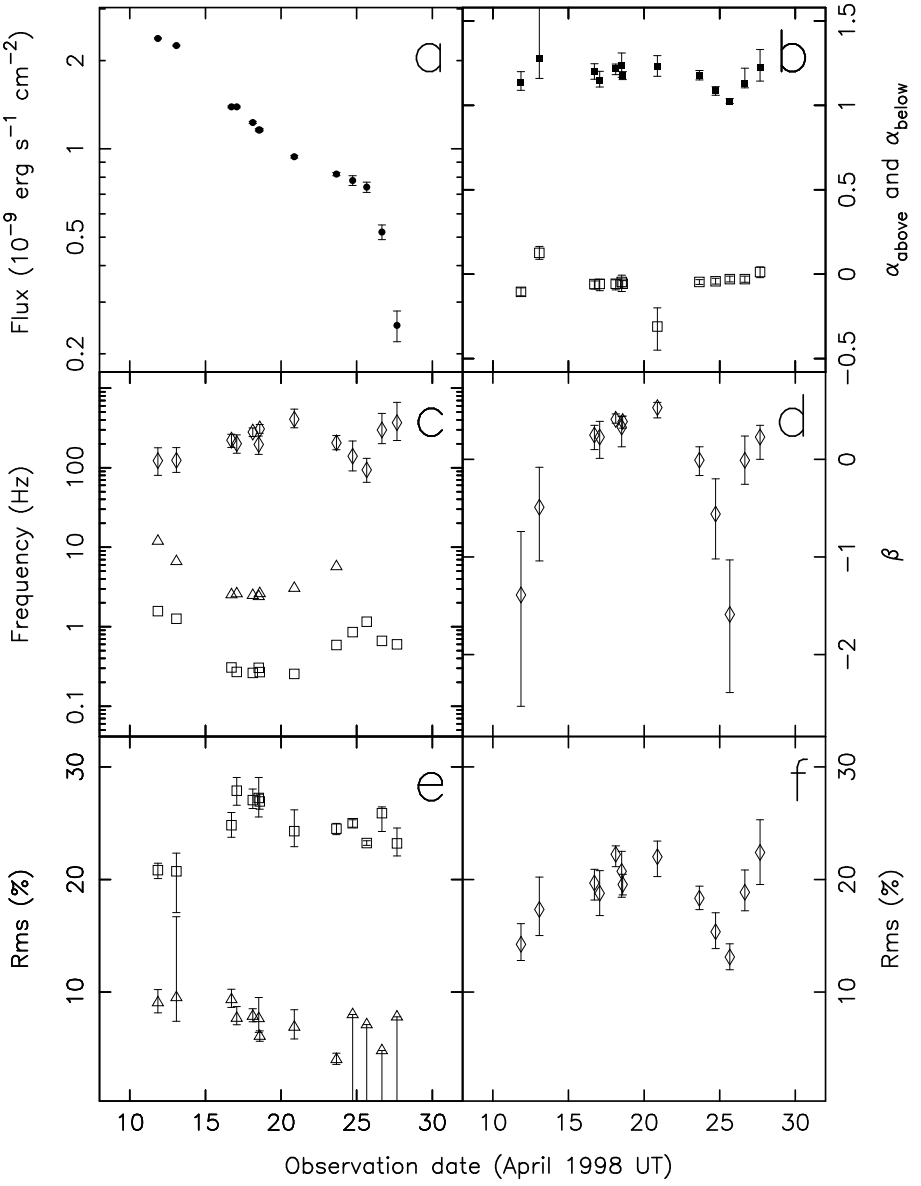

Figure 12.3: (*a*) The 3–25 keV flux (after Gilfanov et al. 1998); (*b*) the power law index of the band-limited noise above the break frequency (*open squares*; $\alpha_{\rm above}$) and the power law index of the band-limited noise below the break frequency (*filled squares*; $\alpha_{\rm below}$); (*c*) the break frequency of the band-limited noise (*open squares*), the frequency of the bump (*open triangles*), and the cutoff frequency of the high frequency noise component (*open diamonds*); (*d*) the power law index of the high frequency noise; (*e*) the rms amplitude (2–60 keV) of the band-limited noise (*open squares*), the rms amplitude (2–60 keV) of the bump (*open triangles*); (*f*) the rms amplitude (2–60 keV) of the high frequency noise component during the decay of the 1998 outburst. Error bars are indicated except where they are smaller than the data points.

to about 0.6 Hz. By this time, the bump had become undetectable.

The rms amplitude (Fig. 12.3*e* [*squares*]; integrated over 0.01–100 Hz; energy range 2–60 keV) of the band-limited noise is anticorrelated with its break frequency. The rms increased from 20% at the highest break frequencies to about 28% at the lowest break frequencies. The power-law index below the break frequency ($\alpha_{\rm below}$) increased slightly during the decay (from -0.1 to 0.0; Fig. 12.3*b*). The power law index above the break ($\alpha_{\rm above}$) varied between 1.0 and 1.3 (Fig. 12.3*b*), with no clear correlation with X-ray flux or the break frequency of the band-limited noise. After April 29 no broad band power was detectable any more. The 20%–30% rms amplitude upper limits during these late stages of the outburst are not very stringent and the presence of similar noise components as before cannot be excluded.

The rms amplitude of the ∼10 Hz bump gradually dropped from 10% to 4% during the outburst (2–60 keV; Fig. 12.3*e* [*triangles*]), without any correlation with its frequency. After April 23 it is no longer detectable with upper limits of 5%–8%. The ratio of the FWHM and the frequency of this bump varied slightly between 0.5 and 1.0.

The third noise component, between 100 and 400 Hz, has an rms amplitude (2–60 keV; integrated over 10–1000 Hz) between 13% and 23% (Fig. 12.3*f*). The index β of the cut-off power law (Fig. 12.3*d*) increases from ∼–1.4 (thus the noise component is peaked) on April 11 to ∼0.5 on April 20, then decreased again to ∼–1.6 on April 25. During the last two observations for which this noise component could be detected the index was ∼0. The cut-off frequency and the rms amplitude vary in good correlation to this, and all are anticorrelated with the break frequency of the band-limited noise component. These variations together result in keeping the effective cut-off of this higher frequency noise component approximately constant around 200 Hz.

We measured the rms amplitude as a function of the photon energy of the above noise components on three occasions during the decay. All components tend to increase slightly with photon energy. However, this is not usually very significant.

No kilohertz quasi-periodic oscillations (kHz QPOs) are detected. The (conservative) upper limits for a QPO with a FWHM of 150 Hz between 500 and 1500 Hz are between 7% and 8% at the highest observed luminosities (April 11 and 13, respectively), and 4% or worse (depending on the source flux and the amount of observing time) further along the decay of the outburst. We also searched for kHz QPOs using only the highest energy channels, but none were found.

12.4 Discussion

The rapid X-ray variability of SAX J1808.4–3658 is dominated by a broad band-limited noise component with a break frequency between 0.25 and 1.6 Hz. During

Table 12.1: The fit parameters[a]

Observation ID	Start Time (1998, UT)	End Time (1998, UT)	#[b]	Bump Rms (%)	Bump FWHM (Hz)	Bump Frequency (Hz)	Band-limited noise Break Frequency (Hz)	Band-limited noise Rms (%)	Band-limited noise α_{above}	Band-limited noise α_{below}	High frequency noise Rms (%)	High frequency noise β	High frequency noise Cut-off Frequency (Hz)	Flux[c] ($\times 10^{-9}$) (erg s^{-1} cm^{2})
30411-01-01-00	11/04 19:16	11/04 21:28	7	$9.1^{+1.2}_{-0.9}$	$7.6^{+1.7}_{-1.5}$	12.0±0.3	$1.57^{+0.07}_{-0.05}$	$20.8^{+0.6}_{-0.8}$	−0.11±0.02	$1.13^{+0.07}_{-0.05}$	$14.2^{+1.8}_{-1.4}$	$-1.4^{+0.7}_{-1.1}$	123^{+55}_{-43}	2.38±0.01
30411-01-02-00	13/04 01:37	13/04 02:22	2	$9.5^{+7.2}_{-2.1}$	$7.7^{+3.1}_{-2.5}$	$6.6^{+0.8}_{-1.4}$	1.3±0.1	$20.7^{+1.6}_{-3.7}$	+0.13±0.04	$1.3^{+0.4}_{-0.1}$	$17.3^{+2.9}_{-2.3}$	$-0.5^{+0.4}_{-0.6}$	124^{+55}_{-37}	2.25±0.01
30411-01-03-00	16/04 17:17	16/04 22:59	19	$9.3^{+0.9}_{-0.7}$	$3.0^{+0.4}_{-0.2}$	2.5±0.1	$0.31^{+0.09}_{-0.06}$	24.8±1.1	−0.06±0.03	1.20±0.05	$19.7^{+1.2}_{-1.5}$	+0.3±0.2	222±42	1.39±0.01
30411-01-04-00	17/04 01:39	17/04 04:38	9	$7.7^{+1.0}_{-0.6}$	2.3±0.5	2.6±0.1	$0.270^{+0.010}_{-0.008}$	27.9±1.3	−0.06±0.04	1.15±0.05	18.8±2.0	+0.2±0.2	201^{+58}_{-49}	1.39±0.01
30411-01-05-00	18/04 03:07	18/04 08:53	25	$7.9^{+0.7}_{-0.5}$	2.1±0.2	$2.48^{+0.08}_{-0.10}$	$0.263^{+0.013}_{-0.006}$	$27.1^{+1.0}_{-0.8}$	$-0.06^{+0.02}_{-0.04}$	1.22±0.03	$22.2^{+0.8}_{-1.1}$	$+0.41^{+0.06}_{-0.04}$	281±35	1.23±0.01
30411-01-06-01	18/04 12:32	18/04 13:18	5	$7.6^{+1.9}_{-1.2}$	$2.0^{+0.7}_{-0.5}$	2.4±0.3	0.30±0.02	27.3±1.8	$-0.05^{+0.04}_{-0.06}$	1.24±0.08	$20.7^{+1.8}_{-2.3}$	+0.3±0.2	197^{+54}_{-50}	1.16±0.01
30411-01-06-00	18/04 14:08	19/04 00:53	44	6.1±0.5	1.8±0.2	2.62±0.07	0.269±0.006	26.9±0.7	−0.06±0.03	1.18±0.03	19.6±0.9	+0.39±0.07	308^{+42}_{-36}	1.16±0.01
30411-01-07-00	20/04 21:02	20/04 23:07	8	$6.9^{+1.6}_{-1.1}$	$2.5^{+0.8}_{-0.6}$	3.1±0.3	0.26±0.02	$24.3^{+1.9}_{-1.4}$	−0.3±0.1	1.23±0.06	$22.0^{+1.4}_{-1.8}$	$+0.53^{+0.05}_{-0.11}$	407^{+138}_{-89}	0.94±0.01
30411-01-08-00	23/04 15:51	23/04 23:19	30	$4.0^{+0.6}_{-0.4}$	$1.9^{+0.7}_{-0.4}$	5.7±0.2	0.59±0.01	24.5±0.5	−0.05±0.02	1.18±0.03	18.3±1.1	−0.01±0.16	206^{+48}_{-38}	0.82±0.01
30411-01-09-02	24/04 17:32	24/04 23:19	25	<8.0			0.86±0.03	25.0±0.4	−0.04±0.02	1.09±0.03	15.4±1.7	−0.6±0.5	139^{+78}_{-48}	0.78±0.03
30411-01-09-03/04[d]	25/04 15:55	25/04 21:40	26	<7.1			1.16±0.03	23.2±0.2	−0.03±0.02	1.03±0.02	13.1±1.2	$-1.6^{+0.6}_{-0.8}$	94^{+37}_{-28}	0.74±0.03
30411-01-09-00	26/04 15:59	26/04 23:19	31	<4.8			0.66±0.02	$25.9^{+0.6}_{-1.6}$	−0.03±0.02	$1.13^{+0.09}_{-0.03}$	$18.9^{+2.0}_{-1.6}$	−0.01±0.25	299^{+182}_{-98}	0.52±0.03
30411-01-10-02/01/00[e]	27/04 14:31	29/04 18:28	26	<7.8			$0.60^{+0.07}_{-0.05}$	$23.2^{+1.4}_{-1.1}$	+0.01±0.03	$1.23^{+0.10}_{-0.08}$	22.4±2.9	+0.2±0.2	367^{+294}_{-149}	0.25±0.03

[a] Errors on the fit parameters were determined using $\Delta\chi^2 = 1$. Upper limits were determined using $\Delta\chi^2 = 2.71$ and a FWHM of 5 Hz

[b] Number of power spectra averaged

[c] The 3–25 keV fluxes were obtained from Gilfanov et al. 1998

[d] The power spectra obtained for the observations with ID 30411-01-09-03 and 30411-01-09-04 were averaged before fitted

[e] The power spectra obtained for the observations with ID 30411-01-10-02, 30411-01-10-01, and 30411-01-10-00 were averaged before fitted

the initial decay of the outburst, this frequency was correlated with the mass accretion rate, but at lower luminosities it was anticorrelated. On top of this noise component a broad bump is detected whose frequency is strongly correlated with the break frequency. The third component is a broad noise component between 100 and 400 Hz, whose properties also correlate to the break frequency. As all characteristic frequencies describing the broad-band noise appear to vary in correlation, it is possible that the three components together describe one complex physical phenomenon rather than three independent processes.

Similar band-limited noise components are found in other LMXBs with similar luminosities, such as 4U 1728–34 (Fig. 12.1*b*; Ford & van der Klis 1998). The high frequency noise component was not previously reported in other LMXBs than 4U 1728–34. We find by reexamination of the data of 4U 0614+09 published by Méndez et al. (1997) that it is also present in this source. Also, in the power spectra published by Ford, van der Klis, & Kaaret (1998a) of 4U 1705-44, a similar component can be seen. It seems that this component is a common feature in the power spectra of neutron star low-luminosity LMXBs at low mass accretion rates and not unique to the millisecond X-ray pulsar.

So, the rapid X-ray variability below a few hundred hertz between the millisecond X-ray pulsar and low-luminosity neutron star LMXBs is remarkably similar in terms of which components are present. There may be differences in how these components depend on mass accretion rate. From our detailed description of these dependencies in SAX J1808.4–3658, one possible difference is already apparent: the break frequency of SAX J1808.4–3658 does not have a strict correlation with the mass accretion rate, whereas in the other sources it has been observed that a strong positive correlation exists (see, e.g., Yoshida et al. 1993; Prins & van der Klis 1997; Méndez & van der Klis 1997; Méndez et al. 1997; Ford & van der Klis 1998). However, an analysis as detailed as we performed for SAX J1808.4–3658 has not yet been done for when those sources were at their lowest mass accretion rates. We cannot exclude that there, also the break frequency is anticorrelated with the mass accretion rates at certain (low) luminosities.

We detect no kHz QPOs in SAX J1808.4–3658, with upper limits well below detected amplitudes in other low-luminosity LMXBs (see, e.g., Méndez et al. 1997). However, in those sources below a critical luminosity no kHz QPOs are detected either (Méndez et al. 1997; Ford & van der Klis 1998). In one case, 4U 0614+09 (Méndez et al. 1997), this critical luminosity may be below the peak outburst luminosity we observe for SAX J1808.4–3658, however, due to uncertainties in the distance determinations no conclusive statements can be made. Also these critical luminosities appear to be higher in other sources (see, e.g., Ford et al. 1998a; Ford & van der Klis 1998; Smale, Zhang, & White 1997). However, it is remarkable that when no kHz QPOs were detected in 4U 0614+09, the break frequency of the band-limited noise was 0.7 Hz (Méndez et al. 1997), in the range of the break frequencies observed in SAX J1808.4–3658. However,

when kHz QPOs were detected in 4U 0614+09 the break frequency was above 6.6 Hz (Méndez et al. 1997), which is above our maximum observed break frequency. The same is true for 4U 1705-44 (Ford et al. 1998a). It seems that the break frequency can be used to predict whether kHz QPOs are observable or not. If true, we expect kHz QPOs to be observable in SAX J1808.4–3658 when the break frequency is slightly higher (above $\sim$7 Hz) and, thus, when the mass accretion increases to higher values than we observed during the 1998 outburst. Such higher mass accretion rates are possible in view of the higher ASM count rates observed during the 1996 outburst of SAX J1808.4–3658.

We conclude that, although there may be some differences in the details of how the power spectrum depends on the mass accretion rate, at this stage there is no evidence for any intrinsic difference in the rapid aperiodic X-ray variability between SAX J1808.4–3658 and other LMXBs. So if, for example the magnetic field would be considerably lower in the non-pulsating neutron star LMXBs compared to that of the millisecond X-ray pulsar or it would be oriented differently, then this difference in magnetic field does not affect the aperiodic timing behavior. The conclusion would have to be that the aperiodic X-ray variability is produced in the accretion disk and has little interaction with what happens inside the magnetosphere or even the magnetopause. If, on the other hand, it is a lower inclination that allows SAX J1808.4–3658 to pulse where other LMXBs do not, then the fact that this does not significantly alter the rapid aperiodic X-ray variability implies a roughly spherically symmetric emission pattern for these variations, whereas the pulsations would be strongly beamed along the polar axis. This once again suggests an origin for the rapid aperiodic variability away from the center, where the pulses originate, and most likely in the accretion disk outside the magnetosphere.

Acknowledgments. This work was supported in part by the Netherlands Foundation for Research in Astronomy (ASTRON) grant 781-76-017. R. W. and M. v. K. acknowledge stimulating conversations about the broad-band limited noise components in LMXBs with Eric Ford, Jeroen Homan, and Peter Jonker.

Chapter 13

The broad-band power spectra of X-ray binaries

Rudy Wijnands & Michiel van der Klis
Astrophysical Journal **514** (April 1, 1999)

Abstract

We analyzed the rapid aperiodic X-ray variability of different types of X-ray binaries (black hole candidates, atoll sources, the recently discovered millisecond X-ray pulsar, and Z sources) at their lowest inferred mass accretion rates. At these accretion rates, the power spectra of all sources are dominated by a strong band-limited noise component, which follows a power law with an index roughly 1 at high frequencies and breaks at a frequency between 0.02 and 32 Hz below which the spectrum is relatively flat. Superimposed on this, a broad bump (sometimes a quasi-periodic oscillation) is present with a 0.2–67 Hz centroid frequency that varies in good correlation with the frequency of the break. The black hole candidates and the low-luminosity neutron star systems (including the millisecond X-ray pulsar) have the same relation between the frequency of the bump and the frequency of the break. These similar characteristics strongly suggest that in all those different types of sources the band-limited noise and the bump are produced by the same physical mechanism. This mechanism cannot then depend on the presence or absence of either a small magnetosphere or a solid surface, so that it is most likely related to an instability in the flow in the accretion disk that modulates the accretion rate. The Z sources, which are more luminous than the other sources discussed here, follow a similar, but slightly shifted correlation between the break frequency and the frequency of the bump. The data suggest that the band-limited noise in Z sources is more complex than that in the other sources.

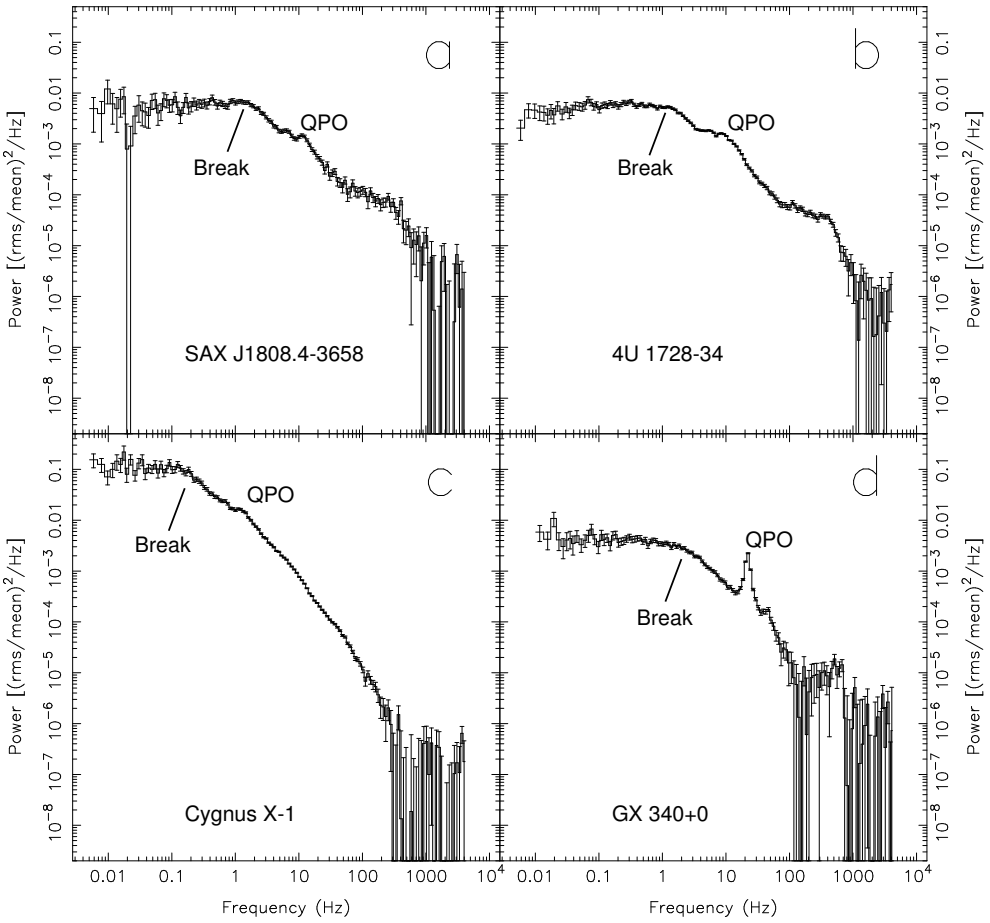

Figure 13.1: Typical power spectra of the millisecond X-ray pulsar (SAX J1808.4–3658; *a*), an atoll source (4U 1728–34; *b*), a BHC (Cyg X-1; *c*), and a Z source (GX 340+0; *d*). The dead-time modified Poisson level (Zhang 1995; Zhang et al. 1995) has been subtracted.

13.1 Introduction

At their lowest observed mass accretion rates ($\dot{M}$) the low-luminosity neutron star low-mass X-ray binaries (LMXBs; these are usually atoll sources; Hasinger & van der Klis 1989) and the black hole candidates (BHCs) are remarkably similar with respect to their X-ray spectra (e.g., Barret & Vedrenne 1994; see, however, Heindl & Smith 1998) and their rapid aperiodic X-ray variability (e.g., van der Klis et al. 1994a, 1994b; Berger & van der Klis 1998). So far, the only clear observable difference is the detection of quasi-periodic oscillations (QPOs) between 200 and 1200 Hz in the atoll sources (Strohmayer et al. 1996d; see van der Klis 1998 for a review) and not in the BHCs (e.g., Remillard et al. 1999). Apart from these high frequency phenomena, the power spectra are (almost) indistinguishable. At their

lowest observed $\dot{M}$ the power spectra of both the atoll sources and the BHCs are dominated by a strong band-limited noise component, which follows a power law with index of roughly 1 at high frequencies and breaks at a certain frequency ($\nu_{\rm b}$) below which the spectrum is relatively flat. Superimposed on this noise component, above $\nu_{\rm b}$, a broad bump is present. This broad bump is sometimes called a QPO although it usually does not satisfy the commonly used criterium (the ratio of the full width at half maximum and the centroid frequency is less than 0.5) to be called QPO. It was shown that the recently discovered (Wijnands & van der Klis 1998; Chapter 11) millisecond X-ray pulsar SAX J1808.4–3658 was indistinguishable with respect to the X-ray spectrum (Gilfanov et al. 1998; Heindl & Smith 1998) and the rapid aperiodic X-ray variability (Chapter 12) from the atoll sources. It has been suggested that the same physical mechanism is responsible for the rapid aperiodic timing behavior in these different types of sources (van der Klis 1994a, 1994b), and from the properties of the millisecond X-ray pulsar it was concluded that it most likely originated outside the magnetosphere (Chapter 12).

Due to the large flow of data generated by the *Rossi X-ray Timing Explorer* (*RXTE*) satellite, detailed quantitative comparisons between atoll and BHC power spectra are only now becoming possible. In this chapter, I present a detailed analysis of the low-frequency power spectra of atoll sources, BHCs, and the millisecond X-ray pulsar. We show that $\nu_{\rm b}$ is well correlated with the frequency of the bump for the three different source types, strongly indicating that indeed the same physical mechanism is responsible in these sources. We also show that the brightest neutron star LMXBs (the Z sources) at their lowest observed mass accretion rates have similar power spectra, however, they follow a somewhat different correlation.

13.2 Observations, analysis and results

We used data obtained with the proportional counter array (PCA) onboard *RXTE* to study the low-frequency power spectra of the different types of X-ray binaries. When a strong band-limited noise component was detected with superimposed on it a broad bump or a QPO (hereafter usually referred to as QPO), we fitted the 0.004–4096 Hz (or 0.004–2048 Hz when the time resolution was insufficient to go to 4096 Hz) power spectra. Before fitting the power spectra the dead-time modified Poisson level (Zhang 1995; Zhang et al. 1995) was subtracted. The fit function consisted of a broken power law ($P \propto \nu^{-\alpha_{\rm below,above}}$, where $\alpha_{\rm below}$ and $\alpha_{\rm above}$ are the power law index below and above $\nu_{\rm b}$, respectively) to represent the band-limited noise, and a Lorentzian with centroid frequency $\nu_{\rm qpo}$ representing the QPO. In the case of Cyg X-1 and GX 339–4 we used a twice broken power law instead of a once broken power law to fit the band-limited noise adequately. The second break occurred at frequencies between 4.6 and 7.3 Hz, well

above the frequency of the bump in those sources. Above this second break the spectrum steepened further with an index of typically 1.8. For some atoll sources we had to include an extra cut-off power law ($P \propto \nu^{-\beta} e^{-\nu/\nu_{\rm cut-off}}$), representing a noise component at frequencies above 100 Hz (see also Chapter 12; Ford & van der Klis 1998). Sometimes kHz QPOs were also present, which were fitted with Lorentzians. Errors on the frequencies were determined using $\Delta\chi^2 = 1$.

In many of the power spectra, one or both of the desired components were not present. Usually these power spectra were obtained when the sources were in different source states compared to those where the strong band-limited noise and the QPO were detected. In these states, QPOs are sometimes present, however, the band-limited noise usually is not. It turned out that the power spectra which were suitable for our purposes were usually, with a few exceptions (see § 13.2.1), those taken during the lowest observed inferred mass accretion rates, i.e., during the low states of the BHCs, during times when the atoll sources were in their island states, and when the Z sources were at the leftmost end of their horizontal branches. Typical power spectra of the source types are shown in Figure 13.1.

We also searched the literature for publications of similar power spectra as observed with *RXTE* or other X-ray (*EXOSAT*, *Ginga*) or γ-ray (*CGRO*/OSSE) satellites. When such power spectra were encountered we used the values for $\nu_{\rm b}$ and $\nu_{\rm qpo}$ as they are given in those publications. In Table 13.1 all sources which were found and their references are listed. Most sources we fitted ourselves with the fit function described above. All but two of the sources found in the literature were fitted using the same fit function we used; in GRO J0422+52 (Grove et al. 1998) and 1E 1724–3045 (Olive et al. 1998) the band-limited noise was fitted with a zero-centered Lorentzian and we estimated the break-frequency from the published power spectra. Several other sources (e.g., GRS 1737–31: Cui et al. 1997c) also showed the band-limited noise, however, no evidence for QPOs was found. The very complex sources Cir X-1 (neutron star system) and GRS 1915+105 (BHC) we left out of our analysis. Their complex nature, combined with the sometimes many QPOs, makes it difficult to correctly identify the QPOs and even the break frequency.

13.2.1 The sources

We have found eight BHCs (Table 13.1) which exhibited the band-limited noise *and* the QPO. We fitted *RXTE*/PCA data from the BHCs Cyg X-1, GX 339–4, XTE J1755–324, and GRO J1655–40 (see also Belloni et al. 1996, Cui et al. 1997a, 1997b, Revnivtsev et al. 1998, and Méndez et al. 1998b for more details about the data). From the literature we obtained the results of the BHCs XTE J1755−524 (Fox & Lewin 1998), 1E 1740.7−2942 (Smith et al. 1997b), GRS 1758−258 (Smith et al. 1997b), and GRO J0422+32 (Grove et al. 1998). Usually the BHCs were in the canonical black hole low state (GX 339−4; XTE J1755−324; GRO J0422+32; 1E 1740.7−2942; GRS 1758−258; Cyg X-1) but sometimes they

may have been in one or two other previously described states (intermediate or very high; XTE J1748−288; GRO J1655−40; Cyg X-1; see Méndez & van der Klis 1997 for a recent description of BHC source states). For two sources (1E 1740.7−2942 and GRS 1758−258) a second harmonic to the QPO was detected and in GRO J1655–40 both a genuine QPO and a broad bump are present, not harmonically related (see § 13.2.2).

We have found eight atoll sources (including the millisecond X-ray pulsar; Table 13.1) which exhibited both power spectral phenomena. Most of the data of these sources we fitted ourselves (see Méndez et al. 1997, Chapter 10, and Chapter 12 for more detailed description of the data), but we also used results published in the literature (4U 1728–34: Ford & van der Klis 1998; 4U 1608–52: Yoshida et al. 1993; 4U 1705–44: Berger & van der Klis 1998; Ford, van der Klis & Kaaret 1998a; 1E 1724–3045: Olive et al. 1998). All but one of the sources were in the island state; 4U 1735–44 was in the lower banana branch (Chapter 10).

Of the Z sources we fitted data of Cyg X-2 (Chapter 6), GX 17+2 (Chapter 5), GX 5–1 (Chapter 7), GX 340+0 (Jonker et al. 1998; see also Fig. 13.1*d*), and Sco X-1 (van der Klis et al. 1996e, 1997b) when they were at their lowest observed inferred mass accretion rate (thus at the leftmost end of their horizontal branches). The QPO in this case is the fundamental of the well-known horizontal branch oscillations or HBO. In these sources the second harmonic to the HBO could frequently also be detected. We excluded GX 349+2 from our analysis because so far this source has not exhibited HBO.

13.2.2 The QPO frequency versus the break frequency

In Figure 13.2*a*, $\nu_{\rm qpo}$ is plotted versus $\nu_{\rm b}$ obtained for the BHCs (black), the atoll sources (red), and the millisecond X-ray pulsar (blue). Although intrinsic scatter is present, $\nu_{\rm qpo}$ is well correlated with $\nu_{\rm b}$ for all three types of sources. The principal reason for the scatter could be the complex structure of the QPO. Considerable substructure, usually below the main peak, is often present (see, e.g., Fig. 13.1*a* and *b*). Moreover, in 1E 1740.7–2942 and GRS 1758–258 two QPOs are detected, harmonically related to each other (Smith et al. 1997b). It is possible that in the other sources also higher or sub harmonics are present, which are incorporated into the single Lorentzian used to fit the QPO, resulting in a QPO frequency which is slightly shifted with respect to the correct value. We did not plot the data of 1E 1740.7–2942 and GRS 1758–258 in Figure 13.2*a* (but they are plotted in Fig. 13.2*b*) because it is unclear which one of the two QPO harmonics in those sources is similar to the one fitted in the other sources. A clue to resolve this might be that the fundamentals are in both sources only marginally consistent with the above described relation between $\nu_{\rm b}$ and $\nu_{\rm qpo}$, while the second harmonics are completely consistent with it.

Another source for which the identification of the QPO is uncertain is GRO J1655–40 (also only shown in Fig. 13.2*b*). In this source above $\nu_{\rm b}$ both a genuine

Figure 13.2: The frequency of the QPO versus the break frequency of the band-limited noise. In *a* the black points are black hole candidates (Cyg X-1: *filled circles*; GX 339–4: *filled triangles*; XTE J1748–324: *filled star*; XTE J1755–324: *filled squares*; GRO J0422+32: *open triangle*), the red points are atoll sources, (4U 1728–34: *plusses*; 4U 0614+09: *filled squares*; 4U 1608–52: *open triangles*; 4U 1735–44: *filled triangles*; 4U 1812–12: *cross*; 4U 1705–44: *open diamonds*; 1E 1724–3045: *filled circle*), and the blue filled circles are the millisecond X-ray pulsar SAX J1808.4–3658. In *b* the black points are the BHCs, the atoll sources, and the millisecond pulsar, the red points are the Z sources (Cyg X-2: *open circles*; GX 17+2: *open squares*; GX 5−1: *open diamonds*; GX 340+0: *open triangles*; Sco X-1: *plusses)*, and the blue points are the sources (GRO J1655–40: *filled squares*; 1E 1740.7–2942: *filled circles*; GRS 1758−258: *filled triangles*) for which two QPOs (sometimes harmonically related) are present (both frequencies are plotted). The red filled circles at the upper right in *b* are Sco X-1, however, to determine $\nu_{\rm b}$ not the band-limited noise was used but the extra noise component at $\sim$30 Hz (see text). Error bars are smaller than the size of the data points.

QPO near 6.5 Hz and a broad bump near 9.5 Hz are present (see Fig. 2 of Méndez et al. 1998b). The frequencies of both phenomena are consistent with the relation between $\nu_{\rm b}$ and $\nu_{\rm qpo}$, although the frequency of the genuine QPO sometimes only marginally so. Such confusion might also be present in some of the other sources which do not clearly show both phenomena, although they could be present. This again could result in a $\nu_{\rm qpo}$ somewhat shifted with respect to the correct value.

Despite the intrinsic scatter, the relation between $\nu_{\rm b}$ and $\nu_{\rm qpo}$ is very remarkable, extending over three decades in frequency for both axes, incorporating three different source types (BHCs, atoll sources, and the millisecond X-ray pulsar). The ratio of $\nu_{\rm qpo}$ to $\nu_{\rm b}$ does not remain constant, but it decreases with increasing frequency.

We investigated whether the Z sources at their lowest observed mass accretion

rates also would fit this relation. The Z sources are plotted in Figure 13.2*b* (red). Although a correlation between $\nu_{\rm b}$ and $\nu_{\rm qpo}$ does exist here too, it is clear that the Z sources do not follow the same relationship as the other sources.

13.3 Discussion

We have presented results on the broad band power spectra of different types of X-ray binaries. In BHCs, atoll sources, the millisecond X-ray pulsar, and the Z sources similar power spectral shapes below approximately 100 Hz are observed when they are at their lowest observed mass accretion rates. Figure 13.2 shows that there is a good correlation between the break frequency of the band-limited noise component and the frequency of the QPO that is often observed above this break. The same correlation applies to the BHC, the atoll sources, and the millisecond X-ray pulsar, a slightly different one to the Z sources. Clearly, in Figure 13.2*b* the Z sources are shifted to the left or to above the data obtained for the other source types. Perhaps the QPOs observed in the Z sources are the second harmonic instead of the fundamental, which would shift the data points of the Z sources exactly on top of those of the atoll sources and the BHCs. However, this seems to be ruled out by the tight correlation, covering atoll and Z sources, between these QPOs and the kHz QPOs (Psaltis, Belloni, & van der Klis 1999b), indicating that the QPOs in Z sources are the same phenomenon as those observed in the atoll sources. This means that the $\nu_{\rm b}$ obtained for the Z sources is not the one obtained for the atoll sources, perhaps due to the fact that the strong band-limited noise components are of different origin in the two types of sources.

13.3.1 BHCs, atoll sources, and the millisecond X-ray pulsar

The good correlation between $\nu_{\rm b}$ and $\nu_{\rm qpo}$ in BHCs and atoll sources (including the millisecond X-ray pulsar) suggest that the band-limited noise and the QPO are caused by one and the same physical mechanism (see also Chapter 12). The similarities between these source types show that the presence or absence of a solid surface and a magnetosphere do not affect these rapid X-ray variability components. These components then most likely originate somewhere in the accretion disk at a distance of at least several tens of kilometers from the central compact object outside a possible magnetosphere, which has a radius of approximately 30 km for the millisecond X-ray pulsar (Chapter 11). However, the large amplitudes of the band-limited noise (up to 50% rms) exclude that the emission carrying these fluctuations originates this far out in the accretion disk, because most of the gravitational energy of the accretion disk is released closer to the compact object. The apparent lack of inclination effects excludes, from a statis-

Table 13.1: Sources with band-limited noise and QPO

Source	Type[a]	Break frequency[b] (Hz)	QPO frequency[b] (Hz)	Satellite	References[c]
Cyg X-1	BHC	0.026–2.9	0.29–10.0	*RXTE*	1, 2, 3, 4, 5
GX 339–4	BHC	0.040; 0.064	0.32; 0.37	*RXTE*	1, 2
XTE J1748–288	BHC	5.9	32	*RXTE*	6
XTE J1755–324	BHC	0.2–0.4	1.9–3.3	*RXTE*	2, 7
GRO J1655–40	BHC	0.20; 1.28	0.77 or 1.49; 6.48 or 9.48[d]	*RXTE*	2, 8
GRO J0422+32	BHC	0.03[e]	0.23	*CGRO*/OSSE	9
1E 1740.7–2942	BHC	0.43	2.0[f]	*RXTE*	10
GRS 1758–258	BHC	0.125	0.394[f]	*RXTE*	10
4U 1728–34	A	1.4–25.7	8.0–49.2	*RXTE*	11
4U 0614+09	A	0.69–13.9	6.3–35.1	*RXTE*	1, 12
4U 1608–52	A	0.2–1.0	1.0–6.7	*RXTE*; *Ginga*	1; 13
4U 1735–44	A	23.5; 31.9	61.7; 67.0	*RXTE*	1, 14
4U 1812–12	A	0.095	0.85	*RXTE*	1
4U 1705–44	A	0.35; 1.67	2.3; 11.3	*EXOSAT*; *RXTE*	15; 16
1E 1724–3045	A	0.1[e]	0.8	*RXTE*	17
SAX J1808.4–3658	P	0.26–1.6	2.4–12.0	*RXTE*	2, 18
Cyg X-2	Z	3.0–9.9	36.1–55.6[f]	*RXTE*	1, 19
GX17+2	Z	1.8–9.2	30.3–61.1[f]	*RXTE*	1, 20
GX5–1	Z	2.1–5.6	22.3–37.0[f]	*RXTE*	1, 21
GX 340+0	Z	2.1–4.3	19.2–34.9[f]	*RXTE*	1, 22
Sco X-1	Z	5.0–8.0	41.6–46.4[f]	*RXTE*	1, 23, 24

[a] BHC: black hole candidate; A: atoll source; Z: Z source; P: millisecond X-ray pulsar

[b] When two data points are present they are given separately; when more are present only the range of observed frequencies is given. The archival, proprietary, and public TOO *RXTE*/PCA results were obtained by fitting the data (see § 13.2); the other results were obtained from the literature. Typical relative errors on the QPO frequencies were 0.1%–1% for the Z sources and 1%–10% for the other sources; typical relative errors on the break frequencies were 2%–20% for the all sources, except for Sco X-1 they were typically ∼1%.

[c] 1: Archival/proprietary *RXTE*/PCA data; 2: Public TOO *RXTE*/PCA data; 3: Belloni et al. 1996; 4: Cui et al. 1997a; 5: Cui et al. 1997b; 6: Fox & Lewin 1998; 7: Revnivtsev, Gilfanov, & Churazov 1998; 8: Méndez et al. 1998b; 9: Grove et al. 1998; 10: Smith et al. 1997b; 11: Ford & van der Klis 1998; 12: Méndez et al. 1997; 13: Yoshida et al. 1993; 14: Chapter 10; 15: Berger & van der Klis 1998; 16: Ford, van der Klis, & Kaaret 1998a; 17: Olive et al. 1998; 18: Chapter 12; 19: Chapter 6; 20: Chapter 5; 21: Chapter 7; 22: Jonker et al. 1998; 23: van der Klis et al. 1996e; 24: van der Klis et al. 1997b

[d] A QPO and a broad bump present, see text

[e] ν_b estimated from the power spectrum published in the literature

[f] Presence of a second harmonic

tical point of view, line of sight obscuration as a mechanism. A modulation of the accretion rate due to instabilities in the flow in the region of the disk outside several 10 km from the compact object then remains as the most likely mechanism for generating the band-limited noise and the QPO. Another conclusion is that the HBOs observed in the Z sources, if they are indeed due to the same physical mechanism as the QPOs seen in the atoll sources (see above), cannot be explained by magnetospheric beat frequency models (Alphar & Shaham 1985; Lamb et al. 1985).

The question arise which fundamental properties of the sources determine the exact values of $\nu_{\rm b}$ and $\nu_{\rm qpo}$. The effect of the magnetic field of the compact object is probably small in the region of the disk where the frequencies are determined. The other physical parameters which can affect the accretion disk are the mass and spin of the central object, and the mass accretion rate. For a given source the mass and spin do not change and most likely only the mass accretion rate determines $\nu_{\rm b}$ and $\nu_{\rm qpo}$ (both are thought to be positively correlated with $\dot{M}$; see, e.g., van der Klis 1994b). Usually the relation between the frequencies and the inferred mass accretion rate is an one-to-one relation, however, it was shown that this is not the case for the millisecond X-ray pulsar (Chapter 12). The reason for this is as yet unknown, but it could be related to the transient nature of this source (see also Chapter 12). The difference between the sources with similar mass accretion rates would be the mass or the spin rate, or both, of the compact object. This could explain why on average the BHCs have smaller frequencies than the neutron star systems. However, considerable overlap between these source types occur, indicating that the mass accretion rate differences dominate the frequencies.

13.3.2 The Z source Sco X-1 in more detail

When examining the power spectra of Sco X-1, an extra noise component is present in the frequency region between the band-limited noise and the fundamental of the QPO (van der Klis et al. 1997b; see also Fig. 13.3). A similar noise component just below the QPO can also be observed in GX 17+2 (Homan et al. 1999b). Perhaps this extra noise component is similar to the band-limited noise observed in the other types of sources. The dominant band-limited noise in the Z sources is then something different, and could be related to, e.g., the 6–7 Hz QPO seen in Z sources at higher mass accretion rates (see also van der Klis et al. 1997b).

In order to test the hypothesis that this extra noise component in Sco X-1 is similar to the band-limited noise in the other source types, we fitted the band-limited noise in Sco X-1 with a Lorentzian with a centroid frequency near zero Hertz and the extra noise component with a broken power law. The resulting data points ($\nu_{\rm b}$ between 25.5 Hz and 31.9 Hz; $\nu_{\rm qpo}$ between 41.6 and 46.4 Hz) are shown in Figure 13.2*b* as the red filled circles. The points are shifted to higher

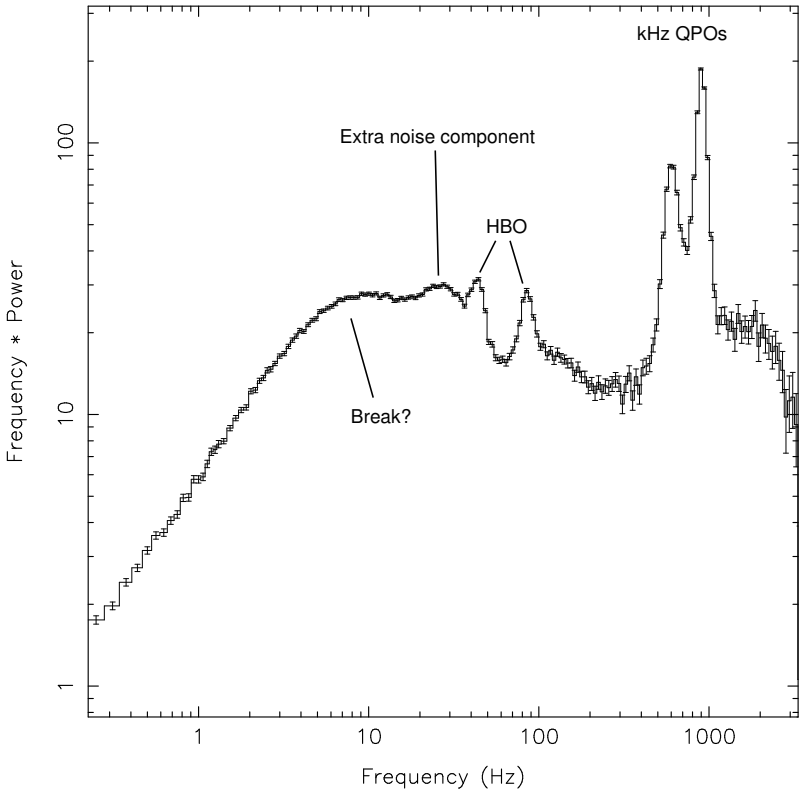

Figure 13.3: Typical Leahy-normalized power spectrum of the Z source Sco X-1 (see also van der Klis et al. 1997b), indicating the extra noise component at ∼30 Hz. On the y-axis not the Leahy power but the frequency times the Leahy power (in units of [(counts s^{-1})(rms/mean)^2)]) has been used in order for the features to be more clearly visible in the power spectrum (see also Belloni et al. 1997). Clearly visible are both the lower frequency and the higher frequency kHz QPO and the fundamental and second harmonic of the HBO; the extra noise component is the bump below the HBO fundamental. The continuum at high frequencies is affected by instrumental effects.

ν_b and, taking into account the systematic effects introduced by using a different fit function, are consistent with the same relation as the other sources. At this point, the relation of the band-limited noise and the extra noise component in the Z sources to the band-limited noise in the other sources is not entirely clear.

Acknowledgments. This work was supported in part by the Netherlands Foundation for Research in Astronomy (ASTRON) grant 781-76-017. We thank many people, including several guests, at the Astronomical Institute "Anton Pannekoek" of the University of Amsterdam for their discussions about the low-frequency power spectra of X-ray binaries. Particularly, we wish to thank Eric Ford for providing the data on 4U 1728–34 and 4U 1705–44. We thank the anonymous referee for his helpful comments.

Chapter 14

Millisecond phenomena in X-ray binary systems: Overview and perspectives

14.1 Introduction

The RXTE satellite fulfilled its promise and produced (and still is producing) a wealth of new data on X-ray binaries. The impact of the new data on our understanding of such systems, and of the LMXBs in particular, is enormous. Important discoveries such as those of the first accretion-driven millisecond X-ray pulsar and of the kHz QPOs improved our knowledge of LMXB systems. In this chapter, I will summarize the main discoveries made by *RXTE* and how they affect our understanding of neutron star LMXBs.

14.2 The accretion-driven millisecond X-ray pulsar

An important discovery made by *RXTE* was the discovery of the first accretion-driven millisecond X-ray pulsar, SAX J1808.4–3658 (Chapter 11). So far, it is the only known source of its kind, and its existence confirms the predicted evolutionary link between the millisecond radio pulsars and the LMXBs (§ 1.2.2). Studies of its X-ray spectrum (Gilfanov et al. 1998; Heindl & Smith 1998) and of its aperiodic rapid X-ray variability (Chapter 12) show an object that, apart from the pulsations, is remarkably similar to other LMXBs with similar luminosities. It is thus very puzzling that persistent pulsations have only been detected from SAX J1808.4–3658 and not from the other LMXB. SAX J1808.4–3658 must either have a different (higher) magnetic field than the other LMXBs, or some special geometry (e.g., binary or spin inclination, magnetic field inclination) must be responsible.

14.2.1 The orbital parameters

Already by using the data of the 1998 outburst the spin frequency of the neutron star and the orbital parameters could be measured with great accuracy. Stringent

upper limits were placed (Chakrabarty & Morgan 1998b) on the orbital eccentricity ($e < 5 \times 10^{-5}$) and the pulse frequency derivative ($\dot{\nu} < 7 \times 10^{-12}$). Using the upper limit on $\dot{\nu}$, Psaltis & Chakrabarty (1998) argued that standard accretion torque theory (e.g., Ghosh & Lamb 1979; assumptions include a dipole stellar magnetic field and a gas-pressure dominated inner accretion disk) does not hold for SAX J1808.4–3658, and that the effects of multipole magnetic moments of the neutron star, of radiation drag forces, and of general relativity should be taken into account.

In the course of two and a half years, two outbursts were observed from SAX J1808.4–3658. Therefore, it is possible that at least one more outburst could be observed during the remaining life of *RXTE*. If SAX J1808.4–3658 has another outburst, it would be possible to search for the change in the spin frequency, which occurred in between the outbursts and to, hopefully, detect $\dot{\nu}$ during the outburst. Detection of these values will help to constrain the models for the interactions between the inner accretion disk and the magnetosphere of the neutron star. Pulse timing measurements during the next outburst would also provide an independent, precise measure of the binary period at a second epoch, and the opportunity to study the evolution of the binary orbit. In a close binary system such as SAX J1808.4–3658, the orbit is strongly affected by gravitational radiation and by mass loss due to ablation of the companion. The relevant characteristic magnitude of $\dot{P}_{\rm orb} \sim 10^{-11}$ (Chakrabarty & Morgan 1998b) could be easily detected if the outburst epochs are at least a year apart.

In the X-ray light curve of SAX J1808.4–3658 a 2% orbital modulation was reported (Chakrabarty & Morgan 1998b). However, this modulation has to be confirmed during the next outburst of the source, because the strength of the modulation is comparable to the *RXTE* background variations, and the spacecraft orbital period (∼96 min) is close to that of the binary (∼121 min). If the small-amplitude flux modulation is confirmed, then a face-on binary is ruled out. Both the highly sinusoidal pulse shape (Chapter 11) and the small companion mass function (Chakrabarty & Morgan 1998b) suggest that we are viewing the binary face-on, a geometric configuration with low a priori probability. Since this improbable perspective might avoid blockage of our line of sight by the accretion disk, this would provide a natural explanation for why similar pulsations are not seen in any other LMXBs. If the 2% modulation is real, this explanation does not hold.

14.2.2 Interior structure of the neutron star

With pulse timing measurements the interaction of the particles in the ultra-dense matter of the neutron star could in principle be investigated. Due to the short pulse period it might be possible to look for short term fluctuations in the pulse phase caused by accretion torque fluctuations and the neutron star response to them with unprecedented precision (Deeter et al. 1989). This would allow detailed investigations of the neutron star interior and, hopefully, the equation of state of ultra-dense matter. Although a difficult analysis, it most likely can already be done with the data obtained during the 1998 outburst.

14.2.3 An millisecond radio pulsar?

The magnetic field strength of SAX J1808.4–3658 as determined from the X-ray pulsations is in the range of that inferred for the millisecond radio pulsars. Therefore, it is likely that the system will switch on as a rotation-powered radio pulsar when the accretion has stopped completely, and maybe even between outbursts (Chapter 11). So far, no reports have been made about the detection of this system in radio, let alone as a millisecond radio pulsar. If the system is detected as a millisecond radio pulsar, then not only during X-ray outburst, but also during quiescence the evolution of the neutron star spin frequency and of the orbital period can be followed. Also, from the period derivative of the radio pulsations the magnetic field strength of the neutron star can be determined independently from estimates from the X-rays, which can be used to cross-check conventional field estimate methods in radio and X-ray astronomy, and to constrain models for the radio pulsar mechanism as well as the interaction of the inner accretion flow with the magnetosphere (§ 14.2.1). Thus, detection of the system as a millisecond radio pulsar would provide new insights for both radio and X-ray astronomy.

14.3 Millisecond aperiodic phenomena

Before the discovery of the first millisecond X-ray pulsar (Chapter 11) the two most important discoveries made by *RXTE* with respect to LMXBs were the discovery of two simultaneous kHz QPOs in many of them with frequencies between 200 and 1200 Hz (e.g., Strohmayer et al. 1996d; van der Klis et al. 1996e; see also Chapters 5–10), and the discovery of nearly coherent oscillations in six LMXBs during thermonuclear X-ray bursts (e.g., Strohmayer et al. 1996d). All sources which show these phenomena are listed in Table 14.1 (updated up to December 21 1998).

14.3.1 The nearly coherent burst oscillations

So far, nearly coherent oscillations during Type I X-ray bursts were observed in six neutron star LMXBs (Table 14.1). These oscillations are called "nearly" coherent because their frequency typically drifts by a few Hz during the burst. On several occasions, the oscillations were coherent for as long as (several seconds) they could be detected (Smith, Morgan & Bradt 1997a; Strohmayer et al. 1996d, 1997a, 1997b, 1998a), with a Q, defined as the ratio between the frequency of the oscillations and the full width at half maximum of the peak, of as high as 900 (KS 1731–260; Smith et al. 1997a). In several sources (4U 1728–34, MXB 1743–29, 4U 1636–53, and Aql X-1) the oscillation frequencies sometimes increased by a few Hz during the tail of the bursts (e.g., Strohmayer et al. 1996d), appearing to reach an asymptotic maximum before they become undetectable.

The high Q values of the burst oscillations support the interpretation that they are closely related to the neutron star spin frequency, which would be in the range expected if the neutron star LMXBs are the progenitors of the millisecond radio pulsars (see Chapter 1.2.2). Most likely we see, during the bursts, a hot spot (or maybe

Table 14.1: Observations of kilohertz quasi-periodic oscillations

Source	Type[a]	Peak separation (Hz)	Burst QPO (Hz)	References
Sco X-1	Z	307–237	No bursts	van der Klis et al. 1996a, 1996b, 1996e, 1997b
GX 5–1	Z	298	No bursts	van der Klis et al. 1996d; Chapter 7
GX 17+2	ZB	294	No QPO	van der Klis et al. 1997a; Chapter 5
Cyg X-2	ZB	346	No QPO	Chapter 6; Smale 1998
GX 340+0	Z	325	No bursts	Jonker et al. 1998
GX 349+2	Z	266	No bursts	Zhang et al. 1998b
4U 0614+091	AB	323	No bursts	Ford et al. 1996, 1997a, 1997b; van der Klis et al. 1996c; Méndez et al. 1997; Kaaret et al. 1998
4U 1608–52	ABT	326–225	No QPO	van Paradijs et al. 1996; Berger et al. 1996; Yu et al. 1997; Méndez et al. 1998a, 1998c, 1999; Kaaret et al. 1998
4U 1636–53	AB	251	290; 581	Zhang et al. 1996, 1997; van der Klis et al. 1996c; Chapter 9; Strohmayer et al. 1998a, 1998b; Méndez et al. 1998d; Miller 1999
4U 1702–43	A	333	330	Markwardt, Strohmayer, & Swank 1999
4U 1705–44	AB	298	No QPO	Ford, van der Klis, & Kaaret 1998a
4U 1728–44	AB	355	363	Strohmayer et al. 1996a, 1996b, 1996d, 1997a, 1998b; Ford & van der Klis 1998
KS 1731–260	AB	260	524	Morgan & Smith 1996; Smith et al. 1997a; Chapter 8
4U 1735–44	AB	296	No QPO	Wijnands et al.1996b; Chapter 10; Ford et al. 1998b
MXB 1743–29	B	No kHz QPO	589	Strohmayer et al. 1996c, 1997b
4U 1820–30	ABG	275	No QPO	Smale et al. 1996, 1997; Zhang et al. 1998c
Aql X-1	ABT	Only one kHz QPO	549	Zhang et al. 1998a; Cui et al. 1998a; Yu et al. 1999
4U 1915–05	BD	355	No bursts	Barret et al. 1997, 1999
XTE J2123–058	AT	268	No QPO	Homan et al. 1998b, 1999a

[a] A: atoll source; Z: Z source; B: burster; G: globular cluster source; T: transient; D: dipper

multiple spots) on the neutron star surface, which are due to inhomogeneous nuclear burning of the accreted matter, spinning around with the neutron star spin. The frequency drifts observed in some sources could be caused by the bursting layer slightly expanding, and then recontracting thereby changing its rotation to conserve angular momentum, and thus modulating the QPO frequency (e.g., Strohmayer et al. 1997a, 1998a). In such an interpretation the frequency reached at the asymptotic limit during the burst decay represents the actual spin period of the neutron star. The stability of the oscillation frequency over a time span of more than 1.5 year (within 0.2 μs for 4U 1728–34; Strohmayer et al. 1998b) also strongly supports the neutron star spin frequency hypothesis. If many bursts could be collected and they are well sampled over the orbital cycles, it could be possible to determine the mass function for a number of systems by using the Doppler shifts due to the orbital velocities (Strohmayer et al. 1998b). Also, by assuming that the burst oscillations are the neutron star spin frequencies they can be used in these systems for highly sensitive searches for the millisecond X-ray pulsations in the persistent emission, which should be present at

some level in those LMXBs if they are the progenitors of the millisecond radio pulsars (§ 1.2.2). A direct test of the hypothesis that the burst oscillations are the neutron star spin frequency would be to observe such oscillations during type I X-ray bursts in the millisecond X-ray pulsar SAX J1808.4–3658 (§ 14.2). Type I X-ray bursts were observed with BeppoSAX during the September 1996 outburst (in 't Zand et al. 1998). Thus, it is highly likely that bursts will be observed again during the next outbursts if enough data are obtained.

The burst oscillations are not detected in all bursts of a source exhibiting this phenomenon and in numerous other LMXBs exhibiting type I X-ray burst no oscillations were detected with upper limits to the rms amplitude significantly lower than reported for those discovered (e.g., 4U 1608–52: Yu et al. 1997; Méndez et al. 1998a; Cygnus X-2: Smale 1998; Chapter 6; 4U 1705–44: Ford, van der Klis, & Kaaret 1998a; 4U 1735−44: Ford et al. 1998b). However, it is still possible that oscillations will be observed in future bursts of those sources. It is unclear what physical mechanism determines whether the oscillations are detected or not. The viewing geometry of the system and the exact place of the hot spot(s) on the surface of the neutron star could be important factors.

14.3.2 The kilohertz quasi-periodic oscillations

Two simultaneous kHz QPOs have been discovered in all six Z sources and 11 atoll sources or probable atoll sources (hereafter also included with the atoll sources). In only one LMXB, the atoll source Aql X-1, so far only one kHz QPO has been observed. The frequencies of the kHz QPOs range from 500 to 1200 Hz for the higher frequency kHz QPO and 200 to 950 for the lower frequency kHz QPO. Inferred from the monotonic relation between the frequencies of the kHz QPO and the count rate or $S_{\rm a}$ (§ 2.6) in atoll sources, and between these frequencies and $S_{\rm z}$ (§ 2.6) in the Z sources, it is clear that the frequencies increase when the mass accretion rate increases.

14.3.2.1 A beat frequency model?

In several of the systems for which the kHz QPOs were detected also the burst oscillations (§ 14.3.1) were observed. In 4U 1702–43 and 4U 1728–44 the frequency difference of these two QPOs are very close to the burst oscillation frequency. However, in 4U 1636–53 and KS 1731–260 the frequency difference is approximately half the burst oscillation frequency. The observations of three commensurable frequencies in these systems suggested a beat frequency model for the kHz QPOs. In such models the higher frequency kHz QPO is the Keplerian frequency of clumps orbiting the neutron star in the inner disk at some preferred radius, and the lower frequency kHz QPO the beat between this frequency and the neutron star spin frequency. Strohmayer et al. (1996d) proposed that the preferred radius is the radius of the magnetosphere of the neutron star, while Miller, Lamb, & Psaltis (1998) proposed that this radius is the sonic radius, which is the radius where the radial inflow velocity becomes supersonic. If such beat frequency models are correct the neutron star spin frequency can be obtained from the frequency separation between the kHz QPOs, which indeed are in the range expected if the neutron star LMXBs are the progenitors of the millisecond radio pulsars (§ 1.2.2). However, in certain sources the burst oscillations would then be twice

the neutron star spin frequency. Although the very high amplitudes of the oscillations seemed to argue against this being true (Strohmayer et al. 1998a; see however Lamb & Miller 1998), it was recently shown that in 4U 1636–53 a significant signal at half the burst oscillation frequency could be detected when combining five bursts of this source (Miller 1999), supporting the beat frequency interpretation.

Recently, the beat frequency interpretation of the kHz QPOs has had to deal with more serious contradictions, indicating that such models are incorrect or much more complicated than thought previously. Very soon after the discovery of the first kHz QPOs it already became apparent that for the bright LMXB Sco X-1 a simple beat frequency interpretation could not hold (van der Klis et al. 1997b). In this source the peak separation decreased by several tens of Hertz when the kHz QPOs increased in frequency on time scales of hours to days, which is to fast to be caused by changes in the spin frequency of the star. Two explanations for this decrease in peak separation with inferred mass accretion rate were put forward, both of which requiring a high, near-Eddington mass accretion rate as known to exist in Sco X-1. White & Zhang (1997) proposed that at high mass accretion rates the photosphere of the neutron star might expand by more than 30%. Due to conservation of its angular momentum the photosphere would slow down as the mass accretion rate increases. Another explanation that was discussed is that at near-Eddington accretion the height of the inner disk increases, and the change in the peak separation reflects the different values of the orbital frequencies at different heights in the disk (F. K. Lamb 1997, private communication).

However, Méndez et al. (1998a, 1998c) showed that also in the much less luminous (< 10 % of the Eddington luminosity) atoll source 4U 1608–52 the peak separation decreased when the frequencies of the kHz QPOs increased. Moreover, this decrease is consistent with the one observed in Sco X-1 in the sense that the same frequency difference is present in both sources when the kHz QPO frequencies are the same. Psaltis et al. (1998) further showed that, within the errors, similar behavior cannot be excluded in eight additional LMXBs, covering a wide range of luminosities. The explanations for the decrease of the peak separation in Sco X-1 mentioned above cannot be used to explain the observed decrease of the peak separation in 4U 1608–52 as the luminosity is too low for them to work.

The observable fact that formed the original motivation for the beat frequency interpretation was that the frequencies of the burst oscillations were equal to, or equal to twice, the kHz peak separation. However, recently is was shown that this does not hold for the atoll source 4U 1636–53 (Méndez, van der Klis, & van Paradijs 1998d). This paper reported a deviation of more than 10σ between the peak separation and half the frequency of the burst oscillations. This means that there are no unambiguous observational facts left which favor beat frequency models above other models to explain the kHz QPOs in this source. However, it is unclear why in at least KS 1731–260 and 4U 1728–44 (see Table 14.1) the peak separation is very close (within the errors) to the burst oscillations frequency (or half it). This still points in the direction of a beat frequency model. From the point of view of their many similarities it is unlikely that the kHz QPOs in 4U 1636–53 are produced by a different mechanism than that producing the kHz QPOs in the other two sources.

At the moment one of the most promising ways to test the beat frequency model

for the kHz QPOs would be by observing kHz QPOs in SAX J1808.4–3658 during its next outburst. In this system the spin frequency is known and thus it could be directly compared to the frequency difference of the kHz QPO. So far, no kHz QPOs have been observed in SAX J1808.4–3658. However, the upper limits obtained during the peak of the outburst were not stringent and the presence of these QPOs could not be excluded (Chapter 12). During the decay no kHz QPOs were detected either, with slightly better upper limits (due to the longer observing times). However, in other low luminosity LMXBs the kHz QPOs are often observed only when the source exceeds a certain critical luminosity (see, e.g., Méndez et al. 1997), while below that luminosity the kHz QPO drop considerably in amplitude and become undetectable. The exact critical luminosity is most likely different between different sources; in 4U 0614+09 (Méndez et al. 1997) it is lower than the maximum observed luminosity for SAX J1808.4–3658 during the 1998 outburst, but in other sources (e.g., 4U 1705–44: Ford et al. 1998a; 4U 1728−54: Ford & van der Klis 1998) it is higher. Moreover, comparing the rapid aperiodic timing behavior of different neutron star LMXBs suggests that kHz QPOs are only observable in LMXBs when the broad band-limited noise has certain characteristics (see Chapter 11) which are only observable above an certain inferred mass accretion rate. In Chapter 11 it was shown that these noise characteristics indicate that the accretion rates needed to observe kHz QPOs were not reached in SAX J1808.4–3658 during the April 1998 outburst.

Therefore, it is quite possible that kHz QPOs will be detected in SAX J1808.4–3658 when the luminosity (and thus the mass accretion rate) is higher than the maximum luminosity observed during the 1998 outburst. Higher mass accretion rates are possible in view of the higher ASM count rates observed during the 1996 outburst of SAX J1808.4−3658. It would be very surprising (in view of the fact that the other aperiodic variability is exactly the same as in other LMXBs; Chapter 12) if kHz QPOs are never observed. Failure to observe kHz QPOs could mean that the magnetic field strength or special geometry that allows SAX J1808.4–3658 to pulse, suppresses the QPOs.

14.3.2.2 Relations between the kHz QPO and other timing phenomena

Recently, several relations between different components in the power spectra have been discovered, which might provide clues to the exact production mechanism of the kHz QPOs and the QPOs below 100 Hz. By combining data obtained of the enigmatic neutron star LMXB Cir X-1 (see Shirey 1998 for the data) and of several Z and atoll sources, Psaltis, Belloni, & van der Klis (1999b) showed that several power spectral features are well correlated with each other in a range of sources extending over Cir X-1, the Z sources, and the atoll sources. The frequency of the lower frequency kHz QPOs in both the Z and the atoll sources are well correlated with the frequency of QPOs observed below 100 Hz (the horizontal branch QPOs in the Z sources). Also QPOs below 10 Hz observed in Cir X-1 follow this correlation if a broad peaked noise component between 20–100 Hz is interpreted as the equivalent of the lower frequency kHz QPO. This suggests that the broad noise component in Cir X-1 is related to the kHz QPOs in the other systems. There are even indications that the same relation

is also valid for certain QPOs and broad noise components in black hole candidates. However, this conclusion should be further investigated by using more data on black hole candidates.

This very good correlation suggests that the lower frequency kHz QPO is in fact the most important one of the two kHz QPO instead of the higher frequency kHz QPO. This is consistent with the observable facts that in some sources the coherence of the lower frequency kHz QPOs is higher than that of the higher frequency kHz QPOs (Méndez et al. 1998a; Jonker et al. 1998), which is difficult to explain if the lower frequency kHz QPO is the beat of the higher frequency kHz QPO with the spin frequency. The good correlation between the different types of QPOs also indicates that some of the QPOs below 100 Hz in the atoll sources are of similar origin as the HBOs observed in the Z sources. When taking into account the good correlation found between these QPOs and a broad noise component (i.e., the band-limited noise) in three different source types (black hole candidates, atoll sources, and the millisecond X-ray pulsar; see Chapter 13) then it is likely that the HBOs in the Z sources are due to the same mechanism as the QPOs observed in black holes (Chapter 13). If true, then this rules out the possibility that the HBOs in the Z sources are due to the magnetospheric beat frequency model (Alpar & Shaham 1985; Lamb et al. 1985) usually used to explain these HBOs (see also Chapter 13). These similarities between the neutron star systems (atoll sources, Z sources, and the millisecond X-ray pulsar) and the black hole candidates indicate that the lower frequency power spectrum components are produced in the disk, outside the magnetosphere (Chapter 13). The good correlation of the lower frequency components with the kHz QPOs (Ford & van der Klis 1998; Psaltis et al. 1999b) could mean that the kHz QPOs are also produced in the disk and are not affected by the presence of a possible magnetosphere or a solid surface in the neutron star systems, which would be consistent with the tentative identification of certain broad noise components in black hole candidates with the kHz QPOs (Psaltis et al. 1999b).

References

Alpar, M. A., Cheng, A. F., Ruderman, M. A., & Shaham, J. 1982, Nature, 300, 728

Alpar, M. A. & Shaham, J. 1985, Nature, 316, 239

Alpar, M. A., Hasinger, G., Shaham, J., & Yancopoulos, S. 1992, A&A, 257, 627

Backer, D. C., Kulkarni, S. R., Heiles, C., Davis, M. M., & Goss, W. M. 1982, Nature, 300, 615

Barret, D. & Vedrenne, G. 1994, ApJS, 92, 505

Barret, D., Olive, J. F., Boirin, L., Grindlay, J. E., Bloser, P. F., Chou, Y., Swank, J. H., & Smale, A. P. 1997, IAU Circ., 6793

Barret, D., Boirin, L., Olive, J. F., Grindlay, J. E., Bloser, P. F., Swank, J., & Smale, A. P. 1999, Astrophysical Letters and Communications, in press

Belian, R. D., Conner, J. P., & Evans, W. D. 1976, ApJ, 206, L135

Belloni, T., Méndez, M., van der Klis, M., Hasinger, G., Lewin, W. H. G., & van Paradijs, J. 1996, ApJ, 472, L107

Belloni, T., van der Klis, M., Lewin, W. H. G., van Paradijs, J., Dotani, T., Mitsuda, K., & Miyamoto, S. 1997, A&A, 322, 857

Berger, M. & van der Klis, M. 1998, A&A, 340, 143

Berger, M., van der Klis, M., van Paradijs, J., Lewin, W. H. G., Lamb, F. K., Vaughan, B., Kuulkers, E., Augusteijn, T., Zhang, W., Marshall, F. E., Swank, J. H., Lapidus, I., Lochner, J. C., & Strohmayer, T. E. 1996, ApJ, 469, L13

Bhattacharya, D. 1995, In *X-ray Binaries*, W. H. G. Lewin, J. van Paradijs, & E. P. J. van den Heuvel (eds.), (Cambridge University Press), p. 233

Bhattacharya, D. & van den Heuvel, E. P. J. 1991, Physics Reports, 203, 1

Bildsten, L. 1995, ApJ, 438, 852

Bildsten, L. & Brown, E. F. 1997, ApJ, 477, 897

Brainerd, J. & Lamb, F. K. 1987, ApJ, 317, L33

Bowyer S., Byram E. T., Chubb T. A., & Friedman H., 1965, Science 147, 394

Bradt, H. V., Rothschild, R. E., & Swank, J. H. 1993, A&AS, 97, 355

Burington R. S. & May D. C., 1970, Handbook of probability and statistics, with tables, second edition, Mc Graw-Hill New York-London, p. 177

Campana, S., Stella, L., Mereghetti, S., Colpi, M., Tavani, M., Ricci, D., Dal Fiume, D., & Belloni, T. 1998, ApJ, 499, L65

Chakrabarty, D. & Morgan, E. H. 1998a, IAU Circ., 6877

Chakrabarty, D. & Morgan, E. H. 1998b, Nature, 394, 346

Christian, D. J. & Swank, J. H. 1997, ApJS, 109, 177

Crampton D. & Cowley A. P. 1980, PASP, 92, 147

Cui, W., Heindl, W. A., Rothschild, R. E., Zhang, S. N., Jahoda, K., & Focke, W. 1997a, ApJ, 474, L57

Cui, W., Zhang, S. N., Focke, W., & Swank, J. H. 1997b, ApJ, 484, 383

Cui, W., Heindl, W. A., Swank, J. H., Smith, D. M., Morgan, E. H., Remillard, R., & Marshall, F. E. 1997c, ApJ, 487, L73

Cui, W., Barret, D., Zhang, S. N., Chen, W., Boirin, L., & Swank., J. 1998a, ApJ, 502, L49

Cui, W., Morgan, E. H., & Titarchuk, L. G. 1998b, ApJ, 504, L27

Daubechies, I. 1988, Communications on Pure and Applied Mathematics, 41, 909

Deeter, J. E., Boynton, P. E., Lamb, F. K., & Zylstra, G. 1989, ApJ, 336, 376

Dieters S. & van der Klis M., 1999, A&A, submitted

Ford, E. C. & van der Klis, M. 1998, ApJ, 506, L39

Ford, E., Kaaret, P., Tavani, M., Harmon, B. A., Zhang, S. N., Barret, D., Bloser, P., & Grindlay, J. 1996, IAU Circ., 6426

Ford, E., Kaaret, P., Tavani, M., Barret, D., Bloser, P., Grindlay, J., Harmon, B. A., Paciesas, W. S., & Zhang, S. N. 1997a, ApJ, 475, L123

Ford, E. C., Kaaret, P., Chen, K., Tavani, M., Barret, D., Bloser, P., Grindlay, J., Harmon, B. A., Paciesas, W. S., & Zhang, S. N. 1997b, ApJ, 486, L47

Ford, E. C., van der Klis, M., & Kaaret, P. 1998a, ApJ, 498, L41

Ford, E. C., van der Klis, M., van Paradijs, J., Méndez, M., Wijnands, R., & Kaaret, P. 1998b, ApJ, 508, L155

Fortner, B., Lamb, F. K., & Miller, G. S. 1989, Nature, 342, 775

Fox, D. & Lewin, W. 1998, IAU Circ., 6964

Gilfanov, M., Revnivtsev, M., Sunyaev, R., & Churazov, E. 1998, A&A, 338, L83

Ghosh, P. & Lamb, F.K. 1979, ApJ, 234, 296

Ghosh, P. & Lamb, F. K. 1992, In : *X-ray Binaries and Recycled Pulsars*, E. P. J. van den Heuvel & S. Rappaport (eds.), (Kluwer, Dordrecht), NATO ASI Series C, 377, p. 487

Giacconi, R. et al. 1962, Phys. Rev. Lett., 9, 439

Giacconi, R., Gursky, H., Kellogg, E., Schreier, E., & Tananbaum, H. 1971, ApJ, 167, L67

Grindlay, J., Gursky, H., Schnopper, H., Parsignault, D. R., Heise, J., Brinkman, A. C., & Schrijver, J. 1976, ApJ, 205, L127

Grove, J. E., Strickman, M. S., Matz, S. M., Hua, X.-M., Kazanas, D., & Titarchuk, L. 1998, ApJ, 502, L45

Gruber, D. E., Blanco, P. R., Heindl, W. A., Pelling, M. R., Rothschild, R. E., & Hink, P. L. 1996, A&AS, 120, 641

Hasinger G. 1987, In: *The Origin and Evolution of Neutron stars*, D. J. Helfand & Z. Huang (eds.), IAU 125, p. 333

Hasinger G. 1988, In: *Physics of Neutron Stars and Black Holes*, Y. Tanaka (ed.), p. 97

Hasinger, G. & van der Klis, M. 1989, A&A, 225, 79

Hasinger G., Langmeier A., Sztajno M., Pietsch W., & Gottwald M. 1985, IAU Circ., 4153

Hasinger G., Langmeier A., Pietsch W., & Sztajno M. 1985b, Space Sci. Rev., 40, 233

Hasinger, G., Priedhorsky, W. C., & Middleditch, J. 1989, ApJ, 337, 843

Hasinger, G., van der Klis, M., Ebisawa, K., Dotani, T., & Mitsuda, K. 1990, A&A, 235, 131

Hayashida, K., Inoue, H., Koyama, K., Awaki, H., & Takano, S. 1989, PASJ, 41, 373

Heindl, W. A. & Smith, D. M. 1998, ApJ, 506, L35

Heindl, W., Marsden, D. & Blanco, P. 1998, IAU Circ., 6878

Hertz P., Vaughan B., Wood K. S., Norris, J. P., Mitsuda, K., Michelson, P. F., & Dotani, T. 1992, ApJ, 396, 201

Hewish, A., Bell, S.J., Pilkington, J.D.H., Scott, P.F., & Collins, R.A. 1968, Nature, 217, 709

Hoffman J. A., Marshall H. L., & Lewin W. H. G. 1978, Nature, 271, 630

Homan, J., van der Klis, M., Wijnands, R., Vaughan, B., & Kuulkers, E. 1998a, ApJ, 499, L41

Homan, J., van der Klis, M., van Paradijs, J., & Méndez, M. 1998b, IAU Circ., 6971

Homan, J., Méndez, M., Wijnands, R., van der Klis, M., & van Paradijs, J. 1999a, ApJLetters, in press

Homan, J. et al. 1999b, A&A, in preparation

Hulse, R. A. & Taylor, J. H. 1975, ApJ, 195, L51

Jonker, P. G., Wijnands, R., van der Klis, M., Psaltis, D., Kuulkers, E., & Lamb, F. K. 1998, ApJ, 499, L191

Joss, P. C. & Li, F. K. 1980, ApJ, 238, 287

Kaaret, P., Ford, E. C., & Chen, K. 1997, ApJ, 480, L27

Kaaret, P., Yu, W., Ford, E. C., & Zhang, S. N. 1998, ApJ, 497, L93

Kahn S. M., & Grindlay J. E. 1984, ApJ, 281, 826

Klein, R. I., Jernigan, J. G., Arons, J., Morgan, E. H., & Zhang, W. 1996, ApJ, 469, L119

Kuulkers, E. & van der Klis, M. 1995a, A&A, 303, 801

Kuulkers, E., van der Klis, M. 1995b, In: *Seventeenth Texas Symposium on Relativistic Astrophysics and Cosmology*, H. Böhringer, G. E. Morfill, & J. E. Trümper (eds.), Ann. New York Ac. Sci. 759, p. 344

Kuulkers, E. & van der Klis, M. 1996, A&A, 314, 567

Kuulkers, E., van der Klis, M., Oosterbroek, T., Asai, K., Dotani, T., van Paradijs, J., & Lewin, W. H. G. 1994a, A&A, 289, 795

Kuulkers, E., van der Klis, M., Oosterbroek, T., van Paradijs, J., & Lewin, W. H. G. 1994b, In: *The Evolution of X-ray Binaries*, S. S. Holt & C. S. Day (eds.), American Institute of Physics, p. 539

Kuulkers, E., van der Klis, M., & van Paradijs, J. 1995, ApJ, 450, 748

Kuulkers, E., van der Klis, M., & Vaughan, B. A. 1996, A&A, 311, 197

Kuulkers, E., van der Klis, M., Oosterbroek, T., van Paradijs, J., & Lewin, W. H. G. 1997, MNRAS, 287, 495

Lamb, F. K. 1989, In: *Proc. 23rd ESLAB Symp. on X-ray Astronomy*, J. Hunt & B. Battrick (ESA SP-296) (eds.), p. 215

Lamb, F. K. 1991, In : *Neutron Stars: Theory and Observations*, J. Ventura & D. Pines (eds.), Kluwer, Dordrecht, NATO ASI Series C, 344, p. 445

Lamb, F. K., Shibazaki, N., Alpar, M. A., & Shaham, J. 1985, Nature, 317, 681

Langmeier, A., Hasinger, G., & Trümper, J. 1990, A&A, 228, 89

Leahy, D. A., Darbo, W., Elsner, R. F., Weisskopf, M. C., Kahn, S., Sutherland, P. G., & Grindlay, J. E. 1983, ApJ, 266, 160

Levine, A. M., Bradt, H., Cui, W., Jernigan, J. G., Morgan, E. H., Remillard, R., Shirey, R. E., & Smith, D. A. 1996, ApJ, 469, L33

Lewin, W. H. G., Li, F. K., Hoffman, J. A., Doty, J., Buff, J., Clark, G. W., & Rappaport, S. 1976, MNRAS, 177, L93

Lewin, W. H. G., Cominsky, L., Holzner, S., & van Paradijs, J. 1980, MNRAS, 193, L15

Lewin, W. H. G., van Paradijs, J., Jansen, F., van der Klis, M., Sztajno, M., & Trümper, J. E. 1985, IAU Circ., 4101

Lewin, W. H. G., Lubin, L. M., Tan, J., van der Klis, M., van Paradijs, J., Penninx, W., Dotani, T., & Mitsuda, K. 1992, MNRAS, 256, 545

Lewin, W. H. G., van Paradijs, J., & Taam, R. E. 1993, Space Sci. Rev., 62, 223

Lewin, W. H. G., van Paradijs, J., & Taam, R. E. 1995, In: *X-ray Binaries*, W. H. G. Lewin, J. van Paradijs, & E. P. J. van den Heuvel (eds.), (Cambridge University Press), p. 175

Lomb, N. R. 1976, Ap&SS, 39, 447

Makino, F. & the ASTRO-C team 1987, Ap. Lett. Comm. 25, 223

Markwardt, C. B., Strohmayer, T. E., & Swank, J. H. 1999, ApJLetters, in press

Marshall, F. E. 1998, IAU Circ., 6876

Marshall, F. E., Gotthelf, E. V., Zhang, W., Middleditch, J., & Wang, Q. D. 1998, ApJ, 499, L179

Méndez, M. & van der Klis, M. 1997, ApJ, 479, 926

Méndez, M., van der Klis, M., van Paradijs, J., Lewin, W. H. G., Lamb, F. K., Vaughan, B. A., Kuulkers, E., Psaltis, D. 1997, ApJ, 485, L37

Méndez, M.,van der Klis, M., van Paradijs, J., Lewin, W. H. G., Vaughan, B. A., Kuulkers, E., Zhang, W., Lamb, F. K., & Psaltis, D. 1998a, ApJ, 494, L65

Méndez, M., Belloni, T., & van der Klis, M. 1998b, ApJ, 499, L187

Méndez, M., van der Klis, M., Wijnands, R., Ford, E. C., van Paradijs, J., & Vaughan, B. A. 1998c, ApJ, 505, L23

Méndez, M., van der Klis, M., & van Paradijs, J. 1998d, ApJ, 506, L117

Méndez, M., van der Klis, M., Ford, E. C., Wijnands, R., & van Paradijs, J. 1999, ApJLetters Issue 511 (January 20)

Mereghetti, S. & Grindlay, J. E. 1987, ApJ, 312, 727

Middleditch, J. & Priedhorsky, W. C. 1986, ApJ, 306, 230

Miller, M. C. 1999, ApJLetters, submitted

Miller, M. C. & Lamb, F. K. 1998, ApJ, 499, L37

Miller, M. C., Lamb, F. K., & Psaltis, D. 1998, ApJ, 508, 791

Mitsuda K. & Dotani T. 1989, PASJ, 41, 557

Miyamoto, S., Kimura, K., Kitamoto, S., Dotani, T., & Ebisawa, K. 1991, ApJ, 383, 784

Morgan, E. H. 1994, American Astronomical Society Meeting, 184, 26.02

Morgan, E. H. & Smith, D. A. 1996, IAU Circ., 6437

Murakami, T., Fujii, M., Hayashida, K., Itoh, M., Nishimura, J., Yamagami, T., Conner, J. P., Evans, W. D., Fenimore, E. E., Klebesadel, R. W., Spencer, K. M., Murakami, H., Kawai, N., Kondo, I., & Katoh, M. 1989, PASJ, 41, 405

Norris, J. P. & Wood, K. S. 1985, IAU Circ., 4087
Olive, J. F., Barret, D., Boirin, L., Grindlay, J. E., Swank, J. H., & Smale, A. P. 1998, A&A, 333, 942
Penninx, W., Lewin, W. H. G., Mitsuda, K., van der Klis, M., van Paradijs, J., & Zijlstra, A. A. 1990, MNRAS, 243, 114
Penninx, W., Lewin, W. H. G., Tan, J., Mitsuda, K., van der Klis, M., & van Paradijs, J. 1991, MNRAS, 249, 113
Priedhorsky, W., Hasinger, G., Lewin, W. H. G., Middleditch, J., Parmar, A., Stella, L., & White, N. 1986, ApJ, 306, L91
Priedhorsky W. C. & Holt S. S. 1987, Space Sci. Rev., 45, 291
Prins, S. & van der Klis, M. 1997, A&A, 319, 498
Psaltis, D. & Chakrabarty, D. 1999, ApJ, submitted
Psaltis, D., Lamb, F. K., & Miller, G. S. 1995, ApJ, 454, L137
Psaltis, D., Méndez, M., Wijnands, R., Homan, J., Jonker, P. G., van der Klis, M., Lamb, F. K., Kuulkers, E., van Paradijs, J., & Lewin, W. H. G. 1998, ApJ, 501, L95
Psaltis, D., Wijnands, R., Homan, J., Jonker, P. G., van der Klis, M., Miller, M. C., Lamb, F. K., Kuulkers, E., van Paradijs, J., & Lewin, W. H. G. 1999a, ApJ, submitted
Psaltis, D., Belloni, T., & van der Klis, M. 1999b, ApJLetters, submitted
Radhakrishnan, V. & Srinivasan, G. 1982, Curr. Sci., 1096
Remillard, R. A., Morgan, E. H., McClintock, J. E., Bailyn, C. D., Orosz, J. A. 1999, ApJ, submitted
Revnivtsev, M. , Gilfanov. M., & Churazov, E. 1998, A&A, 339, 483
Rothschild, R. E., Blanco, P. R., Gruber, D. E., Heindl, W. A., Macdonald, D. R., Marsden, D. C., Pelling, M. R., Wayne, L. R., & Hink, P. L. 1998, ApJ, 496, 538
Scargle, J. D. 1982, ApJ, 263, 835
Schulz, N. S., Hasinger, G., & Trümper, J. 1989, A&A, 225, 48
Schwarzenberg-Czerny, A. 1992, A&A, 260, 268
Shirey, R. E. 1998, Thesis, Massachusetts Insitute of Technology, USA
Smale, A. P. 1998, ApJ, 498, L141
Smale, A. P. & Lochner J. C., 1992, ApJ, 395, 582
Smale, A. P., Kuulkers E., & Wijnands R. A. D. 1996a, IAU Circ., 6452
Smale, A. P., Zhang, W., & White, N. E. 1996b, IAU Circ., 6507
Smale, A., Zhang, W., & White, N. E. 1997, ApJ, 483, L119
Smith, D. A., Morgan, E. H., & Bradt, H. 1997a, ApJ, 479, L137
Smith, D. M., Heindl, W. A., Swank, J., Leventhal, M., Mirabel, I. F., & Rodriquez, L. F. 1997b, ApJ, 489, L51
Srinivasan, G. 1997, In: *Stellar Remnants*, Saas-Fee Advanced Course 25 (Springer-Verlag), p. 97
Stella, L., White, N.E., & Rosner, R. 1986, ApJ, 308, 669
Stella, L. & Vietri, M. 1998, ApJ, 492, L59
Stellingwerf, R. F. 1978, ApJ, 224, 953
Strohmayer, T. E. 1998, In: *Accretion Processes in Astrophysics: Some Like It Hot*, S. S. Holt & T. R. Kallman (eds.), AIP conference proceedings 431, p. 397

Strohmayer, T., Zhang, W., & Swank, J. 1996a, IAU Circ., 6320
Strohmayer, T., Zhang, W., Smale, A., Day, C., Swank, J., Titarchuk, L., & Lee, U. 1996b, IAU Circ., 6387
Strohmayer T., Lee, U., & Jahoda, K. 1996c, IAU Circ., 6484
Strohmayer, T. E., Zhang, W., Swank, J. H., Smale, A., Titarchuk, L., Day, C., & Lee, U. 1996d, ApJ, 469, L9
Strohmayer, T. E., Zhang, W., & Swank, J. H. 1997a, ApJ, 487, L77
Strohmayer, T. E., Jahoda, K., Giles, A. B., & Lee, U. 1997b, ApJ, 486, L47
Strohmayer, T. E., Zhang, W., Swank, J. H., White, N. E., & Lapidus I. 1998a, ApJ, 498, L135
Strohmayer, T. E., Zhang, W., Swank, J. H., & Lapidus, I. 1998b, ApJ, 503, L147
Sunyaev, R. 1989, IAU Circ., 4839
Swank, J. H. 1998, In: *The Hot Universe*, IAU S188, (Kluwer Academic Publishers) K. Koyama, S. Kitamoto, & M. Itoh, (eds.), p. 107
Sztajno, M., van Paradijs, J., Trümper, J., Langmeier, A., Lewin, W. H. G., & Pietsch, W. 1986, MNRAS, 222, 499
Tawara, Y., Hirano, T., Kii, T., Matsuoka, M., & Murakami, T. 1984, PASJ, 36, 861
Tsunemi, H., Kitamoto, S., Manabe, M., Miyamoto, S., Yamashita, K., & Nakagawa, M. 1989, PASJ, 41, 391
Turner, M. J. L., Thomas, H. D., Patchett, B. E., Reading, D. H., Makishima, K., Ohashi, T., Dotani, T., Hayashida, K., Inoue, H., Kondo, H., Koyama, K., Mitsusa, K., Ogawara, Y., Takano, S., Awaki, H., Tawara, Y., & Nakamura, N. 1989, PASJ, 41, 345
van Paradijs, J., Cominsky, L., Lewin, W. H. G., & Joss, P. C. 1979, Nature, 280, 375
van Paradijs, J., Penninx, W., Lewin, W. H. G., Sztajno, M., Trümper, J. 1988, A&A, 192, 147
van Paradijs, J., Zhang, W., Marshall, F., Swank, J. H., Augusteijn, T., Kuulkers, E., Lewin, W. H. G., Lamb, F., Lapidus, I., Lochner, J., Strohmayer, T., van der Klis, M., Vaughan, B. 1996, IAU Circ., 6336
van der Klis, M. 1989, In: *Timing Neutron Stars*, H. Ögelman & E. P. J. van den Heuvel (eds.) (Dordrecht: Kluwer), NATO ASI Series C, 262, p. 27
van der Klis M. 1991, In: *Neutron Stars: Theory and Observations*, J. Ventura & D. Pines (eds.) (Kluwer, Dordracht), NATO ASI Series C, 344, p. 319
van der Klis, M. 1994a, A&A, 283, 469
van der Klis, M. 1994b, ApJS, 92, 511
van der Klis, M. 1995, In: *X-ray Binaries*, W. H. G. Lewin, J. van Paradijs, & E. P. J. van den Heuvel (eds.), (Cambridge University Press), p. 252
van der Klis, M. 1998, In: *The Many Faces of Neutron Stars*, R. Buccheri, J. van Paradijs, & M. A. Alpar (eds.) (Kluwer, Dordrecht), NATO ASI Series C, 515, p. 337
van der Klis, M., Jansen, F., van Paradijs, J., Lewin, W. H. G., van den Heuvel, E. P. J., Trumper, J. E., & Sztajno, M. 1985a, Nature, 316, 225
van der Klis, M., Jansen, F., White, N., Stella, L., & Peacock, A. 1985b, IAU Circ., 4068
van der Klis, M., Jansen, F., van Paradijs, J., Lewin, W. H. G., Sztajno, M., & Trumper, J. 1987a, ApJ, 313, L19

van der Klis, M., Stella, L., White, N., Jansen, F., & Parmar, A. N. 1987b, ApJ, 316, 411

van der Klis, M., Swank, J., Zhang, W., Jahoda, K., Morgan, E., Lewin, W., Vaughan, B., & van Paradijs, J. 1996a, IAU Circ., 6319

van der Klis, M., Wijnands, R., Chen, W., Lamb, F. K., Psaltis, D., Kuulkers, E., Lewin, W. H. G., Vaughan, B., van Paradijs, J., Dieters, S., & Horne, K. 1996b, IAU Circ., 6424

van der Klis, M., van Paradijs, J., Lewin. W. H. G., Lamb, F. K., Vaughan, B., Kuulkers, E., & Augusteijn, T. 1996c, IAU Circ., 6428

van der Klis, M., Wijnands, R., Lamb, F. K., Psaltis, D., Dieters, S., van Paradijs, J., Lewin, W. H. G., & Vaughan, B. 1996d, IAU Circ., 6511

van der Klis, M., Swank, J. H., Zhang, W., Jahoda, K., Morgan, E. H., Lewin, W. H. G., Vaughan, B., & van Paradijs, J. 1996e, ApJ, 469, L1

van der Klis, M., Homan, J., Wijnands, R., Kuulkers, E., Lamb, F. K., Psaltis, D., Dieters, S., van Paradijs, J., Lewin, W. H. G., & Vaughan, B. 1997a, IAU Circ., 6565

van der Klis, M., Wijnands, R. A. D., Horne, K., & Chen, W. 1997b, ApJ, 481, L97

Vaughan, B. A., van der Klis, M., Wood, K. S., Norris, J. P., Hertz, P., Michelson, P. F., van Paradijs, J., Lewin, W. H. G., Mitsuda, K., & Penninx, W. 1994, ApJ, 435, 362

Verbunt, F. & van den Heuvel, E. P. J. 1995, In: *X-ray Binaries*, W. H. G. Lewin, J. van Paradijs, & E. P. J. van den Heuvel (eds.), (Cambridge University Press), p. 457

Vrtilek, S. D., Kahn, S. M., Grindlay, L. E., Seward, F. D., & Helfand, D. J. 1986, ApJ, 307, 698

Vrtilek, S. D., Swank, J. H., Kelly, R. L., & Kahn, S. M. 1988, ApJ, 329, 276

White, N.E. & Zhang, W. 1997, ApJ, 490, L87

Wijnands, R. & van der Klis, M. 1998, IAU Circ., 6876

Wijnands, R. A. D., Kuulkers, E., & Smale, A. P. 1996a, ApJ, 473, L45

Wijnands, R. A. D., van der Klis, M., van Paradijs, J., Lewin, W. H. G., Lamb, F. K., Vaughan, B., Kuulkers, E., Augusteijn, T. 1996b, IAU Circ., 6447

Wijnands, R., van der Klis, M, & van Paradijs, J. 1998, In: *The Hot Universe*, IAU S188 K. Koyama, S. Kitamoto, & M. Itoh (eds.), (Kluwer Academic Publishers), p. 370

Wood, K. S., Hertz, P., Norris, J. P., Vaughan, B. A., Michelson, P. F., Mitsuda, K., Lewin, W. H. G., van Paradijs, J., Penninx, W., & van der Klis, M. 1991, ApJ, 379, 295

Yoshida, K., Mitsuda, K., Ebisawa, K., Ueda, Y., Fujimoto, R., Yaqoob, T., & Done, C. 1993, PASJ, 45, 605

Yu, W., Zhang, S. N., Harmon, B. A., Paciesas, W. S., Robinson, C. R., Grindlay, J. E., Bloser, P., Barret, D., Ford, E. C., Tavani, M., & Kaaret, P. 1997, ApJ, 490, L153

Yu, W., Li, T. P., Zhang, W., & Zhang, S. N. 1999, ApJLetters, in press

in 't Zand, J. J. M., Heise, J., Muller, J. M., Bazzano, A., Cocchi, M., Natalucci, L., & Ubertini, P. 1998, A&A, 331, L25

Zhang, W. 1995, XTE/PCA Internal Memo

Zhang, W., et al. 1993, Proc. SPIE, 2006, 324

References

Zhang, W., Jahoda, K., Swank, J. H., Morgan, E. H., & Giles, A. B. 1995, ApJ, 449, 930
Zhang, W., Lapidus, I., White, N. E., & Titarchuk, L. 1996, ApJ, 469, L17
Zhang, W., Lapidus, I., Swank, J. H., White, N. E., Titarchuk, L. 1997, IAU Circ., 6541
Zhang, W., Jahoda, K., Kelley, R. L., Strohmayer, T. E., Swank, J. H., & Zhang, S. N. 1998a, ApJ, 495, L9
Zhang, W., Strohmayer, T. E., & Swank, J. H. 1998b, ApJ, 500, L167
Zhang, W., Smale, A. P., Strohmayer, T. E., & Swank, J. H. 1998c, ApJ, 500, L171

Milliseconde verschijnselen in röntgendubbelsterren

Introductie

In dit proefschrift beschrijf ik satellietwaarnemingen van lage-massa röntgendubbelsterren, waarin een compacte ster, een neutronenster of een zwart gat, en een lichte normale ster, zoals de zon of kleiner, dicht om elkaar heen draaien. Onder invloed van de sterke zwaartekracht van de compacte ster zal de normale ster vervormen waardoor gas uit haar atmosfeer richting het compacte object zal stromen. Deze materie valt niet rechtstreeks op dit object, maar vormt een zogenaamde accretieschijf (zie Figuur 1). Het in deze platte schijf steeds sneller naar binnen spiraliserende gas zal uiteindelijk op het oppervlak van de neutronenster vallen, of in het zwarte gat verdwijnen. Naarmate het gas dichter bij de compacte ster komt, zal het door interne wrijving steeds heter worden (10 tot 100 miljoen graden); het zendt dan voornamelijk röntgenstraling uit. In principe geldt dat hoe meer gas per seconde naar binnen valt, dus hoe hoger deze massaoverdrachtssnelheid is, des te helderder het systeem is.

Als het compacte object een neutronenster is met een relatief sterk magneetveld (10^{10-12} Gauss), dan kan het gas niet direct op de ster vallen, maar zal het via magnetische veldlijnen naar de magnetische polen worden geleid. Daar zal het op het oppervlak van de ster hete plekken veroorzaken die extra röntgenstraling uitzenden. Als nu de as van het magneetveld niet samenvalt met de rotatieas van de neutronenster, dan draaien deze hete plekken rond met de rotatieperiode van de ster. Hierdoor wordt de röntgenhelderheid periodiek gemoduleerd; we zien dan zogenaamde röntgenpulsaties.

Een ander fenomeen dat alleen wordt waargenomen bij neutronensterren zijn de röntgenflitsen ("X-ray bursts"). Dit zijn kortstondige, zeer heldere flitsen die ontstaan als het gas dat is verzameld op het oppervlak de juiste temperatuur en de juiste dichtheid heeft bereikt zodat er in het gas spontaan kernfusie plaatsvindt. Deze kernfusie is van korte duur en gaat samen met een enorme toename van de röntgenhelderheid van het systeem.

De fysica achter röntgendubbelsterren

Door het bestuderen van de röntgenstraling afkomstig van röntgendubbelsterren hopen we beter inzicht te krijgen in hoe materie zich gedraagt bij zeer hoge dichtheden, zoals in

een neutronenster. Ook probeert men de algemeen-relativistische effecten die optreden in de buurt van een neutronenster of een zwart gat waar te nemen en te onderzoeken. Eén van de fundamentele eigenschappen van een systeem waar men probeert achter te komen is of het compacte object een neutronenster of een zwart gat is. We weten dat in sommige systemen een neutronenster aanwezig moet zijn vanwege het feit dat in die systemen pulsaties of flitsen zijn waargenomen. Voor beide fenomenen is een vast oppervlak nodig dat alleen aanwezig is bij neutronensterren. Voor zwarte gaten zijn (nog) geen observationele eigenschappen bekend die met zekerheid alleen bij zwarte gaten gezien kunnen worden. Als er geen pulsaties of flitsen worden waargenomen is het dan ook heel moeilijk om definitief vast te stellen of de compacte ster een neutronenster is of een zwart gat.

Röntgendubbelsterren versus milliseconde radio pulsars

Röntgendubbelsterren worden ook bestudeerd vanwege hun rol in de evolutie van dubbelsterren. Voor dit proefschrift is voornamelijk het evolutionaire verband tussen de lage-massa röntgendubbelsterren en de milliseconde radiopulsars van belang. Deze radiopulsars zijn oude, zeer snel roterende (rotatieperioden kleiner dan 10 ms) neutronensterren met een zwak magneetveld (10^8 Gauss). Normale radiopulsars zijn jonge, langzaam roterende (rotatieperioden groter dan enkele tientallen milliseconden) neutronensterren met een sterk magneetveld (10^{12} Gauss). De gangbare evolutietheorie is dat de milliseconde radiopulsars ooit ontstaan zijn als gewone radiopulsars, die worden geboren in een supernova explosie waarbij de kern van een zware ster (met een massa van meer dan tien zonsmassa's) ineenstort en een compacte neutronenster vormt. Het sterke magneetveld en de relatief snelle rotatie van deze neutronenster produceren een electrisch veld dat deeltjes uit het oppervlak trekt bij de magneetpolen. Deze deeltjes worden versneld langs de magneetlijnen en zenden daarbij radiostraling uit in een bundel evenwijdig aan de magneetas. Als deze as niet evenwijdig is aan de rotatieas van de ster dan zwiept deze bundel van radiostraling door de ruimte. Als de aarde in het pad van deze bundel ligt dan zien wij periodieke radioflitsjes; we zien de neutronenster als een radiopulsar. De snelst waargenomen spinperiode van zo'n jonge neutronenster is enkele tientallen milliseconden. Het mechanisme achter de radiopulsaties kost veel energie. Deze energie wordt gehaald uit de rotatie-energie van de pulsar. Deze gaat daardoor steeds langzamer draaien totdat er niet meer genoeg energie kan worden opgewekt om radiostraling te produceren. De pulsar dooft uit.

In de meeste gevallen is dit het einde van het "zichtbare" leven van de neutronenster. Draait om de neutronenster echter een andere, zonachtige ster dan kan de pulsar een tweede leven krijgen. Het systeem zal verder evolueren op tijdschalen die overeen komen met de levensduur van de begeleider (enkele miljarden jaren). Aan het einde van zijn leven zwelt de begeleider op waardoor de zwaartekracht van de neutronenster een grotere invloed heeft. In een bepaald stadium van de evolutie vindt er massaoverdracht plaatst van de zonachtige ster naar de neutronenster. Het systeem wordt nu zichtbaar als een lage-massa röntgendubbelster. Het impulsmoment van het gas dat op

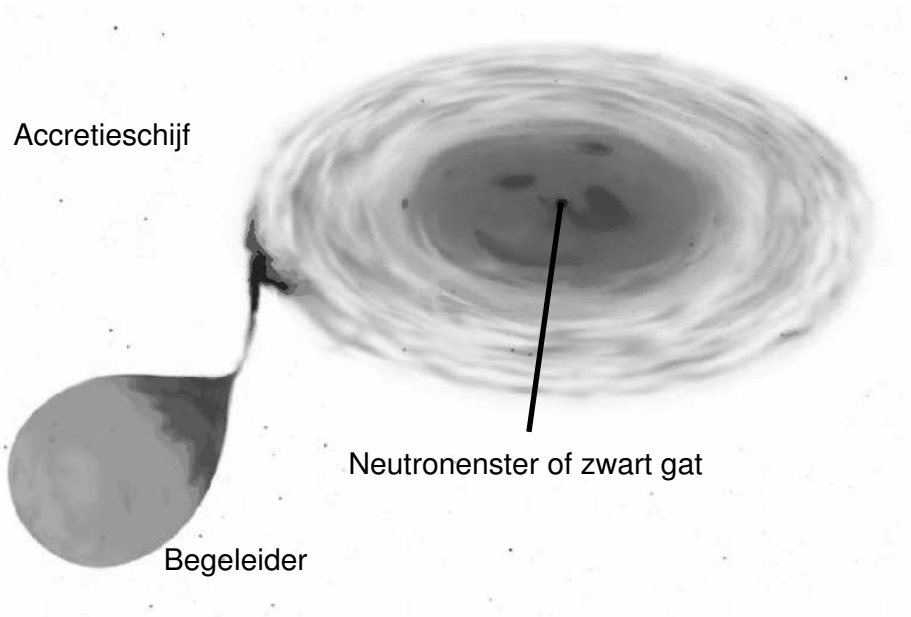

Figuur 1: Een model van een lage-massa röntgendubbelster (credit: NASA/STScI).

de neutronenster valt, wordt gedeeltelijk overgedragen aan de neutronenster die daardoor steeds sneller gaat draaien. Het gas zorgt er ook voor dat het magneetveld van de neutronenster steeds zwakker wordt. Het precieze fysische proces dat hiervoor verantwoordelijk is onbekend. Als de massaoverdracht op een gegeven moment stopt dan draait de neutronenster bijna duizend keer per seconde om zijn as en wordt zichtbaar als een milliseconde radiopulsar.

Deze theorie voorspelt dat tijdens de lage-massa röntgendubbelsterfase het systeem zichtbaar moet zijn als een milliseconde röntgenpulsar. De electrisch geladen deeltjes in het gas worden namelijk via de lijnen van het magneetveld naar de magneetpolen van de ster geleid, alwaar het hete plekken op het oppervlak zal creeëren, die rond draaien met de rotatieperiode van de ster en daardoor de röntgenhelderheid periodiek moduleren. Zulke snelle röntgenpulsaties werden niet waargenomen, hetgeen er voor zorgde dat men aan de theorie ging twijfelen.

Waarnemeningen van röntgendubbelsterren

Het tijdperk vóór *RXTE*

De röntgenstraling die wordt uitgezonden door lage-massa röntgendubbelsterren kan niet rechtstreeks op aarde worden gedetecteerd omdat de aardatmosfeer deze straling absorbeert. Om deze straling toch te kunnen waarnemen worden satellieten gelanceerd die de röntgendetectoren buiten de dampkring brengen. Röntgendubbelsterren kunnen erg helder zijn en daarom goed onderzocht worden. De eerste lage-massa röntgendubbelster, Scorpius X-1, werd al ontdekt in 1962. Daarna werden de eer-

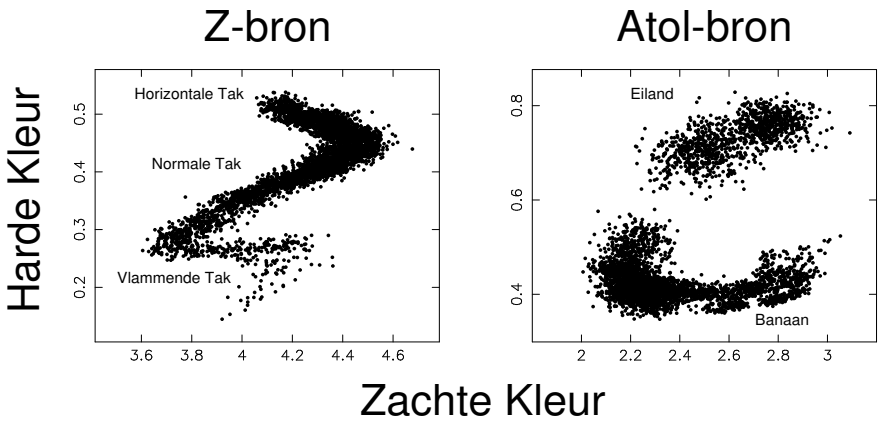

Figuur 2: Het kleur-kleur diagram van een Z en een atol-bron

ste systemen ontdekt die pulsen en flitsen vertoonden. Met behulp van gegevens afkomstig van de *EXOSAT* en de Japanse *Ginga* satellieten werden de fluctuaties in de röntgenhelderheid zeer gedetailleerd bestudeerd. Men ontdekte dat de helderheid van de helderste van de lage-massa röntgendubbelsterren quasi periodiek variëert. Deze variaties worden quasi-periodieke oscillaties of QPOs genoemd. Verschillende modellen voor deze QPOs werden bedacht zoals het magnetosferische verschil-frequentie model of het model dat aanneemt dat bepaalde QPOs veroorzaakt worden door geluidsgolven in de accretieschijf.

Om meer inzicht in lage-massa röntgendubbelsterren en QPOs te krijgen bleek het zeer handig om zogenaamde kleur-kleur diagrammen van deze bronnen te maken (Figuur 2). Om een kleur-kleur diagram te maken wordt het röntgenspectrum van zo'n bron verdeeld in vier brede energiebanden. De hoeveelheid röntgenstraling in elke band wordt gemeten en twee kleuren worden bepaald. De zachte kleur is de verhouding van de hoeveelheid straling in de laagste twee energiebanden, met als noemer de laagste energieband. De harde kleur is het quotiënt van de hoeveelheid straling in de hoogste twee energiebanden, met als noemer de laagste energieband van deze twee. Een kleur-kleur diagram wordt verkregen door de harde kleur tegen de zacht kleur te plotten. Door de kleuren te bepalen voor vaste tijdsintervallen (16 tot 256 seconden) kunnen veranderingen van het spectrum in de tijd worden gevolgd en bestudeerd. Door spectrale veranderingen zal de bron terecht komen op verschillende plaatsen in het diagram en verschillende bronnen zullen een verschillend patroon tonen, zoals in Figuur 2 is te zien.

Onder andere met behulp van deze diagrammen en de studie van de aperiodieke helderheidsfluctuaties, zoals QPOs, konden de helderste lage-massa röntgendubbelsterren worden onderverdeeld in de Z en de atol-bronnen, genoemd naar het patroon dat ze vertonen in het kleur-kleur diagram. De Z bronnen vormen een Z-achtige structuur in het diagram (Figuur 2), waarvan de bovenste tak de horizontale tak wordt genoemd. Wanneer de bron op deze tak wordt waargenomen dan worden er QPOs gedetecteerd met een frequentie van tussen de 15 en de 60 Hz. Op de diagonale tak (de normale

tak) worden deze QPOs ook nog waargenomen, vaak tegelijkertijd met een ander type QPO bij 6 Hz. Op de laatste tak, de vlammende tak, neemt de frequentie van de 6 Hz QPO toe tot ongeveer 20 Hz. Op alle takken worden ook verschillende soorten ruis waargenomen.

De atol-bronnen vormen een kromme tak in het kleur-kleur diagram die een atol-achtige vorm heeft (Figuur 2). Deze tak kan worden onderverdeeld in een eiland en een banaan. Als de bron in een eiland-toestand is wordt er zeer sterke ruis gedetecteerd. De sterkte van deze ruis neemt geleidelijk af als de bron richting de banaan beweegt.

Voor zowel de Z als de atol-bronnen geldt dat de positie in het kleur-kleur diagram en eigenschappen van de snelle helderheidsfluctuaties worden bepaald door de massaoverdrachtssnelheid. In sommige gevallen is deze snelheid niet de enige factor. In hoofdstuk 3 worden alle waarnemingen besproken van de lage-massa röntgendubbelster en Z bron Cygnus X-2 die werden verkregen met de *Ginga* satelliet. Uit deze analyse bleek dat de aperiodieke variabiliteit (de QPOs en de ruis) niet alleen afhangt van de positie in de Z, maar ook van de gemiddelde helderheid van de bron. De gemiddelde helderheid van Cygnus X-2 varieert langzaam op tijdschalen van weken tot maanden, wat goed zichtbaar is in Figuur 2.4. Het blijkt dat op het moment dat deze gemiddelde helderheid het hoogst is de 6 Hz QPO op de normale tak niet kan worden waargenomen, terwijl bij lagere gemiddelde helderheid deze QPO wel is te zien. Er is dus nog iets anders in het spel dat de specifieke eigenschappen van de bron bepaald. Een accretieschijf die periodiek de binnenste delen van het systeem aan de waarneming onttrekt zou een mogelijke verklaring kunnen zijn.

Het tijdperk van *RXTE*

De lancering van de *RXTE* satelliet op 30 december 1995 luidde een nieuw tijdperk in. Voor het eerst werden er milliseconde fenomenen in lage-massa röntgendubbelsterren ontdekt. In de hoofdstukken 5 tot en met 10 worden de ontdekkingen van QPOs met frequenties tussen 200 en 1200 Hz (de kHz QPOs) gerapporteerd in drie Z bronnen (GX 17+2, Cygnus X-2 en GX 5–1) en 3 atol-bronnen (4U 1636–53, KS 1731−260 en 4U 1735–44). Afgezien van 4U 1735–44 werden in alle bronnen twee kHz QPOs tegelijkertijd waargenomen (Figuur 3). Later werden ook in 4U 1735–44 twee kHz QPOs tegelijkertijd waargenomen.

De frequenties van de kHz QPOs zijn het laagst wanneer de massaoverdrachtssnelheid laag is. Als deze toeneemt dan nemen ook de frequenties toe. De kHz QPOs worden slechts binnen een beperkt bereik van de overdrachtssnelheid waargenomen; als de snelheid te hoog of te laag is dan worden geen QPOs gezien. Naast de zes bronnen behandeld in dit proefschrift zijn in nog twaalf andere bronnen dezelfde QPOs ontdekt. De eigenschappen van deze QPOs hebben geleid tot ondere andere het volgende model: de kHz QPO met de hoogste frequentie wordt geïdentificeerd met de frequentie van de baanbeweging van gasdeeltjes op een bepaalde afstand van de neutronenster en de andere kHz QPO wordt geïdentificeerd met de verschilfrequentie van de hoogste frequentie kHz QPO en de neutronensterspinfrequentie. Dit betekent dat uit het frequentieverschil van de kHz QPOs de spinfrequentie van de neutronenster kan worden afgeleid. Eén van de fundamenten van deze theorie is dat in sommige van de bron-

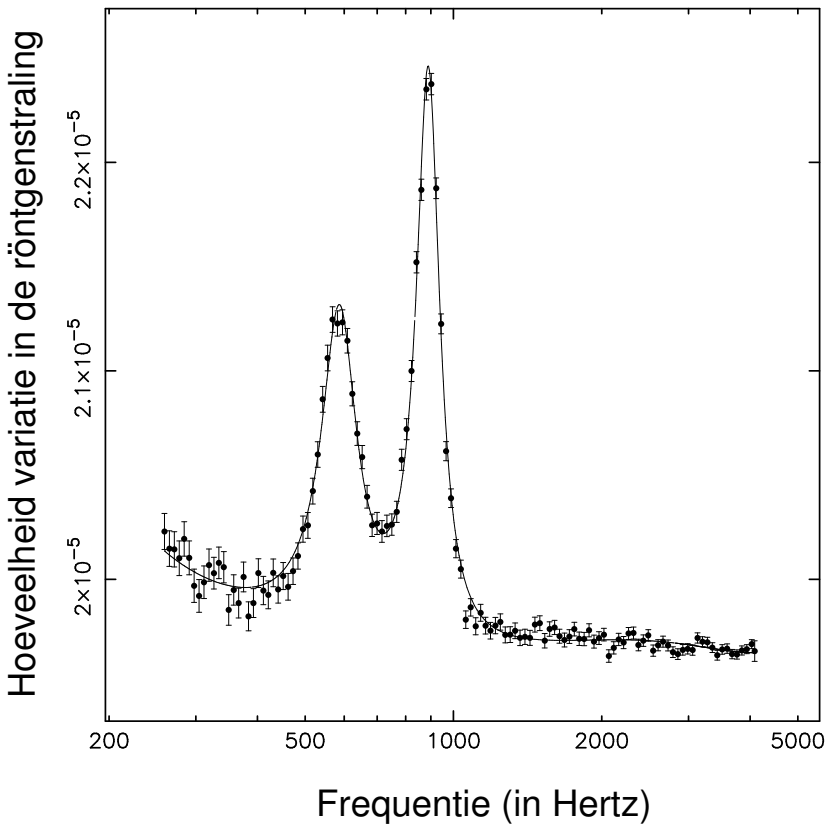

Figuur 3: Kilohertz QPOs in de lage-massa röntgendubbelster Scorpius X-1

nen met twee kHz QPOs er tijdens röntgenflitsen een bijna coherente oscillatie wordt waargenomen. Deze oscillatie wordt geïdentificeerd met de spin van de neutronenster. De frequentie van deze oscillatie is gelijk aan het frequentieverschil van de twee kHz QPOs. Dit maakt het model voor de kHz QPOs erg plausibel.

Helaas, kan deze theorie niet alles verklaren wat is waargenomen. In alle bronnen die in dit proefschrift worden besproken nemen beide QPOs in frequentie zodanig toe dat het frequentieverschil consistent is met een constante waarde. In twee bronnen (de Z bron Scorpius X-1 en de atol-bron 4U 1608–52) is het frequentieverschil van de kHz QPOs echter niet constant, hetgeen men wel zou verwachten als dit verschil gelijk is aan de spinfrequentie van de neutronenster. Bovendien sluiten de fouten op de gemeten waarden voor de frequenties in andere bronnen een soortgelijke afname als gezien is in deze twee bronnen niet uit. Deze afname komt niet door een afname van de spinfrequentie van de ster omdat deze niet op de zeer korte tijdschalen kan veranderen waarop het frequentieverschil variëert. Ook is er één atol-bron bekend waarin de frequentie van de oscillaties tijdens de röntgenflitsen niet precies gelijk is aan het frequentieverschil van de kHz QPOs. Het is duidelijk dat het mechanisme achter de kHz QPOs veel gecompliceerder is dan op het eerste gezicht werd gedacht.

De milliseconde röntgenpulsar

De lage-massa röntgendubbelster die duidelijkheid kan verschaffen in het begrijpen van de aperiodieke milliseconde verschijnselen is de zeer recent ontdekte milliseconde röntgenpulsar SAX J1808.4–3658. Zoals het voorvoegsel SAX al aangeeft werd deze bron voor het eerst waargenomen met de *BeppoSAX* satelliet. In 1996 was deze bron zichtbaar gedurende ongeveer drie weken. *BeppoSAX* heeft toen naar deze bron gekeken en nam röntgenflitsen afkomstig van deze bron waar. Helaas heeft de *RXTE* satelliet toen niet naar deze bron gekeken. Na ongeveer drie weken was de röntgenhelderheid van deze bron zo ver gedaald dat hij niet meer kon worden waargenomen. In april 1998 ontdekte de *RXTE* satelliet dat de helderheid van deze bron weer toenam en nu werd de bron wel waargenomen door *RXTE*. In hoofdstuk 11 rapporteer ik de ontdekking van de 2.5 ms pulsaties in de persistente röntgenstraling van deze bron. Deze pulsaties geven aan dat de neutronenster in dit systeem meer dan 400 keer per seconde om zijn as draait. Sterrenkundigen in de VS ontdekten verder dat om de neutronenster een begeleider draait die een massa heeft van minder dan de helft van de zon en dat deze begeleider elke twee uur om de neutronenster draait. Het bestaan van deze bron bevestigt het evolutionair verband tussen de lage-massa röntgendubbelsterren en de milliseconde radiopulsars dat volgens de gangbare evolutietheorie moet bestaan.

Helaas werden in 1998 door *RXTE* geen röntgenflitsen, en dus geen oscillaties tijdens de flitsen, of kHz QPOs waargenomen. Het waarnemen van deze verschijnselen in de milliseconde röntgenpulsar zou een goede test van de modellen kunnen zijn. Omdat in dit systeem de exacte spinfrequentie bekend is zou direct kunnen worden gecontroleerd of de frequenties van de flitsoscillaties en het frequentieverschil tussen de twee kHz QPOs inderdaad kunnen worden geïdentifeerd met de spinfrequentie. Hopelijk zal deze bron voor het einde van de *RXTE* missie nog één of meerdere uitbarstingen vertonen en zullen tijdens deze uitbarsting(en) de flitsoscillaties en de kHz QPOs worden gedetecteerd.

De ontdekking van de pulsaties van deze bron roept veel vragen op, zoals waarom de andere lage-massa röntgendubbelsterren niet pulseren. Afgezien van de pulsaties lijkt SAX J1808.4–3658 namelijk erg op andere bronnen. In hoofdstuk 12 wordt aangetoond dat de aperiodieke helderheidsfluctuaties niet te onderscheiden zijn van die van andere, niet pulserende lage-massa röntgendubbelsterren. In hoofdstuk 13 wordt zelfs aangetoond dat dit wat betreft fluctuaties langzamer dan een honderste van een seconde ook geldt voor de systemen die een zwart gat bevatten. Deze twee hoofdstukken bewijzen dat het mechanisme dat de aperiodieke fluctuaties veroorzaakt zich ergens in de accretieschijf moet bevinden buiten een eventuele magnetosfeer die aanwezig zou kunnen zijn in de neutronenstersystemen en die vrijwel zeker aanwezig is in de milliseconde röntgenpulsar. In deze laatste is de magnetosfeer kleiner dan 30 km, dus het mechanisme dat deze fluctuaties veroorzaakt is ongeveer drie neutronensterstralen (ongeveer 10 km) verwijderd van de ster zelf. De meeste energie wordt echter veel dichter bij de compacte ster vrijgemaakt en omgezet in röntgenstraling. De hoeveelheid röntgenstraling die wordt uitgestraald op meer dan 30 km van het compact object is niet genoeg om de soms zeer sterke fluctuaties te kunnen veroorzaken. Dit betekent dat het productie mechanisme niet direkt de röntgenstraling beïnvloedt, maar er voor

zorgt dat de hoeveelheid materie die wordt overgedragen variëert. Deze variatie wordt dan dichter bij de compacte objecten overgedragen op de hoeveelheid uitgestraalde röntgenstraling. Het bestuderen van deze aperiodieke verschijnselen en het vergelijken van de resultaten van neutronenstersystemen en zwarte gat systemen kunnen zeer sterke beperkingen stellen aan het exacte productiemechanisme van deze fluctuaties.

List of publications

The millisecond X-ray pulsar

- Wijnands, R. & van der Klis, M.
  A Millisecond Pulsar in an X-ray Binary System
  1998 Nature 394, 344

- Wijnands, R & van der Klis, M.
  The Broadband Power Spectrum of SAX J1808.4–3658
  1998 ApJ 507, L63

Kilohertz quasi-periodic oscillations

- Wijnands, R. A. D., van der Klis, M., van Paradijs, J., Lewin, W. H. G., Lamb, F. K., Vaughan, B., & Kuulkers, E.
  Discovery in 4U 1636–53 of Two Simultaneous Quasi-periodic Oscillations near 900 Hz and 1176 Hz
  1997 ApJ 479, L141

- van der Klis, M., Wijnands, R. A. D., Horne, K., & Chen, W.
  Kilohertz Quasi-Periodic Oscillation Peak Separation Is Not Constant in Scorpius X-1
  1997 ApJ 481, L97

- Wijnands, R. A. D. & van der Klis, M.
  Discovery of Two Simultaneous Kilohertz Quasi-Periodic Oscillations in KS 1731–260
  1997 ApJ 482, L65

- Vaughan, B. A., van der Klis, M., Méndez, M., van Paradijs, J., Wijnands, R. A. D., Lewin, W. H. G., Lamb, F. K., Psaltis, D., Kuulkers, E., & Oosterbroek, T.
  Discovery of Microsecond Time Lags in Kilohertz QPOs
  1997 ApJ 483, L115

- Wijnands, R., Homan, J., van der Klis, M., Méndez, M., Kuulkers, E., van Paradijs, J., Lewin, W. H. G., Lamb, F. K., Psaltis, D., & Vaughan, B.
  Discovery of Kilohertz Quasi-Periodic Oscillations in GX 17+2
  1997 ApJ 490, L157

- Wijnands, R., Homan, J., van der Klis, M., Kuulkers, E., van Paradijs, J., Lewin, W. H. G., Lamb, F. K., Psaltis, D., & Vaughan, B.
Discovery of Kilohertz Quasi-Periodic Oscillations in the Z Source Cygnus X-2
1998 ApJ 493, L87

- Wijnands, R., van der Klis, M., Méndez, M., van Paradijs, J., Lewin, W. H. G., Lamb, F. K., Vaughan, B., & Kuulkers, E.
Discovery of Kilohertz Quasi-Periodic Oscillations in 4U 1735–44
1998 ApJ 495, L39

- Jonker, P. G., Wijnands, R., van der Klis, M., Psaltis, D., Kuulkers, E., & Lamb, F. K.
Discovery of Kilohertz Quasi-periodic Oscillations in the Z Source GX 340+0
1998 ApJ 499, L191

- Psaltis, D., Méndez, M., Wijnands, R., Homan, J., Jonker, P. G., van der Klis, M., Lamb, F. K., Kuulkers, E., van Paradijs, J., & Lewin, W. H. G.
The Beat-Frequency Interpretation of Kilohertz Quasi-periodic Oscillations in Neutron Star Low-Mass X-ray Binaries
1998 ApJ 501, L95

- Wijnands, R., Méndez, M., van der Klis, M., Psaltis, D., Kuulkers, E., & Lamb, F. K.
Discovery of Kilohertz Quasi-Periodic Oscillations in the Z Source GX 5–1
1998 ApJ 504, L35

- Méndez, M., van der Klis, M., Wijnands, R., Ford, E. C., van Paradijs, J., & Vaughan, B. A.
Kilohertz Quasi-periodic Oscillation Peak Separation is Not Constant in the Atoll Source 4U 1608–52
1998 ApJ 505, L23

- Ford, E. C., van der Klis, M., van Paradijs, J., Méndez, M., Wijnands, R., & Kaaret, P.
Discovery of a Second Kilohertz QPO in the X-ray Binary 4U 1735–44
1998 ApJ 508, L155

- Vaughan, B. A., van der Klis, M., Méndez, M., van Paradijs, J., Wijnands, R. A. D., Lewin, W. H. G., Lamb, F. K., Psaltis, D., Kuulkers, E., & Oosterbroek, T.
Erratum: Discovery of microsecond time lags in kilohertz QPOs
1998 ApJ 509, L145

- Méndez, M., van der Klis, M., Ford, E. C., Wijnands, R., & van Paradijs, J.
Dependence of the Frequency of the Kilohertz Quasi-Periodic Oscillations on X-ray Count Rate and Colors in 4U 1608–52
1999 ApJ Letters 511 (January 20)

- Homan, J., Méndez, M., Wijnands, R., van der Klis, M., & van Paradijs, J.
  Discovery of Twin Kilohertz Quasi-periodic Oscillations in the High Galactic Latitude X-ray Transient XTE J2123–058
  1999 ApJ Letters, in press

Other X-ray binaries articles

- Wijnands, R. A. D., van der Klis, M., Psaltis, D., Lamb, F. K., Kuulkers, E., Dieters, S., van Paradijs, J., & Lewin, W. H. G.
  Discovery of a Variable-Frequency, 50–60 Hz Quasi-Periodic Oscillation on the Normal Branch of GX 17+2
  1996 ApJ 469, L5

- Wijnands, R. A. D., Kuulkers, E., & Smale, A. P.
  Detection of a ∼78 day Period in the RXTE, Vela 5B, and Ariel 5 All-Sky Monitor Data of Cygnus X-2
  1996 ApJ 473, L45

- Wijnands, R. A. D., van der Klis, M., Kuulkers, E., Asai, K., & Hasinger, G.
  Ginga Observations of Cygnus X-2
  1997 A&A 323, 399

- Kuulkers, E., Wijnands, R., Belloni, T., Méndez, M., van der Klis, M., & van Paradijs, J.
  Absorption Dips in the Light Curves of GRO J1655–40 and 4U 1630–47 During Outburst
  1998 ApJ 494, 753

- Homan, J., van der Klis, M., Wijnands, R., Vaughan, B., & Kuulkers, E.
  Discovery of a 59–69 Hz Quasi-periodic Oscillation in GX 13+1
  1998 ApJ 499, L41

- Wijnands, R. & van der Klis, M.
  The Broadband Power Spectra of X-ray Binaries
  1999 ApJ 514 (April 1)

- Jonker, P. G., van der Klis, M., & Wijnands, R.
  A Persistent ∼1 Hz Quasi-periodic Oscillation in the Dipping Low-Mass X-ray Binary 4U 1323–619
  1999 ApJ Letters, in press

- Wijnands, R., van der Klis, M., & Rijkhorst, E.-J.
  Discovery of a ∼7 Hz Quasi-periodic Oscillation in the Low-Luminosity Low-Mass X-ray Binary 4U 1820–30
  1999 ApJ Letters 512, (February 10)

- Kuulkers, E., Wijnands, R., & van der Klis, M.
  X-ray Timing Behaviour of Cygnus X-2 at Low Intensities
  1999 MNRAS, submitted

- Homan, J., Jonker, P., Wijnands, R., van der Klis, M., & van Paradijs, J.
  A 0.5–2.5 Hz Quasi-periodic Oscillation in the Eclipsing and Dipping Low-Mass X-ray Binary EXO 0748–676
  1999 ApJ Letters, submitted

- Psaltis, D., Wijnands, R., Homan, J., Jonker, P. G., van der Klis, M., Miller, M. C., Lamb, F. K., Kuulkers, E., van Paradijs, J., & Lewin, W. H. G.
  On the Magnetospheric Beat-Frequency and Lense-Thirring Interpretations of the Horizontal Branch Oscillations in the Z Sources
  1999 ApJ, submitted

Others

- Bloemen, H., Wijnands, R., Bennett, K., Diehl, R., Hermsen, W., Lichti, G., Morris, D., Ryan, J., Schonfelder, V., Strong, A. W., Swanenburg, B. N., de Vries, C., & Winkler, C.
  COMPTEL observations of the Orion complex: Evidence for cosmic-ray induced gamma-ray lines
  1994 A&A 281, L5

IAU Circulars

- van der Klis, M., Wijnands, R., Chen, W., Lamb, F. K., Psaltis, D., Kuulkers, E., Lewin, W. H. G., Vaughan, B., van Paradijs, J., Dieters, S., & Horne, K.
  Scorpius X-1
  1996 IAU Circular 6424

- Wijnands, R. A. D., van der Klis, M., van Paradijs, J., Lewin, W. H. G., Lamb, F. K., Vaughan, B., Kuulkers, E., & Augusteijn, T.
  4U 1735–444
  1996 IAU Circular 6447

- Smale, A. P., Kuulkers, E., & Wijnands, R. A. D.
  Cygnus X-2
  1996 IAU Circular 6452

- van der Klis, M., Wijnands, R., Kuulkers, E., Lamb, F. K., Psaltis, D., Dieters, S., van Paradijs, J., Lewin, W. H. G., & Vaughan, B.
  GX 5–1
  1996 IAU Ciruclar 6511

- van der Klis, M., Homan, J., Wijnands, R., Kuulkers, E., Lamb, F. K., Psaltis, D., Dieters, S., van Paradijs, J., Lewin, W. H. G., & Vaughan, B.
  GX 17+2
  1997 IAU Circular 6565

- Kuulkers, E., Belloni, T., Méndez, M., van der Klis, M., Wijnands, R., & van Paradijs, J.
  GRO J1655–40
  1997 IAU Circular 6637

- Wijnands, R. & van der Klis, M.
  SAX J1808.4–3658 = XTE J1808–369
  1998 IAU Circular 6876

The Astronomer's Telegram

- Wijnands, R. & van der Klis, M.
  Discovery of 7–13 Hz quasi-periodic oscillations in the new X-ray transient XTE J1806−246
  1998 ATEL 17

Conference contributions

- Wijnands, R., van der Klis, M., & van Paradijs, J.
  Non-detection of kHz QPOs in GX 9+1 and GX 9+9
  1998, In *The Hot Universe* the proceedings of IAU Symposium 188 in Kyoto, K. Koyama, S. Kitamoto, & M. Itoh (eds.), p. 370–371

- Wijnands, R. & van der Klis, M
  Kilohertz Quasi-Periodic Oscillations in the Z sources GX 340+0, Cygnus X-2, GX 17+2, GX 5–1, and Scorpius X-1
  1998, In *Accretion Processes in Astrophysical Systems: Some like it hot*, Proc. of the 8th Annual Astrophysics Conference in Maryland, S. S. Holt & T. Kallman (eds.), p. 381–384

- Kuulkers, E., Wijnands, R., Belloni, T., Méndez, M., van der Klis, M., & van Paradijs, J.
  Absorption dips in GRO J1655–40: mapping the inner accretion disk
  1998, In *The Active X-ray Sky: Results from BeppoSAX and Rossi-XTE*, Nuclear Physics B Proceedings Supplements, L. Scarsi, H. Bradt, P. Giommim, & F. Fiore (eds.), Elsevier Science B.V, p. 324–329

Dankwoord

Als ik terug kijk op de vier jaren die ik aan mijn proefschrift heb besteed dan is het duidelijk dat vele mensen hebben bijgedragen aan het tot stand komen van dit proefschrift. Ik wil al deze mensen hartelijk bedanken voor hun moeite en inzet. Enkele van deze mensen wil ik in het bijzonder bedanken.

Allereerste wil ik mijn familie heel erg bedanken voor alle steun die ze me al deze jaren hebben geven. Mamma, pappa, Jolanda (en Gerard) en Miranda (en Nico) van harte bedankt voor jullie hulp.

Naast mijn familie waren ook drie zeer goede vrienden uit Leiden onontbeerlijk tijdens mijn jaren als promovendus. Ard wil ik bedanken voor alle steun. Ik denk met veel plezier terug aan onze zeer geslaagde uitstapjes naar Chili, Bolivia, Peru en Japan. Roel wil ik graag bedanken voor het zijn van een grote steun en toeverlaat. Verder denk ik met veel plezier terug aan onze avonturen in Frankrijk. Ook Sigrid was een grote hulp gedurende mijn promotietijd. Met veel plezier en met een glimlach heb ik altijd haar emailtjes gelezen over haar belevenissen met Juliette. Ik wil haar nog zeer bedanken voor de logeerplaats te Baltimore en voor de leuke tijd aldaar.

Ook in Amsterdam hebben vele mensen bijgedragen aan dit proefschrift. Daarvoor mijn oprechte dank. Ik wil mijn directe collega's in de 'X-ray' groep bedanken voor de vele stimulerende en leuke discussies. Van deze groep wil ik in het bijzonder Jeroen en Peter erg bedanken voor onze discussies tijdens onze dagelijks cola-pauze over werk, maar ook over dingen daar buiten en de gezelligheid die ze hebben gebracht. Ik wil beiden ook nog heel erg bedanken voor het vooraf doorlezen van mijn artikelen en enkele hoofdstukken van mijn proefschrift. Jeroen wil ik nog hartelijk bedanken voor ons dagtochtje naar de Efteling. En Peter, is je auto al af?

Ik wil mijn promotor Michiel ontzettend bedanken voor onze discussies en onze zeer succesvolles samenwerking in de afgelopen vier jaar. Ik hoop, en verwacht, dat er nog vele jaren zullen volgen.

Buiten de 'X-ray' groep waren er nog vele anderen op het instituut die op verschillende manieren hebben bijgedragen tot vier geslaagde jaren. Ten eerste wil ik Jeroen bedanken voor het zijn van mijn kamergenoot de afgelopen jaren. Ik wil ook twee mensen van de 'ISO' groep bedanken voor het brengen van gezelligheid: Frank (ook nog bedankt

voor het Jena avontuur) en Sacha (voor de gespreken in de late uurtjes). Ook Coen wil ik nog bedanken voor twee zeer geslaagde weken in Kyoto toen we kamergenoten waren. En, alhoewel ik vaak verloor en ik daar helemaal niet tegen kan, wil ik toch alle pingpongers bedanken voor ons dagelijks half uurtje zweten.

Verder wil ik de babbelaars van de babbelbox bedanken voor hun vele emailtjes en de gezellige dagjes en avondjes riksen, robo-rallyen, op het strand liggen, barbecuen, picknicken en bioscoopje pakken.

Ik ben zeer vereerd met het feit dat het Genootschap ter Bevoordering van Natuur-, Genees-, en Heelkunde aan mij de Andreas Bonn medaille heeft toegekend. Ik wil het genootschap hier nogmaals hartelijk voor bedanken.

I also wish to thank Steve Bloom for his approval to use, without additional copyright costs, his photograph for the cover of my thesis. Steve, you make wonderful pictures.